Investigation of Mesospheric and Thermospheric Magnesium Species from Space

Dissertation zur Erlangung des Grades
Dr. rer. nat.
der Universität Bremen, Fachbereich 1 (Physik/Elektrotechnik)

vorgelegt von
Dipl. Math. Marco Scharringhausen

Abgabe: 11.6.2007

1. Gutachter: Prof. Dr. John P. Burrows, FB 1
2. Gutachter: Prof. Dr. Justus Notholt, FB 1

Kolloquium: 19.10.2007

Für meine Eltern

Contents

Abstract

The scope of this study is the investigation of mesospheric and thermospheric metallic species. The methodology used in this work provides results in the mesosphere/lower thermosphere region (MLT) extending from approximately 70 to 500 km altitude.

The major source of metal species in the upper atmosphere is influx from cosmic dust. Along with Earth, a variety of celestial bodies orbit the Sun. The asteroid belt between Earth and Mars and the Kuiper belt outside the orbit of Neptune are well-known regions of high abundance of those objects. In addition, a number of regularly returning cometary objects present sources of cosmic material. The origin of these comets is believed to be the Oort cloud surrounding the solar system. After entering the atmosphere, particles from either source are then subject to frictional heating. This leads to sublimation of metallic species from the surface of the particles.

The impact of metal species on the chemistry and physics of the upper and middle (and, eventually, the lower) atmosphere is still a field of intense research. The total influx of meteoric cosmic material into the atmosphere is highly uncertain. Metal species are suggested to impact the removal of ozone in the upper stratosphere and the formation of water vapour in the mesosphere. Additionally, the role of meteoric particles in the formation of stratospheric clouds is of scientific interest.

Space-borne measurements present the most powerful method to investigate global distributions of metal species with moderate vertical and horizontal resolution. The SCIAMACHY instrument is capable to observe emission signals from mesospheric and thermospheric magnesium species on a global scale with good spatial and temporal coverage. This work comprises results from the first six years of measurement (2002 – 2007) of the SCIAMACHY instrument. The results presented here represent the first vertically resolved satellite measurements of mesospheric magnesium species on a global scale and a long period of time.

A comprehensive review of the distribution and variability of the two major atomic mesospheric magnesium species (Mg and Mg^+) in the upper mesosphere and lower thermosphere is provided. Seasonal variations are investigated. In the northern hemisphere, a pronounced seasonal variation with summer maxima has been found for the ionized species Mg^+. The neutral species does not exhibit such variation.

An estimation of the total influx of meteoric material has been derived from the total content of Mg. A total amount of approximately 55 t enters the atmosphere per day.

A long-term study has been carried out to analyze the impact of meteor showers on the total content of magnesium species in the upper atmosphere. The impact of meteoric showers on the total content has been found to be undetectable. It can thus be concluded that the additional mass influx of meteor showers is negligible compared to the average background flux.

The correlation between the abundance of magnesium species and the solar activity is investigated. This includes a general long-term consideration over all six years of measurement as well as short-term observations made during a large outburst of solar particles in October and November 2003. No impact of variations in the solar activity on the total content of either Mg^+ or Mg has been observed. During the October/November 2003 period of high solar particle flux, however, strong enhancements in both magnesium species have been observed.

Part I

Introduction

1 Introduction

1.1 Origin and role of metal species in the upper atmosphere

The scope of this study is the investigation of mesospheric and thermospheric metallic species. The methodology used in this work provides results in the mesosphere/lower thermosphere region (MLT) extending from approximately 70 to 500 km altitude. This region forms the boundary between the atmosphere and space and is subject to a number of energy inputs in the form of solar radiation such as solar wind and electromagnetic radiation. Gravity waves, tides and planetary waves present energy influx from lower altitudes.

The major source of metal species in the upper atmosphere is influx from cosmic dust. Along with Earth, a variety of celestial bodies orbit the Sun. The asteroid belt between Earth and Mars and the Kuiper belt outside the orbit of Neptune are well-known regions of high abundance of those objects. As a result of perturbations by gravitational forces, small particles of micrometer sizes as well as larger objects of sizes up to several meters leave their natural orbits and enter the Earth's gravitational field. In addition, a number of regularly returning cometary objects present sources of cosmic material. The origin of these comets is believed to be the Oort cloud surrounding the solar system. The radius of this cloud is estimated to be several thousand astronomical units. While approaching the Sun, the cometary material is evaporating and sublimating from the comets, forming trails that can often be observed by eye from the ground. This phenomenon lead to the term "comet", derive from the ancient Greek word "kometes" – "star with hairs". Passes of the Earth through these trails result in material influx into the atmosphere (Goldberg and Aikin, 1973).

Meteoric particles are categorized by their composition. Most particles fall into one of four categories:

- *Iron meteorites:* These meteorites consist of mainly iron and nickel. The amount of nickel ranges from 5 to 60% of the iron mass, with an average of 10%. The major part of the whole mass is made up by iron, up to 30% sulfides, metal compounds (containing Mg, Ca and other species) and silicates may be contained in the meteorite.
- *Stony irons:* These type of meteorites features an iron-nickel-silicate composition. The iron-nickel part forms 30 – 70% of the total mass, realized in chunks or granules embedded in the ambient silicates.
- *Achondrites:* These are silicate rich meteorites containing a broad range of minerals and metal compounds. The iron-nickel fraction is rather small and makes up at most 5% of the total mass.
- *Chondrites:* Though the chemical composition of chondrites is not much different from all of the above mentioned types – the iron-nickel fraction makes up between 1 and 35%, and the rest is formed from silicate compounds – the physical manifestation is much more granular and grainy than that of the other three types. This is a result of the 'cooler' history of the chondrites. These particles may originate in accretion or weak collisions between larger bodies, releasing energies too weak to melt the complete particle and thus resulting in partial melting and mixing.

After entering the atmosphere, particles from either source are then subject to frictional heating. This leads to sublimation of metallic species from the surface of the particles.

Early measurements of metal species have been done using rocket-borne as well as satellite spectrographic techniques (see e.g. Anderson and Barth (1971), Fesen and Hays (1982a) and Gérard and Monfils (1978)). As a result of limited computational capacities, the results of those measurements were mainly restricted to total column densities along the line-of-sight of the instrument. An actual inversion of the measurements to obtain vertical profiles of the atmospheric species was not possible those days.

Another method to study high altitude metallic species is lidar. The good vertical resolution of those measurements permits investigation of thin metal layers with thicknesses of 1 km or less. See Clemesha (1995), Granier et al. (1989) and Lübken and Höfner (2004) for results. The major drawback of this method is obviously the limitation to a single point in space. Though long time series of a certain location are easily obtained, a global distribution is far beyond the abilities of even a lidar measurement network.

To overcome this drawback, recent developments in computer science enable scientists to run comprehensive model to investigate metal species on a theoretical basis. This way, the actual ablation as well as chemical and transport processes can be modeled. See Fritzenwallner and Kopp (1998), Plane (2003), Plane and Helmer (1995) for a review of chemistry modeling, McNeil et al. (1998) for a thorough model of the ablation process and Fesen et al. (1983), Bishop and Earle (2003) regarding transport modeling. The major drawback of those models, however, is exact knowledge of the reaction constants used in integration of the chemical equations. It is thus necessary to simulate mesospheric and thermospheric conditions in the laboratory. This comprises pressures, temperatures and radiation environments and requires sophisticated installations and techniques.

Space-borne measurements present the most powerful method to investigate global distributions of metal species with moderate vertical and horizontal resolution. These measurements can be done from permanent satellite platforms as well as using the Space Shuttle orbiter as instrument platform. Aikin et al. (2002), Gumbel et al. (2007), Dymond et al. (2003), Carbary et al. (2003), Gardner et al. (1999) and Scharringhausen et al. (2006) present recent space-borne measurements of metallic species in total content or within the altitude range from 70 to 350 km. However, depending on the measurement geometry and the global coverage, space-borne instruments may be unable to resolve fast processes. For equatorial regions and an orbit of 800 km, the same volume of air is sampled only every three to six days.

The impact of metal species on the chemistry and physics of the upper and middle (and, eventually, the lower) atmosphere is still a field of intense research. Estimations for the total influx of cosmic material differ by more than one order of magnitude, ranging from 20 to 400 t/d ((Hughes, 1978), (McBride and McDonnell, 1999), (Cziczo et al., 2001), (Wasson and Kyte, 1987)). Beside postulations with respect to chlorine catalyzed removal of ozone in the upper stratosphere (Murad et al., 1981), the formation and role of so-called *meteoric smoke* is highly uncertain. Meteoric smoke is a result of polymerization of metal compounds and silicon oxides Kalashnikova et al. (2000). Heterogeneous chemistry on the surface of these particles may then lead to formation of water vapour at altitudes of approximately 70 km (Summers and Siskind, 1999).

Murphy et al. (1998) propose that metal-rich particles such as meteoric smoke particles may act as condensation nuclei for stratospheric clouds. Figure 1.2 gives a visual review of the origin and the role of metal species in the upper and middle atmosphere.

A somewhat inverse question is that of the interaction of meteoric metals with cloud particles in the mesosphere. In the summer mesopause region at altitudes between 82 and 87 km *Polar Mesospheric Clouds* (also termed *Noctilucent Clouds*, NLCs) form from ice particles during periods of very low temperatures around 150 K. It has been proposed that metal species are taken up on the surface of the ice particles and thus removed from the gas phase. Lidar measurements of iron profiles in the South Pole region (Hunten, 2004) are consistent with model calculations done by Plane et al. (2004). Lidar measurements carried out in Spitsbergen, Norway, reported a similar behaviour for potassium (Lübken and Höfner, 2004).

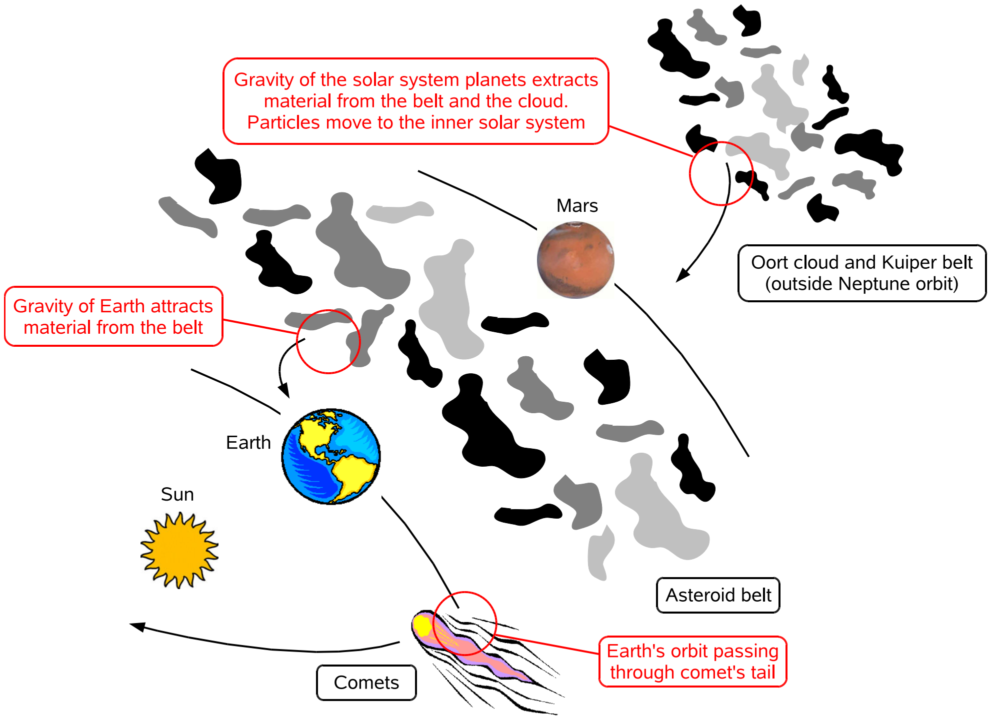

Figure 1.1: Review of major sources of metal species in the atmosphere. Material from the asteroid belt as well as from the Oort cloud and the Kuiper belt outside the orbit of Neptune present sources of meteoric particles to enter the atmosphere. Cometary mass is an additional source. Prominent regularly returning meteor showers such as the Leonids are a result of influx of cometary material into the Earth atmosphere.

1.2 Purpose and outline of this study

Up to now, results from a number of rocket-borne and lidar measurements of meteoric metals have been reported. Sporadic satellite measurements of total column densities have been carried out as well. However, these measurements are restricted either in time or in space. In contrast to this studies, the SCIAMACHY instrument onboard the ENVISAT satellite offers the opportunity to carry out a long-term global survey of meteoric metals. Information about neutral and singly ionized magnesium is derived from emission features in the UV spectral range below 300 nm. This work is dedicated to provide a comprehensive review of the distribution and variability of the two major atomic mesospheric magnesium species (Mg and Mg^+) in the upper mesosphere and lower thermosphere.

Though the number density of mesospheric and thermospheric magnesium species is rather small, these species may act as sensitive tracers of chemical as well as dynamical processes and changes in the upper atmosphere.

The SCIAMACHY instrument is capable to observe a number of airglow emission originating in the upper atmosphere. A short review of basic chemical processes and airglow emissions is given in Section 3. Additionally, this Section presents a number of emissions features observed in the SCIAMACHY limb data.

A general introduction into instrument design and measurement principle is given in Section 5. As will be pointed out, the observation of mesospheric and thermospheric emission species requires a novel retrieval approach. A two-dimensional retrieval scheme simultaneously utilizing limb and nadir data has been developed and implemented. This retrieval allows SCIAMACHY to obtain altitude information above the top tangent altitude. The mathematical basis as well as error estimations of this retrieval scheme are presented in Section 6.

As the influx of cosmic material into the atmosphere is prominently represented by events of strong meteoric activity such as the regularly returning Leonid meteor shower in November, it suggests itself to investigate the behaviour of magnesium species during events of high meteoric activity. Results of studies with respect to this topic are presented in Section 8. A similar topic

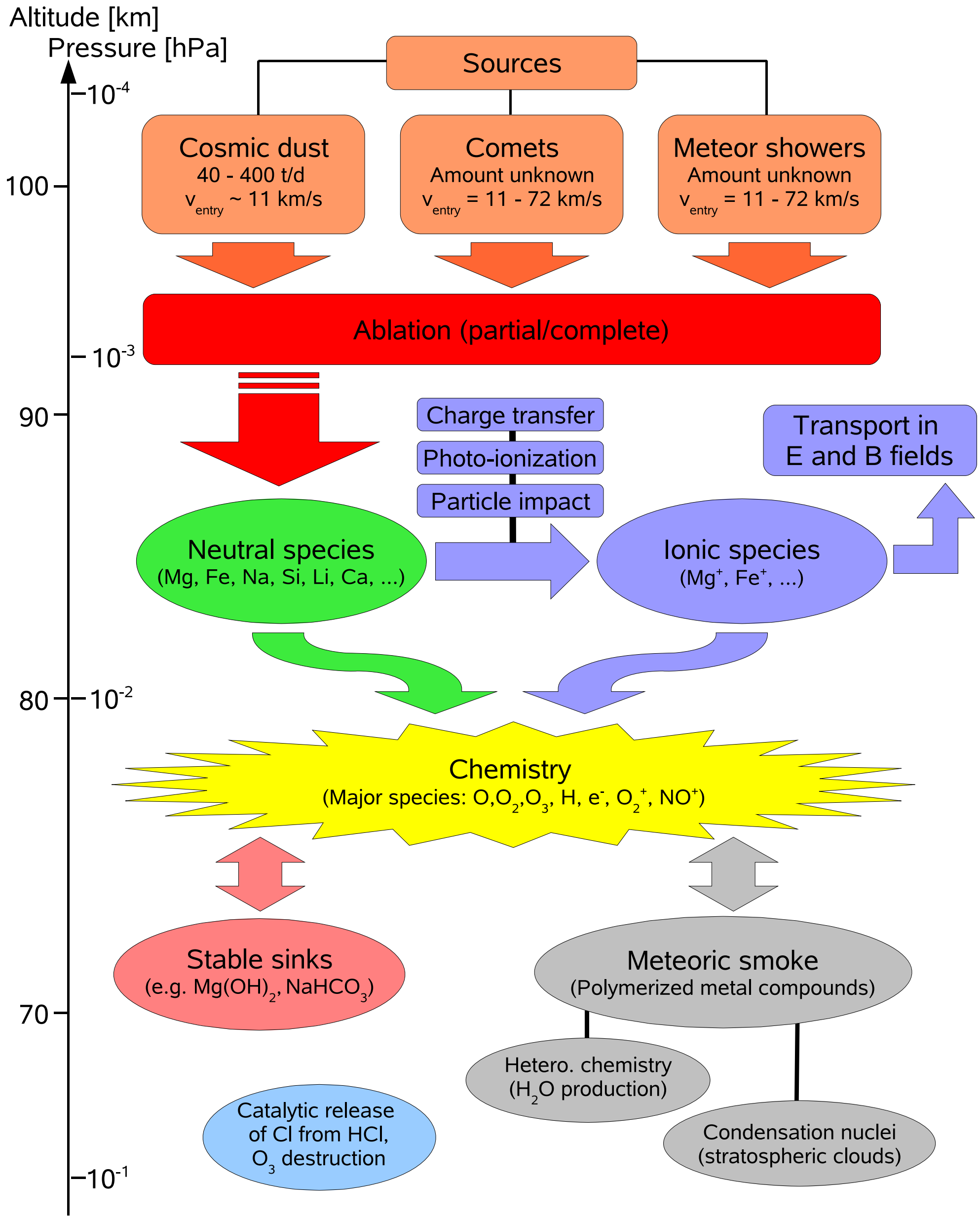

Figure 1.2: Review of major processes for metal species in the upper atmosphere. Major questions arising are the total influx of cosmic material and the role of metal compounds for the physics and chemistry of the middle and lower atmosphere.

is covered by Section 9. There, estimations of the total amount of cosmic material entering the atmosphere per day is derived from measurements of the average total content and estimations of loss rates.

The chemistry and physics of the atmosphere are closely connected to the solar flux, i.e. the average amount of solar radiation and particles penetrating the atmosphere. Section 10 relates the solar flux to the content of magnesium and ionized magnesium in the mesosphere and thermosphere. The following Section 11 presents results of observations made during an event of strongly enhanced proton fluxes within a period of high solar activity near the end of 2003, commonly known as the October 2003 solar proton event.

In November and December 2005, SCIAMACHY observed an anomalous depletion of ionized magnesium and a coincident bloom of the neutral species. Section 12 presents a detailed view on the November/December 2005 magnesium species distributions. This anomalous behaviour cannot be explained thoroughly. However, a number of possible mechanisms are discussed and some processes are be ruled out.

2 General review of the atmosphere

2.1 Vertical structure

As a result of the temperature distribution the atmosphere of the Earth can be subdivided into a number of compartments. The air temperature exhibits a number of maxima and minima (see Figure 2.1), and this extremal values define limits of atmospheric compartments.

The bottom part of the atmosphere is denoted by *troposphere* and exhibits a negative temperature gradient with altitude. The altitude of the first temperature minimum varies with season and location from 8 to 15 km. This is called the *tropopause.* In the troposphere, the air is well-mixed and virtually all processes of weather (such as clouds, precipitation) take place within this altitude region. Higher regions of the atmosphere, however, have a strong impact on tropospheric processes.

As a result of high ozone concentrations and thus short-wave radiative heating by the solar UV radiation within the so-called *stratosphere* above the tropopause and below 50 km, the temperature is increasing again. As a result of this gradient, the layering of air masses is more stable compared to the troposphere. The temperature maximum around 50 km is called *stratopause* and presents the transition the the next compartment, the *mesosphere.*

Within this region, the temperature is decreasing with altitude again. The *mesopause* at approximately 90 km altitude presents temperatures of down to 150 K in summer and is thus the coldest part of the atmosphere. Above 90 km, the temperature gradient changes to positive values. However, the number densities of the atmospheric species are decreasing to very low values and thus one has to be careful about the definition of temperature at high altitudes. Temperature has to be defined as kinetic temperature, i.e. proportional to the mean kinetic energy of the particles. In the lower thermosphere, the diurnal and seasonal variations of temperature exhibit values of several hundreds of degrees.

Beside the temperature distribution, the degree of ionization can be used for subdivision. Above 60 km, gaseous species are ionized primarily by extraterrestrial radiation. The solar irradiance presents the major source of ionizing radiation. The atmospheric region above 60 km is thus called the *ionosphere.* The atmospheric air becomes a plasma and thus electrically conductive. This leads e.g. to impacts on the propagation of radio waves and in particular GPS signals.

Above approximately 80 – 85 km, the atmospheric air can not be treated as being well-mixed. This altitude is the transition region from the *homosphere* to the *heterosphere.* Below 80 km, collisions between molecules are frequent and no separation is possible. Higher up, as a result of a steady-state between gravitational sedimentation and diffusion, molecules and atoms of less mass tend to exhibit higher mixing rations at high altitudes whereas heavier molecules and atoms are concentrated at lower altitudes. The *scale height* (the altitude difference such that pressure drops by a factor of $1/e$) has to be defined for each species separately and varies from 8 km for O_2 and N_2 to approximately 1000 km for atomic hydrogen. For the homosphere, a scale height of approximately 7 – 8 km is valid.

2.2 Mesospheric and thermospheric chemistry

2.2.1 Ionic chemistry

A large part of the mesosphere overlaps with the ionosphere, i.e. the ionic chemistry does not play a negligible role any more. The thermosphere above approximately 100 km is dominated

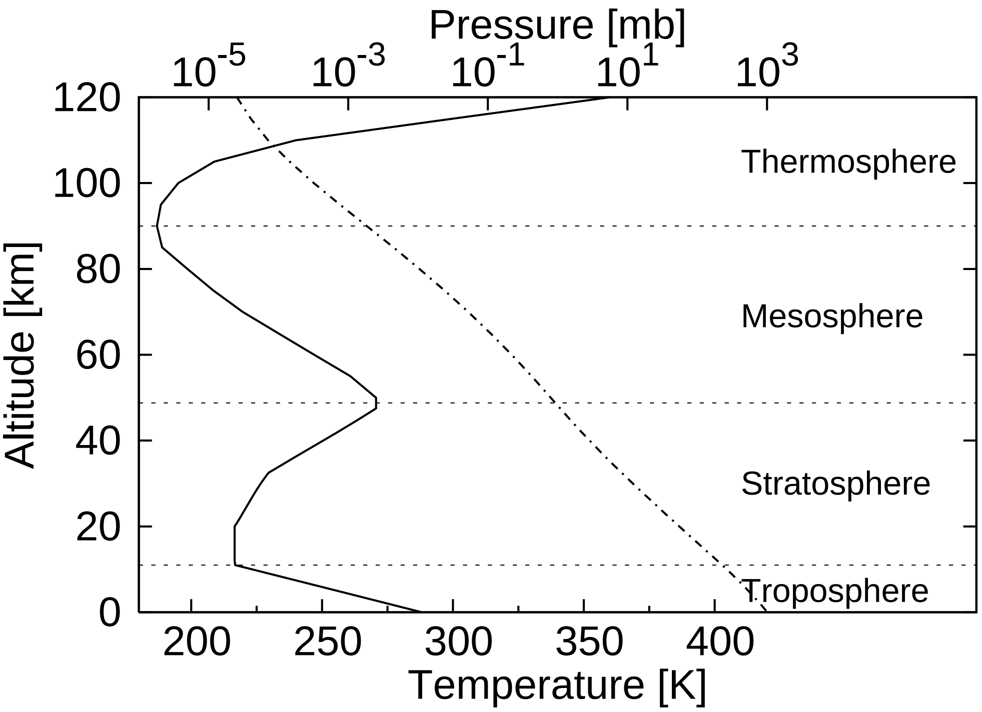

Figure 2.1: General structure of Earth's atmosphere. Solid line: Temperature distribution exhibiting a number of maxima and minima. These can be used to subdivide the atmosphere into different parts. Dot-dashed line: Pressure distribution. In good approximation, the pressure is decreasing exponentially with altitude. As a result of this, about 90% of the total mass of the atmosphere are contained within the bottom 10 km. Data taken from NOAA (1976).

by ion chemistry reactions, and the neutral chemistry is negligible now. A thorough review of ionospheric chemistry is given in Wayne (2000).

The dominant ionization processes in the ionosphere at altitudes above 60 km is photoionization in the UV and X-ray wavelength range. As a result of this, the electron density and the total content show a pronounced diurnal cycle. Additionally, the solar activity varying in its prominent 11-year and 27-day cycles impact the ion density in the ionosphere. Energetic particles play a minor role except in the regions of high geomagnetic latitude near the poles where energetic particles from the Sun and outer space are able to precipitate down to lower altitudes. During periods of enlarged solar activity and thus increased particle flux, the importance of ionization by energetic particles is increasing as well. Galactic cosmic γ rays are an additional minor source of ionization.

It should be noted that ionic chemistry is fundamentally different from neutral chemistry. Whereas neutral species rely on random processes depending on pressure and temperature to approaching close enough to undergo e.g. a two–body reaction, the motion of ions is dominated by Coulomb forces acting over large distances. Additionally, the motion of ionic species at high altitudes is determined by the electric and magnetic field structure and not by the pressure- and temperature-driven motion of the neutral species.

Major molecular species in the ionosphere are the ionic forms of oxygen (O_2), nitrogen (N_2) and nitric oxide (NO). Hydrogen is most abundant in its atomic form H. The most important types of ionic reactions are listed below.

– Charge transfer

$$N_2^+ + O_2 \longrightarrow N_2 + O_2^+ \tag{2.1}$$

$$H^+ + O \longrightarrow H + O^+ \tag{2.2}$$

– Constituents exchanges

$$
\begin{aligned}
N_2 + O^+ &\longrightarrow N^* + NO^+ && (2.3)\\
O_2^+ + N_2 &\longrightarrow NO + NO^+ && (2.4)
\end{aligned}
$$

– Recombinations (non-dissociative and dissociative)

$$
\begin{aligned}
O^+ + e^- &\longrightarrow O + h\nu && (2.5)\\
NO^+ + e^- &\longrightarrow N^* + O && (2.6)
\end{aligned}
$$

– Attachments (source of negative ions)

$$
\begin{aligned}
O + e^- &\longrightarrow O^- + h\nu && (2.7)\\
O_3 + e^- &\longrightarrow O^- + O_2 && (2.8)
\end{aligned}
$$

– Detachments (sink of negative ions)

$$
\begin{aligned}
O_2^- + O &\longrightarrow O_3 + e^- && (2.9)\\
O^- + e^- &\longrightarrow O + e^- && (2.10)
\end{aligned}
$$

– Clustering

$$
\begin{aligned}
O_2^+ + O_2 + M &\longrightarrow O_2^+O_2 + M && (2.11)\\
H^+(H_2O)_n + H_2O + M &\longrightarrow H^+(H_2O)_{n+1} + M && (2.12)
\end{aligned}
$$

Note that a number of these reactions leave one or more of the reactions species in an energetically excited state. Relaxation to the energetic ground state then leads to radiation that can be observed by ground-based or satellite instruments. This phenomenon is called *airglow*. See Section 3 for a review of mesospheric airglow emissions observed by the SCIAMACHY instrument.

At higher altitudes above 200 km (within the *F–region*), the chemistry centers around formation and consumption of the O^+ ion. Molecular species are rather rare as a result of dissociation by short wavelength radiation from the Sun.

At lower altitudes between 100 and 200 km (within the *E–region*), the major ionic constituents are present in molecular form. The primary ionization products are O_2^+ and N_2^+, which are directly produced from the major neutral counterparts. Ionic nitrogen is consumed rather fast to form NO^+ (by release of N) or O_2^+ (by charge transfer with neutral O_2).

The ionic chemistry in the transition region between the ionosphere and the neutral atmosphere at altitudes between 60 and 80 km is rather complex. The dynamics of the species are impacted by the electric and magnetic field structure as well as by neutral dynamics. As a result of the exponential decrease in the atmosphere, the pressure is several orders of magnitude higher compared to the E– and the F–region. Processes such as clustering are more likely to occur within this region. As the solar radiation in the UV and X-ray wavelength range is strongly absorbed at higher altitudes, negative ion in this altitude region have a longer lifetime permitting them to play a role in the chemistry of this region.

2.2.2 Neutral chemistry

As a result of reduced photodissociation in the UV and X-ray wavelength range, the relative abundance of molecular species is higher at lower altitudes. Important molecular species in the ionosphere are oxygen (O_2), nitrogen (N_2), nitrogen species (NO_x), ozone (O_3) water vapour (H_2O) and hydrogen species (HO_x). Important reactions in the mesosphere are listed below:

– Photodissociation

$$H_2O + h\nu \longrightarrow H + OH \tag{2.13}$$

$$O_2 + h\nu \longrightarrow O + O \tag{2.14}$$

– Constituents exchanges

$$O_2^+ + N_2 \longrightarrow NO + NO^+ \tag{2.15}$$

– Dissociation

$$H_2O + O \longrightarrow 2OH \tag{2.16}$$

Being involved in catalytic cycles, odd hydrogen and nitrogen species such as O, OH, HO_2, NO, NO_2 play an important role in the chemistry of mesospheric and stratospheric ozone (Brasseur and Solomon, 1984). Whereas the odd nitrogen species are mainly a result of reactions of atomic nitrogen with molecular oxygen, the odd hydrogen species are mainly produced by consumption of water vapour by photolysis and reaction with oxygen. It is thus clear that the chemistry of the high-altitude thermosphere (where atomic nitrogen is formed and photolysis plays a major role) is closely coupled to the neutral chemistry in the lower mesosphere and stratosphere. Though odd nitrogen and hydrogen species are by far not as abundant as oxygen (O, O_2) or nitrogen species (N, N_2), their impact on the chemistry is not negligible.

As will be shown in Section 4, both odd nitrogen and odd hydrogen species are involved in the chemistry of metal species in the mesosphere and lower thermosphere. Knowledge of the distribution and the variations of metal species are thus suitable to sense changes in the overall chemistry and chemical composition of the stratosphere, mesosphere and lower thermosphere.

Figures 2.2(*a*) and 2.2(*b*) show typical vertical profiles of the major neutral and ionic species in the mesosphere and lower thermosphere for summer mid latitude daylight conditions. As can be seen, the abundance of neutral species is decreasing with altitude. The ion species, however, are present at higher altitudes.

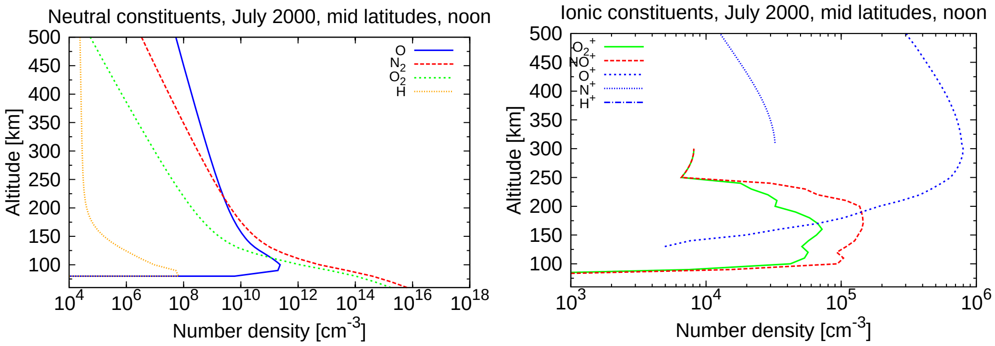

(a) Vertical profiles of neutral species.

(b) Vertical profiles of ionic species.

Figure 2.2: Vertical profiles of major neutral and ionic species in the mesosphere and lower thermosphere. The abundance of neutral species is decreasing with altitude, whereas the ions exhibit maxima at altitudes between 100 and 500 km. As can be ween from the right panel, the region between 250 and 300 km can be interpreted as the transition between the molecular and the atomic regime. Data acquired from NASA Goddard Space Flight Center (2007a) and NASA Goddard Space Flight Center (2007b).

3 Airglow

As a result of a number of chemical and physical processes, atmospheric species are left in quantum-mechanically excited states. Relaxation to lower states then results in emission of electromagnetic radiation. This is called *airglow* in general. More specifically, one may consider *dayglow* or *nightglow* with respect to the ambient illumination conditions.

Despite the fact that first applications of SCIAMACHY were based on principles of absorption spectroscopy, a variety of atmospheric emission signals can be detected in the both the limb and the nadir spectra. As a case study, this section provides an overview over emission signals present in the limb data in the spectral range from ≈ 230 to ≈ 930 nm. This comprises data of channel 1 through 5. See Section 5 for a detailed description of the SCIAMACHY instrument.

Figures 3.1 – 3.6 show sun-normalized limb radiances from SCIAMACHY tangent altitude 92 km. The measured radiances are divided by a solar spectrum of the same day as the measurement to eliminate structures originating in the solar spectrum (e.g. Fraunhofer lines). All measurements presented here were taken on February 28, 2007.

3.1 Resonance fluorescence

As a result of absorption of energetic radiation (see equation (3.1)) from e.g. the sun, atoms as well as molecules can be left in an excited state. De-excitation to energetically lower states then leads to emission of radiation, see equation (3.2). The case of resonance fluorescence is rather simple, as the absorbed and emitted radiation are of equal wavelength.

$$\mathrm{A} + h\nu \longrightarrow \mathrm{A}^* \tag{3.1}$$

$$\mathrm{A}^* \longrightarrow \mathrm{A} + h\nu \tag{3.2}$$

The probably most prominent representative for this kind of excitation is absorption and re-emission of the solar Lyman-α line at 121.6 nm. The transition is between the ground state and the first excited state of the hydrogen atom:

$$\mathrm{H}(^2\mathrm{S}) + h\nu(\lambda = 121.6\ \mathrm{nm}) \longrightarrow \mathrm{H}(^2\mathrm{P}) \tag{3.3}$$

$$\mathrm{H}(^2\mathrm{P}) \longrightarrow \mathrm{H}(^2\mathrm{S}) + h\nu(\lambda = 121.6\ \mathrm{nm}) \tag{3.4}$$

Unfortunately, this emission can not be observed in the SCIAMACHY data, as the wavelength range of the instrument does not extend below 214 nm. Another prominent emission feature clearly being visible in the SCIAMACHY data is the sodium doublet line around 590 nm (see Figures 3.3, 3.4):

$$\mathrm{Na}(^2\mathrm{S}_{1/2}) + h\nu(\lambda = 589.0\ \mathrm{nm}) \longrightarrow \mathrm{Na}(^2\mathrm{P}_{3/2}) \tag{3.5}$$

$$\mathrm{Na}(^2\mathrm{P}_{3/2}) \longrightarrow \mathrm{Na}(^2\mathrm{S}_{1/2}) + h\nu(\lambda = 589.0\ \mathrm{nm}) \tag{3.6}$$

$$\mathrm{Na}(^2\mathrm{S}_{1/2}) + h\nu(\lambda = 589.6\ \mathrm{nm}) \longrightarrow \mathrm{Na}(^2\mathrm{P}_{1/2}) \tag{3.7}$$

$$\mathrm{Na}(^2\mathrm{P}_{1/2}) \longrightarrow \mathrm{Na}(^2\mathrm{S}_{1/2}) + h\nu(\lambda = 589.6\ \mathrm{nm}) \tag{3.8}$$

3.1.1 NO-γ bands

A prominent feature in the SCIAMACHY spectra are the NO-γ bands (see Figure 3.1). In general, molecular species as NO exhibit a comprehensive band structure. As a result of excitation by solar radiation from the ground state to the first excited state and branching to a manifold of different vibrationally and rotationally excited states, the radiative de-excitation does not occur at a single wavelength. Instead, pronounced two-peak band features are observed in the UV airglow below 300 nm (see Figure 3.1). These are results of an electronic transition from the $X^2\Pi$ ground state to the $A^2\Sigma^+$ first excited state. Both states are subdivided into vibrational and rotational states. All possible transitions back from the first electronically excited to the electronic ground state yield one single emission line. The relation between the vibrational levels determines the actual emission band (annotated by NO(x-y), where x and y denote the vibrational levels $v = 0, 1, 2, \ldots$). The rotational lines are too close, however, to be resolved by the SCIAMACHY spectral resolution in the wavelength range below 300 nm ($\approx$ .17 nm).

$$\mathrm{NO(X^2\Pi)} + h\nu(\lambda \leq 300\ \mathrm{nm}) \longrightarrow \mathrm{NO(A^2\Sigma^+)} \tag{3.9}$$

$$\mathrm{NO}(\mathrm{A}^2\Sigma^+, v = 0, 1, \ldots) \longrightarrow \mathrm{NO}(\mathrm{X}^2\Pi, v = 0, 1, \ldots) + h\nu \tag{3.10}$$

3.2 Photodissociation

In case the absorbed radiation is of sufficiently high energy, a molecule may be dissociated and one or both parts may be left in excited states. De-excitation of one or both parts to energetically lower states result in observable radiation, see e.g. equations (3.11) and (3.12).

$$\mathrm{AB} + h\nu \longrightarrow \mathrm{A}^* + \mathrm{B} \tag{3.11}$$

$$\mathrm{A}^* \longrightarrow \mathrm{A} + h\nu \tag{3.12}$$

An example of this reaction is presented by the dissociation of water vapour to yield excited OH:

$$\mathrm{H_2O} + h\nu \longrightarrow \mathrm{OH(A^2\Sigma^+)} + \mathrm{H} \tag{3.13}$$

Note, however, that the population of the $A^2\Sigma^+$ state can be accomplished by absorption of solar radiation as well. The radiative decay of excited OH is leads to a band emission around 306.4 nm being visible in the SCIAMACHY spectra (see Figure 3.2)

$$\mathrm{OH(A^2\Sigma^+)} \longrightarrow \mathrm{OH(X^2\Pi)} + h\nu(\lambda \approx 306.4\mathrm{nm}) \tag{3.14}$$

3.3 Dissociative recombination

Recombination of an ionized molecular species with an electron may lead to dissociation of the molecule with one or both parts left in excited states.

$$\mathrm{AB}^+ + e^- \longrightarrow \mathrm{A}^* + \mathrm{B} \tag{3.15}$$

$$\mathrm{A}^* \longrightarrow \mathrm{A} + h\nu \tag{3.16}$$

As a result of recombination of a positive ion and an electron, the molecular binding energy may be liberated. This leads to one or more fragments to be in excited states after the recombination. A prominent example is recombination of O_2^+:

$$\mathrm{O_2^+} + e^- \longrightarrow \mathrm{O(^1S)} + \mathrm{O(^3P)} \tag{3.17}$$

$$\mathrm{O_2^+} + e^- \longrightarrow \mathrm{O(^1D)} + \mathrm{O(^3P)} \tag{3.18}$$

The transitions $^1S \rightarrow {}^1D$ and $^1D \rightarrow {}^3P$ then lead to the well-known green line and red doublet observed frequently in auroral phenomena. Both emission features can be identified in the SCIAMACHY spectra (see Figure 3.3, 3.5). Note that the red doublet originates at lower altitudes than the green line, thus the 630 nm emission strength at 92 km is weaker than the 557 nm line.

$$\mathrm{O}(^1\mathrm{S}) \longrightarrow \mathrm{O}(^1\mathrm{D}) + h\nu(\lambda = 557.7\mathrm{nm}) \quad (3.19)$$

$$\mathrm{O}(^1\mathrm{D}) \longrightarrow \mathrm{O}(^3\mathrm{P}_{2,1}) + h\nu(\lambda = 630.0/636.4\mathrm{nm}) \quad (3.20)$$

The direct $^1\mathrm{S} \rightarrow {}^3\mathrm{P}$ transition at 297 nm, however, is quantum mechanically forbidden and thus very weak. It is not observed in the SCIAMACHY limb spectra.

3.4 SCIAMACHY measurements of airglow emissions

The SCIAMACHY instrument (see Section 5) provides the capability of global observations of atmospheric airglow with good spectral, spatial and temporal resolution. This Section is dedicated to present exemplary emission features contained in the SCIAMACHY spectra.

The case of resonance fluorescence (Section 3.1) is e.g. observed in channel 1 around 280 nm and 285 nm, see Figure 3.1. This are the emission features of Mg^+ and Mg. Another example is the prominent sodium doublet at 589 nm, see Figure 3.3 and 3.4.

An example of radiative decay of states excited by photodissociation is the emission band of OH around 306 nm (Section 3.2), see Figure 3.2.

The SCIAMACHY channel 3 and 5 exhibit the prominent oxygen red and green line resulting from dissociative recombination with electrons in the upper atmosphere, see Section 3.3 and Figures 3.3, 3.6.

Knowledge of the excitation process and measurement of the emission strength provide column or even volume amounts of atmospheric species. The column density of excited metal species can be estimated using the relation

$$I(\lambda) = \gamma(\lambda) \cdot F(\lambda) \cdot \int_0^{\mathrm{TOA}} N(h) \cdot \tau(h)\, dh \quad (3.21)$$

Here, I denotes the observed radiance, F the solar irradiance, $N(h)$ the volume number density at altitude h, and γ the proportionality factor between I/F and the column density $\int N(h)dh$. This is also called the *emissivity* or *g-factor*. The absorption from the sun to a individual point on the line-of-sight and from this point to the instrument is summarized in $\tau(h)$.

In particular, equation (3.21) states that the observed radiance is the integrated radiance along the instrument's line-of-sight. Depending on the orientation of the line-of-sight, a contributions of a number of altitudes and locations are merged by integration. Multiple column density observations may be combined to estimate altitude-resolved volume number densities in the upper regions of the atmosphere. This method is used within this work to estimate the global distribution of ionized and neutral magnesium.

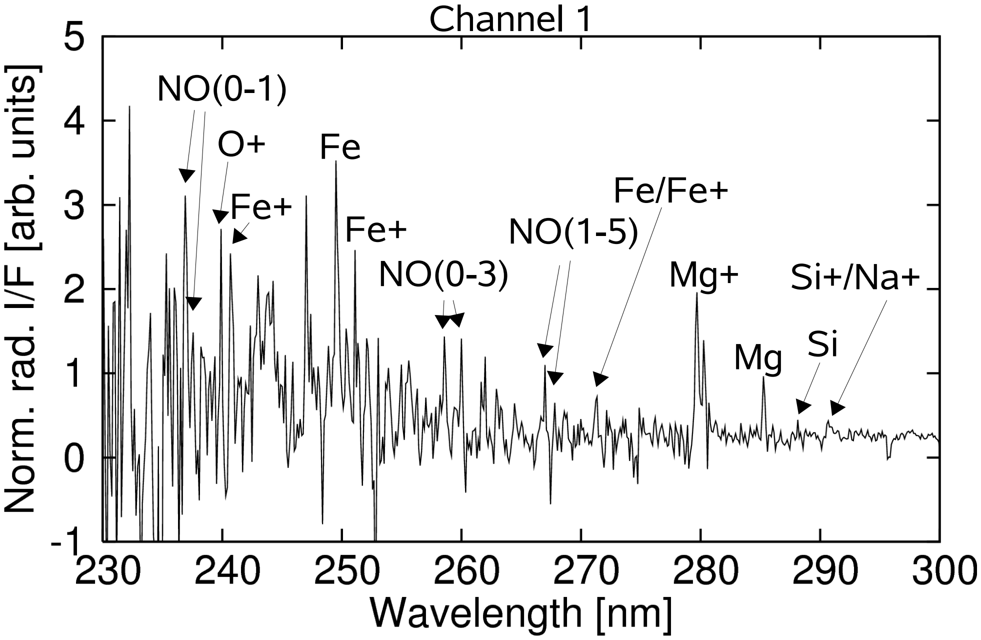

Figure 3.1: Emission features in SCIAMACHY channel 1 as observed on February 28, 2007. The NO gamma bands can be identified as well as a number of emissions of metallic species. The band structure is a result of electronic-vibrational-rotational transitions of different quantum mechanical states of the NO molecule. The single-channel emission features, however, are results of purely electronic transitions between the ground state and the first excited state (this is the case e.g. for the Mg^+ and the Mg emissions around 280 nm and 285 nm, respectively.) or two excited states (as is the case e.g. for the Fe emission at 250 nm).

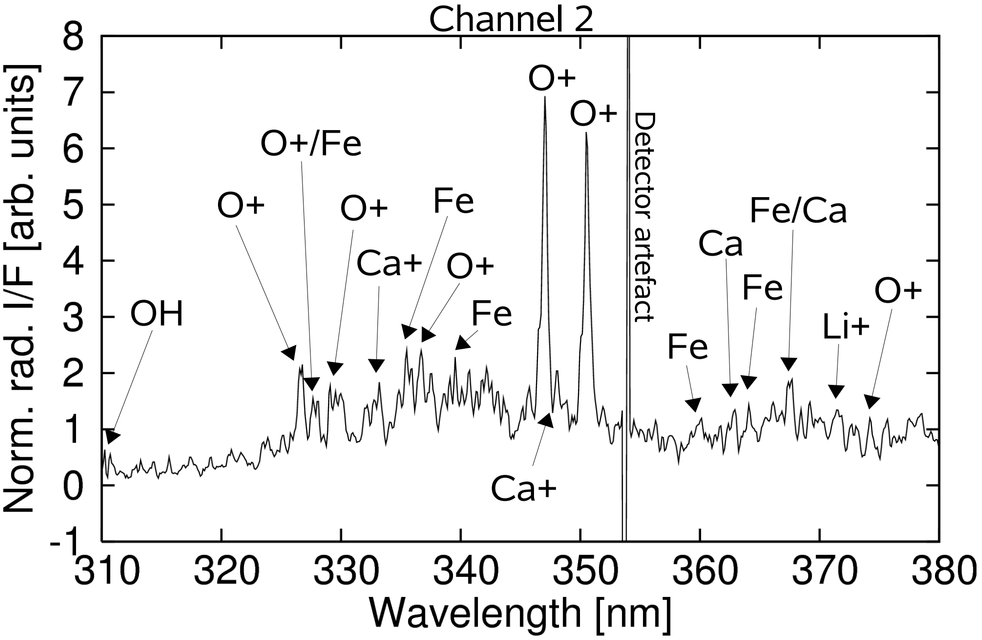

Figure 3.2: Same as Figure 3.1, but for channel 2. Observed radiances are averaged over the complete day and the observed radiance is normalized by the solar irradiance of the same day. This is measured by SCIAMACHY as well.

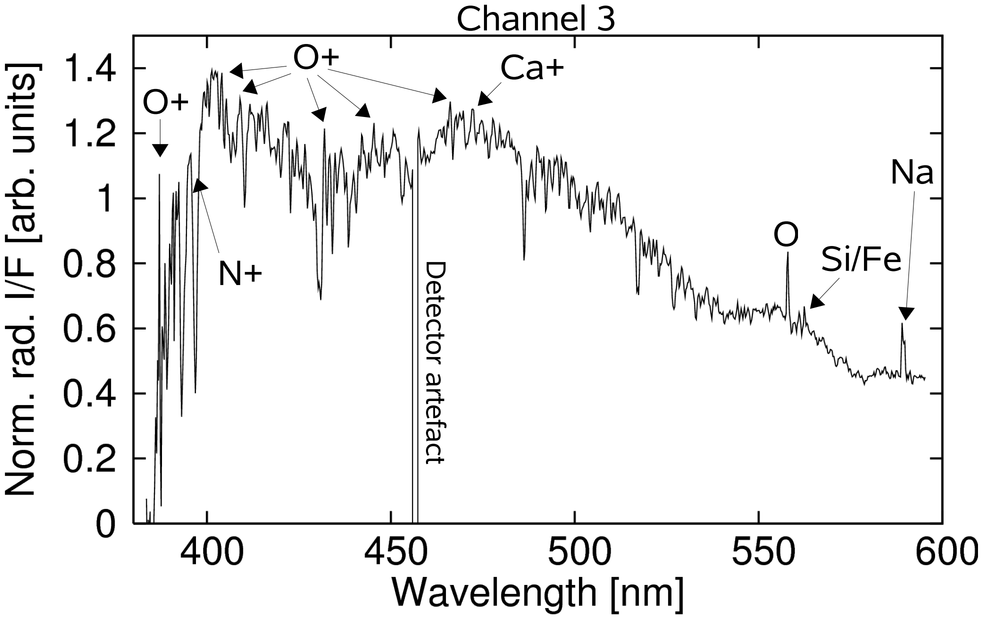

Figure 3.3: Same as Figure 3.1, but for channel 3. Observed radiances are averaged over the complete day and the observed radiance is normalized by the solar irradiance of the same day, as measured by SCIAMACHY. See Figure 3.4 for a detailed view of the sodium doublet at 590 nm. The SCIAMACHY resolution is sufficient to resolve the two emission lines. The oxygen emission at 557 nm presents the auroral green line which is frequently observed by eye from the ground.

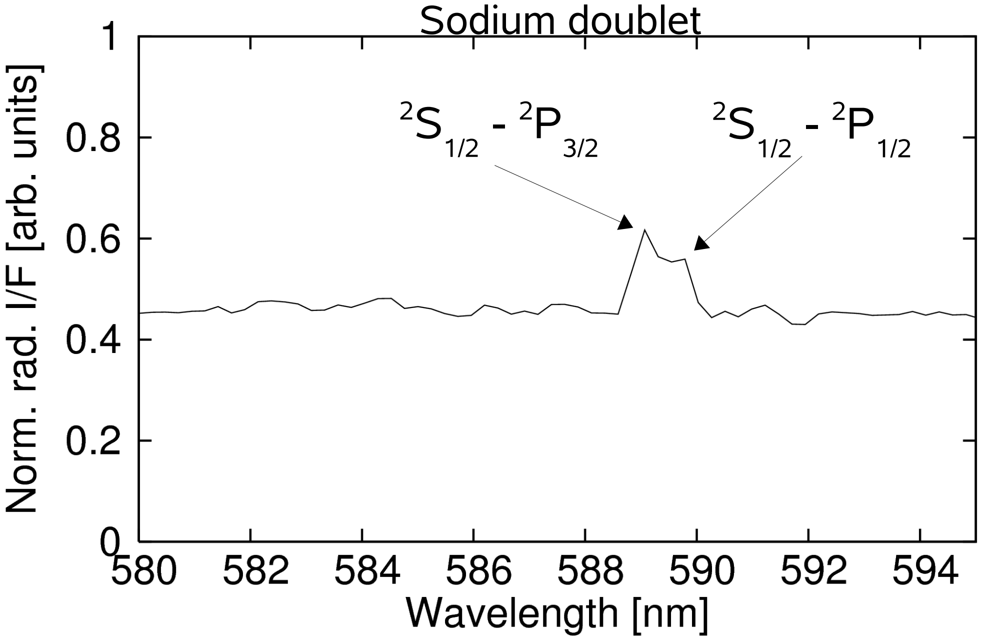

Figure 3.4: Detailed view of the sodium emission doublet at 590 nm as observed on February 28, 2007, tangent altitude 92 km. The SCIAMACHY spectral resolution is sufficient to separate the two emission lines. See reactions (3.5) – (3.8) for a detailed view of the quantum mechanical states being involved. Observed radiances are averaged over the complete day and the observed radiance is normalized by the solar irradiance of the same day, as measured by SCIAMACHY.

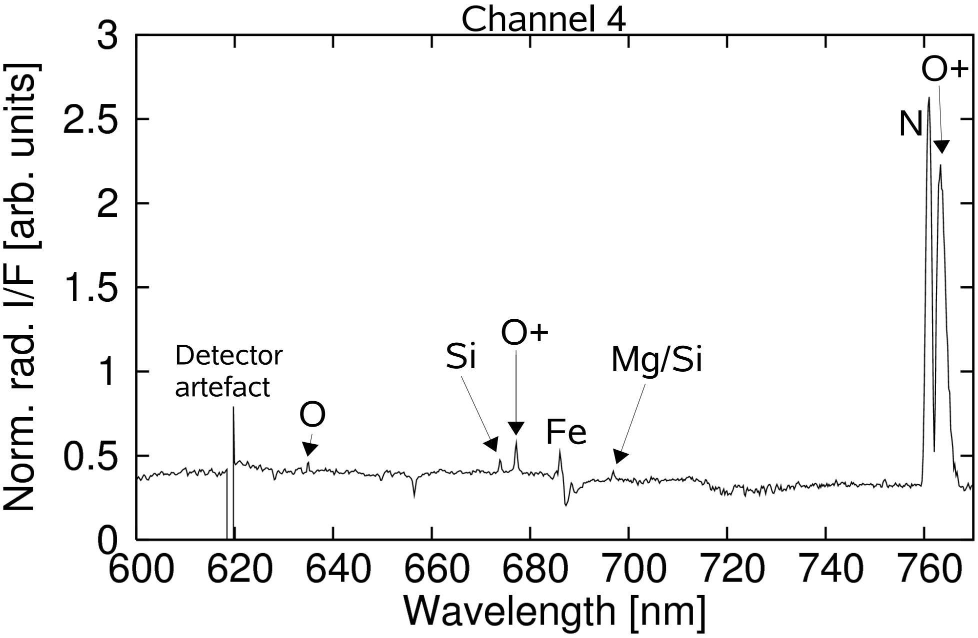

Figure 3.5: Same as Figure 3.1, but for channel 4. Observed radiances are averaged over the complete day and the observed radiance is normalized by the solar irradiance of the same day, as measured by SCIAMACHY. The O emission at 630 nm presents the auroral red line which is sometimes observed by eye from the ground. However, it occurs less frequently than the auroral green line at 557 nm (see Figure 3.3).

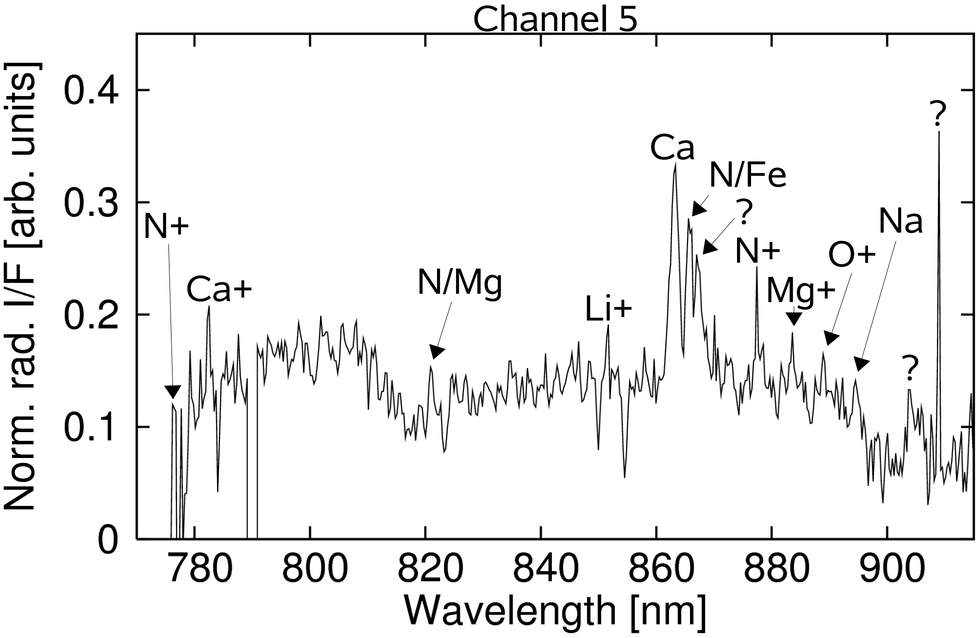

Figure 3.6: Same as Figure 3.1, but for channel 5. Observed radiances are averaged over the complete day and the observed radiance is normalized by the solar irradiance of the same day, as measured by SCIAMACHY.

4 Chemistry of Mg and Mg^+

4.1 Why magnesium?

As lined out in Section 2.2, ionic chemistry plays an important role in the general chemistry of the mesosphere and lower thermosphere. Even more, the largest part of the altitude range considered in this study (70 – 500 km) is dominated by ionic chemistry. Though the number density of magnesium species is rather small in the atmosphere, these species may act as sensitive precursors of chemical changes and dynamic processes in the upper atmosphere and especially the ionosphere. At lower altitudes, impacts of Mg and Mg^+ on mesospheric water vapour and ozone are fields of research.

This study focuses on the magnesium species Mg and Mg^+ for a number of reasons:

- The relative abundance of magnesium is large compared to species such as sodium, silicon, potassium or lithium. Merely iron is of similar abundance as magnesium (see Table 4.1). This leads to a good "S/N" for the determination of the total influx of meteoric material.
- The ablation altitude (see Table 4.1) is near the region of rapidly increasing ion densities around 90 km (see Figure 2.2(*b*) in Section 2.2). This enables the magnesium to play a role in the ionic chemistry as well as in the neutral chemistry. As a result, knowledge about the magnesium provides insight in processes taking place in the neutral as well as in the ionic regime.

  Note that though the ablation altitude of iron is not known from model calculations of measurements, it can be assumed that iron ablates at lower altitudes, as the boiling point is higher than that of magnesium and sodium. Though the metal species rather sublimate from the surface of the particle than actually boil, the boiling point is positively correlated with the altitude of maximal ablation.
- The chemistry is less complex compared to iron and sodium. Whereas the sodium chemistry incorporates ten major species, 13 species are to consider for the iron chemistry, only eight magnesium species present the major part of the magnesium chemistry.
- The observation of mesospheric and thermospheric magnesium is simple. As is the case for sodium, the principal emission feature of magnesium is a result of resonance fluorescence from the ground state to the first excited state. Because of this, excitation and de-excitation incorporate radiation of the same wavelength. Additionally, this process is fast enough to neglect quenching of the excited state. The strongest iron emission features, however, are a result of energetic transitions between excited states. Excitation and relaxation to a lower state may occur at different wavelengths. This complicates the analysis, as e.g. different spectral properties of the instrument have to be accounted for.

4.2 Major chemical compounds and reactions

Though the ionized species Mg^+ has been measured occasionally by rocket-borne ion mass spectrometry, very little is known about the abundances of the neutral atom. This is mainly due to the fact that ground-based measurement techniques (lidar, photometry) using the Mg fundamental emission at 285 nm are impossible due to the strong ozone absorption in the Hartley bands at these wavelengths and lower altitudes.

Intense laboratory studies as well as model simulations have been undertaken (results are reported in Plane and Helmer (1995), Plane (2003), Fritzenwallner and Kopp (1998)) to estimate loss and production processes at respective altitudes.

Species	Boiling point [K]	Maximal ablation [km]	Av. rel. mass [%]
Mg	1363	80 – 90	12.5
Fe	3023	?	11.5
Na	1156	90 – 110	0.6
Si	2628	?	?

Table 4.1: Features of meteoric metals. Abridged from (McNeil et al., 1998). The actual altitude of maximal ablation depends on the initial entry velocity of the dust particle. Faster particles ablate higher up in the atmosphere. This is an issue in the determination of the total influx of meteoric material, see Section 9.

The dominant ionic species at altitudes above 150 km, i.e. within the F-region, are atomic species like ionized oxygen and nitrogen. At lower altitudes within the D– and E–region (60 – 80 km and 80 – 150, respectively), molecular species O_2^+ and N_2^+ become more abundant and thus important for the chemistry.

The prevailing chemical processes within the mesosphere and thermosphere are of ionic nature. A number of strong ionization processes leads to high concentrations of ionic species at altitudes above 60 km. The major source of ionization of neutral magnesium is charge transfer. Beside this, ionization is possible by solar UV radiation, particle impact (a source of increased importance in the auroral regions near the geomagnetic poles), and cosmic rays. However, the impact of cosmic radiation is weak and will be neglected in the discussion of the metallic chemistry.

A thorough overview of the chemistry of mesospheric and thermospheric magnesium is given in Plane and Helmer (1995). See Figure (4.3) for an overview over the chemistry of mesospheric and thermopsheric magnesium. Figure 4.1 presents vertical profiles of major magnesium species in the altitude range from 65 to 110 km for mid–winter, mid–latitude daylight conditions.

According to the work presented in Plane and Helmer (1995), the prevailing source reactions of ionized magnesium Mg^+ in the mesosphere are:

$$\mathrm{Mg} + \mathrm{NO}^+ \rightarrow \mathrm{Mg}^+ + \mathrm{NO} \tag{4.1}$$
$$\mathrm{Mg} + \mathrm{O}_2^+ \rightarrow \mathrm{Mg}^+ + \mathrm{O}_2 \tag{4.2}$$
$$\mathrm{Mg} + h\nu(\leq 162.2\mathrm{nm}) \rightarrow \mathrm{Mg}^+ \tag{4.3}$$

Middle UV radiation as in the Lyman-α emission around 121 nm, penetrates easily down to lower atmospheric levels of 70 – 80 km, depending on solar zenith angle, leading to photoionization of Mg. At altitudes above approximately 80 km, the dominant ionization process to form Mg^+ is charge transfer with one of the dominant molecular species (compare Figure (4.2)).

Dominant loss reactions of singly ionized magnesium to form neutral Mg are radiative recombination (reaction (4.4)) and dissociative recombination (reactions (4.7), (4.8)) after preceding formation of molecular ions (reactions and (4.5), (4.6)). Note that the formation of molecular ions is possible via reaction of the neutral species Mg and following ionization as well.

$$\mathrm{Mg}^+ + e^- \rightarrow \mathrm{Mg}^+ + h\nu \tag{4.4}$$
$$\mathrm{Mg}^+ + \mathrm{O}_3 \rightarrow \mathrm{MgO}^+ + \mathrm{O}_2 \tag{4.5}$$
$$\mathrm{Mg}^+ + \mathrm{O}_2 + \mathrm{N}_2 \rightarrow \mathrm{MgO}_2^+ + \mathrm{N}_2 \tag{4.6}$$
$$\mathrm{MgO}^+ + e^- \rightarrow \mathrm{Mg} + \mathrm{O} \tag{4.7}$$
$$\mathrm{MgO}_2^+ + e^- \rightarrow \mathrm{Mg} + \mathrm{O}_2 \tag{4.8}$$

At high altitudes, however, the regeneration of atomic Mg^+ by reaction with atomic oxygen is very fast (reaction (4.4)). Thus, the radiative recombination is the dominant pathway at high

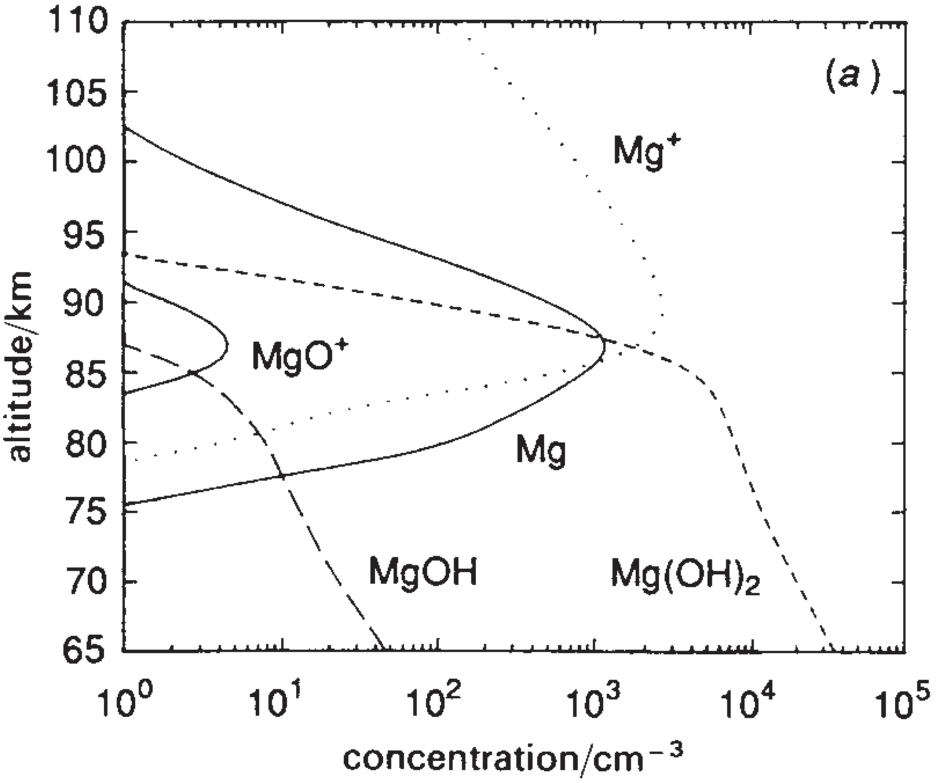

Figure 4.1: Vertical profiles of major magnesium species in the mesosphere for a mid-latitude winter daylight scenario (adapted from Plane and Helmer (1995)). The major reservoir species at lower altitudes is $Mg(OH)_2$. The Mg profiles exhibits a maximum number density at approximately 87 km, whereas the Mg^+ peak abundance is slightly higher up in the atmosphere at approximately 90 km.

altitudes. As a result of the fact that this reaction itself is very inefficient, the lifetime of ionized Mg is quite long at high atmospheric levels.

$$MgO^+ + O \quad \rightarrow \quad Mg^+ + O_2 \tag{4.9}$$

At lower altitudes, major species for reaction with metal species are O, O_2, O_3, H, H_2 and H_2O. Magnesium will form stable oxides or hydroxides as their dominant compounds (Plane, 2003).

The major stable sink species of magnesium species is $Mg(OH)_2$, it is formed by reaction of magnesium oxide with water vapour:

$$Mg + O_3 \quad \rightarrow \quad MgO + O_2 \tag{4.10}$$

$$MgO + H_2O + M \quad \rightarrow \quad Mg(OH)_2 + M(M = O_2, N_2) \tag{4.11}$$

See Figure 4.1 for a vertical profiles of the major sink species. According to Plane and Helmer (1995), possible reservoir species like $MgCO_3$ and MgO_3 are expected to spontaneously decompose, as the reactions (4.12) and (4.13) are highly endothermic.

$$MgO_3 + O \quad \rightarrow \quad MgO_2 + O_2 \tag{4.12}$$

$$MgCO_3 + O \quad \rightarrow \quad MgO_2 + CO_2 \tag{4.13}$$

Neutral Mg is recovered by double hydrogenolysis of the reservoir species ((4.14), (4.15)). This reaction depends on the abundance of atomic hydrogen and is thus most efficient under daylight summer conditions.

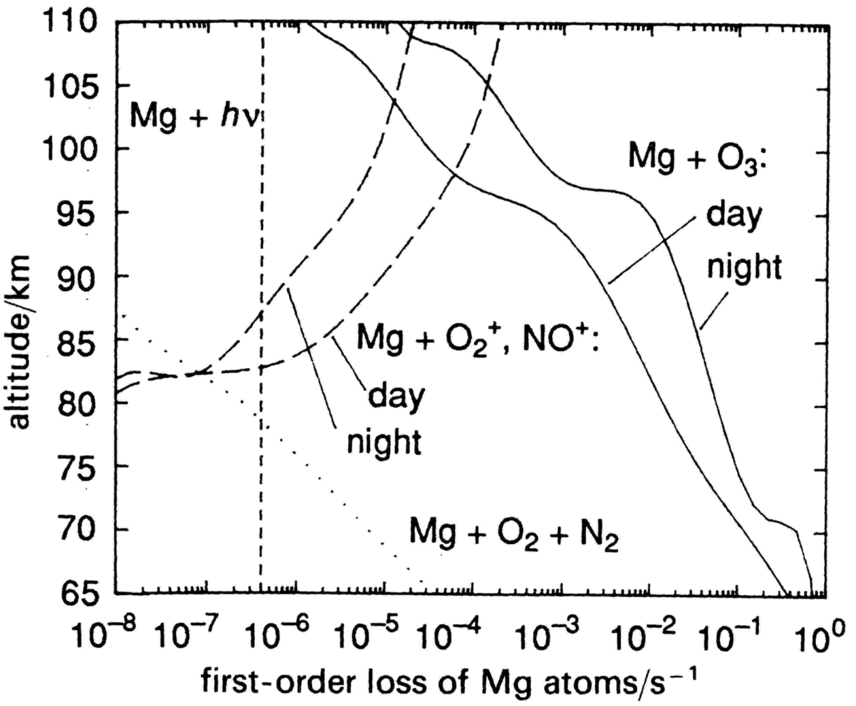

Figure 4.2: Loss rates in the Earth's atmosphere (north mid-latitude winter scenario) for neutral Mg (adapted from Plane and Helmer (1995)). At high altitudes, charge transfer with molecular oxygen and nitrogen ions is the most efficient loss reaction. Lower down in the atmosphere, the major loss reaction is presented by reaction with ozone to form the magnesium oxide MgO. This is then converted to its stable reservoir $Mg(OH)_2$ by reaction with water vapour, see reaction (4.11).

$$\mathrm{Mg(OH)_2 + H} \rightarrow \mathrm{MgOH + H_2O} \quad (4.14)$$

$$\mathrm{MgOH + H} \rightarrow \mathrm{Mg + H_2O} \quad (4.15)$$

A schematic sketch of the magnesium chemistry in the upper atmosphere is presented in Figure 4.3. It should be noted that for less than half of the major reaction pathways, reaction coefficients arev actually measured in the laboratory. The remaining coefficients had to be estimated or calculated from quantummechanical principles. The reliability of model results in general suffers from these uncertainties.

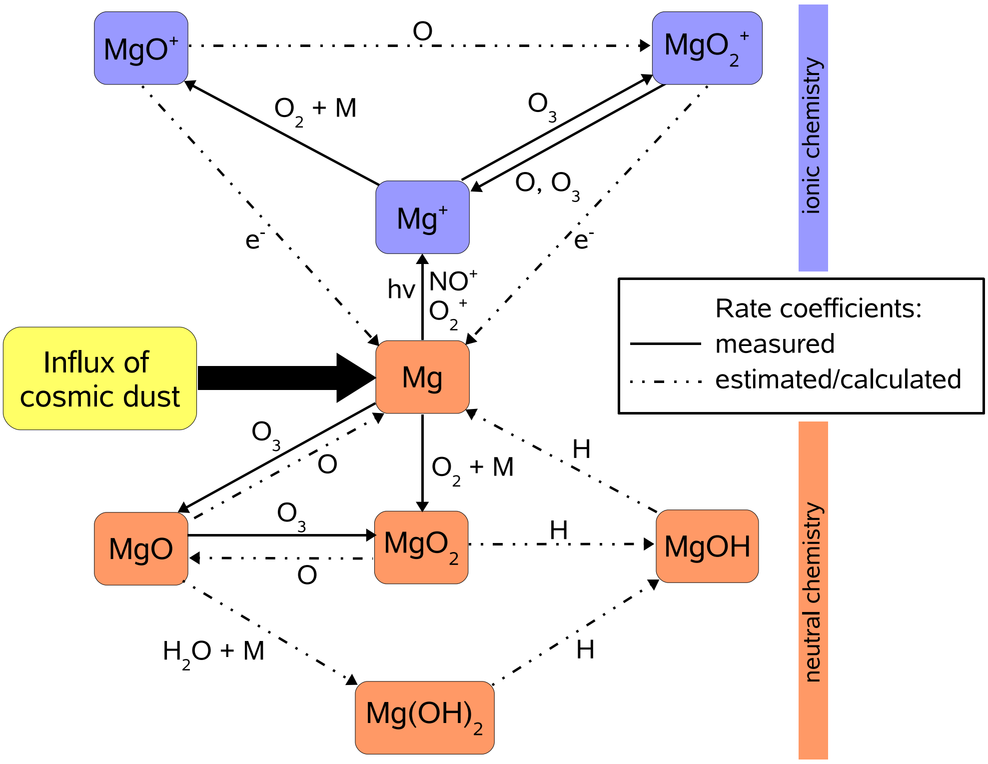

Figure 4.3: Overview of the chemistry of Mg, Mg^+ and respective compounds in the upper atmosphere. Adapted from Plane and Helmer (1995), solid lines indicate reactions for which corresponding rate coefficients have been measured.

Part II

Methodology

5 The SCIAMACHY instrument

The European ENVISAT satellite launched in March 2002 carries three instruments designed to perform observations of the atmosphere. Beside the Fourier transform spectrometer MIPAS, the stellar occultation device GOMOS and seven other instruments there is the SCIAMACHY instrument (**S**canning **I**maging **A**bsorption Spectro**m**eter for **A**tmospheric **Ch**artograph**y**).

The objective of the ENVISAT mission and the SCIAMACHY instrument in particular is the determination of amounts and distribution of atmospheric constituents on a global scale with good spatial and temporal coverage. This will improve the knowledge of the physics and chemistry of the whole Earth's atmosphere from the surface to the transition region between atmosphere and space and from high-latitude regions to the tropics. A detailed description of the SCIAMACHY mission objectives can be found in (Bovensmann et al., 1999).

SCIAMACHY covers a broad wavelength range from the UV-vis to the near-IR with a good spectral resolution (see Section 5.1) and provides nadir, limb and occultation viewing modes (Noel et al., 1999), see Figure 5.1. Limb scans (Section 5.2.2) are used to obtain altitude information of number densities, whereas the nadir mode (Section 5.2.1) provides total columns ranging from the ground to the satellite altitude in principle. In fact, the actual depth of the nadir scans depends on the wavelength range in use. For example, column densities obtained by using the UV channel (214 - 332 nm) do not extend to the ground, as the absorption in the ozone Hartley and Huggins bands prevents radiation within this wavelength range to penetrate the atmosphere as deep as e.g. visible radiation does. The limb viewing mode covers the altitude range from the surface up to the mesosphere. Note, however, that this observation mode suffers from absorption in the Hartley/Huggins at small wavelengths as well. Thus, measurements in the UV channel usually do not provide information about altitudes below approximately 60 km. The same holds for the occultation mode (Section 5.2.3).

5.1 Spectral characteristics

The core of the SCIAMACHY instrument is an eight-channel grating spectrometer covering the spectral range from 214 nm in the UV to 2380 nm in the near-IR with moderate to high spectral resolution. The wavelength range is divided into eight channels of different spectral coverage. Each channel comprises a passively cooled 1024 semiconductor diode array. The spectral resolution of the SCIAMACHY instrument varies from 0.17 nm in the UV region to 1.48 nm in the near-IR region of the electromagnetic spectrum. See Table 5.1 for an overview of the spectral characteristics of each channel.

In the UV-VIS-NIR wavelength region virtually all radiation entering the atmosphere originates from the sun, and virtually all radiation leaving the atmosphere is due to scattering and emission in the Earth's atmosphere or reflection at the surface. The broad spectral coverage allows SCIAMACHY to investigate a huge variety of atmospheric trace gas species by spectroscopical means. Absorption as well as emission features can be used for identification and quantification of trace gas species.

Channel #	WL range [nm]	Spec. res. [nm]	Retrieval targets
1	214 – 332	0.17 – 0.24	O_3, ClO, NO, Metals
2	320 – 403	0.26	NO_2, OClO, BrO
3	391 – 605	0.44	O_3, NO_2, O_4, Aerosols
4	597 – 789	0.48	O_3, NO_3, H_2O, Aerosols
5	774 – 1056	0.54	H_2O, Aerosols
6	990 – 1750	1.48	H_2O, Aerosols
7	1939 – 2040	0.22	H_2O, CO_2
8	2260 – 2384	0.26	H_2O, CO_2, CO

Table 5.1: Overview of the SCIAMACHY spectrometer channels. Listed are wavelength (WL) ranges and spectral resolutions (Spec. res.). The fourth column lists a number of atmospheric trace gases with strong absorption or emission features in the corresponding wavelength range. Thus, these wavelength ranges are likely to be used for retrievals of the respective species.

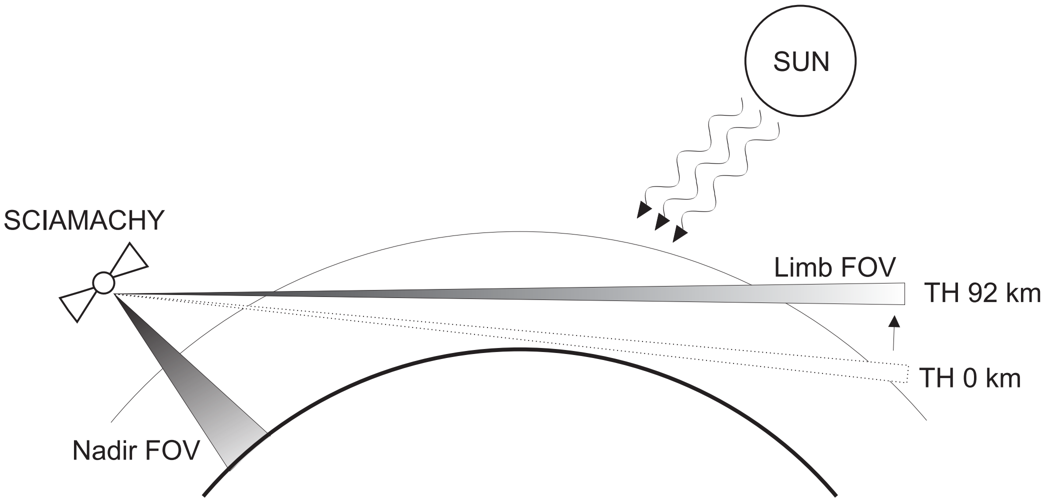

Figure 5.1: SCIAMACHY viewing geometries. The occultation mode (looking directly into the sun) is not shown here.

5.2 Spatial characteristics and measurement modes

5.2.1 Nadir mode

In nadir mode, the instrument scans across the satellite track using its azimuth mirror (see Figure 5.1). Each nadir scan comprises 13 swaths from left to right and back. Each swath spans approximately 960 km across track and approximately 30 km along track. Thus, the best possible spatial resolution along track is 30 km. The maximum resolution across track depends on the integration times and the data readout rate of the instrument, both quantities vary with channel and geolocation. The best resolution is 60 km across track. This is achieved for the most important atmospheric species O_3, NO_2, H_2O and aerosols in mid and high latitudes.

However, the applications presented in this thesis employ radiances of channel 1 exhibiting a rather unfavourable signal-to-noise ratio. Thus, the maximum integration time (and thus minimum data rate) is used. All swaths corresponding to one nadir footprint are integrated, and this leads to a resolution of 450 km along track and 960 km across track for a single nadir scan.

5.2.2 Limb mode

In limb mode, the instrument performs horizontal scans using its azimuth mirror at a number of different tangent altitudes (see. Figure (5.1)). The latter are accessed using an elevation mirror. Starting at the surface, 30 swaths of 960 km from left to right and back are performed, each scan separated by 3.3 km in altitude from the preceding one. This method covers altitudes from 0 to 92 km. A last deep-space scan is taken at approximately 250 km. First mission concepts contained 35 limb scans covering -3 to 115 km in steps of 3.3 km and a last deep-space scan at approximately 150 km. However, optimization of data rates for a better limb-nadir-matching approximately 1.5 years after launch lead to a restriction to 31 altitude steps. The topmost tangent altitude before the deep-space scan is now 92 km.

A typical limb cycle from bottom to the top tangent altitude has a duration of 60 s. During this time, the satellite platform moves 400 km along track. This determines the resolution along track. However, as in most applications, only a subset of 5 to 15 single scans of one limb cycle is used, the resolution along track improves to correspondingly better values.

The vertical and horizontal resolution is limited by the instantaneous field-of-view (IFOV) and the step size of the tangent altitude grid. The IFOV opens 0.045° vertically and 1.8° horizontally. This leads to a potential optimal vertical and horizontal resolution of 2.6 km by 110 km, respectively. The actual resolution depends on the spectral range and the integration time. Similar to the nadir mode, a number data readouts of one swath are integrated to improve the signal-to-noise ratio. This leads to a typical effective horizontal resolution of approximately 960 km across track in channel 1. Note, however, that the actual horizontal resolution is determined by the geolocation as well. Other integration times are used for different channels and the horizontal resolution may differ. The actual vertical resolution is determined by a number of quantities. This will be discussed in further details in Section 6. Note, however, that by no means the vertical resolution can be better than 2.6 km. See Noel et al. (1999) and Bovensmann et al. (1999) for detailed descriptions of possible SCIAMACHY resolutions.

5.2.3 Occultation mode

The occultation mode is very similar to the limb measurement mode. The instrument performs horizontal swaths while tracking the sun or the moon at sunrise and ”moonrise”, respectively. Advantages of this measurement mode are good signal-to-noise ratio due to high signal strengths (e.g. in the UV, those are $\approx 10^3$ times higher than in limb mode) as well as a good vertical resolution. The horizontal resolution, however, suffers from long integration paths. The geographical coverage is very poor, as the measurement depends on terminator crossings. The occultation mode is not used for the work presented in this thesis.

5.3 Limb-Nadir-Matching

The measurement time line of SCIAMACHY operations is designed in a way to offer measurements of tomographic fashion. For every limb scan there is a nadir scan of the same air volume. The time difference between these ”matching” measurements is approximately seven minutes. This can be used to calculate atmospheric columns in different altitude ranges. Originally, this design was intended to obtain tropospheric columns (see e.g. Noel et al. (1999), Sierk et al. (2006)). However, it can be used to separate the mesospheric partial column from the thermospheric partial column. The latter is contained in the total column observed in nadir, but the limb altitude range does not cover the thermosphere. In this study, a widely improved method is presented that involves not only a single pair of one limb and one nadir scan, but all limb and nadir scans of one orbit simultaneously (see Section 6 and Figure 5.2).

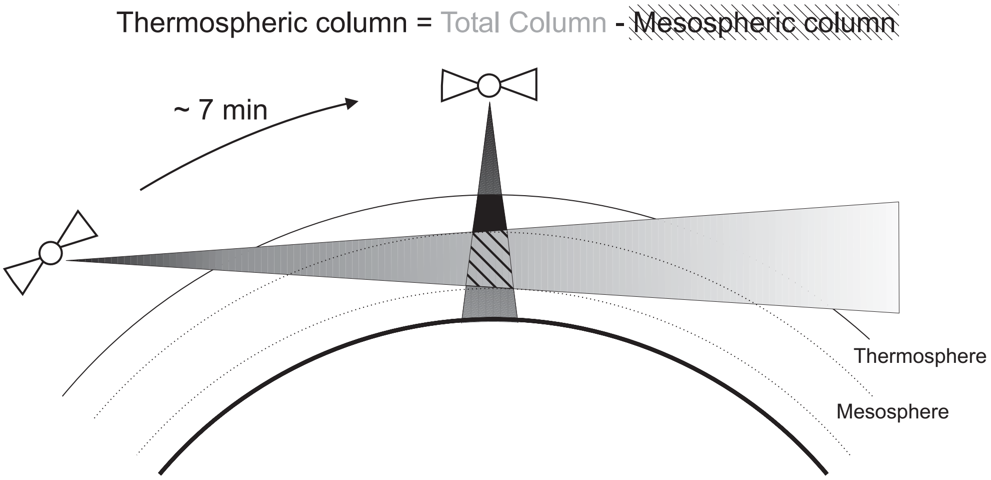

Figure 5.2: Primitive form of limb-nadir matching. A limb scan is followed by a nadir scan of the same volume. Linking these measurements gives access to partial columns of altitude ranges not covered by limb mode. A more sophisticated method involving more nadir and limb scans simultaneously and thus yielding better horizontal as well as vertical information is presented in Section 6.

6 A 2D retrieval scheme for SCIAMACHY limb and nadir data

A comprehensive retrieval scheme for SCIAMACHY limb and nadir measurements is presented in this section. Section 6.1 discusses drawbacks of limb scans used for measurement of emissions at altitudes above the top tangent altitude. The next two sections are dedicated to the description of a two-dimensional retrieval scheme designed to overcome this problems and allow SCIAMACHY to obtain altitude information above the top tangent altitude. The retrieval simultaneously uses all limb and nadir measurements of one orbit. A discussion of the instrumental error is contained in Section 6.4. The last section presents result of studies in terms of reconstruction of synthetic data that are degraded by noise. It is shown that the retrieval is capable to reconstruct the genuine distribution to a good extend.

6.1 Horizontal resolution of a single limb scan – absorption data and emissions

Limb sounding instruments in general have the advantage of providing vertically resolved information of the atmosphere. However, these instruments suffer from long light paths and thus long integration lengths. This may pose problems on the retrieval if a horizontally homogeneous atmosphere is assumed for simplification. This section will discuss in detail the potential horizontal resolution of a limb sounder. It will be shown that the resolution depends on the vertical profile of the species being observed.

SCIAMACHY limb and nadir measurements of backscattered light can yield number densities of atmospheric species on a global scale with good vertical and horizontal resolution. Among other quantities, the intensity of the Rayleigh backscattered radiation depends on the number density of air, and this quantity is decreasing exponentially with altitude. As the altitude above ground of the LOS increases with increasing distance from the tangent point along the line-of-sight (LOS), the number density of any scattering species is decreasing as well. As a result, the lowest part of the LOS contributes the major part to the measured radiation. For air density and assuming a scale height of 6 km, approximately 80% of the intensity of the detected radiation originate within an interval of 450 km centered around the tangent point (see Figure 6.2 for a quantitative and Figure 6.1 for a qualitative illustration). This distance can be interpreted as the spatial resolution of a single limb scan.

Note, however, that this is only true if the atmosphere is not optically thick. In the latter case, it is possible that the absorption within the atmosphere does not allow radiation from more distant parts of the LOS to enter the instrument. In this case, the observed radiation is dominated by the nearest part of the LOS. An optically thick atmosphere is the case e.g. for radiation within the ozone Huggins bands around $\approx$ 260 nm, tangent altitudes below $\approx$ 70 km and solar zenith angles above $\approx 60^\circ$. The retrieval presented here is employed for investigation of magnesium species emitting around 280 nm and 285 nm, however. The lowest tangent altitude used is 70 km. Thus, it can be assumed that the atmosphere is optically thin.

However, the contribution of the radiation originating in an individual LOS segment depends on the altitude profile of the species under consideration. In case of Rayleigh and fluorescence scattering, the amount of radiation emitted or scattered in an individual air volume is proportional to the number density within this volume. It is clear that a constant altitude profile between the ground and an altitude of H results in constant number densities at every point

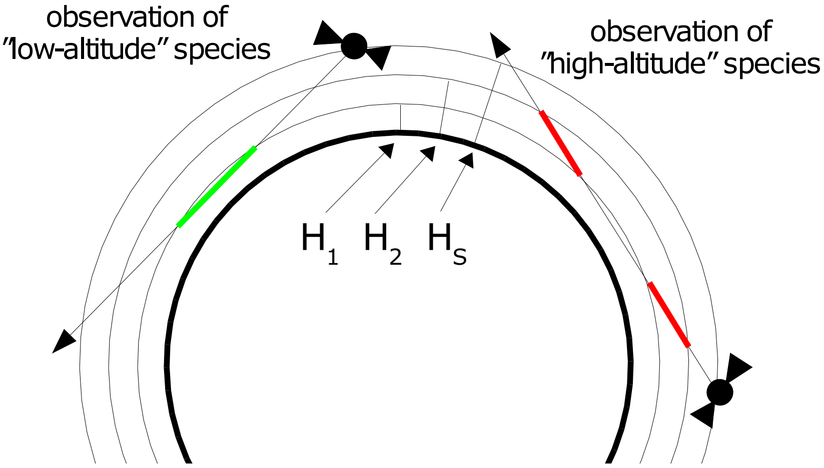

Figure 6.1: Sketch of the measurement geometry and signal contributions for a limb sounder. The instrument is orbiting at an altitude H_S. The thick parts of the respective line-of-sight denote those parts contributing most to the overall signal observed by the instrument. Given a species with major abundance below an altitude H_1, most of the signal originates around the tangent point. This is depicted as "low-altitude" species. A species with maximum abundance at an higher altitude, within the altitude range $[H_1, H_2]$, say, contributes mostly to the signal at parts of the line-of-sight far away from the tangent point. This is depicted as an "high-altitude" species.

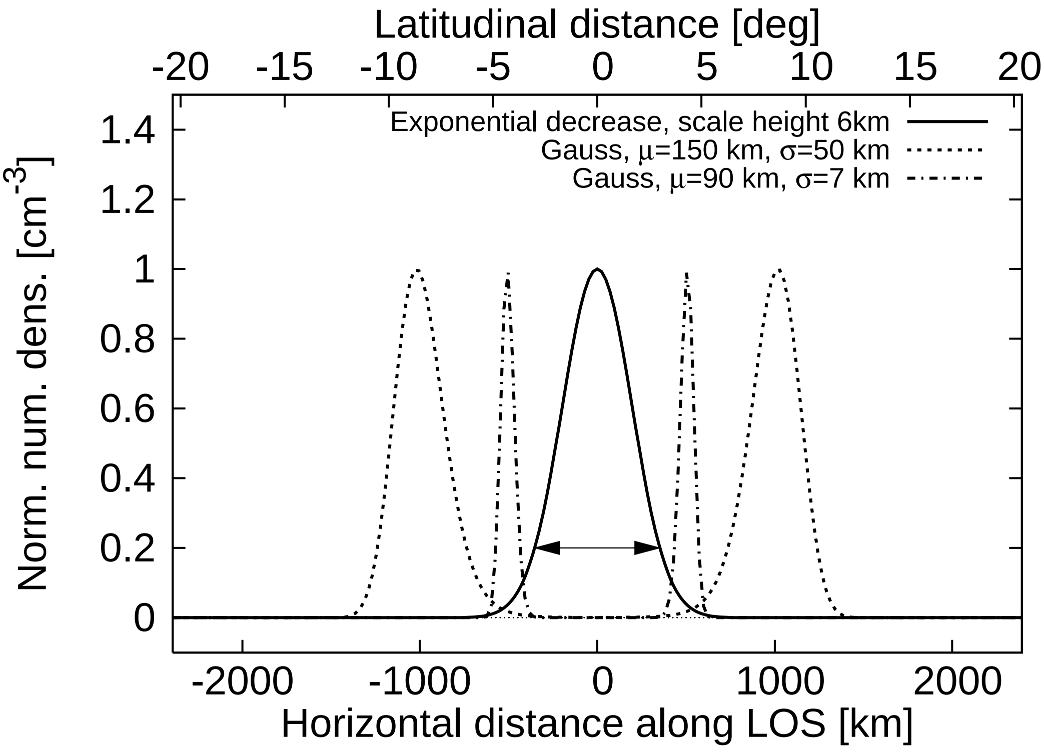

Figure 6.2: Number densities of an arbitrary atmospheric species along a limb line-of-sight at tangent altitude 70 km. The distance from the tangent point along the LOS is transformed to altitude over ground, and this is then used to determine the number densities. Solid: Exponentially decreasing number density with scale height 6 km. This is representative e.g. of air density. The arrow denotes the interval within which the intensity of scattered radiation drops to 20%. For the setting used here, about 80% of the scattered radiation originates in an interval of 450 km length centered around the tangent point. Dashed: Gauß peak with full-width-half-maximum 50 km, centered at 150 km. Dash-dot: Gauß peak with full-width-half-maximum 7 km, centered at 90 km. The major part of the radiation originates at distances of 750 – 1000 km from the tangent point.

on the LOS. In this case, the spatial resolution of a limb scan equals the length of the LOS within the atmosphere, i.e. within the atmospheric shell of radius $R_E + H$, where R_E denotes the Earth radius.

Figure 6.2 shows the number densities along a LOS at 70 km tangent altitude for different altitude profiles of an arbitrary scattering or emitting species. The intensity of radiation emitted in an individual air volume is assumed to be proportional to the number density of the species. The distance from the tangent point along the LOS is converted to altitude over ground, and this is then used to determine the number densities. Beside the exponential altitude profile (this is valid e.g. for air density), a narrow Gauß shaped distribution centered around 90 km with a full width at half maximum of 7 km and a wide Gauß peak with 50 km full-width-half-maximum, centered at 150 km, are chosen. As can be seen, the parts of the LOS contributing most to the observed radiation are located at distances 750 – 1000 km away from the tangent point. Obviously, peak concentrations at larger altitudes yield maximum contributions at higher distances away from the tangent point. The width of the peak in the altitude profile determines the width of the contribution peak along the LOS. As the observed radiance is the integrated radiance along the LOS, these both circumstances decrease the spatial resolution of the limb instrument.

Figure 6.1 depicts this difficulty graphically. As can be seen, a "high-altitude" species with maximum number densities above the top tangent altitude contributes most to the observed radiation at parts of the LOS that are remote of the tangent point.

6.2 Retrieval principle

Figure 6.3 shows a typical orbit measurement sequence of SCIAMACHY. As can be seen from the figure, a number of air volumes is traversed by several lines-of-sight (LOS) in limb as well as in nadir geometry. This circumstance can be used to overcome the drawbacks of integration over a long part on the LOS. A number of SCIAMACHY measurements are evaluated simultaneously.

The retrieval presented in the following is based on the fundamental assumption that the atmosphere is in steady-state during the duration of one orbit. This assumption is reasonable, as the day lit part of a single orbit is completed in approximately 50 minutes.

For a single orbit, a fixed partition of the atmosphere in *nPix* pixel is assumed. A detailed description of the pixel grid is given in Section 6.3.3. Let x_i be the number density within the i-th pixel. It is assumed to be constant within the pixel. As the emitted radiation is proportional to the number density within the i-th pixel as well as to the pathlength s_{ij} of the LOS no. j within the pixel, the contribution of a single pixel is given by

$$I_j(\lambda) = x_i \cdot \gamma_{ij}(\lambda) \cdot s_{ij} \cdot \exp\left(-\tau_{ij}(\lambda)\right) \cdot F(\lambda). \tag{6.1}$$

Obviously the factors s_{ij} are is non-zero only for those pixels being traversed by the LOS no. j (see Sections 6.3.3, 6.3.5). In equation (6.1) $F(\lambda)$ denotes the solar irradiance at the top-of-atmosphere (TOA) at wavelength λ. The emissivity factors γ_{ij} are explained and derived in Section 6.3. These present proportionality factors between the observed radiance and the number densities. The quantity $\exp\left(-\tau_{ij}(\lambda)\right)$ denotes the extinction along the LOS from the pixel to the instrument as well as the extinction from the sun to the pixel along the line-from-the-sun (LFS). Obviously, this quantity depends on wavelength. Within the mesosphere and thermosphere, extinction in the wavelength range of 200 – 300 nm is mainly a result of absorption within the ozone Hartley-Huggins bands and Rayleigh scattering out of the LOS respectively LFS. See Section 6.3.4 for a detailed description of the calculation of the τ values.

The total observed radiance for a single line-of-sight – either limb or nadir – numbered j, is then given by

$$I_j(\lambda) \approx \sum_{i=1}^{nPix} x_i \cdot \gamma_{ij}(\lambda) \cdot s_{ij} \cdot \exp\left(-\tau_{ij}(\lambda)\right) \cdot F(\lambda). \tag{6.2}$$

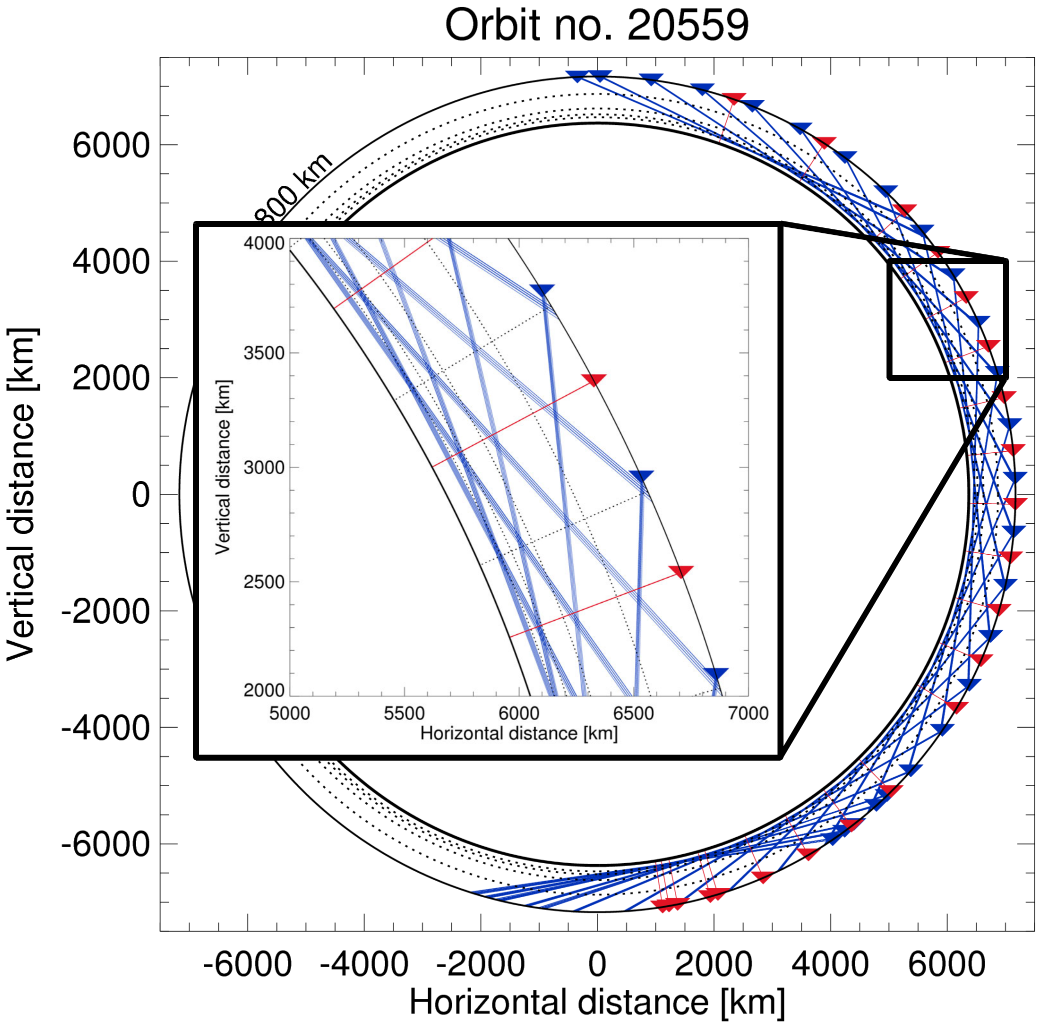

Figure 6.3: Typical orbit measurement sequence of SCIAMACHY. This figure is to scale. Triangles denote the satellite positions, lines-of-sight in limb geometry are drawn blue, and red lines correspond to nadir measurements. An atmospheric pixel grid representative to the one being used in the retrieval presented here is indicated partly by dotted lines. The 100, 150, 250, 500 km altitude levels are represented by dotted circles. Dotted radial lines depict the angular partitioning. In angular direction, each pixel is centered around the average tangent point of a single limb scan sequence from the surface to the top tangent altitude. The SCIAMACHY orbit sequence comprises of limb scans which are on average 7° apart, and this results in pixels of the same angular width on average. See Section 6.3.3 for a detailed description of the pixel grid.

Equation (6.2) presents a system of linear equations and can be written in a more convenient form using matrix notation. Let I denote the vector of limb and nadir measurements, ordered in an arbitrary but fixed way. Given $nLimb$ limb and $nNadir$ nadir measurements, obviously $I \in \mathbb{R}(nLimb + nNadir)$. The quantities x_i are combined in a vector $x \in \mathbb{R}(nPix)$. Equation (6.2) may be written in a more convenient matrix-vector form using the *weighting function matrix* $K \in \mathbb{R}(nLimb + nNadir, nPix)$:

$$I(\lambda) = K(\lambda) \cdot x + \varepsilon(\lambda) \quad , \quad K_{ij} = s_{ij}\gamma_{ij}(\lambda) \exp\left(-\tau_{ij}(\lambda)\right) F_i(\lambda). \tag{6.3}$$

The quantity ε denotes the discretization error. For convenience, the argument λ is omitted from now on. Let $nMeas = nLimb + nNadir$.

Solving equation (6.3) provides the desired values of the number densities x_i. In most cases, however, the matrix K is not quadratic, rank-deficient and not well-conditioned. Thus, it is not possible to solve this system of linear equations uniquely using classical ways such as Gauß elimination. In general, a multitude of solutions to the system exist, and these depend sensitively on variations of the input parameters. The inevitable presence of noise and the discretization error result in huge variations in the retrieval solution.

Instead, a certain amount of additional information about the solution has to be applied. This is accomplished using a *regularization scheme*, see Section 6.3.6.

6.3 Obtaining column densities

This section treats the evaluation of the figures I_j as given in equation (6.2). For simplification, the case of one emitter with number density N is explained.

As a result of absorption of solar radiation, atoms as well as molecules exist in excited energy states. These states are characterized by a number of quantum numbers. See Banwell (1972) for a thorough discussion of atomic and molecular quantum mechanics. For convenient display, the quantum numbers are summarized like $n^{2s+1}l_j$. Here, n is the principal quantum number corresponding to the energy and size of the electronic orbital. The orbital is interpreted as the volume of space in which the electron spends 95%, say, or any other fraction, of its time. This term is closely connected to the probability interpretation of quantum mechanics in general. The shape of the orbital and the angular momentum is governed by l, and the axial angular momentum is taken up by s. The quantity j is assigned to the total angular momentum. If omitted, $n = 0$ holds. The values of l are denoted by capital letters $S(l = 0), P(l = 1), D(l = 2), F(l = 3), G(l = 4), ...$ For $s = 0$, $2s + 1 = 1$ holds, and this state is called a "singlet" state. Accordingly, $s = 1/2$ and $s = 1$ correspond to "doublet" and "triplet" states.

Excitation to electronically elevated states requires large amounts of energy, compared to excitation to vibrationally or rotationally excited states for molecules. Additionally, the life time of excited states is rather short, i.e. spontaneous de-excitation occurs within times similar to 10^{-8} s. Note that the average life time τ_j of an excited state is connected to the Einstein coefficient by $\sum_i A_{ij} = \tau_j$. For typical mesospheric temperatures of 200 K and a mean free path of the order of centimeters (as is the case for altitudes between 80 and 100 km), the mean time between collisions of individual molecules is of the order of 10^{-5} s. It is thus assumed for the retrieval presented here that collisional de-excitation via quenching with air molecules is negligible.

Species	State i (lower)	State j (upper)	λ_{ij} [nm]	$A_{ij}[10^8 s^{-1}]$	$f_{ij}[-]$
Mg^+ (*)	$^2S_{1/2}$	$^2P_{1/2}$	279.553	2.60	0.61
Mg^+ (*)	$^2S_{1/2}$	$^2P_{3/2}$	280.270	2.60	0.31
Mg^+	$^2P_{1/2}$	$4^2S_{1/2}$	292.863	1.2	0.15
Mg^+	$^2P_{1/2}$	$^2D_{3/2}$	279.078	4.0	0.93
Mg^+	$^2P_{3/2}$	$4^2S_{1/2}$	293.651	2.3	0.15
Mg^+	$^2P_{3/2}$	$^2D_{3/2}$	279.793	0.79	0.093
Mg^+	$^2P_{3/2}$	$^2D_{5/2}$	279.800	4.8	0.85
Mg	$^1S_0$	$^1D_2$	215.435	$1.64 \cdot 10^{-5}$	N/A
Mg (*)	$^1S_0$	$^1P_1$	280.213	4.91	1.80

Table 6.1: Spectral data for Mg species. See Figure 6.4 for a sketch of the corresponding Grotrian diagram. This table contains the transition wavelengths λ_{ij} between to states i and j, the Einstein coefficients A_{ij} and the oscillator strengths f_{ij}. Transitions marked with (*) are between the ground state and the first excited state. Those are used for the retrieval of Mg and Mg^+ number densities. Values were obtained from NIST (2005).

The observed emitted radiance I in limb and nadir is linked to the column density (vertical as well as slant) by the emissivity factor ('g-factor') γ_{ij}, which is a proportionality factor between the observed radiance (normalized by the solar irradiance) and the column density. The emissivity factor is assumed to be independent of temperature and pressure.

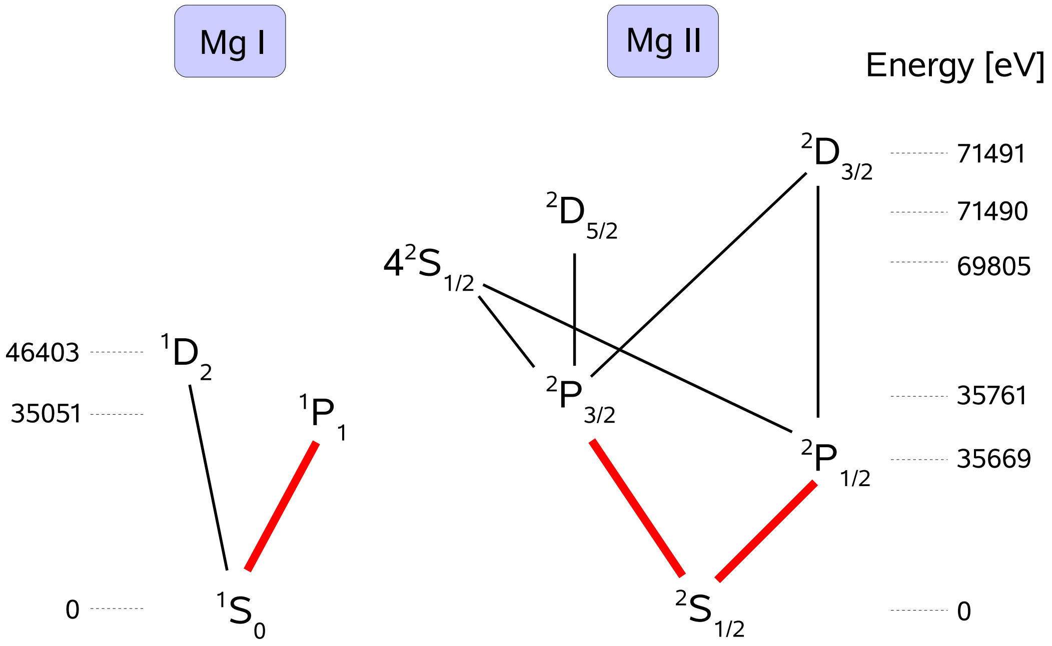

Figure 6.4: Grotrian diagrams of neutral Mg (Mg I) and ionized Mg$^+$ (Mg II). Lines connecting states of different energy denote allowed quantum mechanical transitions. Bold red lines correspond to the transitions used in the retrieval of Mg and Mg$^+$. These correspond to emission features at 280 and 285 nm , see Table 6.1 for significant parameters corresponding to the transitions depicted above.

$$\begin{aligned} I(\lambda) &= \gamma_{ij}(\lambda) \cdot \int_{\mathrm{LOS}} F(s,\lambda) \cdot N(s)\, ds \\ &= \gamma_{ij}(\lambda) \cdot F(\lambda) \int_{\mathrm{LOS}} e^{-\int_s^{\mathrm{TOA}} \tau(s',\lambda) ds'} \cdot e^{-\int_s^{\mathrm{TOA}} \tau(s'',\lambda) ds''} \cdot N(s)\, ds \qquad (6.4) \end{aligned}$$

Here, integration along the LOS is simply integration over altitude for nadir scans. This equation is the continuous form of equation (6.2). The two exponential terms in equation (6.4) represent the extinction along the line-from-the-sun and the line-of-sight, respectively. See Section 6.3.4 for a detailed discussion of the radiative transfer used in the retrieval.

Note that I denotes the net emission, that is, the total observed radiance with the Rayleigh background removed. The calculated emissivity is convolved to the SCIAMACHY wavelength grid and then fitted using a least square fit procedure to the measured spectrum. The fit factor then constitutes the column density. In Figure 6.5 a visual representation of this approach is given.

The g-factor is calculated as the product of the actinic flux, the absorption cross section σ_{ij}, the relative Einstein coefficient of spontaneous emission (Anderson and Barth, 1971) and a phase function term depending on the scattering angle θ (see Section 6.3.1). Here, σ_{ij} depends on the classical electron radius as well as on the transition wavelength λ_{ij} and the oscillator strength f_{ij}. The relative Einstein coefficient presents the probability of relaxation from the excited state j to the lower state i. Note that there may be a number of lower states reachable from state j. This is accounted for by normalizing A_{ij} by the sum of all respective absolute Einstein coefficients. A thorough derivation of the phase function is given in the next section. See Figure 6.4 and Table 6.1 for a review of some transitions of Mg and Mg$^+$.

$$\begin{aligned} \gamma_{ij} &= P(\theta) \cdot \pi F(\lambda_{ij}) \cdot \sigma_{ij} \cdot \frac{A_{ij}}{\sum_{i'} A_{i'j}} \qquad (6.5) \\ &= \underbrace{P(\theta)}_{\text{Phase function}} \cdot \underbrace{\pi F(\lambda_{ij})}_{\text{actinic flux}} \cdot \underbrace{\frac{\pi e^2}{mc^2} f_{ij} \lambda_{ij}^2}_{\text{abs. cross section}} \cdot \underbrace{\frac{A_{ij}}{\sum_k A_{kj}}}_{\text{rel. Einstein coeff.}} \qquad (6.6) \end{aligned}$$

All values necessary for numerical calculations are obtained from the NIST database (NIST, 2005).

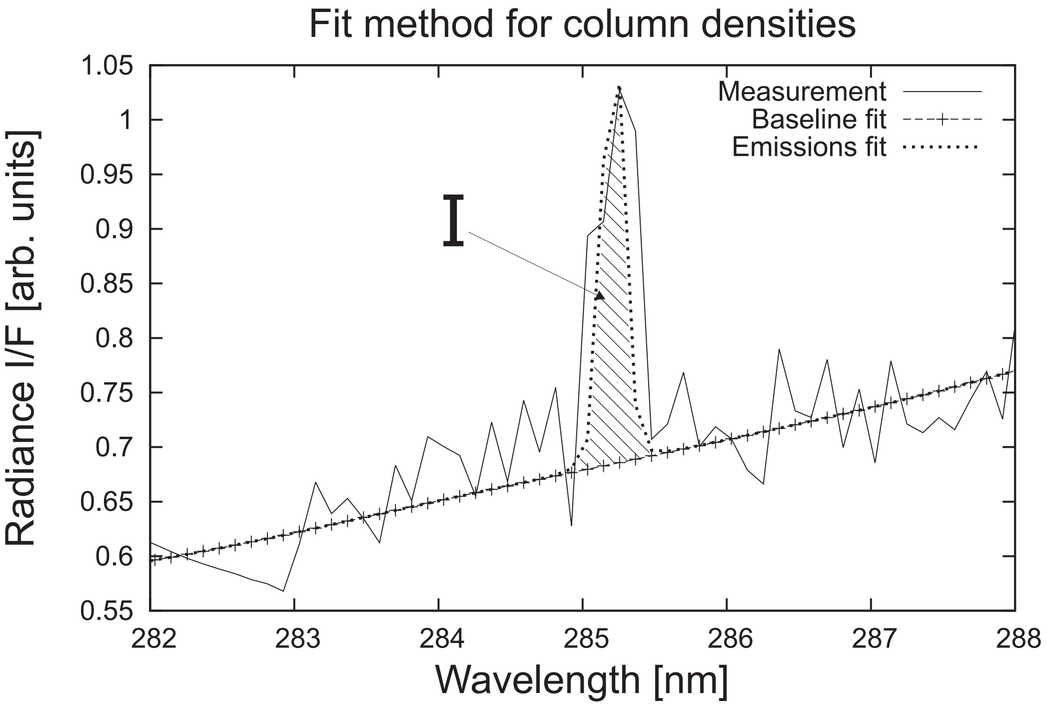

Figure 6.5: Sketch of the method to estimate column densities for the example of neutral Mg. The emission of neutral Mg around 285 nm observed in nadir view is shown. However, the fit method described here applies for all emissions under consideration and both measurement modes. The background is fitted using spline approximation within those wavelength ranges not containing any emission signal. In this example, the spline fit would extend from 282 to 285 nm and from 285.5 to 288 nm. The background radiance at the emission wavelengths is estimated by interpolation (spline or linear is possible, the results do not change significantly).

6.3.1 Phase function for resonance line scattering

We use the Chandrasekhar form (Chandrasekhar, 1960), slightly abridged from (Hamilton, 1947) of the phase function for resonance line emission. That is, the phase function $P(\theta)$ for radiation emitted by resonance fluorescence is a superposition of an isotropic part as well as an anisotropic part similar to Rayleigh scattering by spherical particles.

$$P(\theta) = \frac{3}{4}E_1(\cos^2(\theta) + 1) + E_2 \tag{6.7}$$

The first term weighted by a constant E_1 takes up the angular dependent part of the phase function, whereas the second term weighted by another constant E_2 represents the isotropic part. The probability of scattering into a solid angle $d\Omega$ under the emission angle θ is given by $P(\theta)d\Omega/4\pi$.

The constants E_1 and E_2 depend on the angular momentum number j of the energy states involved in the observed transition as well as on the difference Δj of same. The factors can be calculated via the following rules given in Table 6.2 (Chandrasekhar, 1960).

Table 6.3 shows values for E_1 and E_2 with respect to the three Mg and Mg$^+$ transitions that have been obtained using the rules given in Table 6.2.

Note that according to these values, the case of total isotropic emission is given for $\lambda =$ 280.270 nm, whereas the transition $\lambda = 279.553$ nm is a mixture of isotropic and anisotropic emission. Neutral Mg, however, exhibits scattering following Rayleigh's phase function for isotropic particles.

6.3.2 Polarization for resonance line scattering

Though natural (i.e. solar) light is unpolarized, Rayleigh scattered radiation is partially polarized depending on the scattering angle θ. The largest degree of polarization is present for

Δj	E_1	E_2
+1	$\frac{(2j+5)(j+2)}{10(j+1)(2j+1)}$	$\frac{3j(6j+7)}{10(j+1)(2j+1)}$
0	$\frac{(2j-1)(2j+3)}{10j(j+1)}$	$\frac{3(2j^2+2j+1)}{10j(j+1)}$
-1	$\frac{(2j-3)(j-1)}{10j(2j+1)}$	$\frac{3(6j^2+5j-1)}{10j(2j+1)}$

Table 6.2: Formulas for the calculation of E_1 and E_2 as used in equation (6.7). From Chandrasekhar (1960).

Species	λ [nm]	j	Δj	E_1	E_2
Mg^+	279.553	1/2	+1	1/2	1/2
Mg^+	280.270	1/2	0	0	1
Mg	285.213	0	+1	1	0

Table 6.3: Coefficients for use in equation (6.7) calculated for the transitions under consideration. Values for j and Δj taken from NIST (2005).

$\theta = 90°$. Denote by $I_{||}$ and $I_\perp$ the intensity of the scattered radiation parallel and perpendicular to the plane of scattering (i.e. the plane containing incident and scattered rays), respectively. The ratio of these intensities at $\theta = 90°$ is given by the depolarization factor ρ:

$$\frac{I_{||}(90°)}{I_\perp(90°)} = \rho \tag{6.8}$$

The commonly chosen value $\rho = 0.0295$ reflects the fact that scattered light at $\theta = 90°$ is virtually completely polarized in direction perpendicular to the plane of scattering.

Resonance line scattering, however, does not in any case produce radiation polarized in the same direction as Rayleigh scattered light. As grid spectrometers like SCIAMACHY suffer from polarization sensitivity, calibration factors depending on the scattering angle have to be applied in order to treat different states of polarization.

Only the case $\theta = 90°$ is considered here. Depending on the specific transition under consideration (and thus on the particular values of E_1 and E_2), a number of situations occur. We assume that natural light of intensity I is completely unpolarized, that is

$$I_{||}^{(e)} = I_\perp^{(e)} = \frac{1}{2}I. \tag{6.9}$$

Here, the superscript $^{(e)}$ denotes emitted radiation. It is clear that both intensities must sum up to the incident intensity.

Following Chandrasekhar (1960), the ratio $I_{||}^{(e)}/I_\perp^{(e)}$ at $\theta = 90°$ can then be calculated:

$$\frac{I_{||}^{(e)}(90°)}{I_\perp^{(e)}(90°)} = \frac{E_2}{\frac{3}{2}E_1 + E_2} \tag{6.10}$$

Using values given in Table 6.3, the fractions of polarized light are easily derived, see Table 6.4.

The transition at $\lambda = 285.213$ nm is again very similar to Rayleigh scattering, as the emitted light is completely polarized in direction perpendicular to the emission plane. The Mg^+ emission at 280.270 nm, however, exhibits complete polarization in direction parallel to the plane of emission. The third emission at 279.553 nm presents unpolarized light in good approximation.

it should be noted that the polarization correction factors applied during the calibration of the SCIAMACHY spectral that assume all light entering the instrument being scattered in the

Species	λ [nm]	$I_{\|\|}^{(e)}/I_{\perp}^{(e)}$ $(\theta = 90°)$
Mg^+	279.553	2/5
Mg^+	280.270	1
Mg	285.213	0

Table 6.4: Fractions of polarized and unpolarized light contained in the Mg^+ and Mg emissions for an angle of 90° between incoming and emitted radiation.

atmosphere. Emissions are not considered. Thus, the calibration must fail at the Mg^+ and Mg emissions. This introduces errors of ± 15% in the retrieval.

6.3.3 Choice of the retrieval pixel grid

In principle, the retrieval pixel grid can be chosen arbitrarily. The mathematics of the retrieval do not relate the retrieval grid to the measurement grid. However, in practice it is desirable to adapt the retrieval grid to the measurements. Obviously, it is not reasonable to choose a grid with rectangular pixels in a Cartesian grid. Instead, a polar coordinate system is used, describing each pixel by a latitude and an altitude.

As can be seen from equation (6.2), the contribution of the number density in pixel no. i mainly depends on the path length s_{ij} of the LOS of measurement j within that pixel. Note that as a result of $\exp(-\tau_{ij}(\lambda)) \approx 1$, the quantity $F_i(\lambda)$ is near the value of the solar irradiance outside the atmosphere. It is desirable to have the values of s_{ij} as large as possible for each pixel to obtain a good sensitivity within pixel no. i. On the other hand, it is reasonable to design the pixel grid in a way to obtain similar values of s_{ij} for all pixels and measurements. Thus, the retrieval is more or less equally sensitive to all pixels. Additionally, coefficients of similar size improve the behaviour and stability of the equation solving algorithm (see Golub and v. Loan (1996) and Section 6.3.6).

Thus, a good compromise is to define pixels centered around the limb tangent points (Fig. 6.6). That is, low altitude pixels have the shape

$$[\frac{1}{2}(\phi_k + \phi_{k-1}), \frac{1}{2}(\phi_k + \phi_{k+1})] \times [\frac{1}{2}(h_l + h_{l-1}), \frac{1}{2}(h_l + h_{l+1})]$$

$$\phi_i = \text{Latitude of TP no. } k \quad , \quad h_j = \text{Tangent altitude no. } l$$

Note that the retrieval uses a different pixel grid for each individual orbit. The retrieval works within the altitude range of 70 − 500 km. Low altitude pixels denote pixels within the SCIAMACHY tangent height range below 92 km. Obviously, each pixel is easily described by two numbers, namely the corresponding indices of the limb measurement. However, for purposes of the retrieval it is necessary to number all pixels from 1 to *nPix*. SCIAMACHY limb scan tangent heights do not extend into the thermosphere, thus the pixel grid has to be designed 'freely' above the top tangent altitude of ≈92 km. Retrieval tests using synthetic data (see Section 6.7) yielded good results using four fixed altitude bins above 100 km, see Table 6.5. Obviously, the pixel grid cannot extend into the night side of the Earth.

A typical pixel grid is given in Table 6.5.

6.3.4 Calculation of optical depths $e^{-\tau_{ij}}$

At high altitudes, the solar irradiance at a certain wavlength is virtually constant and not dependent on solar zenith or azimuth angle. Similarly, absorption along the line-of-sight in

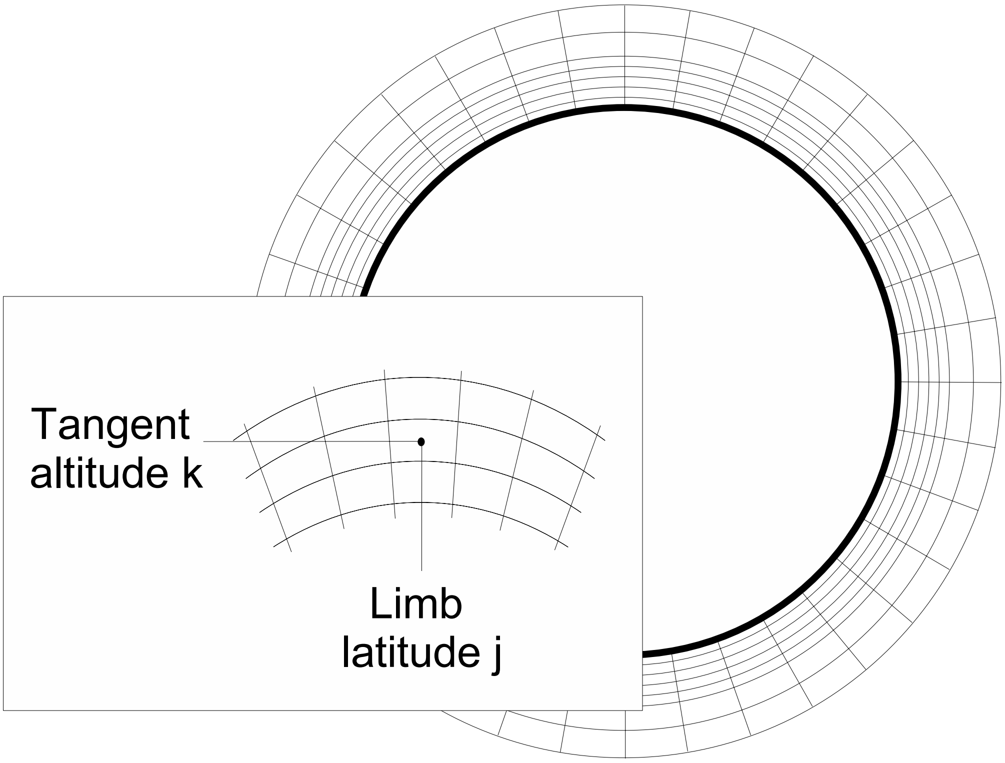

Figure 6.6: Outline of the retrieval pixel grid. Each latitude bin is subdivided into a number of altitude layers. Low altitude pixels are centered around limb tangent points to obtain maximum path lengths of limb lines-of-sight within the pixels. Thus, each pixel is approximately 3 km high and 7 – 15° wide. The altitude steps are increasing towards higher altitudes. This reflects SCIAMACHY's limited vertical resolution at high altitudes. See Table 6.5 for a quantitative description of a typical retrieval grid.

either limb or nadir can be neglected. For altitudes below 85 km and wavelength below 300 nm, however, absorption in the ozone Hartley-Huggins bands and Rayleigh scattering out of the LOS becomes significant. This is in particular the case for limb measurements, as the zenith angle of the line-of-sight is 90° . This yields long light paths. Figures 6.7 and 6.8 show limb radiances calculated by the radiative transfer model SCIARAYS (Kaiser, 2001). One calculation is done using a pure Rayleigh atmosphere without any absorption. The limb radiance is decreasing exponentially as the simulated limb sounder proceeds to higher tangent altitudes. If absorption in the ozone bands is included, the simulated radiance differs significantly from the calculated values without ozone. Figures 6.7 and 6.8 show exemplary results for 60° solar zenith angle and 60° solar azimuth angle. The 'full atmosphere'-radiances deviate by more than 5% at altitudes below 75 km. At 70 km, the relative difference reaches 15%. Note that these deviations increase for longer light paths in the atmosphere, e.g. higher solar zenith angles.

In the following, the calculation of the optical depth factors τ_{ij} used in equation (6.3) is discussed. The radiative transfer model presented here is based on a ray-tracing approach. Two fundamental types of rays exist. First, each line-of-sight is traced analytically and the differential absorption terms are integrated to obtain the absorption along the line-of-sight. Second, the same is done for sun-bound rays from every pixel. Both task share done using an reduced radiative transfer model. This model incorporates single scattering into and out of the line-of-sight respectively the line-from-the-sun) as well as absorption in the ozone Hartley-Huggins bands. The major advantage of this model compared to other models (see e.g. Kaiser (2001), Rozanov (2001)) is the fast computational speed and the simplicity of the source code. The model is modular and expandable for other species.

Each ray is defined by a starting point p_0 and a directional vector v_0. Using the law of cosine,

Bottom [km]	Center [km]	Top [km]
250.0	375.0	500.0
150.0	200.0	250.0
120.0	135.0	150.0
93.6	106.8	120.0
90.3	91.9	93.6
87.0	88.7	90.3
83.8	85.4	87.0
80.5	82.1	83.8
77.2	78.8	80.5
73.9	75.6	77.2
70.7	72.3	73.9

North [°]	Center [°]	South [°]
71.7	69.7	68.2
68.2	66.7	63.2
63.2	59.7	56.2
56.2	52.6	49.0
49.0	45.4	41.8
41.8	38.2	34.5
34.5	30.9	27.3
27.3	23.6	19.9
19.9	16.3	12.6
12.6	8.9	5.3
5.3	1.6	-2.1
-2.1	-5.8	-9.5
-9.5	-13.2	-16.9
-16.9	-20.6	-24.3
-24.3	-27.9	-31.6
-31.6	-35.3	-39.0
-39.0	-42.7	-46.3
-46.3	-50.0	-53.6
-53.6	-57.2	-60.8
-60.8	-64.4	-67.8
-67.8	-71.2	-74.3
-74.3	-77.4	-79.4
-79.4	-81.4	-83.4

Table 6.5: Typical pixel grid as used for the retrieval. In total, $11 \times 23 = 253$ pixels are defined. Figures denote the borders and center values of each pixel in altitudinal and latitudinal direction, respectively. Most pixels are approximately 3.3 km high and 7 – 15° wide. This holds not for the thermospheric pixels above the top tangent altitude. These values are set according to retrieval tests (see sec. 6.7). All values exemplarily shown here are derived from orbit no. 20559. Compare Figure 6.3 for a visualization of the orbit measurement sequence and Figure 6.6 for a graphical sketch of the grid.

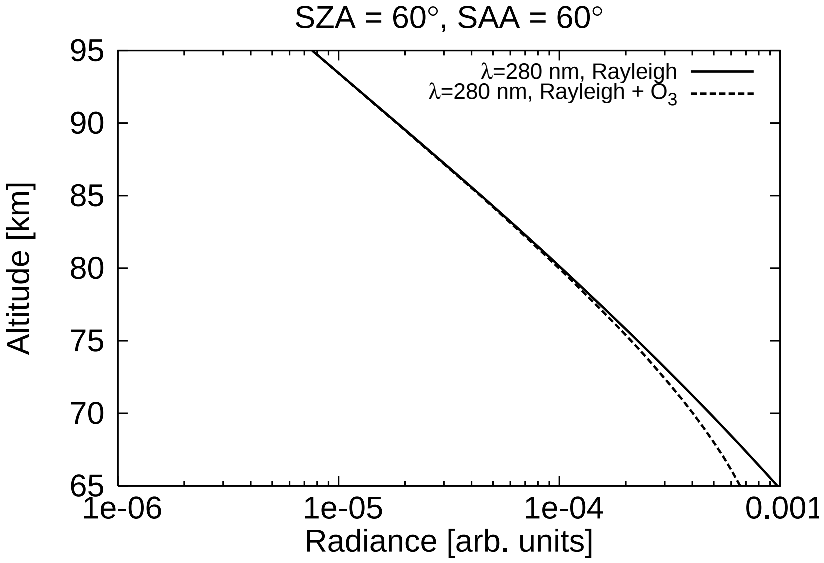

Figure 6.7: Limb radiances at 280 nm for different tangent altitudes and 60° solar zenith and azimuth angle. Solid: Calculated for a pure Rayleigh scattering atmosphere. Dotted: Calculated including absorption in the ozone Hartley-Huggins bands. The deviations exceed 5% at altitudes below 75 km, compare Figure 6.8.

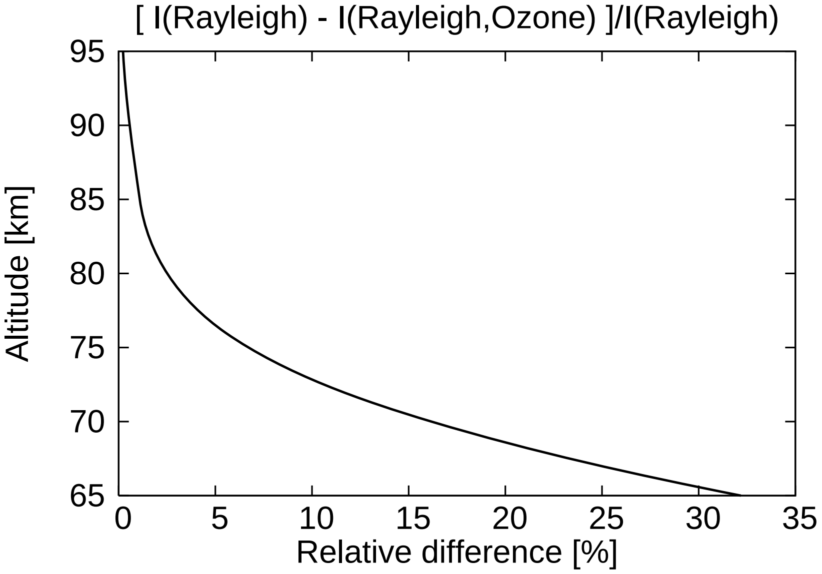

Figure 6.8: Relative differences of limb radiances at 280 nm, calculated for a pure Rayleigh scattering atmosphere and calculated including absorption in the ozone Hartley-Huggins bands. Compare Figure 6.7, solar angles are the same as given there.

the length of the ray within the atmosphere is calculated as follows, see Figure 6.9: .

$$s = -||p_0||\cos(\mathrm{SZA}) + \sqrt{||p_0||^2(\cos(\mathrm{SZA})^2 - 1) + (R_E + \mathrm{TOA})^2} \tag{6.11}$$

Here, the center of Earth was used as the origin of the underlying coordinate system, and R_E denotes the Earth radius. The top-of-atmosphere is defined to be the top of the topmost altitude pixel. The retrieval results presented in this work use 500 km as TOA. The length of the ray within the atmosphere is divided in N intervals.

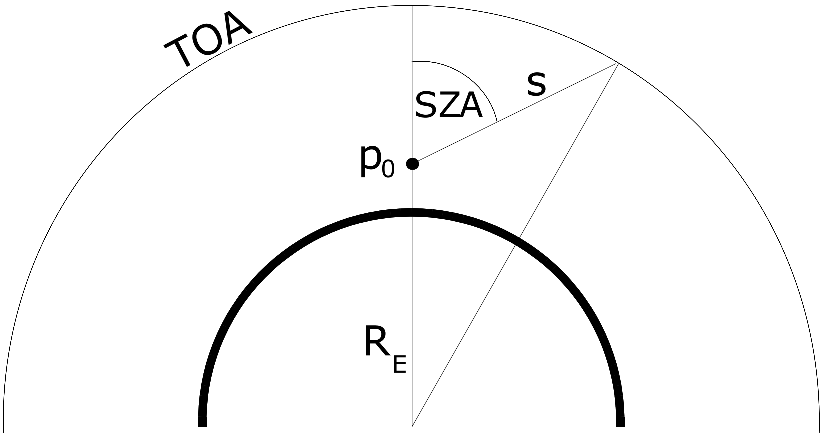

Figure 6.9: Calculation of the traverse length of an arbitrary ray within the atmosphere, given its starting point and the zenith angle at this point.

According to Beer's Law, the total absorption along a single ray can now be written in integral as well as in discrete form:

$$\tau(p_0, v_0, \lambda) = \int_{p_0}^{\mathrm{TOA}} \langle c(h), \sigma(h,\lambda)\rangle \, dr \quad , \quad h = h(r) \tag{6.12}$$

$$\approx \sum_{i=1}^{N} \langle c(h_i), \sigma(h_i)\rangle \frac{s}{N} \tag{6.13}$$

The brackets $\langle,\rangle$ denote the usual scalar product. The altitude h_i is easily calculated from $h_i = ||p_0 + iv_0|| - R_E$. Here, c denotes the vector of all species that contribute to the extinction,

σ contains the corresponding extinction cross sections. Extinction is assumed to be a result of scattering out of the ray and absorption by ozone alone, thus

$$c = (c_{\mathrm{Air}}, c_{\mathrm{Ozone}}) \quad , \quad \sigma = (\varepsilon_{\mathrm{Rayleigh}}, \sigma_{\mathrm{Ozone}}). \tag{6.14}$$

The extinction cross sections depend on the wavelength λ. However, the temperature and pressure dependences are negligible in the Hartley bands. That is, in particular, σ is assumed to be independent of altitude. Reference spectra measured by Burrows et al. (1999) were used for the retrieval.

For every pixel and every measurement, the total optical depth τ_{ij} is calculated from two line integrals, one describing the optical depth from pixel j to the instrument and another one holding the optical depth from the pixel to the sun:

$$\tau_{ij}(\lambda) = \tau(p_{\mathrm{Sat},i}, v_{\mathrm{Sat},i}, \lambda) + \tau(p_{\mathrm{Pixel},j}, v_{\mathrm{Sun},j}, \lambda) \tag{6.15}$$

Here, $p_{\mathrm{Sat},i}$ and $p_{\mathrm{Pixel},j}$ denote the locations of the satellite and the pixel under consideration, respectively. Accordingly, $v_{\mathrm{Sat},i}$ and $v_{\mathrm{Sun},j}$ denote the directional vectors from the satellite to the pixel and from the pixel to the sun, respectively.

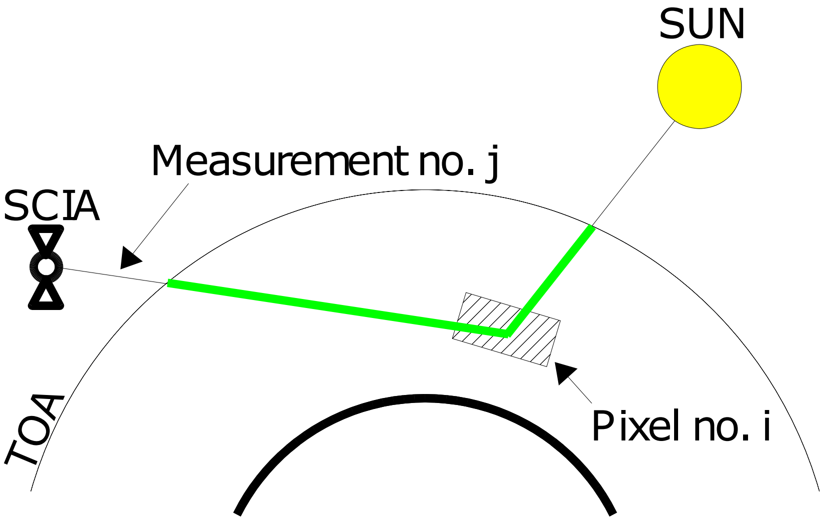

Figure 6.10: Outline of the calculation of optical depths to be used in equation (6.3). Integration along the two rays depicted here yields τ_{ij}. The part of the ray being actually within the atmosphere and thus suffering from extinction is marked green. The length of this part depends on the top-of-atmosphere (TOA). The retrieval uses a TOA of 500 km.

6.3.5 Calculation of geometrical path lengths s_{ij}

The calculation of the geometrical path lengths s_{ij} is rather straightforwardly implemented. Instead of using sophisticated analytical solutions, a simple ray tracing method is used. Using an arithmetical rather than an analytical approach has the advantage of more flexibility. The shape as well as number of pixels can be chosen arbitrarily, and the grid does not have to be equidistant or uniform in any sense.

The geometrical path lengths are calculated by ray tracing of each single line-of-sight of limb as well as nadir scans. The following pseudocode summarizes the crucial loop:

```
do
    choose line-of-sight no. $j$, starting point $p_0$, viewing vector $v_0$
    calculate the length $s$ of this LOS within the atmosphere
    set step size $\delta = s/N$
    do k=1,N
```

```
        if $p_0 + k\cdot\delta\cdot v_0 \in$ pixel no. $i$ then
            $s_{ij} = s_{ij} + \delta$
        end if
    end do
end do
```

Using values of $N \approx 10000$, the accuracy for the values s_{ij} in comparison to analytical calculated path lengths is less than 0.1 km. This a satisfactory value compared to the SCIAMACHY tangent height steps of 3.3 km.

As a result of the small density of air at mesospheric and thermospheric altitudes, refraction is negligible.

6.3.6 Regularization

Instead of solving (6.3) explicitly, it is reasonable to minimize the residual between the forward calculated state Kx and the measurement y:

$$||Kx - y||^2 \longrightarrow \min \tag{6.16}$$

In general, this problem does not have a unique solution. It is thus necessary to feed additional information about the true state x into the problem. However, this has to be done carefully to avoid introduction of unjustified bias. At first, information about noise and other errors can be introduced in the functional using a covariance matrix S_y. This results in a weighting of the components of the residual vector $Kx - y$:

$$||Kx - y||^2_{S_y} = (Kx - y)^T S_y (Kx - y) \tag{6.17}$$

Good results are obtained using a diagonal form of S_y with the diagonal elements taking up the estimations of the measurement errors, i.e.

$$S_y = \mathrm{diag}(\frac{1}{\sigma_1^2}, \dots, \frac{1}{\sigma_{nMeas}^2}). \tag{6.18}$$

If a good guess of the real state of the atmosphere exists (e.g. from model calculations or other measurements), this information is introduced into the retrieval by adding the vector norm of the difference of the retrieval solution to the *a priori* vector x_a:

$$||Kx - y||^2_{S_y} + ||x - x_a||^2_{S_a}. \tag{6.19}$$

The a priori covariance matrix S_a allows the user to weight the a priori information entering the retrieval. The retrieval setting used in this work uses $x_a = 0$. This way, the regularization term prevents the retrieval solution to take unreasonable large values. Oscillations in x tend to increase $||x - x_a||$, since positive and negative deviations from the a priori state do not cancel in the computation of the vector norm: $||x - x_a||^2 = (x_1 - x_{a,1})^2 + \cdots + (x_1 - x_{a,nPix})^2$. Thus, the retrieval solution tends to be smooth if the a priori state is smooth. However, during retrieval tests it turned out that this regularization is not sufficient. The smoothness of the retrieval solution has to be expressed explicitly using the discretization of the first derivative. To do this, it is necessary to sort the elements of x according to altitudes and latitudes. The vector x rewritten as a matrix $X \in \mathbb{R}(nLats, nTH)$:

$$X_{ij} = \text{Value of } x \text{ within latitude bin } j \text{ and altitude bin } i \tag{6.20}$$

Now, the k-th column of X contains the altitude profile at latitude k. Accordingly, row no. l contains the latitude cross section at altitude l. It is reasonable to assume that values of X within neighboured pixels are related to each other. That is, the functional

$$S = \sum_{j=1}^{nPix} \sum_{i=1}^{nPix} \lambda_H (X_{i+1,j} - X_{i,j})^2 + \lambda_\phi (X_{i,j+1} - X_{i,j})^2 \tag{6.21}$$

is supposed to be small. The first summand approximates the gradient in altitudinal direction whereas the second summand corresponds to the estimate of the gradient in angular direction (see Figure 6.11). The factors λ_H and λ_ϕ allow to weight the gradient approximations to the value of S. Equation (6.21) can be expressed in matrix notation using two matrices S_H and S_ϕ to give

$$S = \lambda_H ||S_H x||^2 + \lambda_\phi ||S_\phi x||^2 \tag{6.22}$$

In general, instead of the weighting factors λ_H, λ_ϕ, generalized covariance matrices (S_H, S_ϕ, say) similar to S_a (comp. equation (6.19)) may be used. However, retrieval tests yield no significant influence on the retrieval solution, and thus scalar factors λ_H, λ_ϕ are used throughout the work presented here.

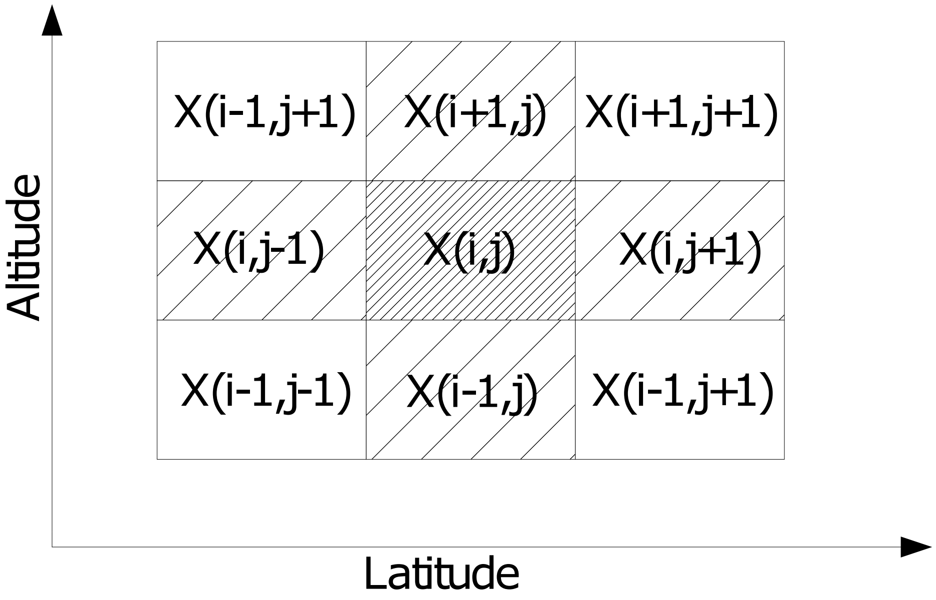

Figure 6.11: Sketch of the pixel grid covariances. Number densities in neighboured pixels are assumed to be similar. To constrain the retrieval solution, the weighted sum of number density values of those pixels enter the functional (6.23), which is to be minimized. For simplification, pixel difference values enter the functional only if the pixels share an edge and not just a corner (see equation (6.21)), these pixels are hatched in the above figure.

The complete functional to be minimized can thus be written as follows:

$$||Kx - y||_{S_y}^2 + ||x - x_a||_{S_a}^2 + \lambda_H ||S_H x||^2 + \lambda_\phi ||S_\phi x||^2. \tag{6.23}$$

The minimizing parameter vector can be calculated by solving the normal equations of (6.23) for x:

$$(K^T S_y K + S_a + \lambda_H S_H^T S_H + \lambda_\phi S_\phi^T S_\phi) x = K^T S_y y + S_a x_a \tag{6.24}$$

In general the above system is conditioned very well, thus any solver of linear equations (e.g. Gaussian elimination) can be used.

The a priori profiles x_a can be chosen according to a climatology (not available for metal species), a model (available, see e.g. Plane and Helmer (1995), Fritzenwallner and Kopp (1998), McNeil et al. (1998), Roddy et al. (2004)), or an estimation derived from the measurement itself. The latter can be accomplished e.g. using nadir total columns and converting these to number densities of the pixels contained in the respective column:

$$\text{Total column density} = \frac{\text{Average number density in the column}}{\text{Length of the column}} \tag{6.25}$$

However, the most stable results have been obtained using a zero a priori. For the results presented in this work, $x_a = 0$ is used without exception. For sake of generality, however, x_a will not be omitted in equations.

6.3.7 Iterative improvement

Use of an a priori distribution x_a introduces a bias into the retrieval process. For $x_a = 0$, the retrieval solution will be biased towards values near zero. To overcome this disadvantage, an iterative improvement approach is applied. Iterating until a predefined maximal number of iterations is reached, the system of normal equations (6.24) is solved, each time using the retrieval solution x^{k-1} obtained in the $(k-1)$-th iteration as the a priori x_a^k in the k-th iteration. The iteration is aborted if $||x^k - x^{k-1}||/||x^{k-1}|| < \varepsilon$ is fulfilled. The threshold ε can be chosen arbitrarily according to the desired precision of the retrieval result. A proper value is e.g. $\varepsilon = 0.1$. The following pseudocode summarizes this method:

```
$x_a^1 = 0$
do $k = 1$, Itmax
    solve
        $(K^T S_y K + S_a + \lambda_H S_H^T S_H + \lambda_\phi S_\phi^T S_\phi) x^k = K^T S_y y + S_a x_a^k$
    if $k \neq 1$ and $||x^k - x^{k-1}||/||x^{k-1}|| < \varepsilon$ then stop
    set $x_a^{k+1} = x^k$
end do
```

In general, the relative differences between the results of two successive iterations settle down to values below a threshold of 0.1 within five to ten iterations.

6.3.8 Retrieval errors and resolution

Similar to classical optimal estimation, averaging kernels of the functional (6.23) can be calculated to investigate the information content of the measurement. By definition, the averaging kernel matrix contains the derivatives of the retrieved state $\hat{x}$ with respect to the true state x_t, i.e.

$$A = \frac{\partial \hat{x}}{\partial x_t} \tag{6.26}$$

Noting $y = Kx_t + \varepsilon$ (with an error vector ε), this matrix can be calculated easily from (6.24):

$$A = (K^T S_y^{-1} K + S_a + \lambda_H S_H^T S_H + \lambda_\phi S_\phi^T S_\phi)^{-1} K^T S_y^{-1} K \tag{6.27}$$

This derivative reflects the influence of the true state on the retrieved one. If the measurement grid is identical to the retrieval grid, an ideal measurement and retrieval would result in an unity matrix A. As a real instrument like a limb sounder has a limited spatial resolution, the retrieved number density at an altitude and a latitude may be influenced by number density at lower and higher altitudes as well as lower and higher latitudes. This is quantified by the off-diagonal elements of the rows of A. The vertical and the angular resolution can thus be estimated as the full-width-half-maximum (FWHM) of the averaging kernel functions (which are discretely represented by the rows of A).

Figures 6.12 and 6.13 show typical averaging kernel functions for the retrieval presented here. Both the altitudinal and the angular resolution of the retrieval are good. The angular resolution can be estimated from the averaging kernel functions presented in Figure 6.12. At all three altitudes shown, the resolution in latitude is approximately 10° . This is true for all altitudes. In comparison to the sampling of SCIAMACHY, the vertical resolution is approximately 5 km, as can be seen from Figure 6.13. This is a good value in comparison to the 3.3 km vertical sampling of SCIAMACHY. As SCIAMACHY limb scans do not extend into the thermosphere and the pixel sizes are larger than at lower altitudes within the mesosphere, the vertical resolution is decreased. Typical values are given in Table 6.6.

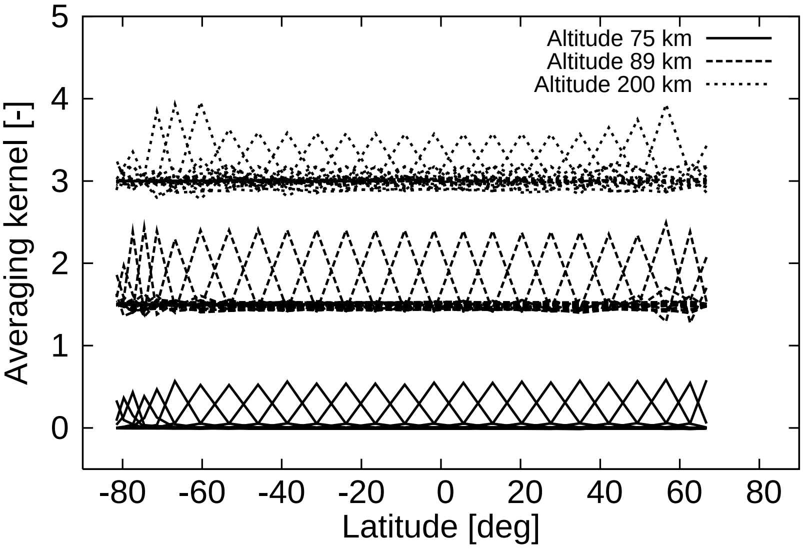

Figure 6.12: Averaging kernels for 75, 89 and 200 km altitude. The full-width-half-maximum is a estimate for the latitudinal resolution of the retrieval. At all three altitudes shown here, the resolution is approximately 10° . Note that the quantities shown here are $\partial \hat{x}_i / \partial (x_t)_j$ with only those components of x_t corresponding to the same altitude being considered.

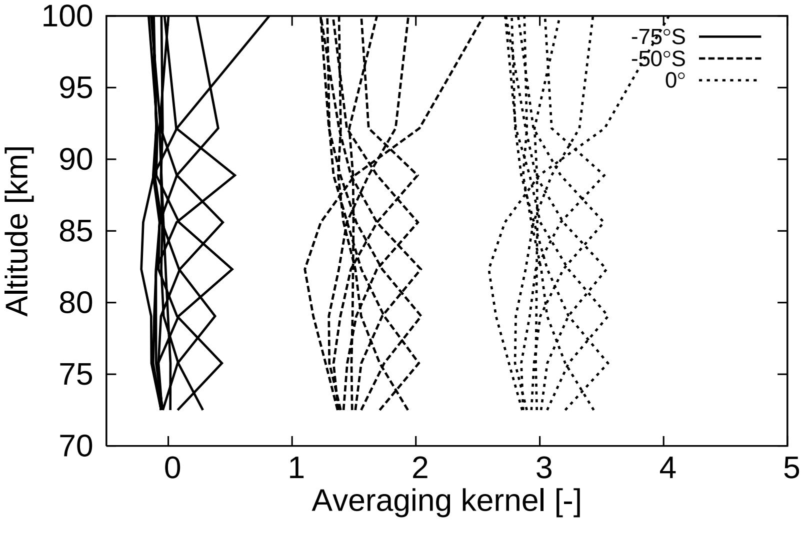

Figure 6.13: Averaging kernels for -75° , -50° and 0° latitude. The full-width-half-maximum is an estimate for the altitude resolution of the retrieval. At all three latitudes shown here, the resolution is approximately 5 km. Note that the quantities shown here are $\partial \hat{x}_i / \partial (x_t)_j$ with only those components of x_t corresponding to the same latitude being considered.

The retrieval error matrix S contains the covariances of x_i with respect to x_j, for all i, j. In

Altitude bin [km]	Latitude bin [°]	FWHM [km]
250.0 – 500.0	-46.3 – -53.6	200 km
150.0 – 250.0	-46.3 – -53.6	115 km
120.0 – 150.0	-46.3 – -53.6	35 km
93.6 – 120.0	-46.3 – -53.6	25 km

Table 6.6: Full-width-half-maximum figures of some averaging kernel functions not shown in Figure 6.13. These values are calculated for a typical orbit (used here: orbit no. 20559, see Figure 6.3).

particular, the square roots of the diagonal elements of S present the standard deviations of the retrieval quantities x_i. This matrix is calculated as follows:

$$S = (K^T S_y^{-1} K + S_a + \lambda_H S_H^T S_H + \lambda_\phi S_\phi^T S_\phi)^{-1} \tag{6.28}$$

Figures 6.14 and 6.15 exhibit the total retrieval errors for Mg^+ and Mg for a typical orbit with good limb and nadir sampling. Note that the errors are virtually the same for both species. For the orbit used here, 23 limb scan sequences and 23 nadir scans enter the retrieval. For both species, the total error is well below 130 cm^{-3}. This a good value in comparison with the absolute values found in case studies and retrieval tests. At high altitudes, the error is slightly lower. This may be a result of the worse sampling rate at high altitudes.

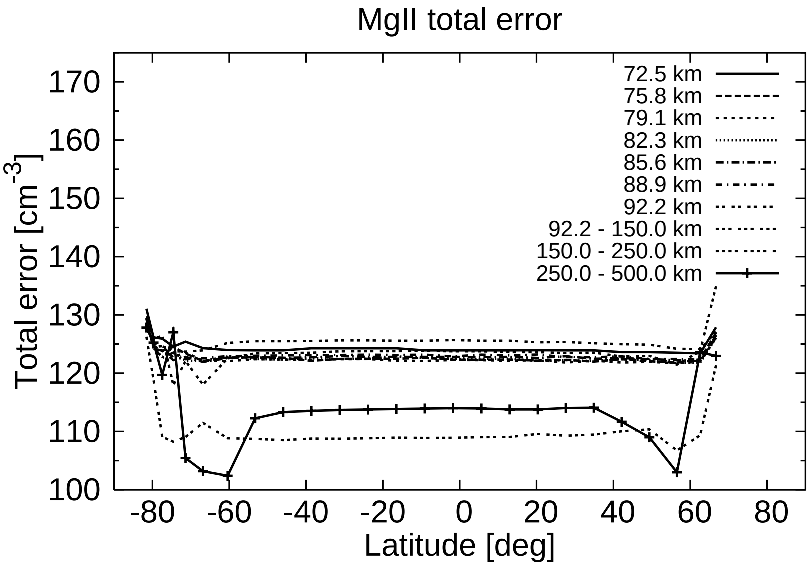

Figure 6.14: Total retrieval error for Mg^+, orbit no. 20559, as calculated from equation (6.28). For all altitudes and all latitudes, the error is below 130 cm^{-3} with a slight increase to high latitudes. This is likely a result of the decreased spatial sampling rate of SCIAMACHY. High altitudes exhibit error values of 110 – 115 cm^{-3}.

6.4 Instrument noise

The spectral noise of SCIAMACHY is mainly shot noise due to the discrete nature of the electron motions within the instrument electronics. It can be calculated for the observed radiance I as well as for the sun-normalized radiance I/F. Since the latter is used in the retrieval of major interest within the scope of this work, only the noise $\sigma_{I/F}$ for the sun-normalized radiance is considered here.

The noise depends on a number of quantities:

- The signal I itself. However, the upper tangent altitudes of SCIAMACHY yield a small measurement signal, and thus the noise of I/F does not depend significantly on the value of

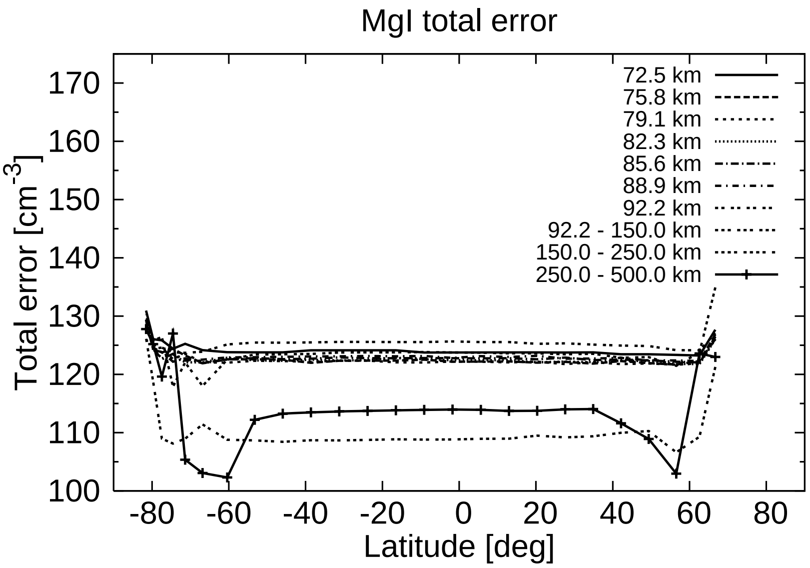

Figure 6.15: Total retrieval error for Mg^+, orbit no. 20559, as calculated from equation (6.28). For all altitudes and all latitudes, the error is below 130 cm^{-3} with a slight increase to high latitudes. This is likely a result of the decreased spatial sampling rate of SCIAMACHY. High altitudes exhibit error values of 110 – 115 cm^{-3}.

I. As a result, the noise spectrum does not differ from an inverted and scaled solar spectrum. Thus, the noise of I/F is increasing in regions where the magnesium signal is observed, i.e. 280 and 285 nm (see Fig. 6.17).

- The throughput T. A good average value for channel 1 is $1.5 \cdot 10^6$ electrons· nm^{-1}·cm^{-2}·s^{-1}.
- The readout noise σ_{readout}. An average value for channel 1 is 1000 electrons·s^{-1}
- The dark current S_{dark}. It is assumed to be zero.
- The exposure time t_{exp} of the detector pixels. This varies with channel, typical values are 1 s for channel 1a (240 – 282 nm) and 0.5 s channel 1b (282 – 313 nm) in limb. In nadir, these values increase to 1.5 s for both subchannels.
- The coadding factor. A number of data sets is added onboard to reduce the data transfer rate. For limb and nadir measurements in channel 1, this number is 1.

The radiance noise σ_I is calculated through the following equation (comp. (de Vries and Hoogeveen, 1999) and see Figure 6.16):

$$\sigma_I = \frac{1}{T\,t_{\text{exp}}}\sqrt{\frac{\sqrt{t_{\text{exp}}(TI + S_{\text{dark}})}^2 + \sigma_{\text{readout}}^2}{n_{\text{coadd}}}} \approx \frac{\sigma_{\text{readout}}}{T\,t_{\text{exp}}} \tag{6.29}$$

The noise of the sun-normalized radiance is calculated as follows (comp. Fig. 6.17):

$$\begin{aligned} \sigma_{I/F} &= \sqrt{\left(\frac{\sigma_I}{F}\right)^2 - \left(\frac{\sigma_I \sigma_F}{F^2}\right)^2} \approx \frac{\sigma_I}{F} && (6.30) \\ &= \frac{1}{F\,T\,t_{\text{exp}}}\sqrt{\frac{\sqrt{t_{\text{exp}}(TI + S_{\text{dark}})}^2 + \sigma_{\text{readout}}^2}{n_{\text{coadd}}}} && (6.31) \end{aligned}$$

Note that the signal that is fed into the retrieval is in fact the difference of the measured signal and the background radiance. As can be seen from equation (6.29), the noise is virtually independent from the signal strength I but depends only on the solar spectrum. Thus, the noise of the total measurement signal I and the background I_{bg} signal can be assumed to be equal. The noise of the difference signal $I_{\text{diff}} = I - I_{\text{bg}}$ is

$$\sigma_{I_{\text{diff}}} = \sqrt{\sigma_I^2 + \sigma_{I_{\text{bg}}}^2} = \sqrt{2}\sigma_I \tag{6.32}$$

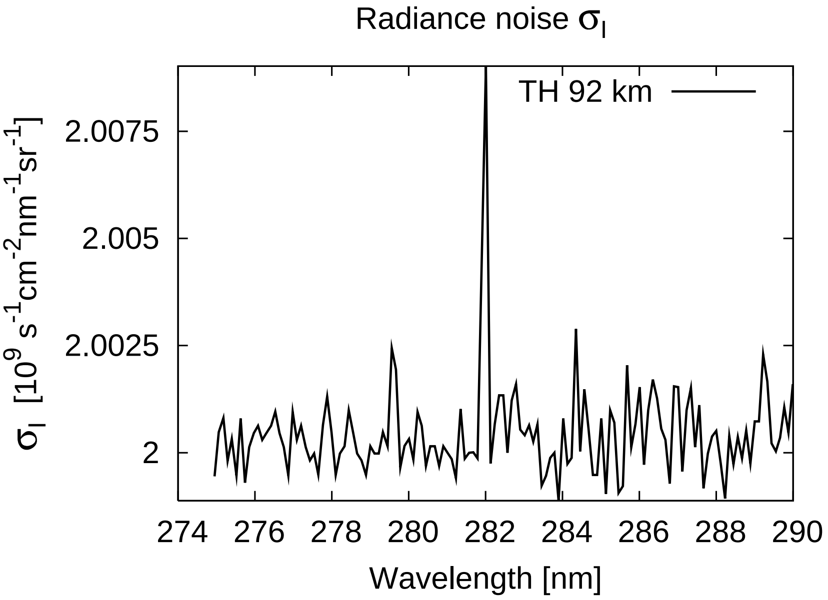

Figure 6.16: SCIAMACHY radiance noise in parts of channel 1 calculated using equation (6.29). The spiky structure at 282 nm is a result of a subchannel transition.

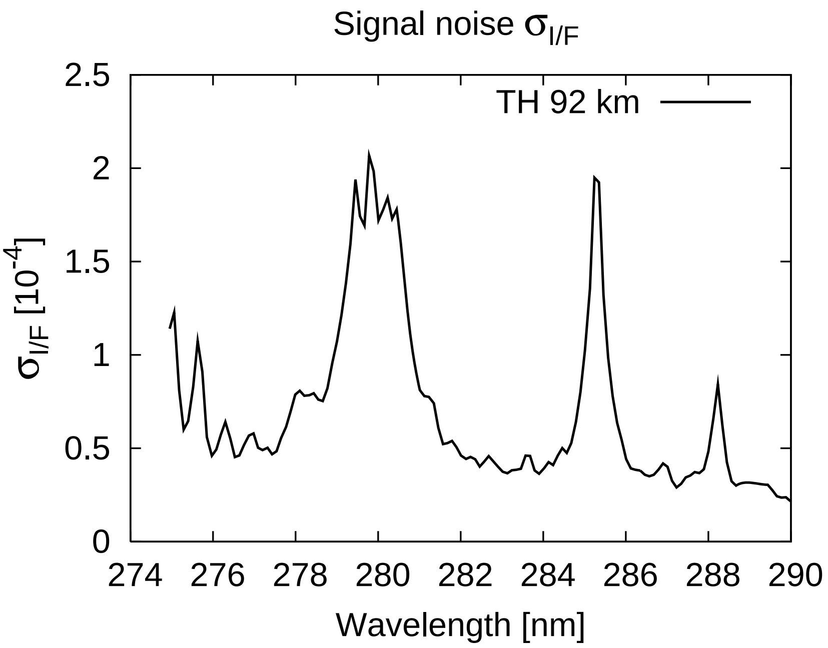

Figure 6.17: SCIAMACHY noise of normalized radiance R/I calculated using equation (6.30). As a result of the small measurement signal at high tangent altitudes, the actual radiance values do not contribute significantly to the noise. The noise is virtually equal to a scaled and inverted solar spectrum.

The actual noise is reduced by integration of spectra during the retrieval. This can be regarded as a retrieval-based coadding. For limb viewing measurements, four individual spectra are read out during a swath from left to right. These four spectra are averaged to improve the signal-to-noise ratio. The noise as calculated by (6.30) and (6.32) is thus reduced by a factor of $\sqrt{4} = 2$. Similarly, in general 65 individual readouts of a single nadir state are integrated. This decreases the noise by a factor of $\sqrt{65} \approx 8$.

To estimate the error of a single measurement due to detector spectral noise, the above calculated noise spectrum is taken as input spectrum, and the emissivities of Mg and Mg^+ are fitted in a least-squares sense (see equation (6.4), compare Figure 6.5. The corresponding column densities are interpreted as errors of a single measurement. Note that the noise depends on the measurement mode (limb/nadir) and the emissivity depends on the scattering angle.

Scat. angle [deg]	$\Delta c(\mathrm{Mg}^+)$ $[\mathrm{cm}^{-2}]$ (L,N)	$\Delta c(\mathrm{Mg})$ $[\mathrm{cm}^{-2}]$ (L,N)
0	$7.5 \cdot 10^9$, $2.5 \cdot 10^9$	$1.5 \cdot 10^9$, $1.1 \cdot 10^9$
30	$7.5 \cdot 10^9$, $2.5 \cdot 10^9$	$2.8 \cdot 10^9$, $2.3 \cdot 10^9$
60	$7.5 \cdot 10^9$, $2.5 \cdot 10^9$	$1.5 \cdot 10^9$, $1.3 \cdot 10^9$
90	$7.5 \cdot 10^9$, $2.5 \cdot 10^9$	$2.3 \cdot 10^9$, $2.0 \cdot 10^9$
average	$7.5 \cdot 10^9$, $2.5 \cdot 10^9$	$2.0 \cdot 10^9$, $1.6 \cdot 10^9$

Table 6.7: Estimated single measurement errors due to noise of SCIAMACHY Mg^+ and Mg measurements. Values are derived from theoretical values of the measurement noise (see Figure 6.5). Since the emissivities depend on the scattering angle, so do the measurement errors. Shown are errors for limb as well as nadir measurements (L,N). The last line shows the average column density errors, all scattering angles weighted equally.

The observed column density error is calculated from the spatially varying number density errors along the LOS as follows:

$$\Delta c(M) = \sqrt{\int \Delta x(M,s)^2 \, ds} \quad , \quad M = \mathrm{Mg}^+, \mathrm{Mg} \tag{6.33}$$

To convert column density errors to number density errors, a vertical profile of Mg^+ of Mg has to be assumed. For an estimation of the number density error, a layer of constant number density x_0, thickness 5 km and center altitude 95 km for Mg^+ respectively 87.5 km for Mg is assumed. This setting is derived from model studies (Plane and Helmer, 1995). Obviously, real atmospheric conditions may be different, however, a rough estimation of the error can be made this way. Equation (6.33) can be rewritten as follows:

$$\Delta c(M) = \sqrt{\int \Delta x_M^2(s) \, ds} = \Delta x_0(M) \cdot s \quad , \quad M = \mathrm{Mg}^+, \mathrm{Mg} \tag{6.34}$$

Here, s denotes the path length of the line-of-sight within the layer. For limb measurements at an tangent altitude of 92 km, $s \approx 23$ km for the Mg^+ holds. For Mg, the limb measurement at 85 km tangent altitude is chosen for the estimation, and this gives $s \approx 28$ km.

In nadir, $s = 5$ km is obvious in both cases. Table 6.8 contains the number density errors for Mg^+ and Mg using the above described setup. Note that these are the errors of a single limb respectively nadir measurement. The retrieval uses a number of measurement simultaneously, thus the errors are reduced to smaller values (see Figures 6.14 and 6.15).

Scat. angle [deg]	$\Delta x(\mathrm{Mg}^+)$ [cm^{-3}] (L,N)	$\Delta x(\mathrm{Mg})$ [cm^{-3}] (L,N)
0	1630 , 2500	268 , 2200
30	1630 , 2500	500 , 4600
60	1630 , 2500	268 , 2600
90	1630 , 2500	410 , 4000
average	1630 , 2500	357 , 3200

Table 6.8: Estimated single measurement errors of number density due to noise of SCIAMACHY Mg^+ respectively Mg measurements. Values are derived from theoretical values of the measurement noise (see Figure 6.5). For conversion of column density errors (see Table 6.7) to number density errors, a layer of constant number density of Mg^+ and Mg is assumed. For Mg^+, the layer is centered at 100 km, the Mg layer is assumed to be centered at 85 km. Values for limb measurements given above denote the single measurement error of the topmost scan.

6.5 Systematic errors

This section presents sources of systematic errors in the SCIAMACHY measurements. Beside self-absorption on the emission lines of the magnesium species (Section 6.5.1), the SCIAMACHY pointing error is discussed, see Section 6.5.2. Satellite measurements of any kind are often affected by increased particle impact in the vicinity of the Southern Atlantic Anomaly, a region of anomalous igh particle fluxes located eastward of South America. Effects and extend of this anomaly are presented in Section 6.5.3. The *Ring effect* leads to a filling up of the Fraunhofer lines in the solar spectrum if observed in scattering. The background and error estimation of this phenomenon are discussed in Section 6.5.4.

6.5.1 Self absorption

Retrievals of atmospheric species from emission data often require allowance for self absorption (compare Stevens (1995)). To estimate the impact of self absorption on the retrieval of metallic species Mg and Mg^+, the absorption is calculated for different number densities and path lengths in the atmosphere. Current model studies assume a negligible amount of Magnesium species at altitudes above 500 km (see in particular Gardner et al. (1999), Roddy et al. (2004), and also Fritzenwallner and Kopp (1998), Plane and Helmer (1995), Fesen and Hays (1982a), Fesen et al. (1983) and Gérard and Monfils (1978)). Due to this and the fact that only single scattering is used in the radiative transfer model used here, path lengths s within the atmosphere do not exceed 6000 km.

The total absorption is estimated using the following simplification of the Lambert-Beer's law:

$$a(N,s) = \exp\left(-N \cdot s \cdot \sigma\right) \tag{6.35}$$

Here, the absorption cross section σ is calculated by (compare (6.5)):

$$\sigma = \frac{\pi e^2}{mc^2} f_{ij} \lambda_{ij}^2, \tag{6.36}$$

where λ denotes the wavelength of the emission and f_{ij} the oscillator strength. The first fraction presents the effective electron radius computed from well known physical constants. Values for the absorption cross sections presented in Table 6.9 have been calculated using data from the NIST data base (NIST, 2005),

The total absorption factors calculated from these parameter show negligible self absorption of 1% or less for number densities $N \leq 10^3$ cm^{-3} and path lengths below 6000 km (Figure 6.18). Self absorption values increase to 5% for number densities of 5000 cm^{-3} and path lengths

Species	λ [nm]	σ [cm^{-2}]
Mg	285.213	$3.5 \cdot 10^{-14}$
Mg$^+$	279.553	$1.3 \cdot 10^{-14}$
Mg$^+$	280.270	$6.8 \cdot 10^{-15}$

Table 6.9: Absorption cross sections for Mg and Mg$^+$ as calculated from equation 6.36.

of 6000 km. From case studies carried out in course of retrieval tests, number densities that large seem unreasonable to occur at the complete length of the line-of-sight.

Additional evidence for expectably negligible values of self absorption can be draw from model calculations. Model studies as presented e.g. by Plane and Helmer (1995), Roddy et al. (2004) and Fritzenwallner and Kopp (1998) predict number densities of both Mg$^+$ and Mg to be 10^4 cm^{-3} at most within a narrow altitude region. The full-width-half-maximum of the peak abundance is calculated to be approximately 6 km at altitudes of 85 to 100 km. For a typical limb scan at tangent altitudes above 70 km (note that 70 – 92 km is the tangent height range considered in this retrieval, see Section 6.3.3), this results in path lengths of approximately 700 km within the layer.

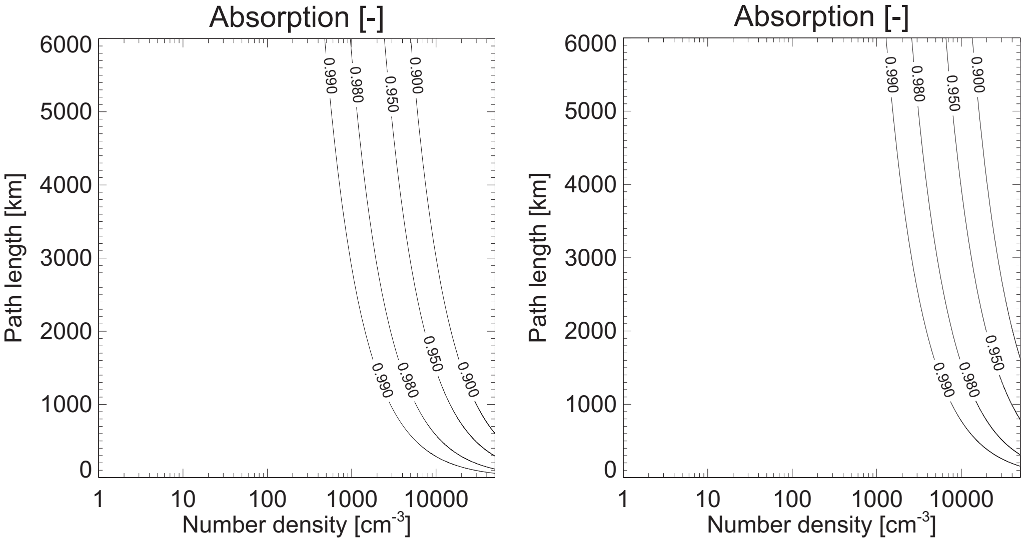

(a) Self absorption of Mg$^+$ in the 279.553 nm emission. Values are negligible for number densities below 5000 cm^{-3}.

(b) Self absorption of neutral Mg in the 285.213 nm emission. As a result of a larger value for the absorption cross section, this line suffers less from self absorption.

Figure 6.18: Self absorption of Mg and Mg$^+$. Contours represent $a(N, s)$, see equation (6.35).

6.5.2 Pointing error

The SCIAMACHY limb measurements are affected by tangent height errors of approximately 1.5 km. First indicators for this misalignment with the data product were found during retrievals of tropical ozone profiles, which are deviating systematically from a corresponding climatology. v. Savigny et al. (2005), v. Savigny et al. (2006) and von Savigny et al. (2007) characterized this pointing errors in detail.

The retrieval presented here employs SCIAMACHY data of version 5 and 6. In version 6, the pointing error is "corrected" by adding a fixed altitude offset to the limb measurements. Version 5, however, does not contain this improvement.

Within the altitude range considered here (70 – 500 km), the atmosphere is optically thin, and self-absorption can be neglected (see Section 6.5.1). Thus, the retrieval acts virtually linearly on the data. That is, the optical depths do not change significantly is the light path is shifted a small amount up- or downwards. The same applies for the geometrical path lengths. It is thus feasible to correct the data afterwards with the pointing error offset. This is done for the version 5 data using an offset of 1.5 km. All data presented in the following are thus corrected by 1.5 km, either already in the data product or after the retrieval.

6.5.3 The Southern Atlantic Anomaly

The axis of the Earth magnetic field is titled by approximately 11 as well as shifted against the geographical center of the Earth by approximately 500 km. As a consequence, the lower edge of Van Allen radiation belts trapping charged particles can reach down to altitudes of 200 − 300 km. The region of smallest distance to the Earth surface is centered off the east coast of Brazil and is called the "Southern Atlantic Anomaly" (SAA). It extends from approximately 30° E to 75° W and from the equator to 50° S (see fig. (6.19)). The exact shape, extension and position, however, vary with altitude and season.

This region suffers from high particle precipitation of electrons as well as protons. This environment is harmful for spacecraft electronics of all kind. Thus, many devices have to be shut down for orbit passage through the SAA.

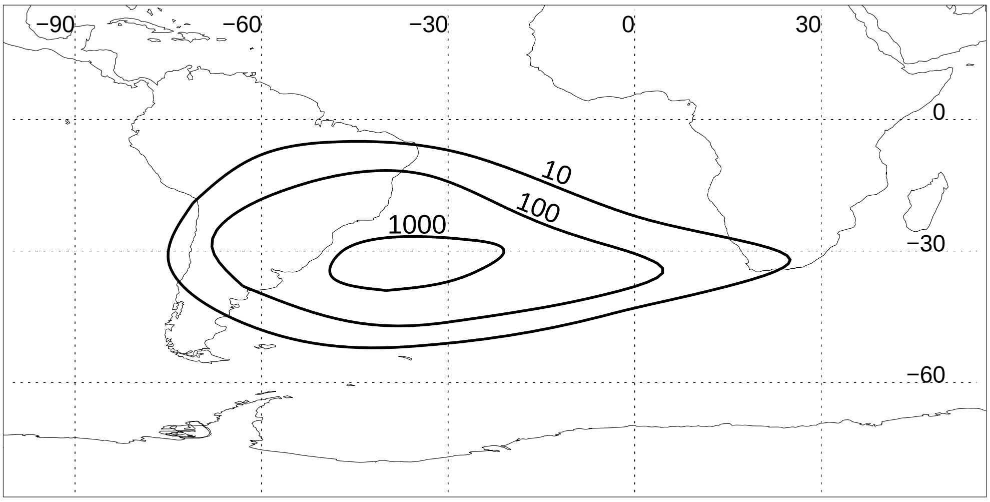

Figure 6.19: Southern Atlantic Anomaly at 500 km altitude as modelled by the AP8MIN model. Contour lines correspond to particle fluxes of protons with energies >50 MeV (given in photons/s/sr/cm^{-2}, see (Daly, 1988).

As a result of this particle flux, measurements of SCIAMACHY are often affected. Limb and nadir spectra suffer from increased noise or incorrect high radiance values. Though a rudimentary filter routine is run before the spectra are passed to the actual retrieval routine, the retrieval results then exhibit unrealistic high (e.g. 10^10 cm^{-3}) or negative values (e.g. -10^5 cm^{-3}) of both magnesium species. Tp avoid these outlier measurements to affect the results presented here, measurements within the SAA are sorted out when compiling time series of total contents or number densities. The same holds for zonal cross sections. An exception is made for contour plots of the global distribution at an individual altitude, see Figure 6.20 for an illustrative example. This kind of presentation clearly exhibits the SAA as a region of significantly negative or large values.

As can be seen in Figure 6.20, the negative values occur south-west of the actual position of the SAA, as defined by the AP8MIN model. This is a result of the measurement geometry of SCIAMACHY. When looking in limb, the satellite's position is approximately 3000 km behind the tangent point along the orbit track. Obviously, measurements are affected if the satellite itself is within the Southern Atlantic Anomaly. However, the measurement data sets contain only the location of the tangent points 3000 ahead of the satellite, and these coordinates are used to compile the contour plots. Figure 6.21 shows a simplified sketch of this fact.

For nadir data, the satellite position above the Earth surface is identical to the location of the measurement. If a measurement is corrupted by the SAA, the incorrect values appear just within the actual position of the SAA. This would then lead to incorrect values just within the real location of the SAA. The retrieval, however, is dominated by limb measurements. This is a results of two circumstances. First, limb measurements are much more frequent than nadir measurements, approximately 8 limb measurements between 70 and 92 km enter the retrieval for each nadir scan. Second, the light path of limb measurements is longer than that of nadir measurements, approximately 4600 km for limb (at tangent altitude 70 km) and approximately 430 km for nadir.

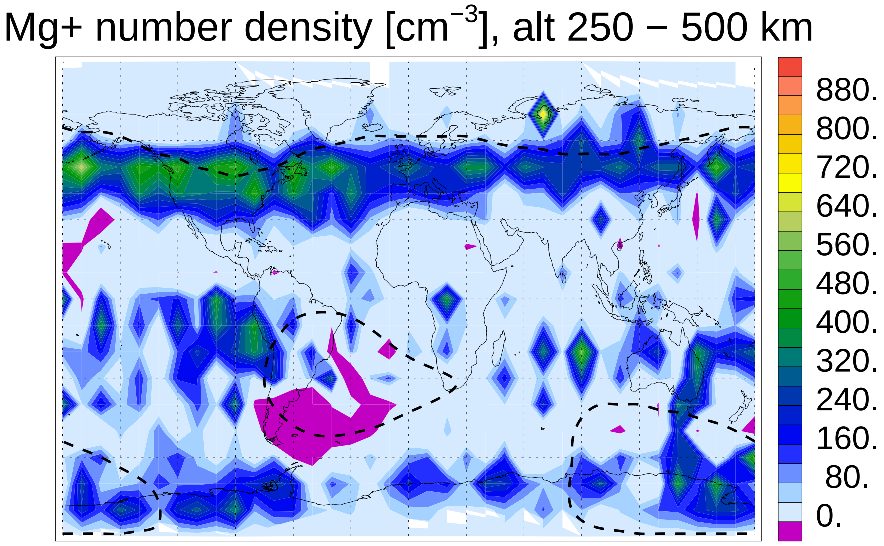

Figure 6.20: Mg$^+$ number densities between 250 and 500 km as measured on November 11, 2004. All data points of one month are averaged and binned into 10° × 10° fields. Dashed lines correspond to ±60° geomagnetic latitude and the border of the Southern Atlantic Anomaly (10 photons/s/sr/cm^{-2} isoline). As can be seen, incorrect negative values occur south-west of the actual position of the SAA, compare Figure 6.21.

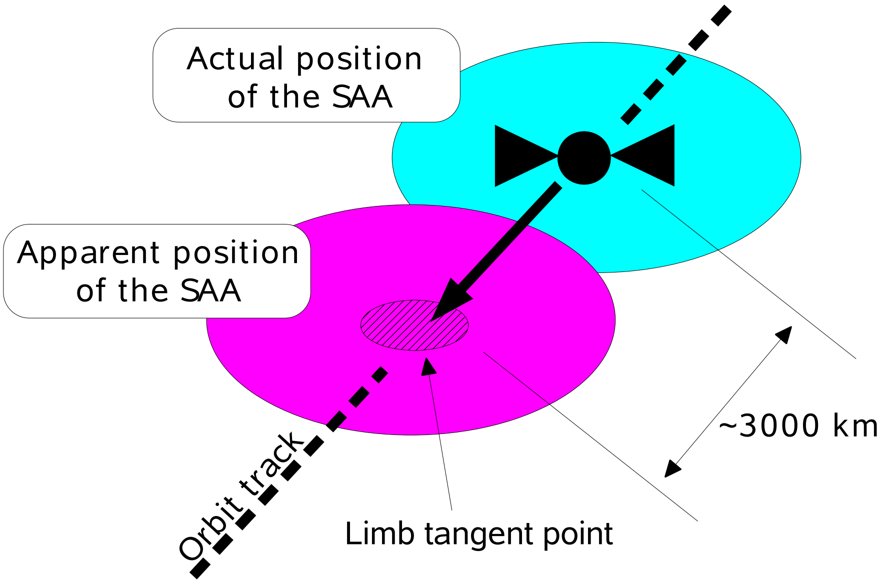

Figure 6.21: Sketch of SCIAMACHY's viewing geometry in limb. In limb, the SCIAMACHY instrument looks approximetyl 300 km ahead in orbit direction. Measurements are affected if the satellite is within the region of increased particle flux. As the coordinates of the limb tangent points are given in the measurement data set to locate a individual measurement, the apparent position of the SAA is shifted approximately 3000 km in orbit direction, i.e. in south-west direction. Figure 6.20 presents results of one month of SCIAMACHY measurments. The SAA is clearly visible within the data.

6.5.4 Ring effect

As a result of inelastic scattering at the air molecules, the depth of Fraunhofer lines is reduced in scattered spectra. This effect was first discovered and reported by Grainger and Ring (1962). The effect was later named after Ring, one of the authors of this first work to cover the problem.

The Ring effect introduces systematic error in the retrieval of magnesium species in particular, as the emission lines used here to investigate Mg^+ and Mg are superimposed on two major Fraunhofer lines. The retrieval version used in this work does not contain a correction for the Ring effect. Later versions of the code may include precomputed Ring cross sections similar to absorption cross sections as look-up tables.

In contrast to pure elastic Rayleigh scattering, a number of molecules such as O_2 and N_2 are *Raman active*. As a result the molecules exhibit scattering not only in the spatial regime, but also in the energy realm. That is, beside the major elastically scattered Rayleigh line, a number of discrete wavelengths above and below the wavelength of incident radiation are populated, i.e. radiation at these wavelengths is observed.

As the intensity of scattered light depends on the intensity of the incident radiation, a larger amount of radiation is scattered from the high-intensity flanks of the Fraunhofer line *into* the line than *out of* the low-intensity center of the lines to the flanks. Thus, a filling-up of the line is observed. Figure 6.22 gives a graphical representation of inelastic scattering as well as the filling-up process of the Fraunhofer lines.

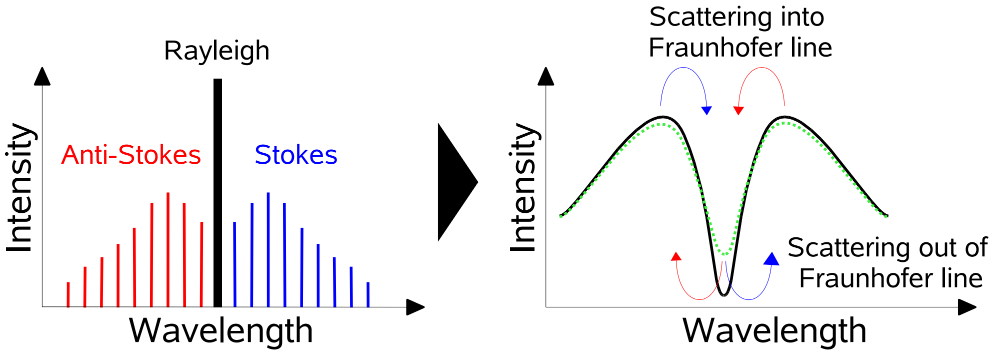

Figure 6.22: Graphical sketch of the Ring effect. Left panel: Depiction of Stokes and Anti-Stokes scattering contributions. Incident radiation has wavelength λ_0. The intensities of Rayleigh elastic and Raman inelastic scattering contributions are not to scale. Right panel: Filling-up of Fraunhofer lines. As a result of higher intensities at the flanks of the line, a higher amount of radiation is scattered into the lines than out of the line. The net effect if thus a filling-up of the Fraunhofer line.

As reported in Vountas (1999), Fraunhofer lines observed in scattering can exhibit a depth that is up to 15% reduced compared to that observed in direct radiation. It was found that the effect is generally strengthened in multiple scattering. However, for the wavelength range ($\leq$ 300 nm) and the altitude range ($\geq$ 70 km) considered here, one may safely assume single scattering. To a first approximation, the results of the retrieval presented in this section depend linearly on I/F, where I is the measured radiance and F is the solar flux. Thus, a filling-up of the Fraunhofer line is approximately linearly propagated through the retrieval. Thus, the Ring effect yields an additional error of up to 15%.

6.6 Comparison with other measurements and model calculations

The total column values presented here show good agreement with other data (see Figure 6.23 and Section 7.1.2 for a more comprehensive review of column densities of both magnesium species, compare Table 6.10). Modelled total column densities are of the order of 10^7 to 10^{10} cm^{-2}, exhibiting a large variability depending on measurement and model input though. The measured column densities are of the order of $10^9 - 10^{10}$ cm^{-2} with a large variability of approximately one order of magnitude.

Slant columns (not shown here) observed by SCIAMACHY are of the order 10^8 to 10^{10} cm^{-2}, in good agreement with previous measurements of slant column densities published by (Fesen and Hays, 1982a), (Fesen et al., 1983), (Gérard and Monfils, 1978) and (Joiner and Aikin, 1996).

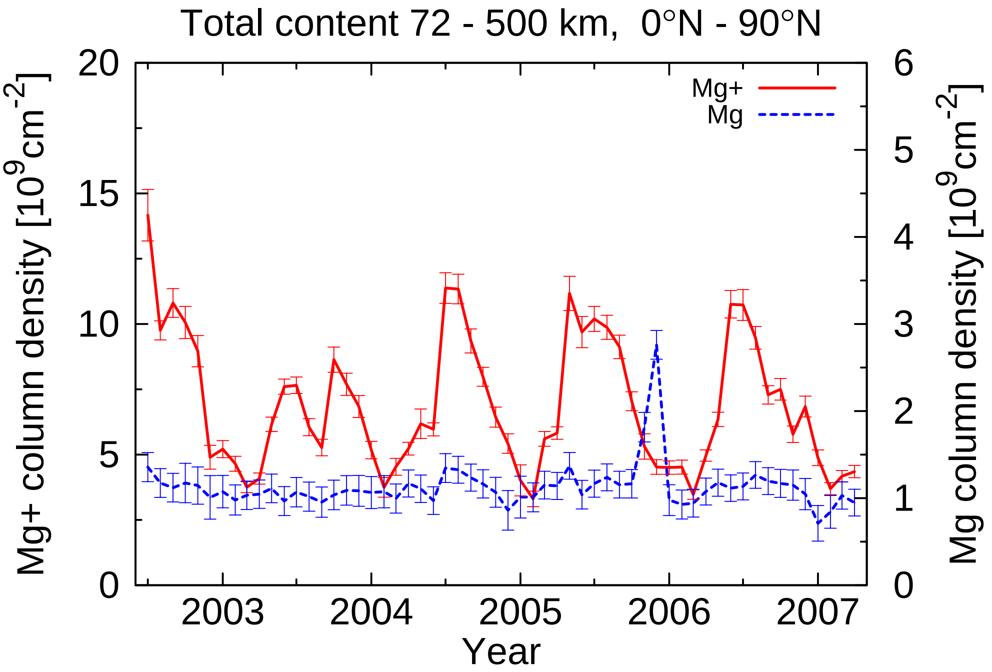

Figure 6.23: Total column densities of Mg^+ (solid) and Mg (dotted) for the northern hemisphere, zonally and meridionally averaged. Measured column densities of Mg^+ are between $3 \cdot 10^9$ and $1.5 \cdot 10^{10}$ cm^{-2} . The Mg total columns are of the order of 10^9 cm^{-2} . See Section 7.1.2 for a thorough discussion of this figure.

The total column comparisions presented here do not give information about the performance of the retrieval with respect to vertical profiles and latitudinally varying distributions. However, no satellite data were present that are comparable to the SCIAMACHY data set in temporal and spatial coverage. Thus, a set of synthetic data has been generated. Section 6.7 presents results of retrieval tests with respect to the reconstruction of the synthetic distributions.

6.7 Reconstruction of synthetic data

To estimate the performance of the retrieval, a set of synthetic measurements sets has been compiled. The limb and nadir measurement geometries used are those of orbit no. 20559, see Figure 6.3 and Table 6.5. Four scenarios have been investigated:

1. An isolated Mg^+ bloom centered at 85 km altitude and 45° S extending approximately 16 km in altitude and 30° in latitude. Maximum values within the bloom are 750 cm^{-3}. See Figure 6.24(a).
2. An isolated Mg^+ bloom centered at 121 km altitude and 45° S extending approximately 25 km in altitude and 30° in latitude. Maximum values within the bloom are 750 cm^{-3}. Compare Figure 6.26(a).
3. A homogeneous layer of 6 km thickness centered at 85 km altitude. Maximum values within the layer are 750 cm^{-3}. See Figure 6.25(a).
4. A homogeneous layer of 20 km thickness centered at 107 km altitude. Maximum values within the layer are 750 cm^{-3}. See Figure 6.27(a).

The recovery is done for Mg^+ as well as for Mg distributions. The results differ not significantly, thus only Mg^+ is presented here. An estimate of the SCIAMACHY instrument noise

Species	Total column [cm^{-2}]	Reference
Mg^+	$2.6 \cdot 10^{1}0$ (∗)	(Aikin et al., 2004)
	$8.5 \cdot 10^{9}$ (†)	(Plane and Helmer, 1995)
	$4.1 \cdot 10^{9}$ (∗)	(Roddy et al., 2004)
	$2.4 \cdot 10^{9}$ (†)	(McNeil et al., 1998)
	$1.0 \cdot 10^{9}$ (†)	(Fritzenwallner and Kopp, 1998)
	$4.3 \cdot 10^{9}$ (†)	(Fritzenwallner and Kopp, 1998)
	$1.7 \cdot 10^{10}$ (∗)	(Fritzenwallner and Kopp, 1998)
	$2.1 \cdot 10^{9}$ (∗)	(Fritzenwallner and Kopp, 1998)
Mg	$7.9 \cdot 10^{9}$ (∗)	(Aikin et al., 2004)
	$3.5 \cdot 10^{9}$ (†)	(Plane and Helmer, 1995)
	$9.9 \cdot 10^{8}$ (†)	(McNeil et al., 1998)
	$1.0 \cdot 10^{8}$ (†)	(Fritzenwallner and Kopp, 1998)
	$7.0 \cdot 10^{9}$ (†)	(Fritzenwallner and Kopp, 1998)

Table 6.10: Measurements (∗) and model calculations (†) of Mg^+ and Mg total vertical column densities. Note the wide range of values and in particular the results from (Fritzenwallner and Kopp, 1998), exhibiting a variability of one order of magnitude.

(see Section 6.4) has been added to the synthetic measurements to obtain a more realistic measurement sequence.

In general, the retrieval reconstruction of the synthetic scenarios is good. The low altitude bloom (scenario 1) and the low altitude layer (scenario 2) are reconstructed well, deviations from the true distribution are within the error range of 150 cm^{-3}, see Figures 6.24 and 6.26. In particular, the latitudinal extension as well as the thickness of the bloom respectively the layer are recovered to a good extend.

For the two high altitude scenarios no. 3 and 4, the recovery is not as good, however. The recovered distributions differ significantly from the initial ones, see Figures 6.25 and 6.27. The general structure is recovered, but the absolute maximal values of approx. 400 – 500 cm^{-3} within the retrieval solution are much smaller than the initial ones of 750 cm^{-3}. Additionally, the bloom structure of scenario no. 2 exhibits a second maximum at 200 km, which is not part of the original distribution (Figure 6.27).

The bad recovery is probably a result of the coarse retrieval grid at altitudes above the top tangent altitude and the low altitude resolution, which is partly resulting from the coarse grid and partly from the long integration paths. Finer retrieval grids do not yield better results, though. The major drawback is the relatively small path length of each SCIAMACHY line-of-sight within the high altitude pixels. Note that the low altitude pixel below the top tangent altitude are designed in a way to maximize the geometrical path length of the limb lines-of-sight within the pixels, compare Section 6.3.3. As a result of this, the retrieval is less sensitive to those pixels.

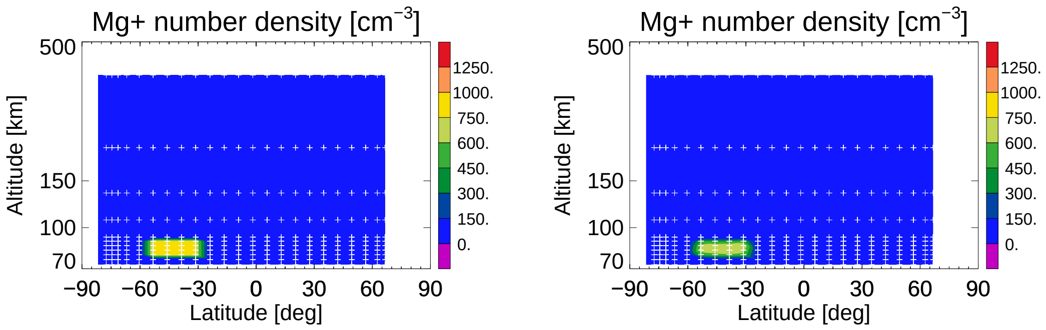

(a) Original Mg$^+$ distribution.

(b) Reconstructed Mg$^+$ distribution.

Figure 6.24: Reconstruction of a single isolated Mg$^+$ bloom centered at 85 km altitude and 45° S. Maximum values within the bloom are 750 cm^{-3}. The deviations are within the error ranges of the retrieval, i.e. $\approx$ 150 cm^{-3}. White crosses denote the center points of the retrieval pixels, see Section 6.3.3. For altitudes below 100 km, these are equal to the tangent points of SCIAMACHY limb scans.

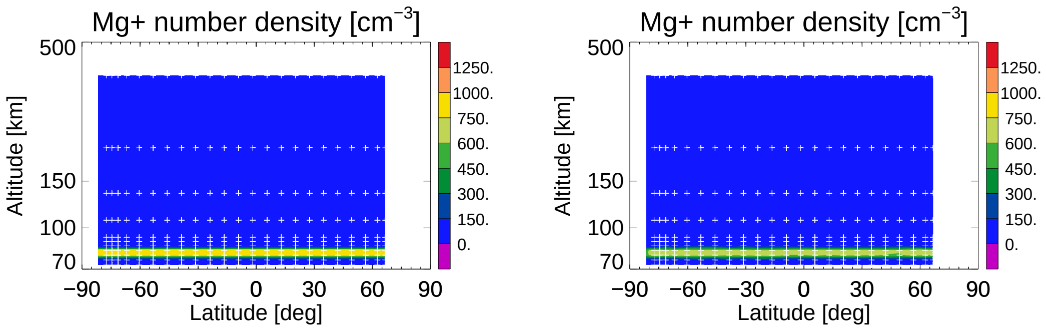

(a) Original Mg$^+$ distribution.

(b) Reconstructed Mg$^+$ distribution.

Figure 6.25: Reconstruction of a homogeneous layer of Mg$^+$ of 6 km thickness, centered at 85 km. Maximum values within the layer are 750 cm^{-3}. The deviations are within the error ranges of the retrieval, i.e. $\approx$ 150 cm^{-3}. White crosses denote the center points of the retrieval pixels, see Section 6.3.3.

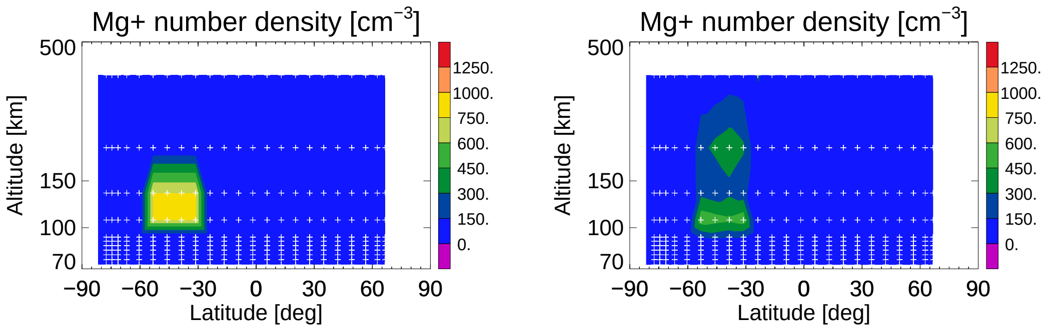

(a) Original Mg$^+$ distribution.

(b) Reconstructed Mg$^+$ distribution.

Figure 6.26: Reconstruction of a single isolated Mg$^+$ bloom centered at 121 km altitude and 45° S. Maximum values within the bloom are 750 cm^{-3}. The retrieval results exhibit a bad altitude resolution, as the bloom is stretched to higher altitudes. The latitudinal extend is recovered rather good, however. Absolute values differ significantly (factor 2) from the true values. White crosses denote the center points of the retrieval pixels, see Section 6.3.3.

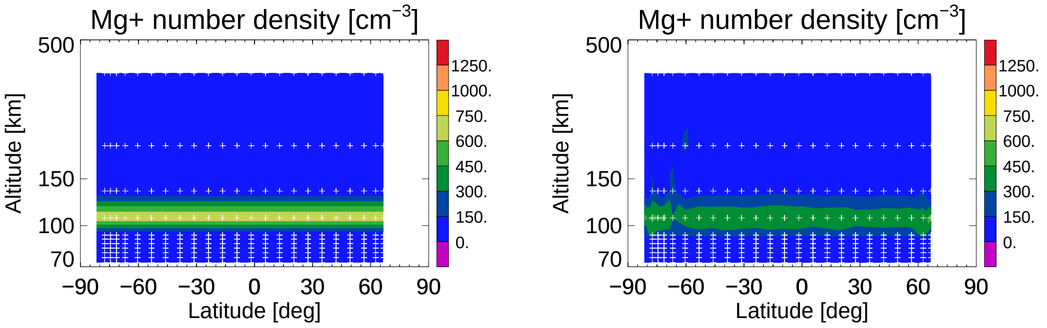

(a) Original Mg$^+$ distribution.

(b) Reconstructed Mg$^+$ distribution.

Figure 6.27: Reconstruction of a homogeneous layer of Mg$^+$ of 25 km thickness, centered at 107 km. Maximum values within the layer are 750 cm^{-3}. The retrieval results resemble the original structure in general. The thickness of the layer is sustained. Absolute values, however, differ significantly (factor 2) from the true values. White crosses denote the center points of the retrieval pixels, see Section 6.3.3.

Part III

Results

7 Review of the complete SCIAMACHY data set

This chapter presents a general review of the total abundance of both magnesium species in the atmosphere. The SCIAMACHY instrument is operational since March 2002 and performs measurements on a daily basis. The data set presented here comprises observations from July 18, 2002 until April 14, 2007. All latitudes between 82° N and 82° S are covered, a global coverage is achieved within 6 days of observation, compare Section 5. The SCIAMACHY instrument thus offers unique capabilities to study the chemistry and physics of mesospheric and lower thermospheric magnesium species on a global scale and a long time range. In particular, four complete years, ten solstices and eleven equinoxes are contained in the data set presented here.

Seasonal and latitudinal variations of both species are discussed. Though the ablation of magnesium from cosmic dust is restricted to rather low altitudes around 100 km, the ionic species is observed at high altitudes of up to 500 km as well. Possible escape mechanisms for the ionic species from the source layer are suggested.

7.1 Observations

7.1.1 Vertical distribution

Figures 7.1 and 7.2 show yearly and globally averaged vertical profiles of Mg^+ and Mg. Note that in Figure 7.1, the altitude axis is drawn in logarithmic scale, whereas Figure 7.2 uses a linear scale and a restricted altitude range to show a detailed profile at altitudes below 120 km.

As can be seen, the Mg^+ profile (Figures 7.1(a) and 7.2(a)) exhibits a pronounced layer with maximal densities of 600 cm^{-3} between 92 and 120 km. The alitude resolution of the retrieval is worse above the top tangent altitude, see Section 6.3.3. Thus, the peak height of the layer cannot be localized better than to be within the altitude range of 92 – 120 km. Above 120 km, the number densities of Mg^+ are decreasing to values of approximately 75 cm^{-3} at altitudes around 400 km. Below 120 km, Mg^+ values decrease to 50 cm^{-3} around an altitudes of 80 km. At even lower altitudes, the number densities are increasing again to values of approximately 150 cm^{-3} on average (Figure 7.1(a)).

The neutral species Mg shows a somewhat different behaviour, see Figures 7.1(b) and 7.2(b). The most striking feature is that number densities at all altitudes are lower compared to the ionic species. Similar the Mg^+, the neutral species exhibits increasing number densities below 80 km and towards lower altitudes. Maximum number densities of up to 150 cm^{-3} are observed at the lowest retrieval altitude of 70 km. A second maximum is observed around 89 km, average number densities are approximately 125 cm^{-3} here (Figure 7.2(b)). On average, the Mg number densities are constant between 90 and 120 km, values are approximately 75 cm^{-3} in this altitude range. At higher altitudes, the Mg concentration tends to zero values.

It should be noted that the detection limit of the retrieval is approximately 120 cm^{-3} . Thus, the only features of the Mg profile that can be considered significant are the layer around 89 km and the high abundances at the lowest retrieval altitudes.

7.1.2 Seasonal variations of the total content

In the northern hemisphere, the total content of the ionized species shows a distinct seasonal variation with pronounced maxima in summer, see Figure 7.3(a) (shown are monthly averaged

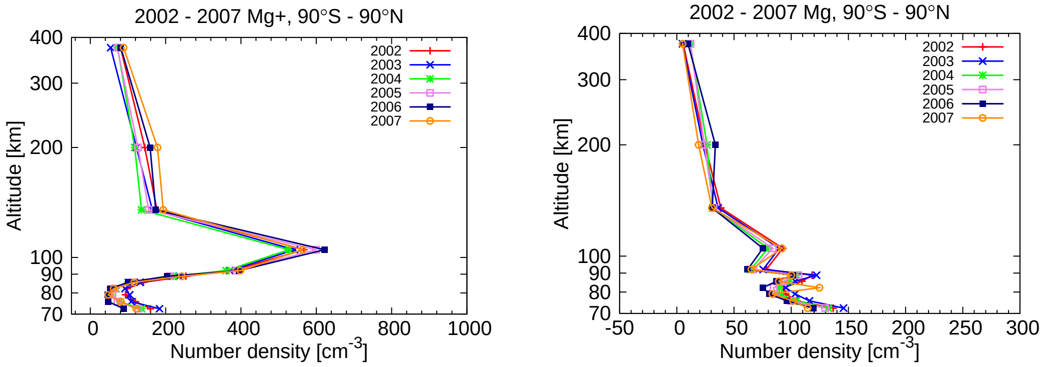

(a) Vertical profile of Mg^+, logarithmic altitude axis.

(b) Vertical profile of Mg, logarithmic altitude axis.

Figure 7.1: Vertical profiles of both magnesium species in the altitude range from 70 to 500 km. Note that the topmost data point corresponds to measurements between 250 and 500 km (see Section 6.3.3). The Mg^+ layer between 92 and 120 km with maximum number densities of 600 cm^{-3} is clearly visible. Mg^+ exhibits larger abundances in the lower thermosphere than neutral Mg. Note the different scale for the x axis. The maximal number density (125 cm^{-3}) for Mg is observed around 89 km and at the lower border of the retrieval range.

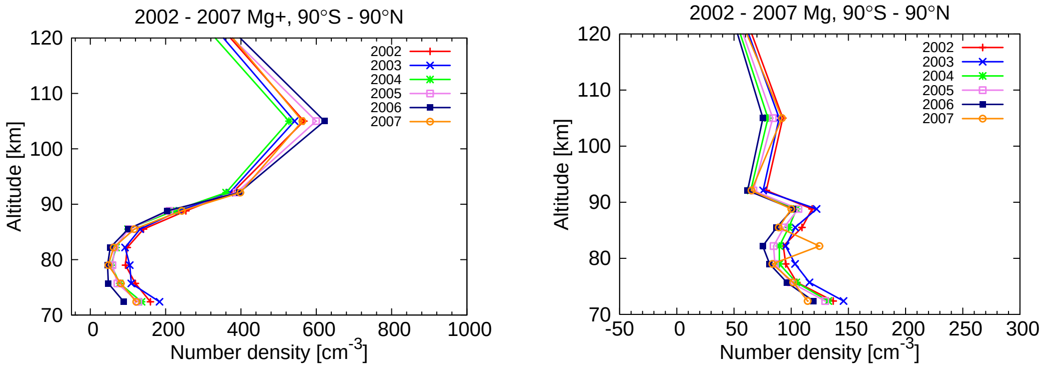

(a) Vertical profile of Mg^+ from 70 to 120 km, linear altitude axis.

(b) Vertical profile of Mg from 70 to 120 km, linear altitude axis.

Figure 7.2: Vertical profiles of Mg^+ and Mg in the altitude range from 70 to 120 km. Note that the altitude axis is in linear scale now. Neutral Mg forms a layer around 89 km, as can be seen from the increased number densities at that altitude. The increased number densities of Mg observed in 2007 around 82 km cannot yet be explained. It should be noted, however, that the data sample of 2007 covers only January through April.

values, zonally averaged). Values of the total column enhance from $3-4 \cdot 10^9$ cm^{-2} to approximately $12 \cdot 10^9$ cm^{-2} during summer. The seasonal variation is strongest in the tropics and the polar region. Both latitudinal bins exhibit variations of more than $10 \cdot 10^9$ cm^{-3} , whereas the mid latitudes show a summer-winter difference of only $5-6 \cdot 10^9$ cm^{-3} .

A seasonal variability is not observed in the southern hemisphere, however. Though the tropical latitudes 0° – 20°S (Figures 7.3(b) and 7.4(b)) show a similar seasonal variability as the northern tropical and mid-latitude regions, the pattern is much less pronounced at higher southern latitudes. On average over all southern latitudes, the Mg^+ shows rather irregular behaviour (Figure 7.4(a)).

A corresponding seasonal variability is not observed in the neutral species Mg. Beside a weak variation between 20°N and 60°N (Figures 7.3(c) and (7.3(d)) which cannot be considered significant with respect to the total errors, no variation can be identified in neither latitude region.

The regions of geomagnetic latitude $\geq 60°$ and $\leq -60°$ do not exhibit a different behaviour as the corresponding hemispheres, see Figures 7.5(a), 7.5(b). In the northern geomagnetic cap, the seasonal cycle of Mg^+ is well pronounced, whereas the southern polar cap does not show any seasonal cycle. The neutral species is can be considered constant with respect to the measurement errors.

The exceptionally large values of Mg towards the end of 2005 – which can be identified in all latitudes – are discussed in further detail in Section 12.

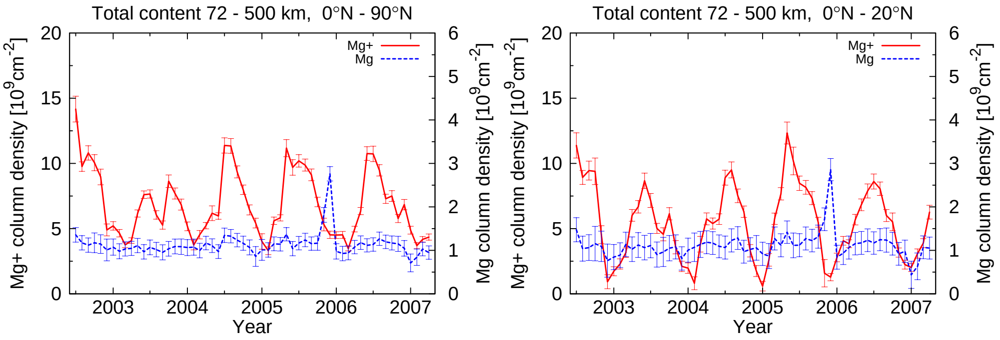

(a) All latitudes

(b) Tropics

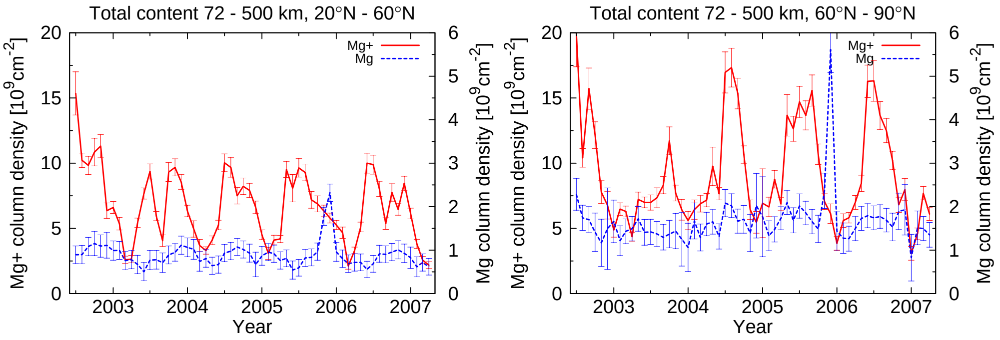

(c) Mid latitudes

(d) Polar regions

Figure 7.3: Time series of the total column density of both magnesium species in the northern hemisphere. Each data point represents averages of one month of SCIAMACHY data. Annotated tickmarks denote January 1 of the corresponding year. Beside a total content series for the whole northern hemisphere, three individual latitude bands are considered: Tropics (0° – 20° N), mid-latitudes (20° – 60° N) and polar regions (60° – 90° N). As can be seen, Mg^+ exhibits a pronounced seasonal variation with summer maxima. The neutral species Mg does not show a significant seasonal cycle.

7.1.3 Latitudinal distribution

Panel 7.6 shows the total column densities of Mg^+ versus geographical latitude for the two solstices and the two equinoxes and all years of observation. For all seasons, both magnesium species exhibit three maxima in the total column, two maxima near the polar caps around ±60° geographic latitude and one maximum near the equator. Whereas the two polar maxima are located at constant latitudes throughout the year, the third maximum near the equator follows the position of the sub-solar point. The latter maximum will be referred to as "tropical maximum" in the following.

For the neutral species (see Figure 7.7, the three maxima are of similar magnitude for all years of observation. Additionally, within an individual year, all three maxima are of similar magnitude. The typical value of a single maximum is $1.5 - 2.0 \cdot 10^9$ cm^{-2} .

The ionized species Mg^+ shows more variability, however. Whereas in all years of northern spring equinox observations, the northern and southern maximum are of rather similar magnitude of approximately 10^{10} cm^{-2} , northern autumn equinox as well as summer and winter favour the northern maximum. The northern summer maximum is a factor of two larger than the southern maximum. In 2002, an increase by a factor of four is observed. The southern maximum is of similar magnitude as the tropical maximum ($\approx 1.2 \cdot 10^{10}$ cm^{-2}) for the July measurements. The same values as for July hold for northern autumn equinox conditions in

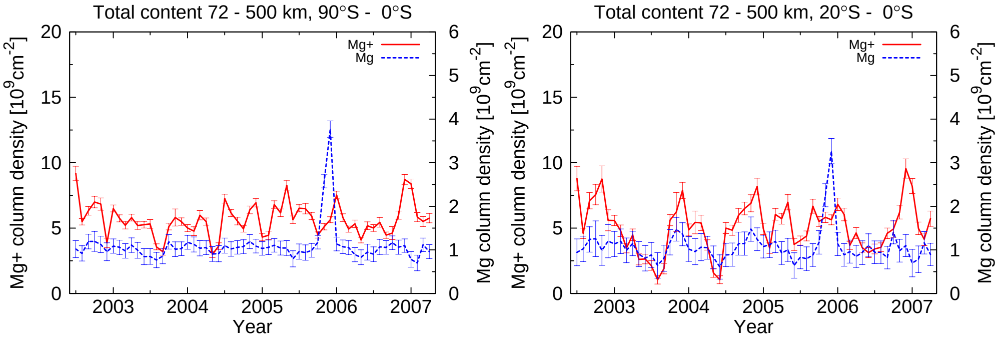

(a) All latitudes (b) Tropics

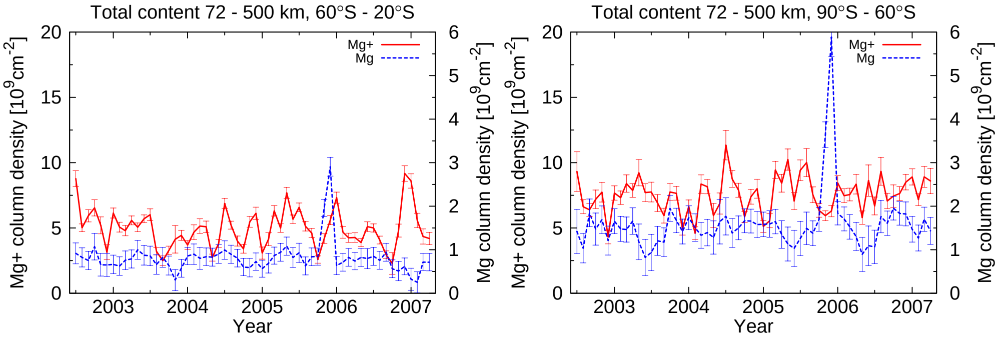

(c) Mid latitudes (d) Polar regions

Figure 7.4: Time series of the total column density of both magnesium species in the northern hemisphere. Tickmark setting, averaging and binning as in Figure 7.3. The seasonal variability of Mg$^+$ is much less pronounced in the southern hemisphere. The neutral species Mg does not show a significant seasonal cycle.

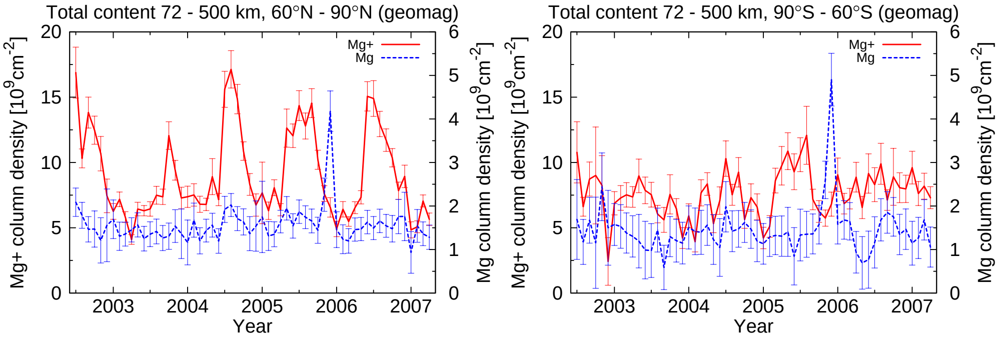

(a) Total contents of Mg and Mg$^+$ near the northern geomagnetic pole (b) Total contents of Mg and Mg$^+$ near the southern geomagnetic pole

Figure 7.5: Time series of the total column density of both magnesium species for regions of geomagnetic latitudes $> 60°$. Tickmark setting and averaging in Figure 7.3. The northern hemisphere seasonal cycle is observed in the northern auroral oval as well, whereas the southern auroral oval does not show a seasonal cycle.

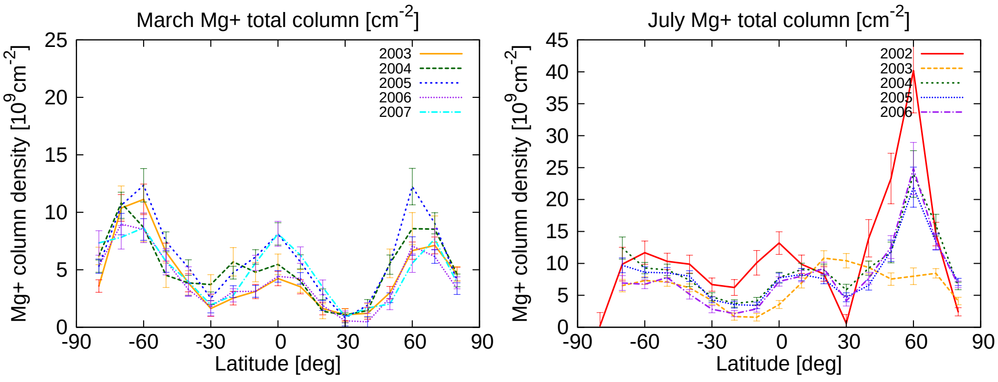

(a) All latitudes (b) Tropics

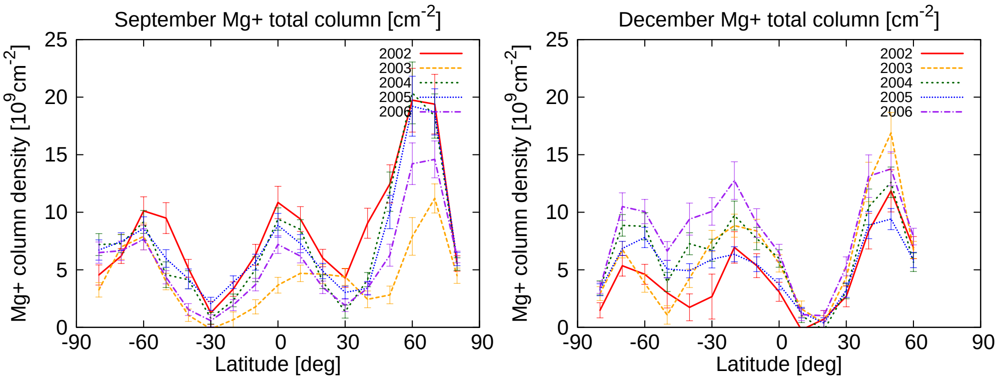

(c) Mid latitudes (d) Polar regions

Figure 7.6: Total column densities of Mg^+ versus latitude for March, July, September and December. Three maxima near the equator and ±60° are observed for all seasons. The Southern Atlantic Anomaly (see Section 6.5.3) is excluded.

September. Around northern winter solstice in December, the northern maximum is a factor of approximately 1.5 larger than the other two maxima.

An exception is presented by December 2005 (Figure 7.7(d)). Here, total column densities at all latitudes are shifted to values that are more than a factor of two higher compared to other months. This is a result of a November/December 2005 anomaly in both magnesium species. In particular the neutral species was affected and exhibited number densities of up to one order of magnitude higher than the average. See Section 12 for a detailed discussion.

Figures 7.8 – 7.11 show zonally averaged number densities of both species for equinox and solstice conditions. The data are averaged over a month (March, July, September and December, respectively) and binned to a 10° latitude grid. Note that the retrieval grid extends to 500 km altitude and the top pixel covers the range from 250 to 500 km (see Section 6.3.3). In this figure, the center altitudes of the individual pixels are given. Thus, the topmost number density is assigned to altitude (250+500)/2=375 km.

The probably most striking feature in the Mg^+ distribution is a pronounced layer of Mg^+ centered around 100 km. Number densities within this layer are of the order of 400 – 700 cm^{-3} . It should be noted that the retrieval resolution is not sufficient to actually resolve the thickness of the layer.

This depiction allows to separate the contributions of different altitudes to the total column. The northern and southern maxima of column density can be identified (Figures 7.8(a), 7.9(a), 7.10(a), 7.11(a)). As can be seen, the increased number densities of Mg^+ are a result of a pronounced flow of Mg^+ out of the layer around 100 km to higher altitudes of up to 500 km. In the northern hemisphere, values of up to 500 cm^{-3} are observed at altitudes of up to 500 km. In the southern hemisphere, maximum number densities between 250 and 500 km are approximately 250 cm^{-3} . The same applies for the enhanced values of Mg^+ beneath the sub-solar point. The seasonally varying location of maximal values near the equator can

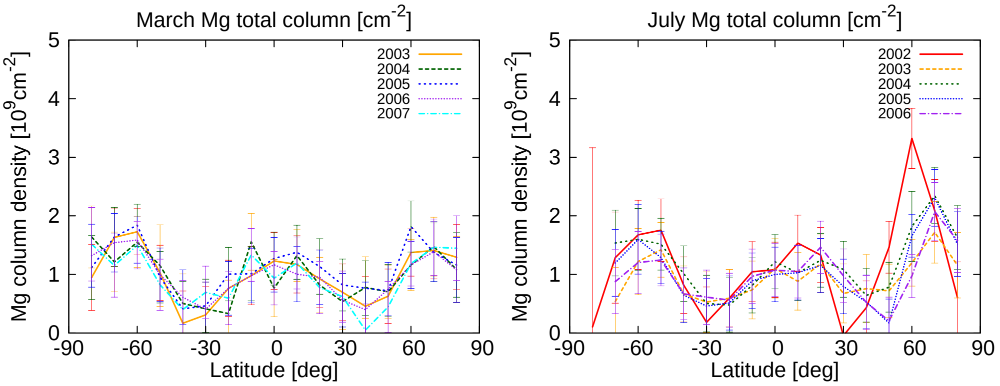

(a) All latitudes (b) Tropics

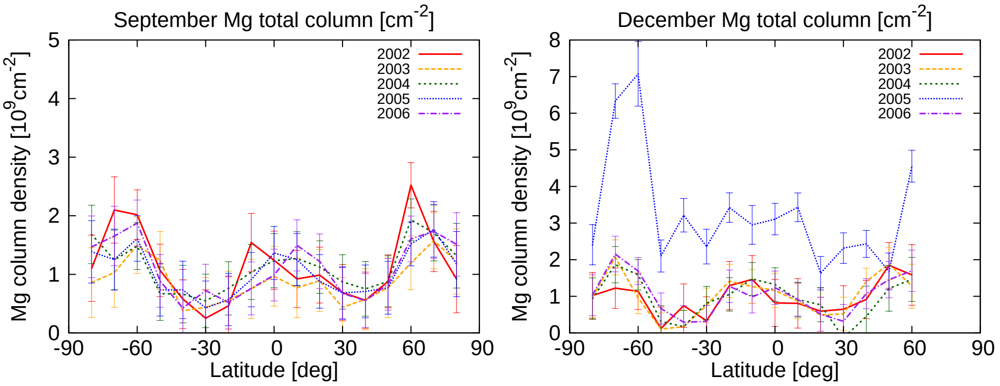

(c) Mid latitudes (d) Polar regions

Figure 7.7: Total column densities of Mg^+ versus latitude for March, July, September and December. Three maxima near the equator and ±60° are observed for all seasons. The Southern Atlantic Anomaly (see Section 6.5.3) is excluded.

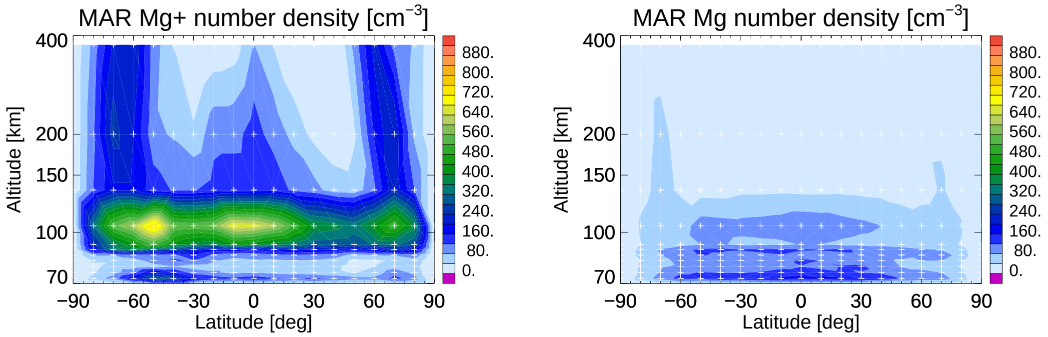

(a) Mg^+ latitudinal cross sections. (b) Mg latitudinal cross sections.

Figure 7.8: Zonally averaged number densities of Mg^+ (left panel) and Mg (right panel) during northern spring equinox. Values are averaged over March 2003 – 2007 and binned to a 10° wide latitude grid and an altitude grid that is derived from an averaged SCIAMACHY tangent altitude grid below 92 km. Above 92 km, a fixed altitude grid is used for the retrieval and the cross sectional plot. White crosses denote the center locations of the grid pixels. Note that the ordinate axis is in logarithmic scale. The Southern Atlantic Anomaly (see Section 6.5.3) is excluded.

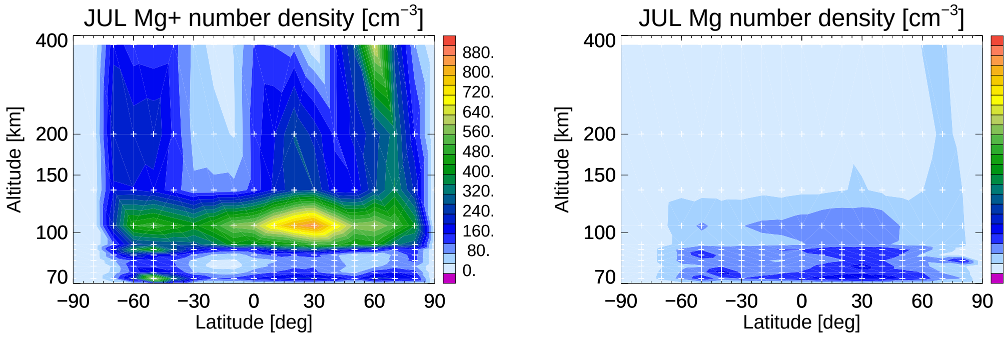

(a) Mg^+ latitudinal cross sections.

(b) Mg latitudinal cross sections.

Figure 7.9: Zonally averaged number densities of Mg^+ during northern summer solstice. Values are averaged over July 2002 – 2006. Binning as in Figure 7.8(a).

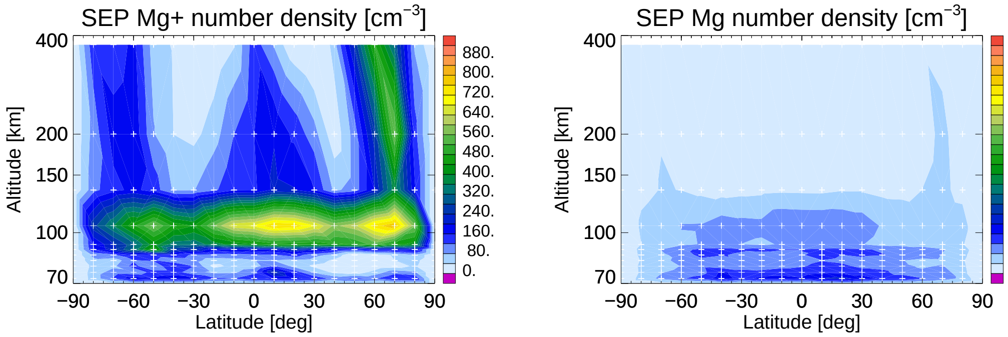

(a) Mg^+ latitudinal cross sections.

(b) Mg latitudinal cross sections.

Figure 7.10: Zonally averaged number densities of Mg^+ during northern autumn equinox. Values are averaged over September 2002 – 2006. Binning as in Figure 7.8(a).

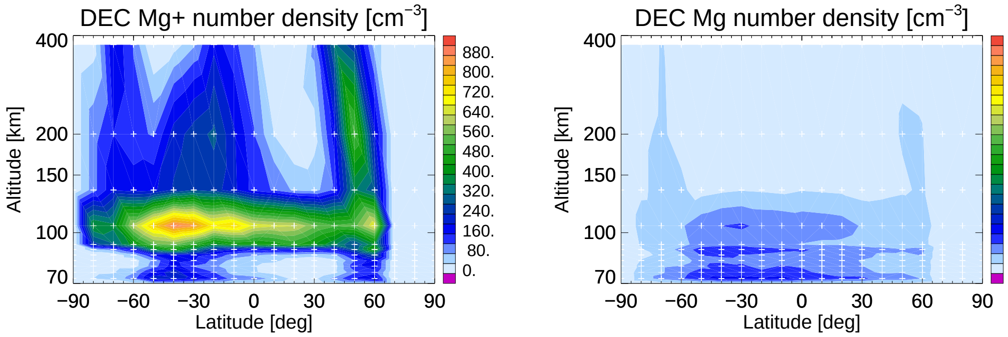

(a) Mg^+ latitudinal cross sections.

(b) Mg latitudinal cross sections.

Figure 7.11: Zonally averaged number densities of Mg^+ during northern winter solstice. Values are averaged over December 2002 – 2006. Binning as in Figure 7.8(a).

be identified. Maximum values are 750 cm^{-3} , which is significantly larger than the average number density between 92 and 120 km.

The northern Mg^+ bloom is most intense during the second half of the year from July to December (Figures 7.9(*a*), 7.11(*a*), other months not shown). During January to June (Figure 7.8(*a*), other months are not shown here), the abundance of Mg^+ around 60° N is on average lower at all altitudes compared to the July to December values. Whereas the absolute number densities within the southern bloom, it can be observed that the extend in latitudinal direction is larger during January to June.

The distribution of neutral Mg exhibits largest number densities around the sub-solar point at low altitudes (Figures 7.8(*b*), 7.9(*b*), 7.10(*b*), 7.11(*b*)). The number density of Mg reaches values of 150 – 200 cm^{-3} near the sub-solar point. The abundance of Mg is below 40 cm^{-3} for tropical and mid-latitude regions above approximately 130 km.

The behaviour of the Mg outflow at polar latitudes is different from that of the ionized species. For neutral Mg, the outflow over polar regions is only observed during local summer. The January distribution (not shown here) shows an outflow above the southern polar cap, but not above the northern cap. The distribution of December is not as pronounced as in January. At least, Figure 7.11(*b*) exhibits a outflow to higher altitudes and over a wider latitude range above the summer pole. A contrary distribution occurs during July (Figure 7.9(*b*)). For equinox conditions in March and September (Figure 7.8(*b*) and 7.10(*b*)), the outflow is observable over both polar regions. It is much less pronounced and does not extend to the highest retrieval altitudes, however.

7.2 Discussion

The variations in the total column in the northern hemisphere can be attributed to an enhanced release of Mg from the reservoir species $Mg(OH)_2$. Higher summertime abundances of atomic hydrogen and reaction of this species with $Mg(OH)_2$ and MgOH release neutral Mg, see reactions (4.14) and (4.15). This enhanced density of Mg does is not observed, however, as it is balanced by an increased rate of charge transfer with O_2^+ and NO^+ and a higher rate of photo-ionization (reactions (4.1), (4.2) and (4.3)).

In the southern hemisphere, the seasonal variations are damped by a mechanism that cannot be explained fully yet. In fact, a suitable mechanism is needed to retard just the summer enhancements. As can be seen from Figures 7.3(*a*) and 7.4(*a*), the winter total column is of similar magnitude of $3 - 4 \cdot 10^9$ cm^{-2} in both hemispheres. The northern summer values, however, are increased by a factor of up to three (Figure 7.3(*a*)), in contrast to the southern total column densities (Figure 7.4(*a*)).

Removal of ionized Mg^+ to be recombination is rather unlikely, as the number densities of electrons in the northern and southern hemisphere do not differ very much. The same applies for the abundance of the reaction partners for charge transfer O_2^+ and NO^+. Thus, it cannot be assumed that different rates of charges transfer or recombination account for the absence of southern summer Mg^+ enhancement. A possible reaction to remove both Mg and Mg^+ is reaction with ozone (see reactions (4.5) and (4.10)).

The most peculiar feature of the Mg^+ distribution is the layer of large Mg^+ abundance around 100 km, within retrieval pixel 92 - 120 km (Figures 7.8 – 7.11). Note that the altitude resolution of the retrieval at this altitude is similar to the width of the pixel (see Section 6.3.8), thus the actual width and peak of the layer is not resolved. Model studies suggest the peak density to be located at approximately 95 km, with a full-width at half-maximum of approximately 4 km (Plane and Helmer, 1995), (Fritzenwallner and Kopp, 1998).

Figure 7.12 shows vertical profiles of major ionic species in the mesosphere and lower thermosphere. As can be seen, the number densities of ions is rather low below 85 km. The dominant amount of ionized species can be found above this altitude. The layer of Mg^+ around 100 km coincides with a rapid increase in the concentration of O_2^+ and NO^+ ions (Figre 7.12), which are the most important partners for charge transfer with neutral Mg. Below 90 km, the lifetime of Mg^+ is short because of reaction with ozone (rection (4.10), see Section 4) and molecular oxygen (rection (4.6)). It can thus be concluded that above 90 km, the major amount of neutral Mg is ionized to form Mg^+. The ionic species is then deposited in an stable layer between 92 and 120 km.

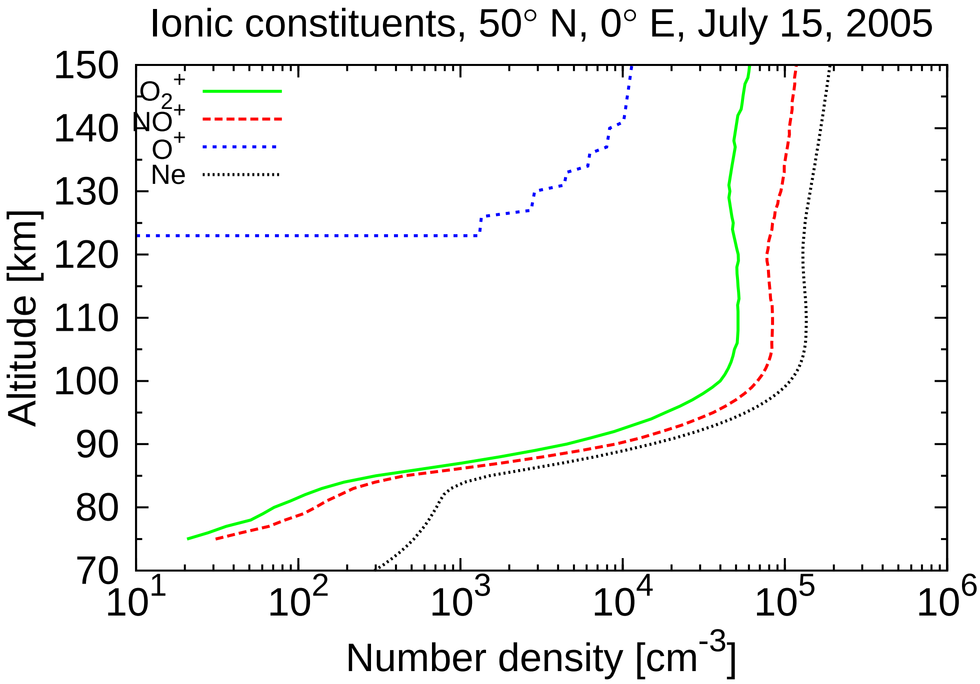

Figure 7.12: Vertical profiles of major ionic species in the mesosphere and lower thermosphere. All ionic species show a strong increase in concentration between 90 and 100 km. This is coincident with the altitude region where the dominant amount (with respect to the total column density) of Mg^+ is observed. Data are obtained from the IRI model (NASA Goddard Space Flight Center, 2007a).

The Mg vertical profile exhibits a maximum around 89 km (Figures 7.1(*b*), 7.2(*b*)). This is suggested by model simulations and coincides with a minimum in the removal rate of neutral magnesium (see Plane and Helmer (1995) and Section 9, Figure 9.1 for a discussion of removal rates for neutral magnesium). Assuming a constant source presented by influx of comic dust and a constant rate of descent by gravitational sedimentation, the enrichment of Mg at the altitude of minimum removal is self-evident.

A constant influx can be assumed safely since the occurrence of meteoric showers does not seem to have an impact on either magnesium species (see Section 8). It can thus be assumed that the major source of cosmic dust is asteroidal material from within the solar system. This assumption is supported by the work of McNeil et al. (1998) who propose the dominant influx velocity to be approximately 11 km/s, which is just the escape velocity of the Earth's potential well. They concluded that the major source of cosmic dust is a stationary source within the solar system. However, no publication was found that supported any large-scale inhomogeneities in the asteroidal material distribution within the solar system.

Both species show an enhancement in the number density towards lower altitudes (see Figures 7.1 and 7.2). In particular, the number densities at the lowest retrieval altitude of 70 km exceed the number densities in Mg at 89 km. This behaviour can not be explained yet. Model studies (Fritzenwallner and Kopp, 1998), (Plane and Helmer, 1995) suggest an increasing number density of the reservoir species $Mg(OH)_2$ at lower altitudes (see reaction (4.11), Section 4). This is reasonable as potential partners for loss reactions of Mg^+ and Mg such as O_2, O_3 and H_2O are more abundant at lower altitudes. There is no hint that during the time of SCIAMACHY measurements an increased release rate from the reservoir species could have been occurred. Note that the release rate is increasing with temperature and abundance of atomic hydrogen (see reactions (4.14) and (4.15)).

The enhancement may be a result of the ozone profile used in the retrieval scheme. To first order, the number density of the retrieval species is proportional to the product of the emitted radiance measured by the instrument and the extinction, i.e. $[N] \sim I \cdot e^{-\tau}$. Obviously, an under-estimation of the absorption would result in an over-estimation of the retrieval species. A drawback of the retrieval scheme presented in Section 6 is that a fixed ozone profile is used for all measurements. As ozone is considered to be the major absorption species at lower retrieval altitudes, increasing values in both Mg species hint to a systematic under-estimation of the absorption. Use of an comprehensive ozone climatology or even an ozone model – simultaneously driven to the retrieval – are necessary to shed light on this issue.

The outflow of Mg^+ ions near the equator has been discussed in Hanson and Sterling (1972). However, Hanson and Sterling (1972) suggested the outflow to be restricted within a narrow region of ±3° around the magnetic equator. The mechanism to lift the ions is based on the equatorial electrojet. The equatorial electrojet is an intense electric current which flows at approximately 100 km altitude over the magnetic equator. It consists of a daytime flow of electrons in the westward direction. It is driven by an eastward electric field which leads to the production of a vertical polarization field required in order to prevent the vertical flow of current. This polarization field is mathematically equivalent to the enhancement of the direct conductivity of the ionosphere between 95 and 120 km and is believed to be directly responsible for the intense eastward current.

It should be noted that Hanson and Sterling (1972) neglected neutral winds within the source region of the ions around 100 km. However, this assumption is not feasible, as at 100 km, the ion-neutral collision frequency is still large enough that the ions bulk velocity is dominated by the neutral wind. Model runs carried out by Fesen et al. (1983) included a neutral wind across the equator and were able to show that the ions in fact can escape the source regions up to 30° away from the equator. This was confirmed by sporadic satellite observations (Fesen and Hays, 1982b), (Fesen and Hays, 1982a), (Gérard and Monfils, 1978). It was proposed that the neutral wind pushes the ions up the magnetic field lines, thus allowing for further escape. The meridional circulation from the summer pole to the winter pole (Brasseur and Solomon, 1984) presents neutral winds in north-south direction. The occurrence of significant Mg^+ amounts above 150 km and outside a region of ±3–4° around the magnetic equator is thus consistent with the model results reported by Fesen et al. (1983).

The outflow of ionized magnesium over the regions of ±60° geomagnetic latitudes, i.e. the auroral ovals, cannot be explained fully yet. In 1985, in-situ measurements in polar regions were made using a retarding ion mass spectrometer (RIMS) on the Dynamics Explorer 1 (DE-1) spacecraft. As reported by Lockwood et al. (1985) and Moore et al. (1986), these measurements suggested a pronounced uplift of positive ions such as O^+ and H^+ over the auroral oval regions near the day side equatorward polar cap boundary. As this regions near the northern and southern geomagnetic pole present clefts in the magnetosphere and to let particles precipitate to lower altitudes, the effect was later named the "cleft fountain" (Lockwood et al., 1985).

Lockwood et al. (1985), Moore et al. (1986) and Lockwood et al. (1985) suggest that this fountain is basically driven by Joule heating near the auroral ovals. As a result of high conductivity within the auroral regions, strong current (the "auroral electrojets") systems are formed in the southern and the northern hemisphere, following the boundary of the auroral ovals defined by increased airglow intensities. The currents in the auroral ovals are part of large-scale ring currents in the magnetosphere (see). Friction of the electrons and the atomic and molecular species within these currents in the upper atmosphere leads to Joule heating in the auroral ovals in both hemispheres. The ions thus gain enough energy to escape the region of relatively high atmospheric density below 100 km, where the ionic motion is dominated by the neutral wind.

Once left the neutral regime and within the cleft fountain, positive ions move along the magnetic field lines and the electric field lines and populate the polar magnetosphere. Though heavier species such as O^+ undergo convection and sediment down on the night side of the Earth, the fountain is suggested to present a loss mechanism for lightweight ions such as H^+ (Lockwood et al., 1985). This presumption was supported by model calculations (Horwitz and Lockwood, 1985).

It should be noted that the in-situ observations of the RIMS instrument onboard the DE-1 satellite were carried out at high altitudes of 2000 km and more. The Mg^+ uplift observed by SCIAMACHY, however, is effective even at altitudes slightly above 100 km. Thus, the results found by Lockwood et al. (1985) and others cannot be transferred directly to explain the "Mg^+ polar fountain". The basic mechanisms that produce the cleft fountain such as Joule heating apply to the lower thermosphere at 100 km as well, however. In addition, the motion of ions above 100 km is not dominated by the neutral motion but by E and B fields. Thus, it is not unreasonable to suggest that the Mg^+ outflow is closely associated with the O^+ fountain observed near the auroral regions.

Figure 7.13 gives a graphical review of the two major processes of Mg^+ uplift.

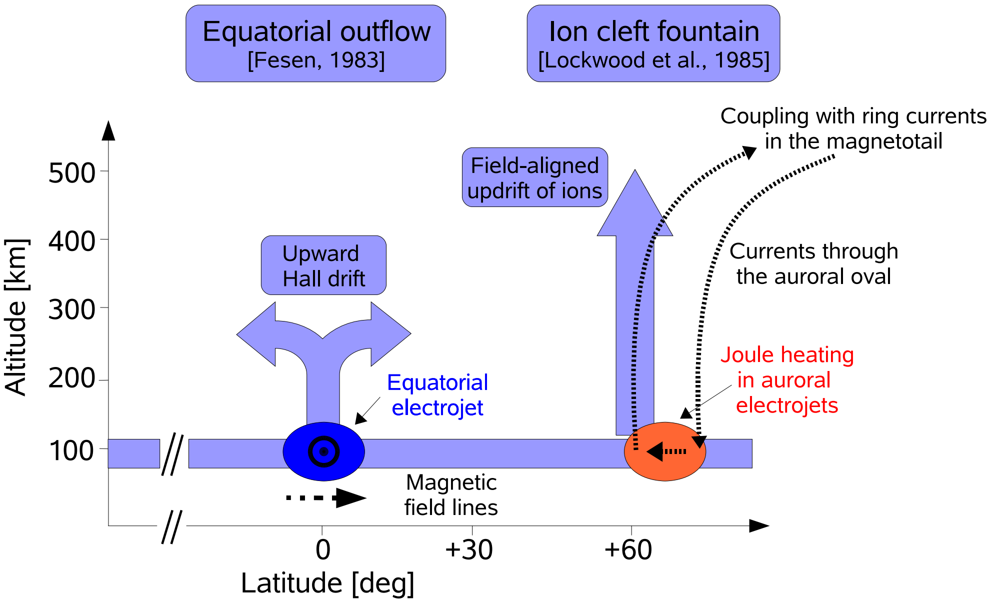

Figure 7.13: Simplified review of the major uplift processes for Mg^+. The equatorial fountain was suggested by Hanson and Sterling (1972). The simplified approach of Hanson and Sterling (1972) was extended later to explain increased number densities of Mg^+ at high altitudes and higher latitudes by (Fesen et al., 1983). The polar outflow was first discussed by Lockwood et al. (1985), this work features the term "cleft fountain" for the first time. See text for details of uplift mechanisms.

8 Magnesium species and meteor activity

The meteoric influx is not constant throughout the year. In fact, there are a number of *meteor showers* the Earth encounters on a regular basis. These showers results from the passage through the trail of a comet as both the Earth and the comet are orbiting the Sun. A number of comets are returning regularly, and these may in turn cause regularly returning meteor showers. The strength of such a shower is then measured by the *Zenithly Hourly Rate.* This value gives the number of meteors that would be observed under ideal conditions (i.e. clear sky, no clouds) if the shower would originate in zenith. The actual count rate depends on the flight direction of the shower as well as on the observer's field-of-view and viewing direction. However, the ZHR is a suitable means to compare the relative strengths of different meteor showers. The strongest regularly returning showers exhibit ZHRs of 100 – 120.

As is it generally believed that meteoric influx of cosmic dust is the major source of mesospheric and thermospheric metal species (compare Section 1), it is suggestive to expect that the total abundance of metal species is correlated with the meteoric influx. In particular, periods of high meteoric activity should result in correspondingly higher values of the total columns of Mg and Mg^+.

In this chapter, the five strongest regularly returning meteor showers are considered and their impact on the Mg^+ and Mg content is investigated. Table 8.1 gives a review of these showers. Each shower is characterized by its activity period, its day of maximal activity and the corresponding ZHR value.

To investigate the impact of meteoric showers on the Mg^+ and Mg content, daily average values in periods of high meteoric activity are compared to values in times of low activity. The period of highest meteoric influx is mid November through mid January, as three meteoric showers of high ZHR occur. Note that the strength of the Leonid shower is highly variable. The respective ZHR varies from 20 to 120, depending on the particular year (compare Table 8.1).

Shower	Activity period	Maximum	ZHR	Associated comet
Quadrantids	Jan 1 – Jan 5	Jan 3	120	C/1490 Y1
η-Aquarids	Apr 19 – May 28	May 5	60	Halley's comet
Perseids	Jul 17 – Aug 24	Aug 12	100	Swift-Tuttle
Leonids	Nov 14 – Nov 21	Nov 17	$\leq$120(*)	Temple-Tuttle
Geminids	Dec 7 – Dec 17	Dec 14	120	3200 Phaeton

Table 8.1: Review of prominent periodically returning major meteor showers. The ZHR value denotes the *Zenithal Hourly Rate*, i.e. the number of meteors that can be seen under clear, dark sky conditions and the shower assumed to come from zenith direction. The actual meteor count depends on the flight direction of the shower and the viewing direction of the observer. The ZHR is an upper estimate, but can be conveniently used to compare the strengths of different showers. Note that the activity periods do not exceed one week. The ZHR of the Leonids (*) varies from year to year (e.g. 2006: ZHR = 100). The given value is a lower estimate.

8.1 Observations

This section presents a detailed view on each shower as listed in Table 8.1 for 2002 – 2006 and the corresponding Mg^+ and Mg total content. SCIAMACHY data from July 2002 until December 2006 are included in the analysis. The 2007 data are excluded, as only data from

January 1, 2007 to April 15, 2007 are available, and only the Quadrantids shower lies within this period. Additionally, this shower is very short, thus it is reasonable to neglect it if not significant impact of longer and stronger showers can be found. As will be seen later, this is the case.

Figures 8.1 – 8.9 show the daily averaged total content of Mg^+ and Mg. Major meteor showers as listed in Table 8.1 are marked in light green, the day of maximal activity is marked dark green.

8.2 Quadrantids (January 1 – January 5)

2003

Neither Mg species shows significant increased values during the shower period.

2004

Both magnesium species exhibit increasing total column amounts during the shower. Mg^+ values are increasing from $3 \cdot 10^9$ cm^{-2} to $5 \cdot 10^9$ cm^{-2} , neutral Mg increases from $7.5 \cdot 10^8$ cm^{-2} to $1.25 \cdot to 10^9$ cm^{-2} .

2005

Mg as well as Mg^+ is increased at the end of the shower.

2006

The 2006 Quadrantids do not affect the magnesium content significantly. This holds for both species.

8.3 η-Aquarids (April 19 – May 28)

2003

Both species undergo a minimum around May 20 and increase towards the end of the shower. Average values of both species during the activity period do not exceed off-shower values.

2004

Both Mg species undergo a minimum around May 1. In case of Mg, this cannot be considered significant. Mg^+ column amounts are increasing towards the end of the shower and are decreasing shortly after the end of the Aquarids.

2005

Whereas the total column amount of Mg is rather constant during the shower, Mg^+ exhibits a strong decrease from $5 \cdot 10^9$ cm^{-2} to $1.3 \cdot 10^{10}$ cm^{-2} . Note, however, that the last minimum in Mg^+ occurred already in March 2005. It can be noted merely that the rate of increase is larger during the time of the shower.

2006

No trend in neither magnesium species can be observed during the shower.

8.4 Perseids (July 17 – August 24)

2002

Mg^+ values are decreasing during the first half of the Perseid, encounter a minimum near the maximum activity and increase then again. Column amounts of neutral Mg show a similar behaviour, though the minimum the subsequent increase is not as pronounced as for Mg^+. Note that the errors are rather large, thus the variations of Mg cannot be considered significant.

2003

No significant trend in neutral Mg is observable during the shower. Total column amounts of Mg^+ decrease on average during the activity period of the 2003 Perseids.

2004

Neutral Mg column amounts do not change significantly during the activity time of the Perseids in 2004. Singly ionized Mg^+ values oscillate around 10^{10} cm^{-2} , but do not show any trend.

2005

With respect to the measurement errors, neutral Mg is constant throughout the time of the shower. Mg^+ total column values oscillate around $8 \cdot 10^9$ cm^{-2} , but do not show any trend.

2006

Total column amounts of Mg^+ exhibit a minimum around August 1 and increase during the second half of the shower. Neutral Mg is constant during the shower with respect to measurement errors.

8.5 Leonids (November 14 – November 21)

2002

The Leonids shower was rather weak in 2002, the maximum ZHR was 20. During the activity time of the Leonids, neither Mg^+ nor Mg show significant variations. Both species are decreasing around the time of maximum activity. However, these variations do not exceed the usual variations.

2003

In 2003, the Leonid shower was quite strong, exhibiting maximum ZHRs of 120. Mg^+ total column amounts are increasing during the 2003 Leonid activity period. However, no significant short-term maximum can be observed around the time of maximum activity. Total column amounts of neutral Mg are constant on average. It should be noted, however, that the increase of Mg^+ began already early in November and lasts longer than the activity period of the Leonids.

2004

Total column amounts of both species are decreasing during the shower. However, changes in Mg are not significant with respect to the errors. The ZHR of the 2004 Leonids was approximately 100.

2005

Neither magnesium species shows any trend during the shower. Values are not changed significantly compared to periods of low meteoric activity. The ZHR of this year was approximately 100.

2006

The ZHR of this year was approximately 110. Values of Mg^+ exhibit a maximum near the day of maximal activity of the 2006 Leonids. During the second half of the shower, values of Mg^+ are decreasing. However, variations during the 2006 Leonids do not exceed the magnitude of 2006 variations in general. The same holds for neutral Mg.

8.6 Geminids (December 7 – December 17)

2002

For 2002, only one measurement during the activity period of the shower is present, thus a reliable statement can not be given.

2003

As for the Leonids of the same year, total column amounts of Mg^+ is increasing during the shower. The increase is not as pronounced as for the Leonids, however. Neutral Mg does not show any trend during the shower.

2004

Both magnesium species exhibit rather decreased values during the shower, compared to the times just before and just after the shower activity period. However, in case of Mg, the errors are too large to consider the changes significant.

2005

In 2005, a period of strongly increased neutral Mg values is present that lasts from late November until mid of December. During this time, Mg^+ total column amounts are decreased. The Geminid shower occurs at the end of this period. In fact, the end of the shower coincides with the end of the Mg/Mg^+ anomaly.

2006

No significant trend in neither Mg species is observed.

8.7 Conclusions

Within the measurement error margins, no significant impact of periods of high meteoric activity on the total content of neither Mg species has been observed. The variations during the showers are either not significant or are of the same order of magnitude as variations in periods of low meteoric activity.

Assuming influx of cosmic dust to be the primary source of mesospheric and thermosphere magnesium species, it can be concluded that the additional mass influx brought along with prominent and bright meteor showers is negligible compared to the background flux of cosmic dust into the atmosphere. Variations in both magnesium species have to be explained using other mechanisms.

These results are consistent with findings of former investigations carried out by Fesen and

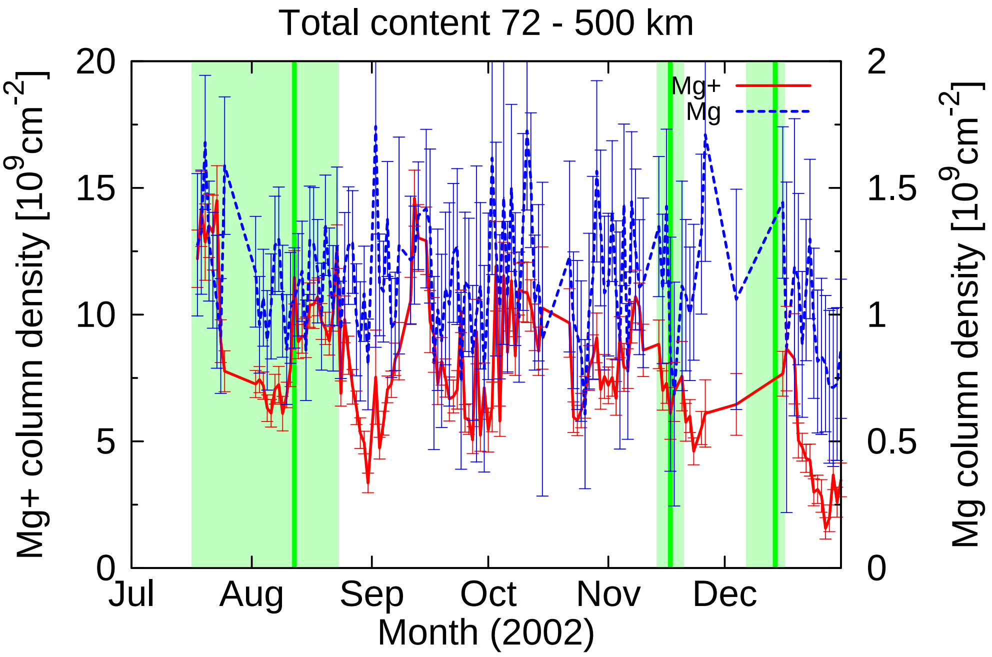

Figure 8.1: Total content of Mg^+ (solid) and Mg (dashed) during July 2002 – December 2002. Tick marks denote the first day of the month. Green strips denote periods of high meteoric activity, dark green areas refer to days of maximal activity, see Table 8.1.

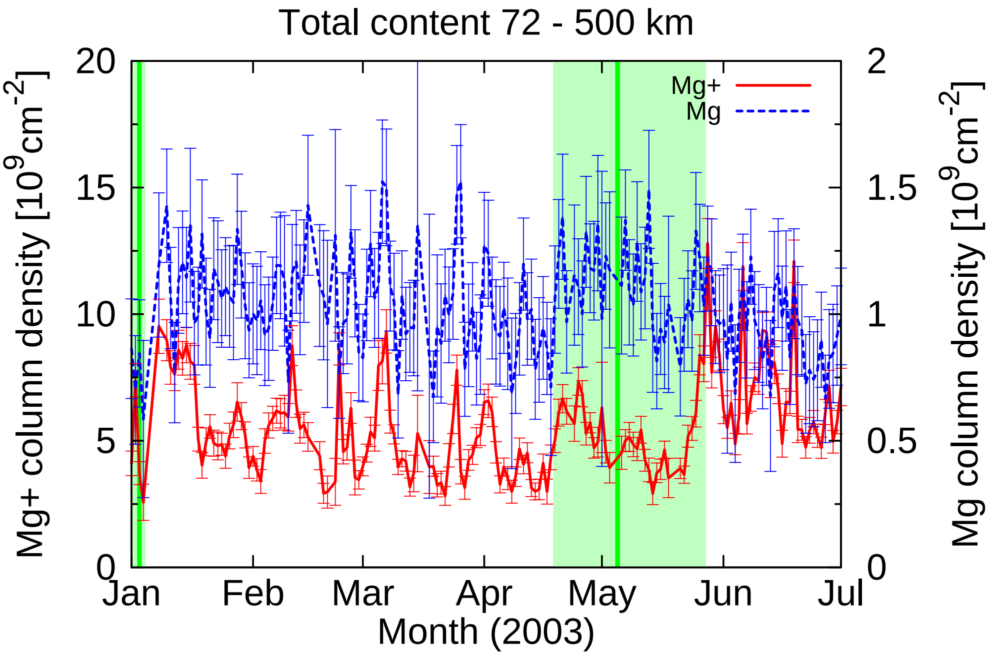

Figure 8.2: Total content of Mg^+ (solid) and Mg (dashed) during January 2003 – June 2003. Meteor showers are marked, see Figure 8.1.

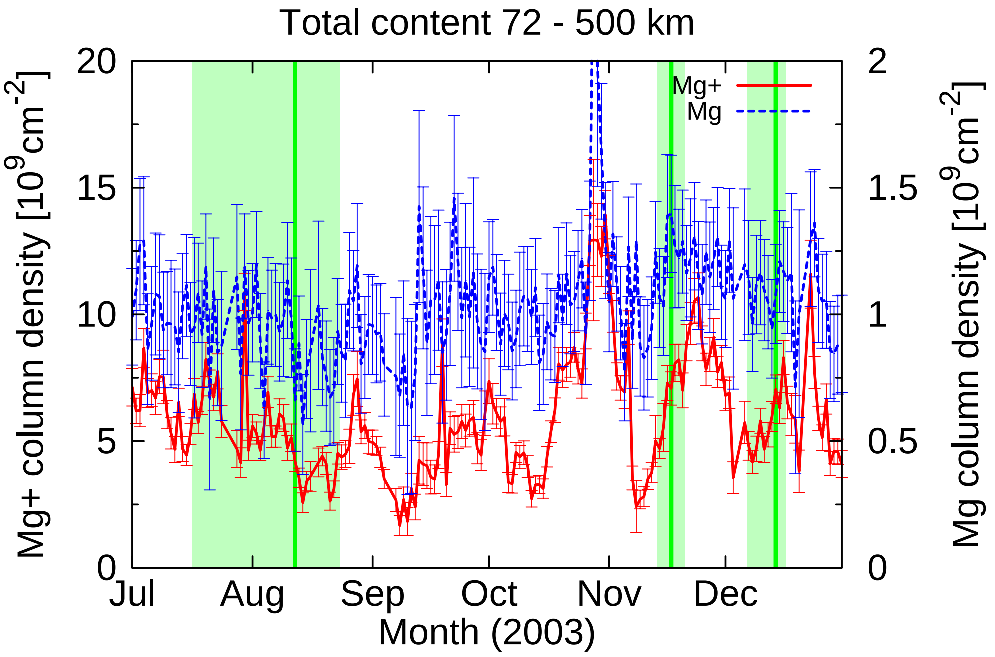

Figure 8.3: Total content of Mg^+ (solid) and Mg (dashed) during July 2003 – December 2003. Meteor showers are marked, see Figure 8.1.

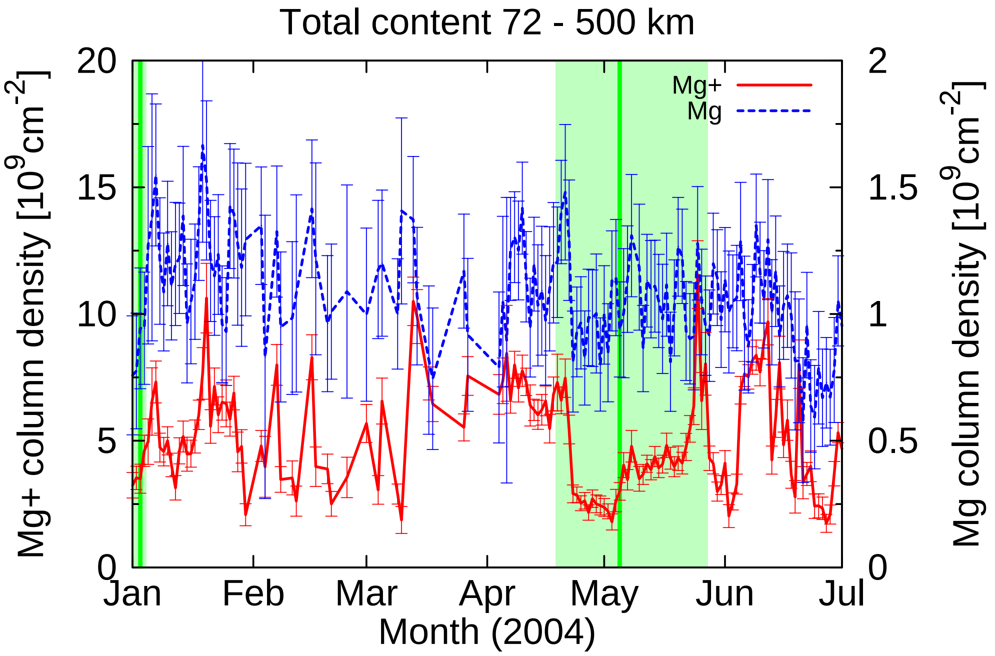

Figure 8.4: Total content of Mg^+ (solid) and Mg (dashed) during January 2004 – June 2004. Meteor showers are marked, see Figure 8.1.

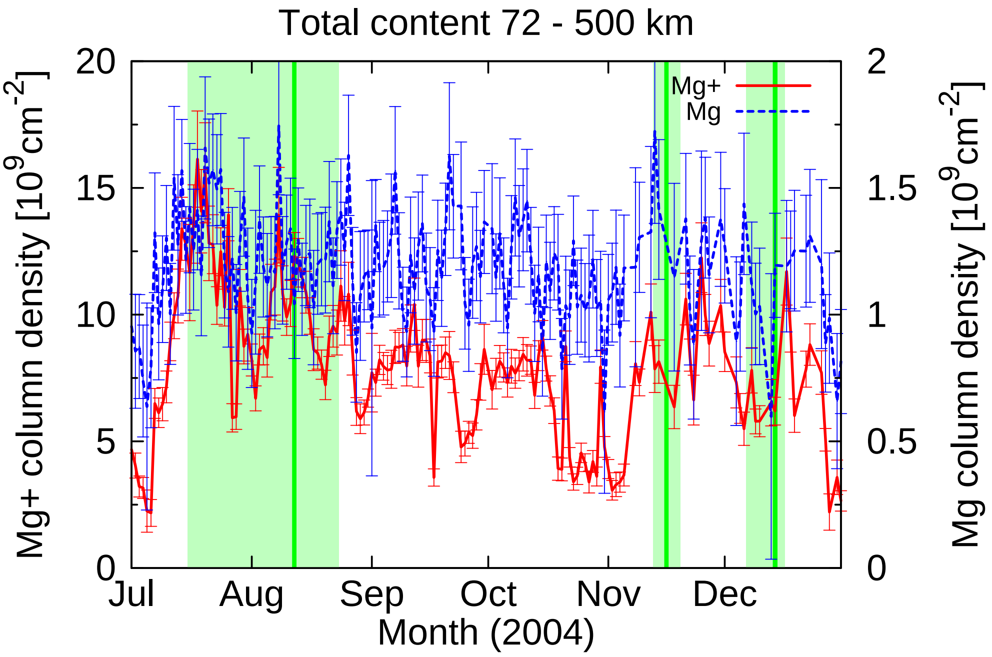

Figure 8.5: Total content of Mg^+ (solid) and Mg (dashed) during July 2004 – December 2004. Meteor showers are marked, see Figure 8.1.

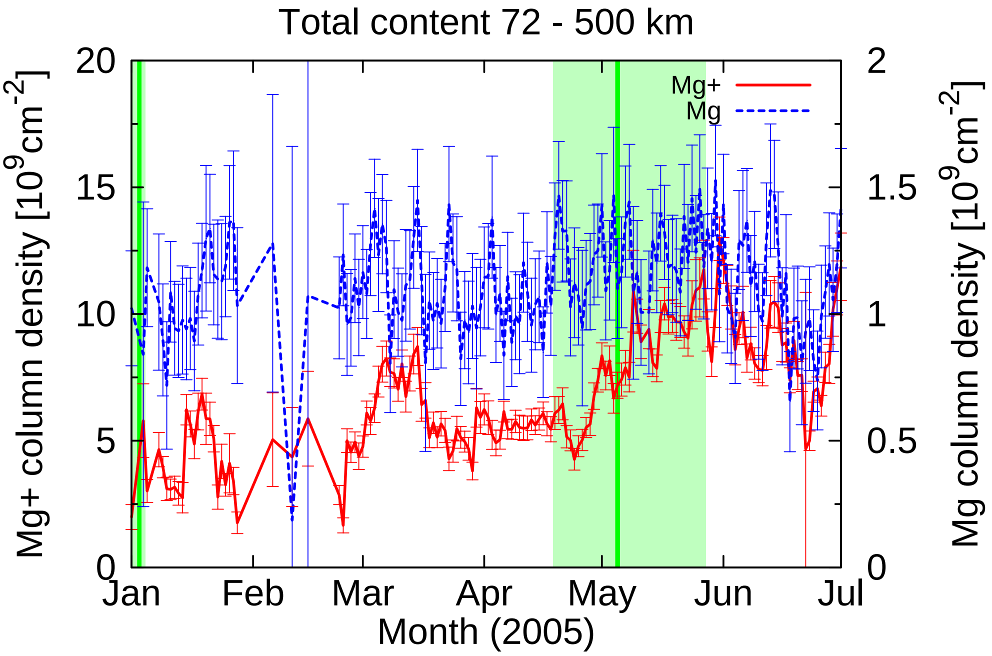

Figure 8.6: Total content of Mg^+ (solid) and Mg (dashed) during January 2005 – June 2005. Meteor showers are marked, see Figure 8.1. The period of anomalous increased Mg values and coincidently depleted Mg^+ values is discussed in further detail in Section 12.

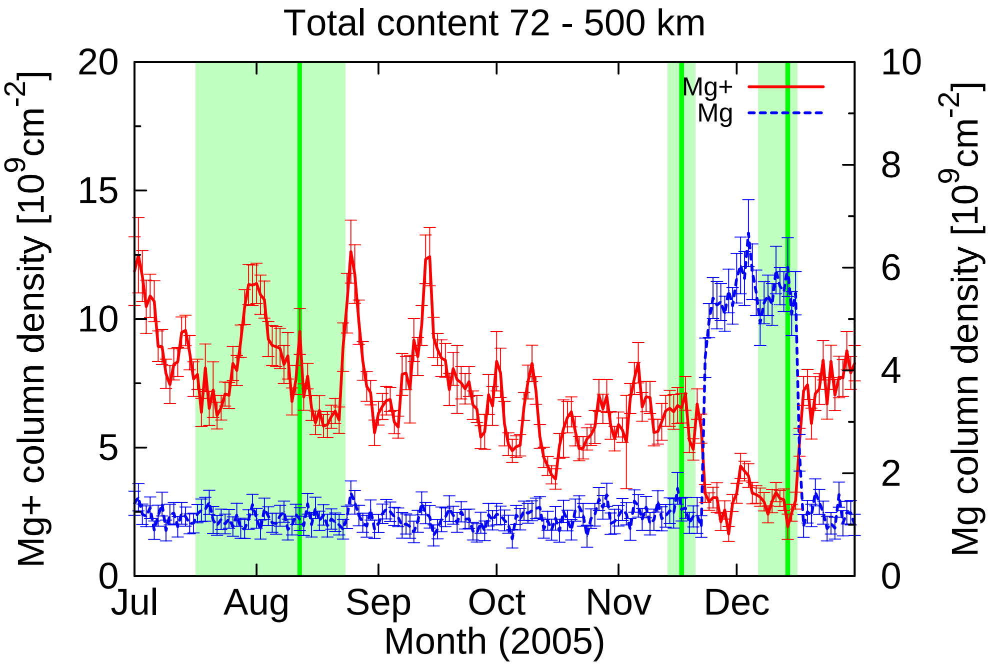

Figure 8.7: Total content of Mg$^+$ (solid) and Mg (dashed) during July 2005 – December 2005. Meteor showers are marked, see Figure 8.1.

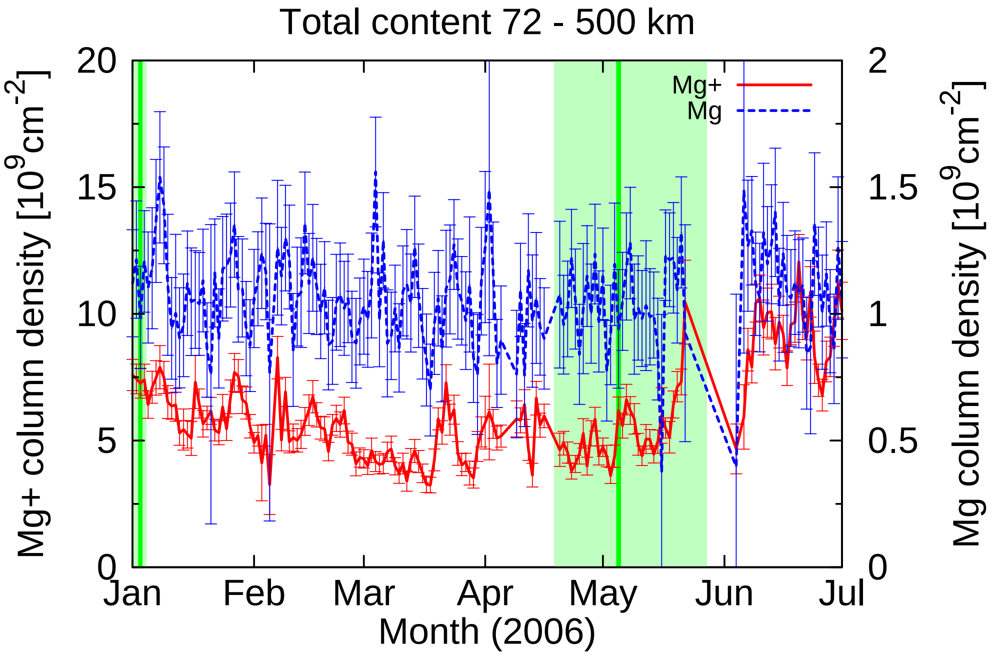

Figure 8.8: Total content of Mg$^+$ (solid) and Mg (dashed) during January 2006 – June 2006. Meteor showers are marked, see Figure 8.1.

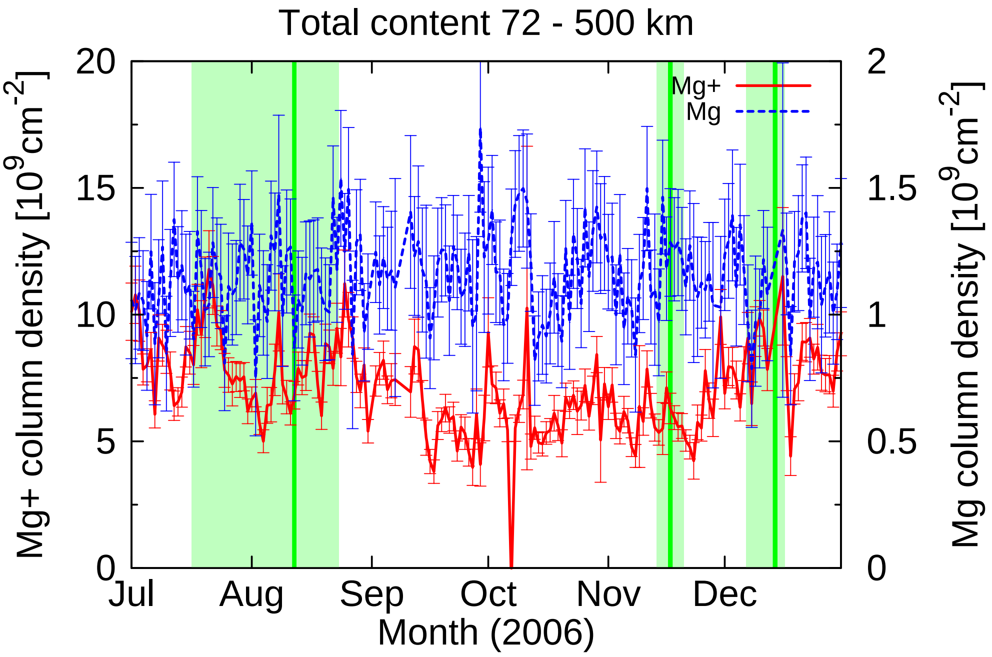

Figure 8.9: Total content of Mg^+ (solid) and Mg (dashed) during July 2006 – December 2006. Meteor showers are marked, see Figure 8.1.

Hays (1982a) and Joiner and Aikin (1996). While the authors of the first publication report on results of the limb-viewing satellite instrument on the Atmospheric Explorer E satellite, Joiner and Aikin (1996) present results using the GOME nadir-viewing instrument onboard the ERS-2 satellite. However, neither data set suggests a significant impact of meteoric shower activity on the Mg^+ content of the upper atmosphere. In case of Joiner and Aikin (1996), the analysis extends to the neutral Mg as well, with negative result for all meteor showers under consideration.

9 Estimation of the total influx of cosmic dust from total content and loss rates of Mg

The total influx of meteoric material into the atmosphere is subject to intense research, but still no certain numbers are known. Early radar measurements suggest a total mass of approximately 44 t/d (Hughes, 1978). These estimates have been revised to 80 – 120 t/d. Long exposure measurements based on satellite platform instruments yielded estimates of about 130 t/d (McBride and McDonnell, 1999). Rather indirect methods are the investigation of stratospheric aerosols and the corresponding content of meteoric iron and investigations or iridium sediments in the Earth's ocean floors. While the first method yielded values of 20 – 100 t/d (Cziczo et al., 2001), the second suggested higher values of 240 t/d (Wasson and Kyte, 1987).

For a steady state, the sources and sinks have to equal. Thus, knowing the fraction of neutral magnesium contained in meteoric material, an estimation of the loss rate in the Earth's atmosphere will yield an estimate of the total mass of meteoric material entering the atmosphere per day. See Section 4 for a detailed description of loss reactions for Mg and Mg^+. Figure 9.1 presents the total loss rate of neutral Mg due to reaction with ozone, charge transfer with O_2^+ and NO^+ and photoionization (see reactions (4.10), (4.3), (4.2),(4.1) in Section 4).

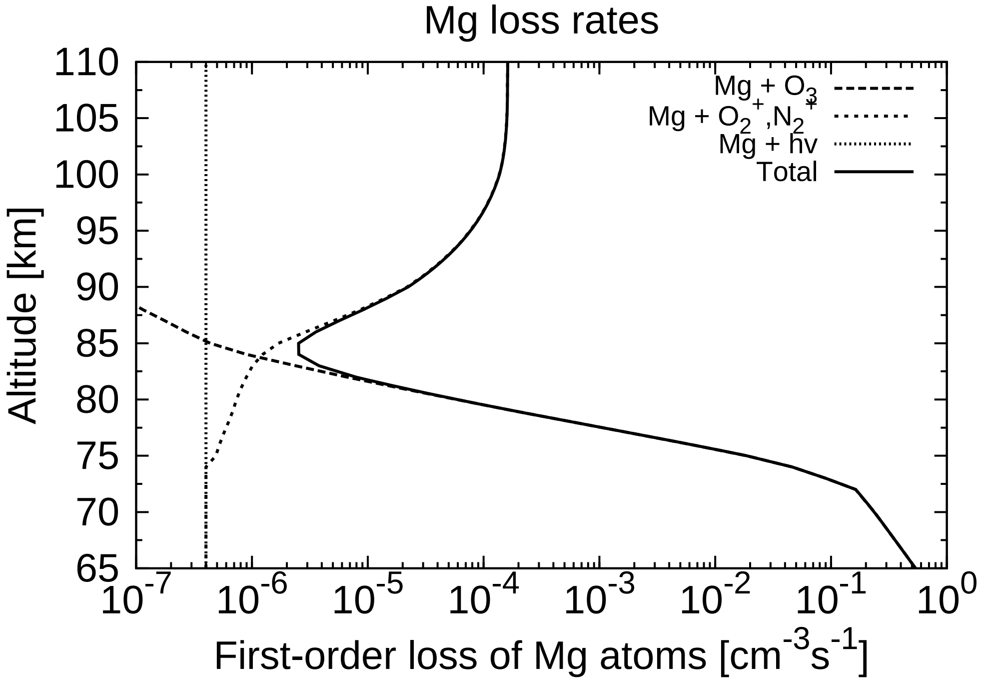

Figure 9.1: First-order loss rates of neutral magnesium in the mesosphere. Shown are loss rates for photoionization (fine-dotted, constant over the altitude range considered here), charge transfer with O_2 and NO^+ (dotted) and reaction with ozone (dashed). The solid line corresponds to the total loss rate. Note that there is a minimum in the total loss rate around 85 km. This results in an enrichment of neutral Mg around this altitude. Data for this Figure taken from Plane and Helmer (1995).

The loss of Mg at an particular altitude h is calculated as the product of the loss rate δL and the number density [Mg]:

$$L(h) = \delta L(h) \cdot [\mathrm{Mg}](h) \tag{9.1}$$

Multiplication of this value with the area $A(h)$ of the shell at atmospheric level h yields the global loss at altitude h. This value has to be multiplied with 86400 s/d to obtain the loss per cm^{-2} and day. Assuming a constant isotropic influx, the global loss per day is then calculated as

$$
\begin{aligned}
L^* &= 86400 \cdot \int_{H_0}^{H_1} \delta L(h) \cdot [\mathrm{Mg}](h) \cdot A(h)\, dh \\
&\approx 86400 \cdot A_0 \cdot \int_{H_0}^{H_1} \delta L(h) \cdot [\mathrm{Mg}](h)\, dh. \qquad (9.2)
\end{aligned}
$$

Here, A_0 denotes the surface area of the atmospheric shell at level 120 km. The second equation is a good approximation of the first, since the surface areas of the atmospheric shells at 0 and 120 km differ only by 3%. Thus, $A(h)$ can be considered constant. Integration over altitude is performed between $H_0 = 70$ km and $H_1 = 120$ km. This choice is reasonable as the measurements do not extend to lower altitudes and on average no significant Mg abundance has been measured above 120 km. Reading the values from Figure 9.1 and using an average vertical profile of Mg as given in Figure 9.2 and inserting all these quantities in equation (9.2), a global influx of 927 kg/d of neutral Mg is estimated.

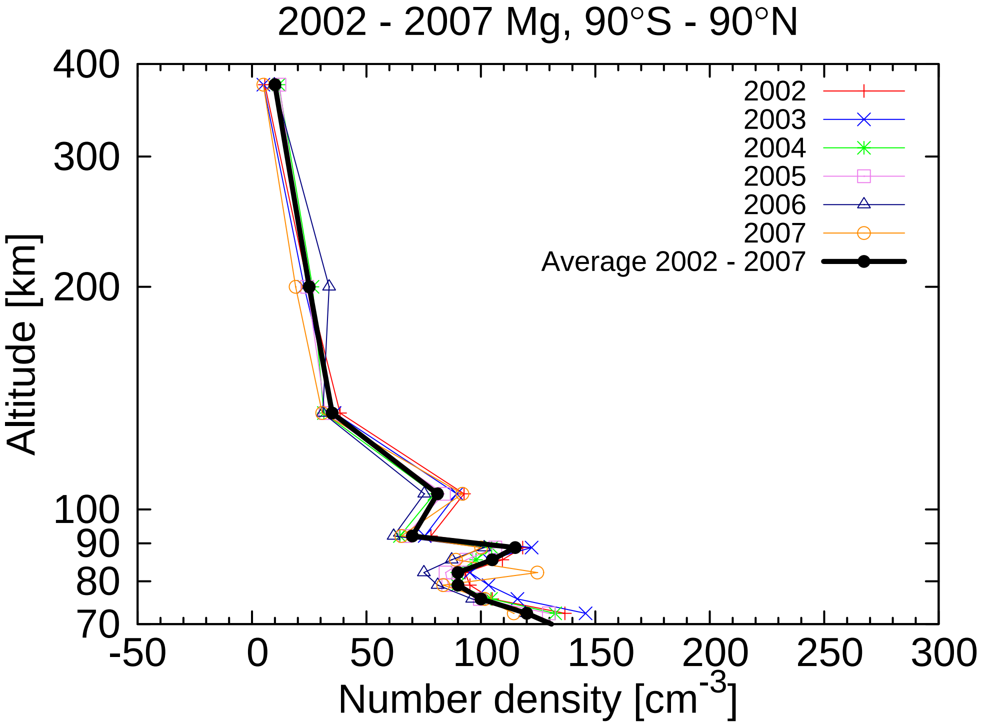

Figure 9.2: Average profiles of neutral magnesium, measured in 2002 – 2007. Each profile corresponds Mg number densities averaged over one year of measurement and all latitudes and longitudes. As can be seen in the Figure, the Mg content is fairly stable through all years of measurement. The average profile (black) for all years is used for the estimation of the total Mg loss and the corresponding influx (see text for details).

It can be assumed that the magnesium in meteoric material is not ionized. The average mass fraction of Mg in cosmic dust has been reported by Hughes (1978) to be approximately 13%. Assuming that the total meteoric content of MG is ablated and transferred into the gas phase, a total influx of approximately 7130 kg/d would result. However, McNeil et al. (1998) noted that contrary to sodium, magnesium and calcium may not ablate completely from the dust particle. A differential ablation model accounting for individual ablation altitudes and different particle sizes and entry velocities was applied to estimate the deposition of meteoric material in the upper atmosphere. The results provided strong evidence that the fraction of metal species that do not ablate completely from the dust particle depends primarily on the entry velocity of the particle. This velocity is not constant throughout the total particle population. Higher velocities result in a more complete ablation of magnesium and other meteoric metals from the dust particles. At approximately 30 km/s, the complete content of sodium, magnesium and calcium is ablated from the particle (McNeil et al., 1998), whereas e.g. 14 km/s leaves half of the metallic content of calcium and magnesium in the particle.

A number of velocity distributions have been tested by McNeil et al. (1998), and the resulting metal profiles have been compared with measured values. However, the resulting picture is far from being homogeneous. Best matches with measured column density ratios of Na/Ca, Na^+/Ca^+ and Mg^+/Na^+ have been obtained assuming a population of fast particles with entry velocity 60 km/s and another larger population of slow particles with 11 km/s. The latter particles are assumed to make up 98% of the total particle amount. This velocity distribution results in 87% residual amount (not ablated) of magnesium in the dust particles. Using 927 kg/d of ablated magnesium input into the atmosphere, 55 t/d of meteoric material have to enter the atmosphere every day. This is well within the range of earlier estimates.

It should be noted that 11 km/s is the lowest possible velocity for a dust particle to enter the atmosphere, as this is just the minimal velocity for escape from the Earth's potential well. A dust particle originating a an infinite distance would therefore enter the atmosphere with approximately the escape velocity.

However, the origin of meteoric dust is still not clear. McDonnell (1980) suggested that the Earth is surrounded by a cloud of cosmic dust of mainly asteroidal origin. This cloud is stationary within the solar system and particles leave the cloud and hit the Earth as a result of gravitational or other perturbations. Another possible origin of cosmic dust, however, are regular or irregular cometary objects. These objects enter the solar system with higher velocities. The maximum velocity for an regularly returning object on an parabolic (i.e. circular or elliptical) orbit is 72 km/s at 1 astronomical unit.

It can be concluded that the velocity distribution of cosmic dust particles significantly impacts the amount of ablated material and that this distribution is still not known to a good extend. Thus, the best estimate to do is assuming the majority of comic dust entering the atmosphere at the smallest possible velocity of 11 km/s. This yields an lower estimate of the meteoric influx of 55 t/d.

It should be noted that this mass influx is negligible compared to the total mass of Earth of $5.97 \cdot 10^{21}$ t. Assuming that the Earth of approximately 5 billion years old and that during this time the influx of meteoric material has not changed, a total mass of 10^{14} t has been added to the Earth's mass. This is more than seven orders of magnitude below the mass of Earth and thus negligible.

10 Correlation with solar activity

The solar radiation is subject to variations of intensity. This holds for all wavelength regions. However, shorter wavelengths are subject to larger variations. During a 11-year solar cycle, the 200 – 300 nm irradiance changes by 10%, the Lyman-α hydrogen emission line at 121 nm varies by up to 30%. As the shorter wavelengths render a large input of energy into the Earth's atmosphere, it is reasonable to investigate the impact of solar variations on the magnesium content in the upper atmosphere. Additionally, the impact of variations of the particle flux from the Sun, the so-called solar wind is discussed. The solar wind consists of both electrons and protons and affects the atmosphere at all levels.

A convenient proxy of the solar activity rendered to be the intensity of the solar electromagnetic radiation at 10.7 cm wavelength (i.e. $\approx$ 2800 MHz). It has been found that this emission correlates with the daily sunspot number and is determined by the same mechanisms and processes affecting the visible and X-ray wavelength range (Tapping and Murdin, 2000). Additionally, the radio fluxes in the 1000 – 9400 MHz range correlate well with the total solar irradiance (Schmahl and Kundu, 1994).

This emission is routinely observed by ground-based stations since the late 1940's. Thus, an extended time series from a number of different sources is readily available. In this section, the time series generated by the Dominion Radio Astrophysical Observatory near Penticton, Canada is used. This observatory is operationally measuring the 10.7 cm flux since the late 1960's. See (Covington, 1969) for a review of the measurement technique and the data processing procedure. Figure 10.1 shows the radio flux intensity during the SCIAMACHY operation.

As a result of the rather low energy of the 10.7 cm radio flux ($E(10.7\text{cm}) = 1.2 \cdot 10^{-15}$ eV, $E(300\text{nm}) = 4.13$ eV), the chemistry of the upper atmosphere is not directly affected by solar radiation of this wavelength. Within this section, the 10.7 cm flux will be used rather as a proxy for higher energetic radiation inserting energy into the upper and middle atmosphere. A direct and strong impact can be attributed to particle fluxes from the Sun. Particles contained in the solar wind enter the Earth's magnetic field and are trapped within the field lines. These particles gyrate around the field lines and are reflected near regions of geomagnetic latitude $\pm$ 60° , where the distance of the field lines gets small and revertive forces push the particles back to regions of lower geomagnetic latitude. As a result of perturbations of the magnetic field of the Earth, these particles can precipitate down to lower altitudes and affect the chemistry of stratospheric and higher levels. Perturbations can origin in increased particle fluxes from the Sun. See Figure 10.2 for a time line of the proton fluxes with energies > 10 MeV during the SCIAMACHY mission.

Within the next section, the linear correlation between the magnesium species content and the solar activity will be investigated using the Pearson correlation index r. See equation. (10.1) and let x, y denote the metal content and the solar activity proxy in use, respectively. Overlined quantities denote mean values.

$$r = \frac{\sum_{i=1}^{n}(x_i - \bar{x})(y_i - \bar{y})}{\sqrt{\sum_{i=1}^{n}(x_i - \bar{x})^2 \sum_{i=1}^{n}(y_i - \bar{y})^2}} \tag{10.1}$$

A value of r near unity indicates a strong correlation between the quantities x and y, whereas $r = -1$ indicates an anti-correlation between x and y. It should be noted that the correlation coefficient r as given in equation 10.1 does only quantify the linear correlation. Any other functional relation between the two quantities under consideration may exist, but cannot indicated by the Pearson correlation coefficient.

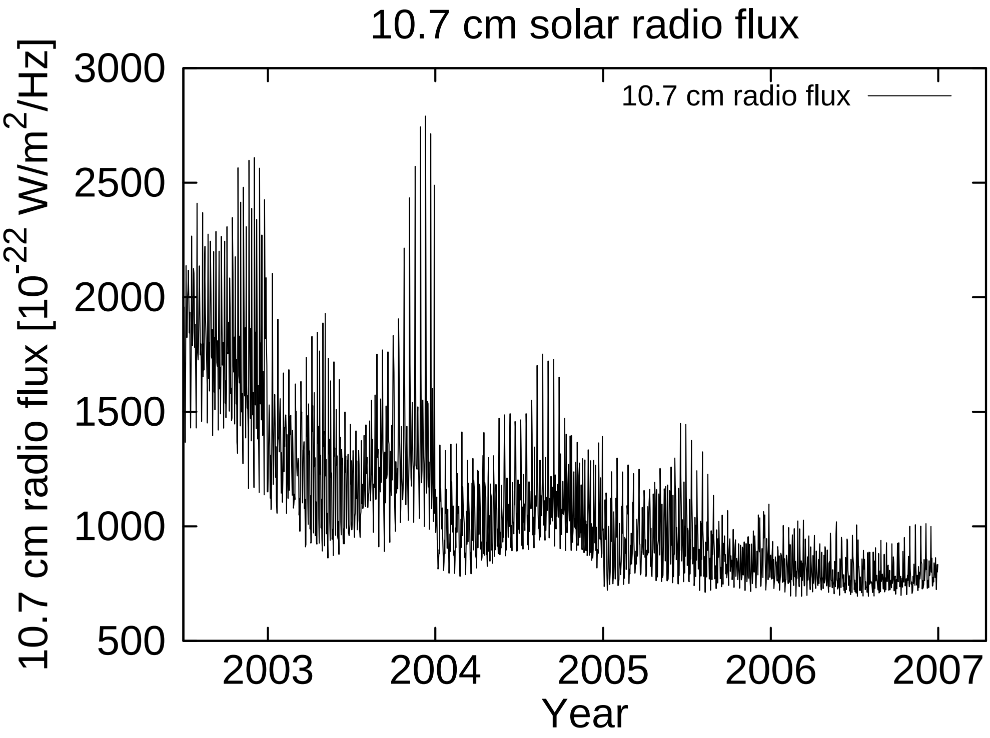

Figure 10.1: Radio emission intensity at 10.7 cm (2800 MHz), as measured by the Dominion Radio Astrophysical Observatory, Penticton, Canada. Tick marks indicate Jan 1 of each year. On average, the intensity of the radio flux is decreasing, indicating an approach to the next solar minimum of the 11-year solar cycle. Increased values of the flux are observed at the end of 2003 during a turbulent period of the Sun. Data obtained from Dominion Radio Observatory, Penticton, Canada (2007).

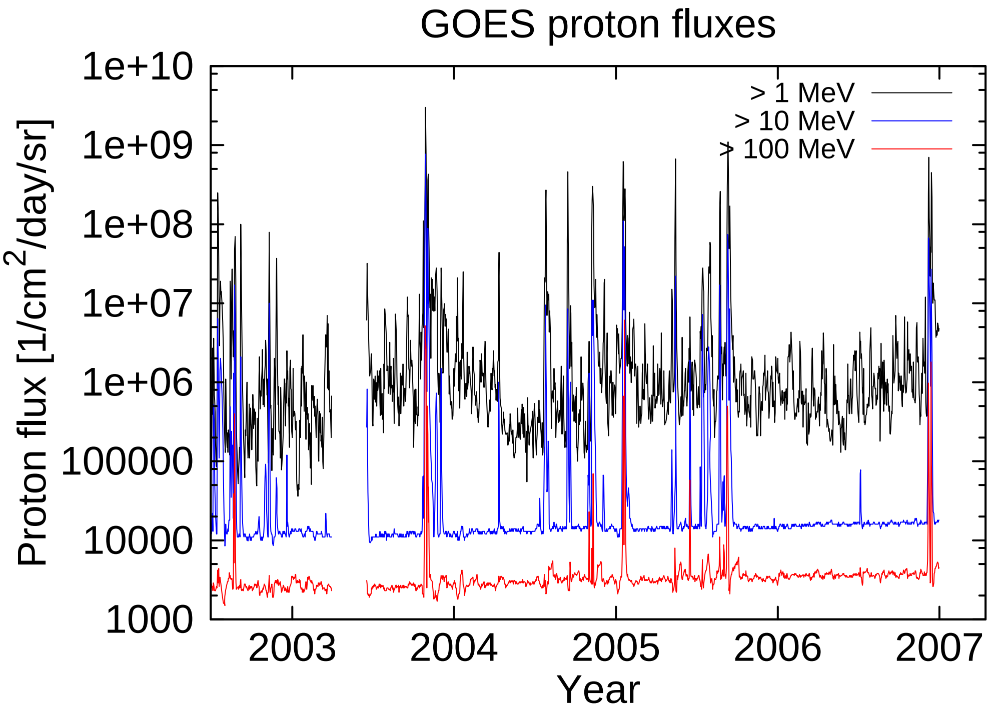

Figure 10.2: Solar proton flux intensity as measured by GOES 12 instrument. Shown are proton fluxes for proton with energies > 1, > 10 and > 100 MeV. Tick marks indicate Jan 1 of each year. Separated solar proton events are clearly visible. The largest peak near the end of 2003 marks the October 2003 solar proton event. See Section 11 for a discussion of the impact of this SPE on the magnesium abundance in the mesosphere and lower thermosphere. Data obtained from NOAA/National Weather Service (2007).

10.1 Correlation with proton fluxes

10.1.1 Globally averaged total column content and proton fluxes

Figures 10.3 and 10.4 show scatter plots of the Mg^+ respectively Mg global total column content versus the proton flux intensity in different energy ranges. The plots show all daily averaged measurements available from July 2002 until April 2007. As can be seen from the plots as well as from the corresponding correlation coefficients (given in the captions, values are in the range 0.05 – 0.12), no linear correlation can be found. Though there are a number of events of high proton flux especially within the 10 MeV and the 100 MeV band (see Figures 10.3(*b*), 10.3(*c*), 10.4(*b*), 10.4(*c*)), no corresponding events of high Mg^+ or Mg content are associated with these episodes.

The corresponding scatter plots do not suggest any other functional relation between the magnesium content and the proton fluxes.

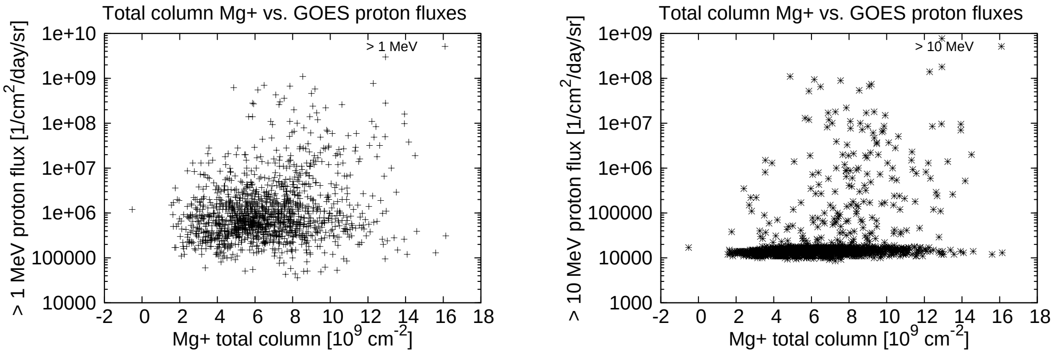

(a) Mg^+ content and proton flux for energies > 1 MeV. The correlation coefficient is $r \approx 0.12$, indicating no linear correlation.

(b) Mg^+ content and proton flux for energies > 10 MeV. The correlation coefficient is $r \approx 0.09$, indicating no linear correlation.

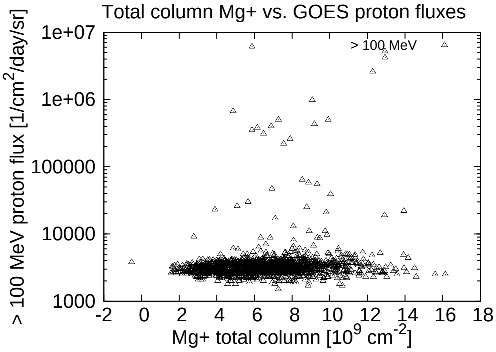

(c) Mg^+ content and proton flux for energies > 100 MeV. The correlation coefficient is $r \approx 0.08$, indicating no linear correlation.

Figure 10.3: Scatter plots of the Mg^+ total column content versus the solar proton fluxes in three different energy bins (Figure 10.4(*a*): >1 MeV, Figure 10.4(*a*): > 10 MeV, Figure 10.4(*c*): > 100 MeV). As can be seen from the plots as well as from the correlation coefficients given in the respective captions, there is no linear correlation between the total Mg^+ column and the solar proton fluxes.

10.1.2 Vertical profiles and proton fluxes

Figures 10.5 – 10.7 show the correlation indices as calculated from equation (10.1) for Mg^+ and Mg at different altitudes with the 1 MeV, the 10 MeV and the 100 MeV solar proton flux. All measurements are averaged daily and binned into five categories. These consist of four geographical latitude ranges and the geomagnetic polar regions, i.e. regions of geomagnetic latitude > 60° .

Consistently with the total columns, the vertical profiles do not exhibit any correlation be-

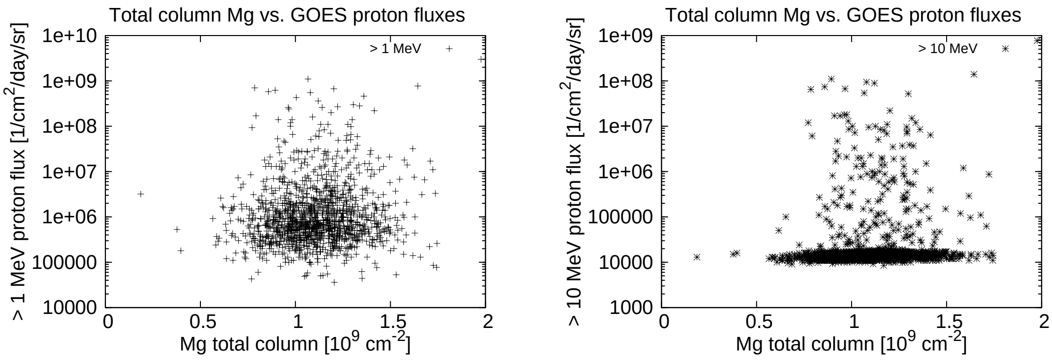

(a) Mg content and proton flux for energies > 1 MeV. The correlation coefficient is $r \approx 0.06$, indicating no linear correlation.

(b) Mg content and proton flux for energies > 10 MeV.The correlation coefficient is $r \approx 0.05$, indicating no linear correlation.

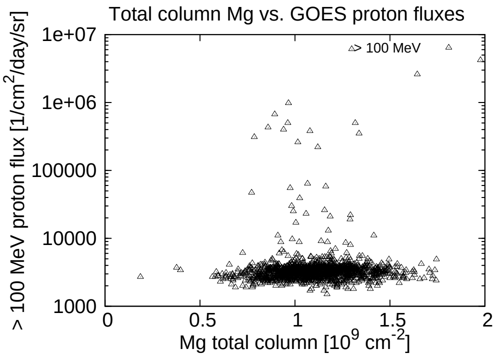

(c) Mg content and proton flux for energies > 100 MeV.The correlation coefficient is $r \approx 0.07$, indicating no linear correlation.

Figure 10.4: Scatter plots of the neutral Mg total column content versus the solar proton fluxes in three different energy bins (Figure 10.4(*a*): >1 MeV, Figure 10.4(*a*): > 10 MeV, Figure 10.4(*c*): > 100 MeV). As can be seen from the plots as well as from the correlation coefficients given in the respective captions, there is no linear correlation between the total Mg column and the solar proton fluxes.

tween the Mg^+ or Mg number density at different altitudes and the solar proton fluxes. This is the case for all latitude ranges and all proton energies.

10.2 Correlation with the 10.7 cm radio flux

10.2.1 Total column content and 10.7 cm radio flux

Figures 10.8 and 10.9 show scatter plots of the Mg^+ respectively Mg total column content versus the radio flux at 10.7 cm. Used are all measurements of Mg^+ and Mg being available from the start of the mission. The measurements are daily averaged to reduce the amount of data. Approximately 1700 data points enter each plot. The linear correlation index between Mg^+ and the radio flux is 0.67, indicating a very weak linear correlation. For neutral Mg, $r = 0.51$ holds. Note that the vertical axis in Figures 10.8 and 10.9 is given in linear scale. This explains why Figure 10.3(*a*) and 10.4(*a*), exhibiting a similar structure, correspond to lower correlation indices each.

10.2.2 Vertical profiles and 10.7 cm radio flux

Figures 10.10 shows the correlation indices for Mg^+ and Mg at different altitudes and the 10.7 cm radio flux. All data are averaged and binned as for Figures 10.5 – 10.7.

Both species show maximal correlations with the solar radio flux at altitudes between 92 and 120 km. Mg^+ exhibits a secondary maximum around 75 km. Maximal correlation indices of

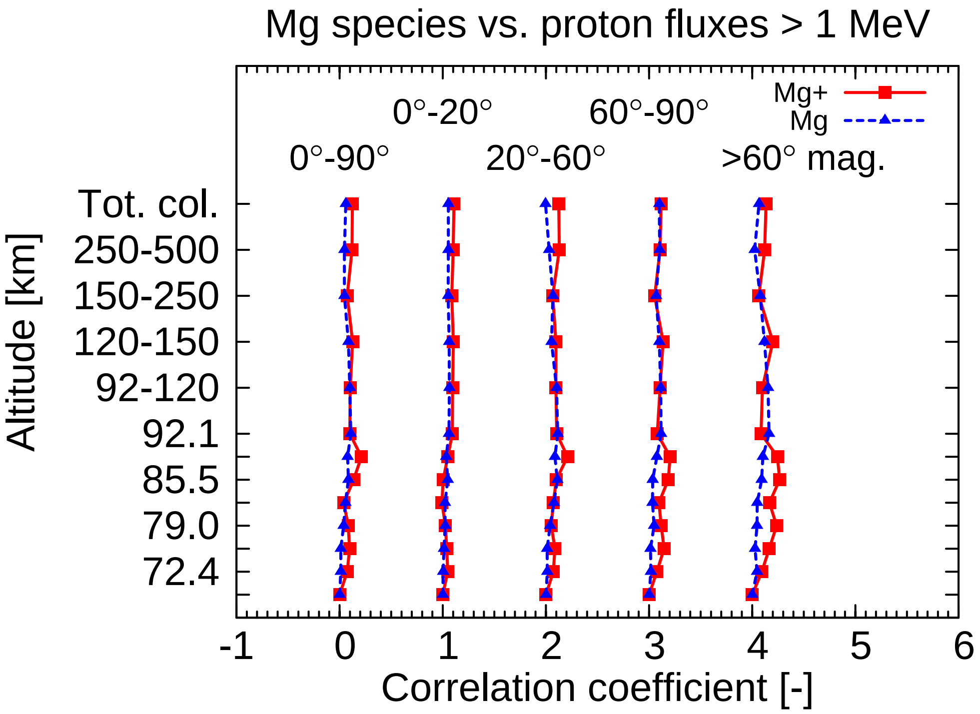

Figure 10.5: Correlation indices for Mg^+ (solid, squares) and Mg (dashes, triangles) contents at different altitudes and the solar proton flux for protons with energies > 1MeV. All correlation indices are well below 0.5, indicating no or a weak linear correlation between Mg species and the proton flux. Curves corresponding to different latitude bands are shifted to the right by multiples of unity for convenience.

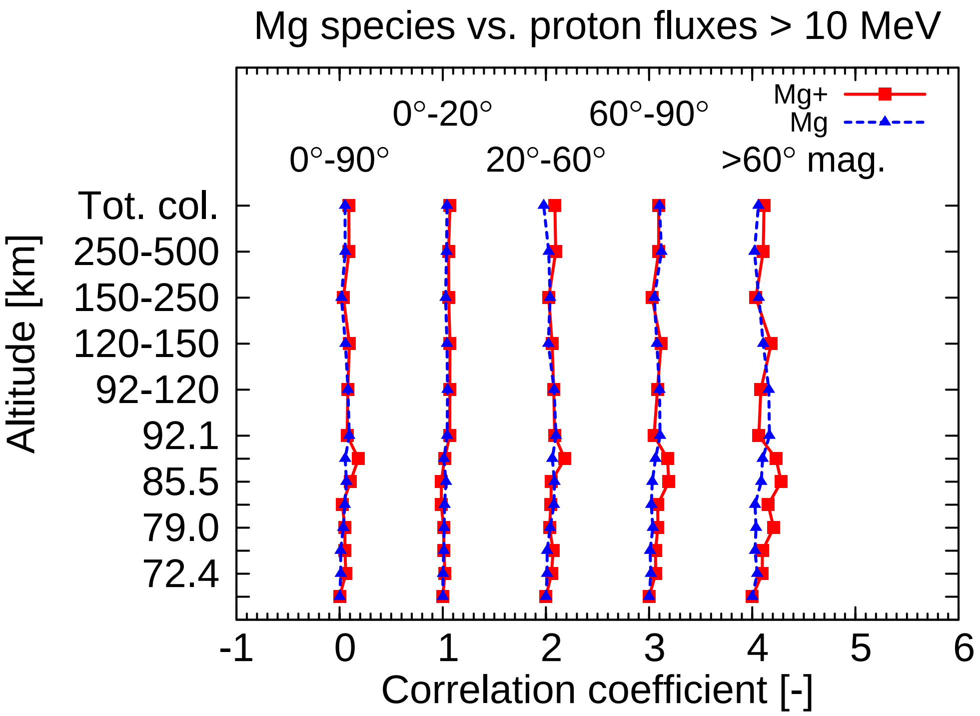

Figure 10.6: Correlation indices for Mg^+ (solid, squares) and Mg (dashes, triangles) contents at different altitudes and the solar proton flux for protons with energies > 10MeV. All correlation indices are well below 0.5, indicating no or a weak linear correlation between Mg species and the proton flux. Curves are shifted as in Figure 10.5.

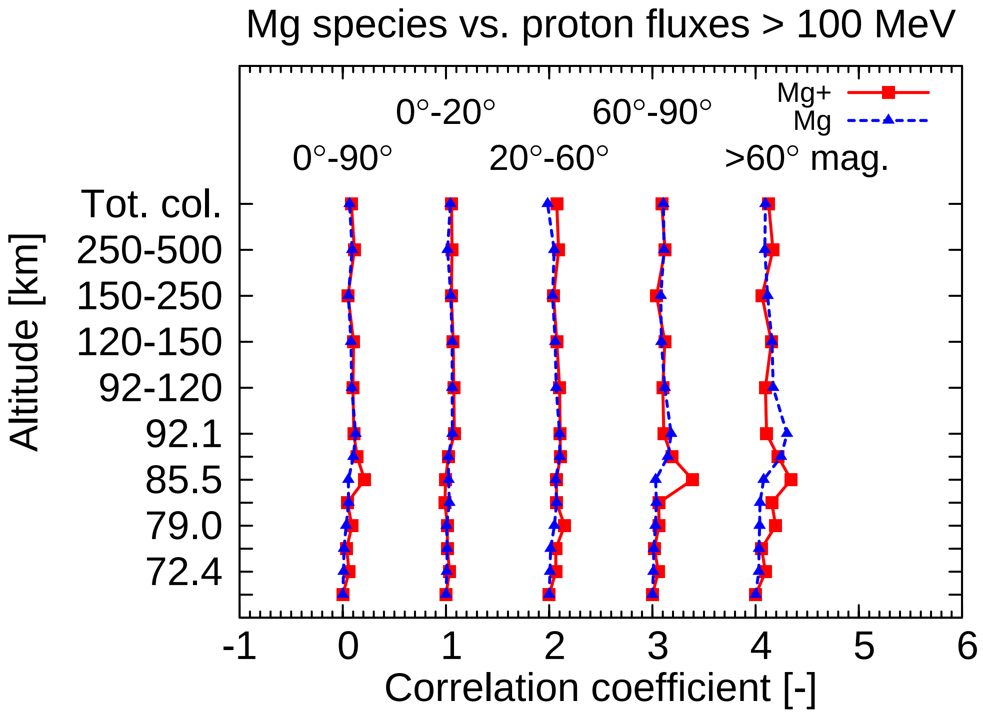

Figure 10.7: Correlation indices for Mg^+ (solid, squares) and Mg (dashes, triangles) contents at different altitudes and the solar proton flux for protons with energies > 100MeV. All correlation indices are well below 0.5, indicating no or a weak linear correlation between Mg species and the proton flux. Curves are shifted as in Figure 10.5.

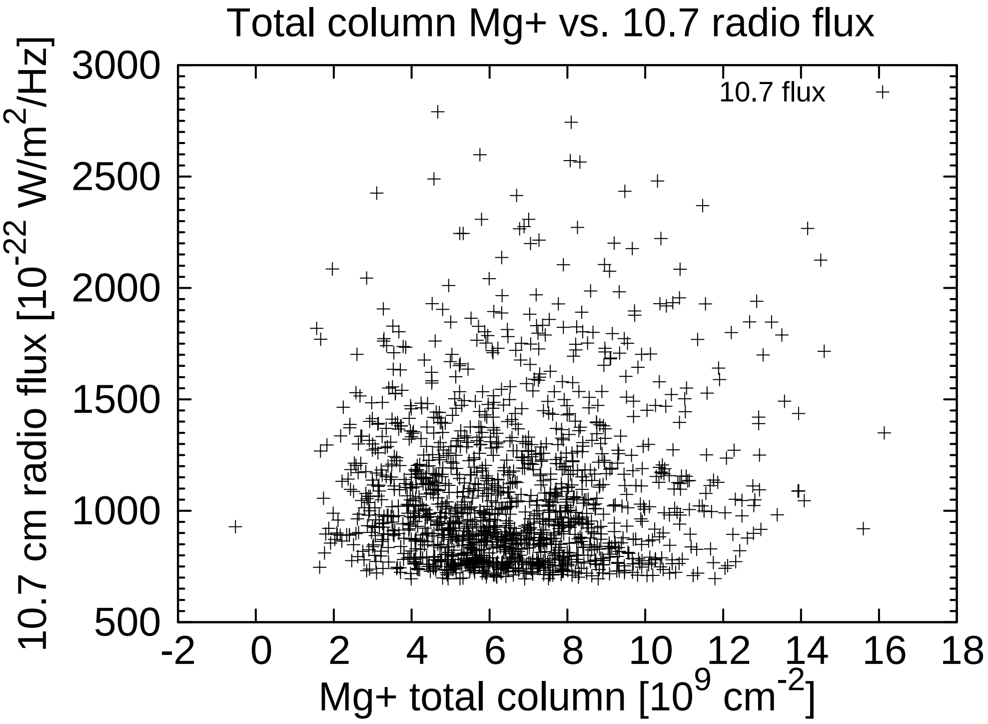

Figure 10.8: Mg^+ content and proton flux for energies > 1 MeV. Note that the abscissa axis is now given in linear scale. The correlation coefficient is $r \approx 0.67$, indicating a weak linear correlation.

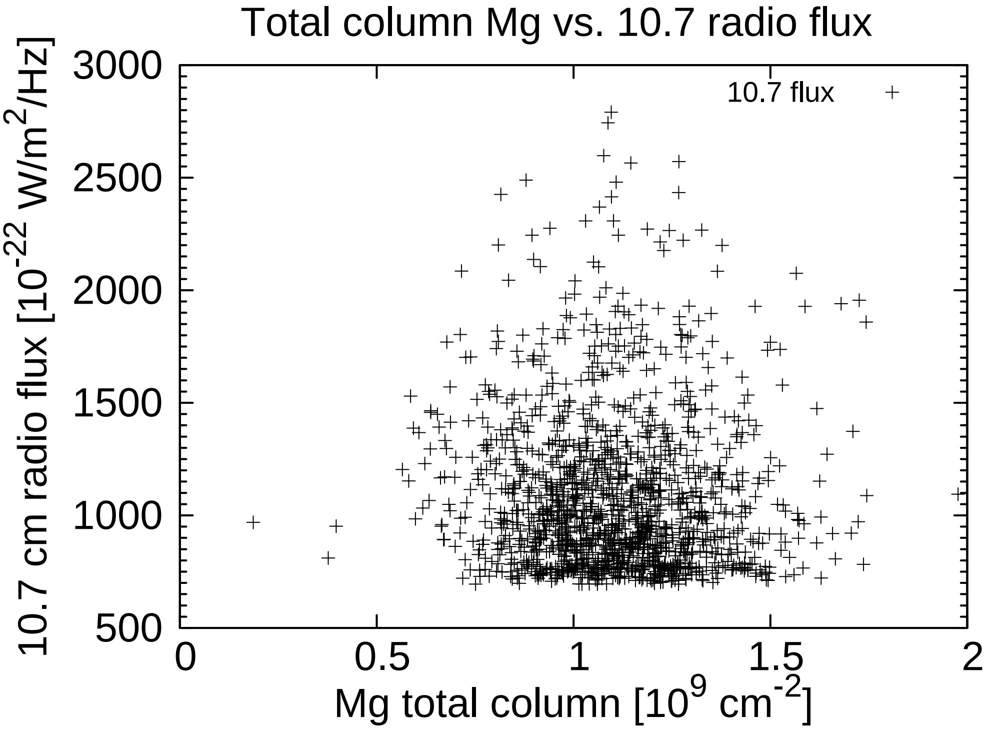

Figure 10.9: Mg content and proton flux for energies > 1 MeV. Note that the abscissa axis is now given in linear scale. The correlation coefficient is $r \approx 0.51$, indicating a very weak linear correlation.

Mg^+ and Mg between 92 and 120 km are found to be approximately 0.7, indicating a moderate linear correlation. Above 120 km, correlation indices of Mg^+ and Mg decrease to values of 0.3 – 0.4 again. Note that the correlation profiles are relatively independent from the latitude band. The general shape and the magnitudes are identical for all five categories.

These results are consistent with those of Minschwaner et al. (2004). Measurements carried out in 1999 by the ISAAC (Ionospheric Spectroscopy And Atmospheric Chemistry) instrument onboard the ARGOS satellite as presented by Minschwaner et al. (2004) suggest similar correlation indices. The ISAAC measurements provided a correlation index of $r = 0.62$ between the Mg^+ total thermospheric column along the limb line-of-sight at 102 km tangent altitude and the solar soft X-ray flux between 2 and 7 nm. The correlation between the Lyman-α flux and the Mg^+ slant column density was found to be maximal at 120 km with $r = 0.71$.

10.3 Conclusions

No significant correlation between the solar activity and the Mg^+/Mg abundance in the upper atmosphere has been found. It should be noted, however, that only a small part of the 11-year solar cycle is covered by the SCIAMACHY measurements. The mission started in 2002, at the maximum of solar cycle no. 23. The latest measurement available for this work was done in April 2007, just before the next minimum in June 2007. Thus, not even a complete cycle is covered. What can be concluded from the investigations carried out in Sections 10.1 and 10.2 is that variations on small time scales of five to six years do not affect the magnesium total content.

The absence of a strong correlation between the solar proton flux and the Mg^+ content does not contradict the findings presented in Section 11. There, observations made during a Solar Proton Event exhibiting a significant increase of both magnesium species are presented. As a result of the extreme nature of Solar Proton events with respect to particle fluxes and impacts on the thermosphere, mesosphere and stratosphere in general, periods of strong proton fluxes such as in October/November 2003 may still affect the magnesium content and distribution in the upper atmosphere.

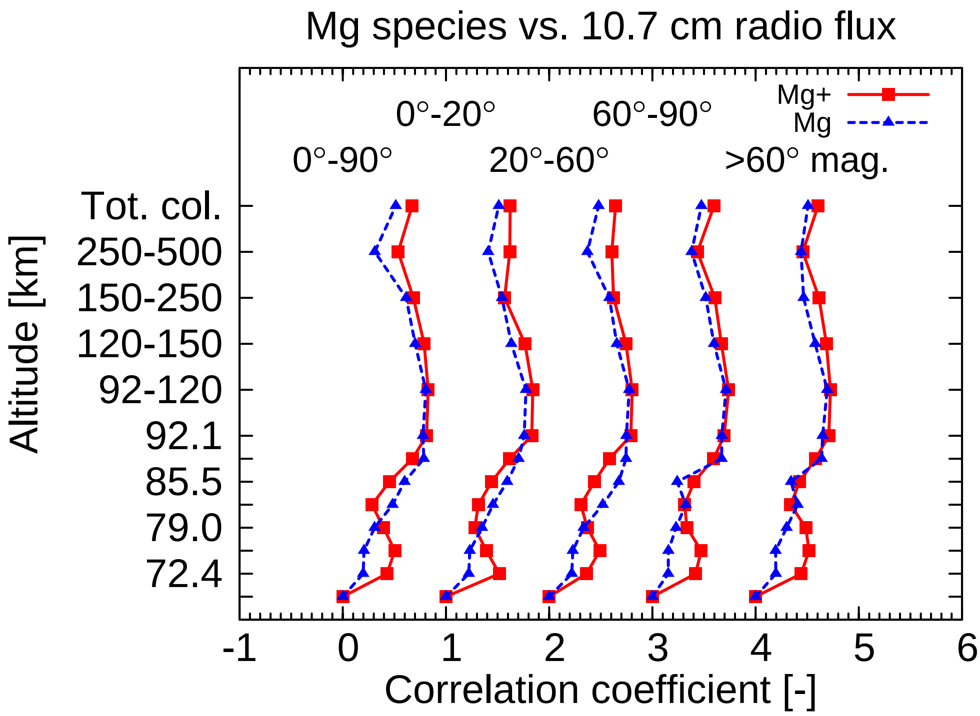

Figure 10.10: Correlation indices for Mg^+ (solid, squares) and Mg (dashes, triangles) contents at different altitudes and the solar radio flux at 10.7 cm. Curves are shifted as in Figure 10.5. The correlation indices for both species are maximal between 92 and 120 km. A secondary maximum is present for Mg^+ around 75 km.

11 Solar proton events and upper atmosphere magnesium

Upper atmosphere chemistry and physics are strongly influenced by the solar radiation as well as particle fluxes from the Sun. This section describes the impact of a strong outburst of solar proton flux in October 2003 on the chemistry and physics of mesospheric and thermospheric magnesium.

The activity of the Sun is varying to a great extend. The intensity of electromagnetic radiation as well as particle fluxes undergo both periodic and sporadic changes. The most prominent periodic variation is the 11-year solar cycle. This term corresponds to a general change of solar activity. In times of high solar activity, the emitted radiation is up to 30% more intense compared to times of quiet Sun. This figure holds for the extreme UV wavelength range. For visible and infrared radiation, the average intensity of radiation is more stable, changes are below 1%. Currently, the Sun is approaching the next minimum of the solar cycle in June 2007. A possible proxy for the solar activity is the MgII index derived from the intensity of radiation at the 280 nm Mg^+ emission line originating in the corona, the solar atmosphere. The MgII index is a dimensionless quantity, calculated from the emission line center and the background intensity measured around 280 nm. See Weber (1999) for a detailed description of the MgII index calculation. Long term time series of the solar activity have been compiled utilizing this MgII index measured by a number of instruments (Viereck and Puga, 1999).

During times of high solar activity, strong short-lived particle outbursts occur more frequently. These outbursts are thought to be a originating from strong solar flares or coronal mass ejections (CME's). As a result of vast perturbations and reconfigurations of the magnetic field of the Sun, ionized particles are accelerated towards outer space. The main constituents of these particle fluxes are energetic protons, though energetic electrons and heavier nuclei such as ionized helium species may accompany the protons. However, it is assumed that the atmospheric impact of these solar phenomena is mainly a result of the flux of energetic protons. The particles exhibit energies reaching from tens of keV to several MeV. Thus, these particle bursts are often called *Solar Proton Event (SPE).*

If directed towards the Earth, severe disturbances for society and technology may appear. Satellite platforms have to be shut down to protect the internal electronics, intercontinental communication is influenced as a result of high atmosphere disturbances in electron and ion density. Large SPE's may cause perturbations in the D-region of the Earth's ionosphere at 50 – 60 km.

Particles form the Sun impact the Earth atmosphere mainly within the polar cap regions, i.e. regions of geomagnetic latitude higher than ±60° . This is a result of the guiding of the particles by the magnetic field lines of the Earth magnetic field. The high-energetic fraction of these particles has enough energy to penetrate the atmosphere down to the upper and middle atmosphere, i.e. the stratosphere and mesosphere. Chemical interactions result in increased production of both HO_x (H,OH, HO_2) and NO_y (NO, NO_2, NO_3 and others) species (Kazeminejad et al., 2006). These species eventually lead to ozone depletion (see e.g. Jackman et al. (2005)).

Shortly after the last maximum of the solar cycle in 2002, the Earth encountered a strong Solar Proton Event (SPE) in October 2003. The 2003 SPE started on October 28 and lasted until October 30. The maximum occurred on October 29. Another event – about an order of magnitude smaller with respect to the particle fluxes – occurred shortly after, with a maximum on November 3. Both maxima are clearly visible in Figure 11.1, depicting the proton flux as measured in 2003 by the GOES-11 satellite instrument. The October 29 increase in proton

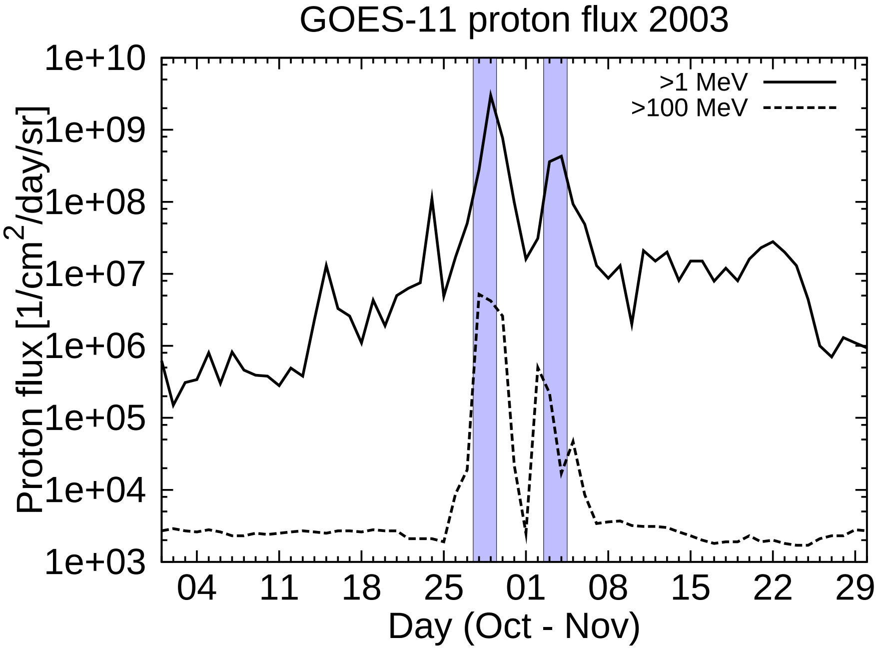

Figure 11.1: The GOES 11 proton flux measurements for October and November 2003. The solid line corresponds to proton energies > 1 MeV. The flux of these particles increases by a factor of $100 - 1000$ within few days. The increase in high energetic protons (energies > 100 MeV) is four to five orders of magnitude. Both proton fluxes exhibit two distinct maxima on October 29 and November 3/4. The high-energetic protons exhibit a maximum on November 3, whereas the low-energetic particle flux is maximal on November 4. These energy bins have been chosen such that the particles deposit the bulk of their energy in the mesosphere and lower thermosphere (1 MeV) respectively the upper stratosphere (100 MeV).

flux is clearly visible. Fluxes in both proton energy regimes shown here increase by two to three orders of magnitude. It should be noted that the bulk of the low-energetic protons of 1 MeV deposit their energy at altitudes between 85 and 90 km, whereas the energy loss of the high-energetic protons is confined to altitudes below 60 km.

11.1 Observations

11.1.1 Global view - all latitudes, $0° \leq |\varphi| \leq 90°$

On a global scale, the effect of the October 29 SPE is clearly visible in the total content of both Mg^+ and Mg, see Figure 11.2. Both Mg^+ as well as Mg show high abundances during the time of the October 29 event. The increase is especially pronounced in the neutral magnesium column. The total column content is increased by a factor of four compared to the average column content during October and November. The variation in Mg^+ during 'quiet' times (i.e. times without strong proton fluxes) is larger, however. Values of Mg^+ column content vary between $2 \cdot 10^9$ and 10^{10} cm^{-2} between October 1 and October 26 respectively November 6 and November 30. The maximum column density of approximately $1.3 \cdot 10^{10}$ cm^{-2} is observed during the October 29 event, though.

The November 3/4 event is not visible in the total content data, however. Both Mg and Mg^+ values decrease between November 3 and 4. Both species show increased values at November 5. However, in case of neutral magnesium, the error is rather large compared to the absolute value, thus the increase is not considered significant. The increase in Mg^+ is significant, but does not exceed the usual variation during the two months considered.

Higher abundances of both Mg species occur in particular at low altitudes, i.e. below 100 km, see Figures 11.3 and 11.5, 11.6. Within the altitude range from 70 to 85 km, neutral Mg increases to values of 200 cm^{-3} on October 29. This a factor of 5 more compared to the average values in October and November ($\approx$ 40 cm^{-3}). Singly ionized magnesium is more abundant below 85 km as well. Absolute values do not exceed 250 cm^{-3} , though. A strong increase in Mg^+ occurs at altitude 89 km, where a pronounced peak is observed during October 29. This peak is neither present one day before nor one day after. Significantly increased values at very high altitudes of approximately 400 km are observed on October 29 as well as October 28 and October 30. The Mg^+ number densities at 400 km reach approximately 400 cm^{-3} on October 28 – 30. This is a factor of three to four more than the average values of October ($\approx$ 80 cm^{-3}) and November ($\approx$ 110 cm^{-3}).

Though the total content is not significantly increased during the November 3/4 event, increased Mg values at altitudes between 70 and 85 km are observed, see Figure 11.7. The absolute values are lower than on October 29, though. Concentrations of Mg^+ are increased significantly at altitudes around 100 km. However, no increase at 89 km is observed. High altitude values of neither Mg nor Mg^+ are increased significantly.

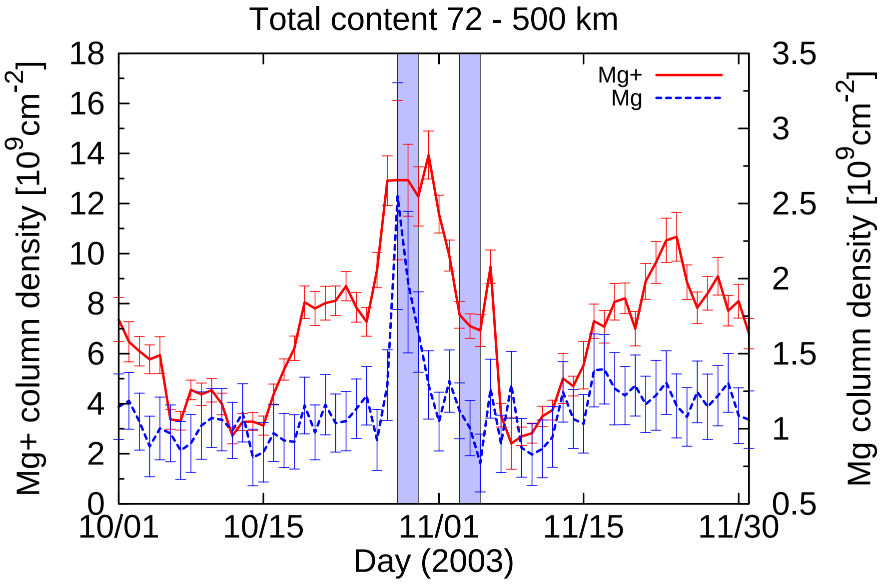

Figure 11.2: Total column amount of Mg^+ (solid) and Mg (dashed) seen during October and November 2003 **averaged from 90°S – 90°N geographical latitude and all longitudes.** Blue strips refer to the first and second SPE under consideration, i.e. the time periods October 28 – 30 respectively November 3 – 5. Maximum proton fluxes occurred on October 29 and November 4, see Figure 11.1. Significantly increased total column contents of both Mg species are observed on October 29, these constitute the maximum values during October and November 2003. On November 6, however, increased column amounts of Mg^+ are observed.

11.1.2 Tropics, $0^\circ \leq |\varphi| \leq 20^\circ$

The total content of neither Mg nor Mg^+ shows a significant change during the October 29 event in the tropical regions, see Figures 11.8, 11.9 and 11.10. Magnesium concentrations at altitudes between 70 and 120 km are increased on October 29, though. As can be seen from Figure 11.5, the neutral Mg peak abundance is approximately 150 cm^{-3} , this is a factor of four more than the average value below 100 km ($\approx$ 40 cm^{-3}). Significantly increased values between 70 and 120 km are observed at all three days of the event. Singly ionized magnesium values are increased at low altitudes as well. Around 120 km, only a slight increase is observed, though. High altitude values of Mg and Mg^+ do not change significantly. A slight increase in Mg^+ at approximately 400 km occurs on October 30, compare Figure 11.6.

On November 3/4, the Mg^+ concentration below 100 km is not significantly different from the October and November average (Figures 11.7, 11.3 and 11.3). The neutral Mg values are increased, however. Peak concentrations of $\approx$ 200 cm^{-3} occur at low altitudes around 73 km. Higher values compared to the October an November average are present at altitudes up to 120 km.

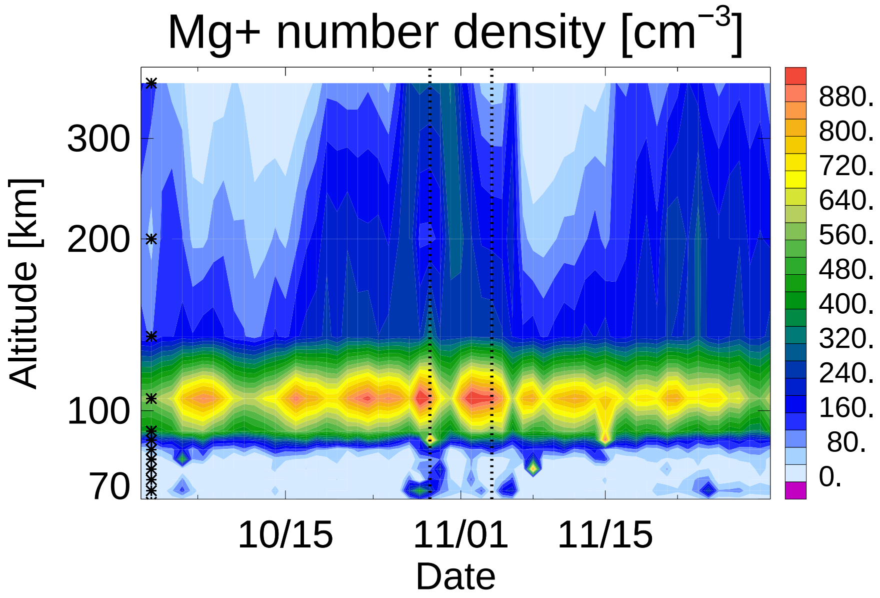

Figure 11.3: Average vertical distribution of Mg^+ during October and November 2003 **averaged from 90°S – 90°N geographical latitude and all longitudes.** Asterisks on the left denote the center altitudes of the retrieval pixel grid, see Section 6.3.3. Increased values occur primarily at low altitudes below 120 km. A short-lived layer of Mg^+ is observed at approximately 89 km altitude on October 29.

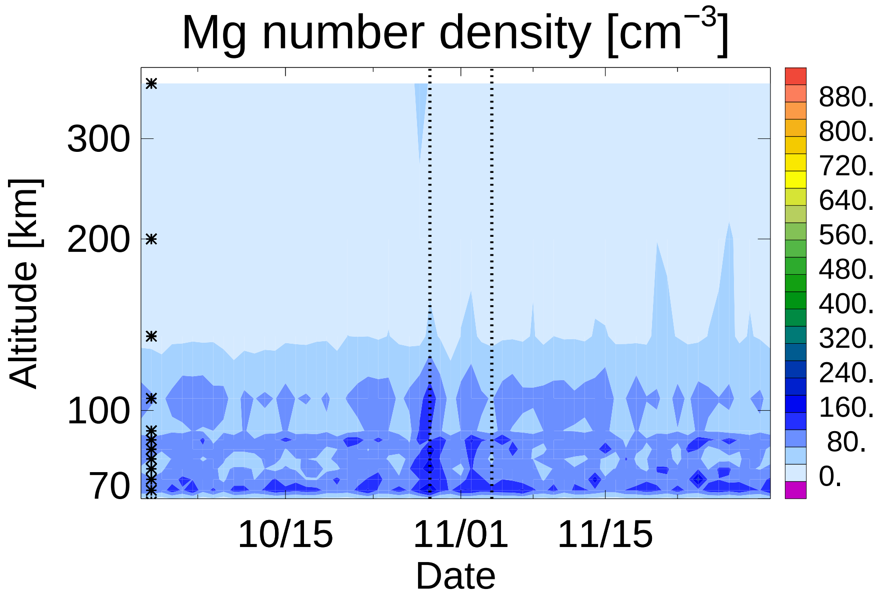

Figure 11.4: Average vertical distribution of Mg during October and November 2003 **averaged from 90°S – 90°N geographical latitude and all longitudes.** Asterisks on the left denote the center altitudes of the retrieval pixel grid, see Section 6.3.3. Increased values of neutral Mg are observed at all altitudes up to 120 km during the first event.

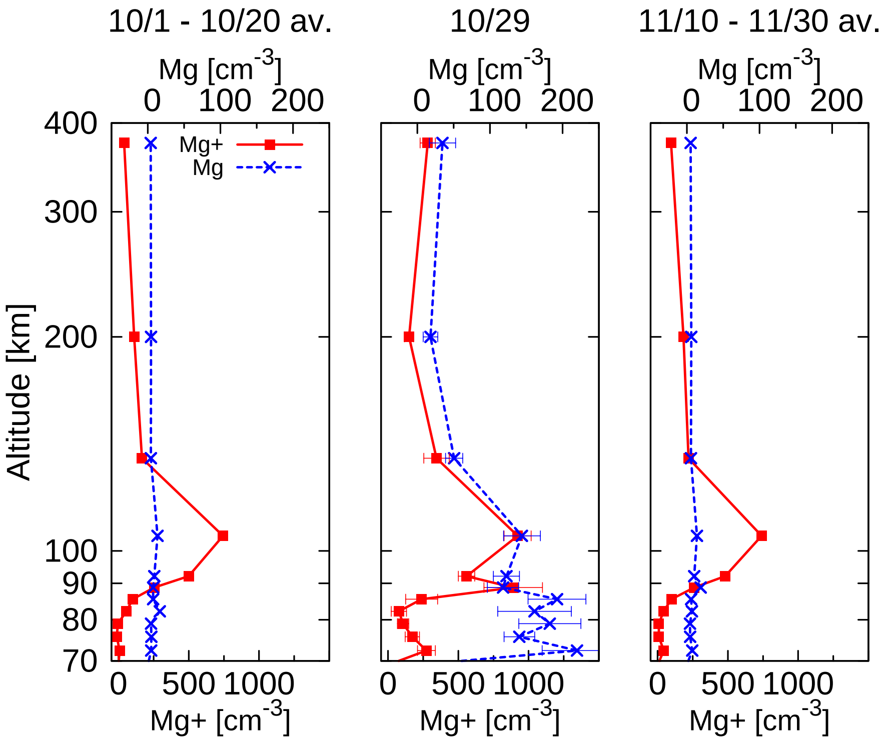

Figure 11.5: Average vertical profiles of Mg^+ (solid) and Mg (dashed) during October 10 – 20, October 29 and November 10 – 20, **averaged from 90°S – 90°N geographical latitude and all longitudes.** A pronounced layer of Mg^+ occurs on October 29 at an altitude of 89 km. Vertical profiles of both Mg^+ and Mg are increased during the solar proton event below 100 km.

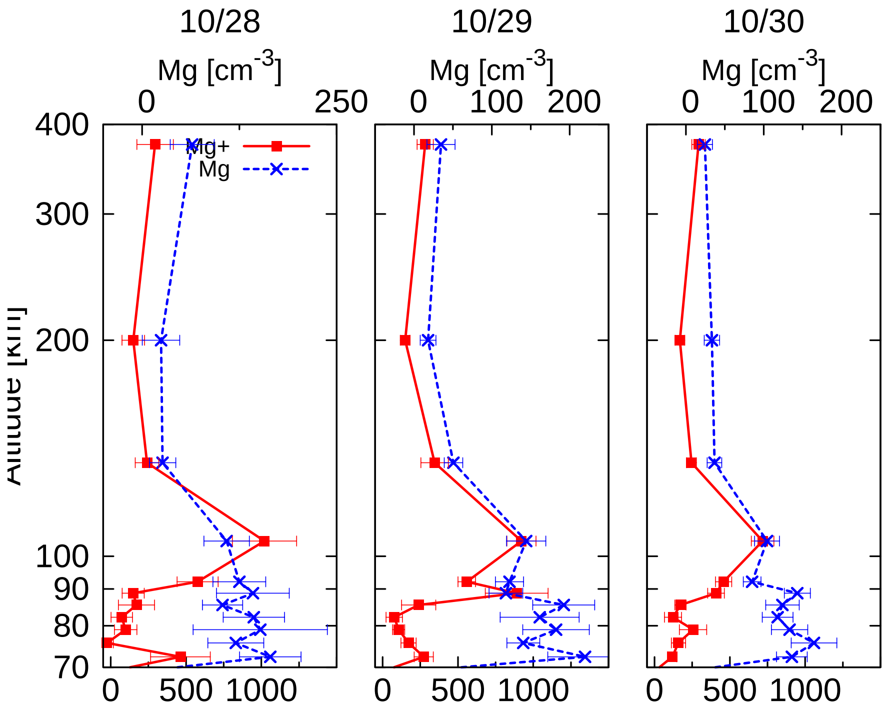

Figure 11.6: Daily average vertical profiles of Mg^+ (solid) and Mg (dashed) during October 28 – 30, **averaged from 90°S – 90°N geographical latitude and all longitudes.** A pronounced short-lived layer of Mg^+ at 89 km altitude is observed on October 29. Maximum values of both species at 400 km altitude are observed on October 28.

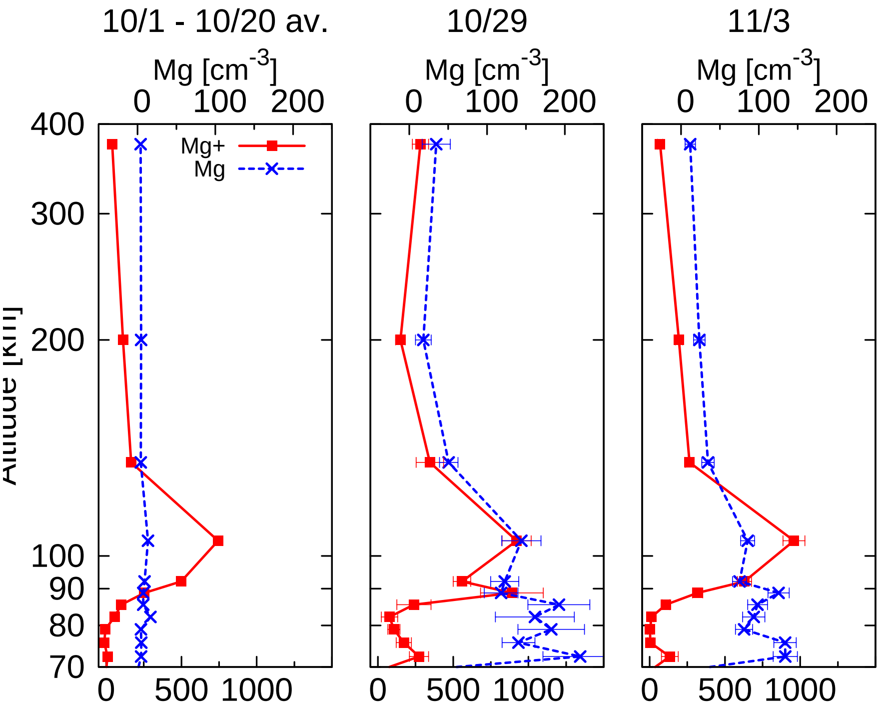

Figure 11.7: Average vertical profiles of Mg$^+$ (solid) and Mg (dashed) during October 29, and daily average profiles on October 29 and November 3, **averaged from 90°S – 90°N geographical latitude and all longitudes.** Singly ionized magnesium is only slightly affected at November 3, neutral Mg, however, shows increased number densities at all altitudes. Largest deviations from the average profile of Mg occur below 120 km.

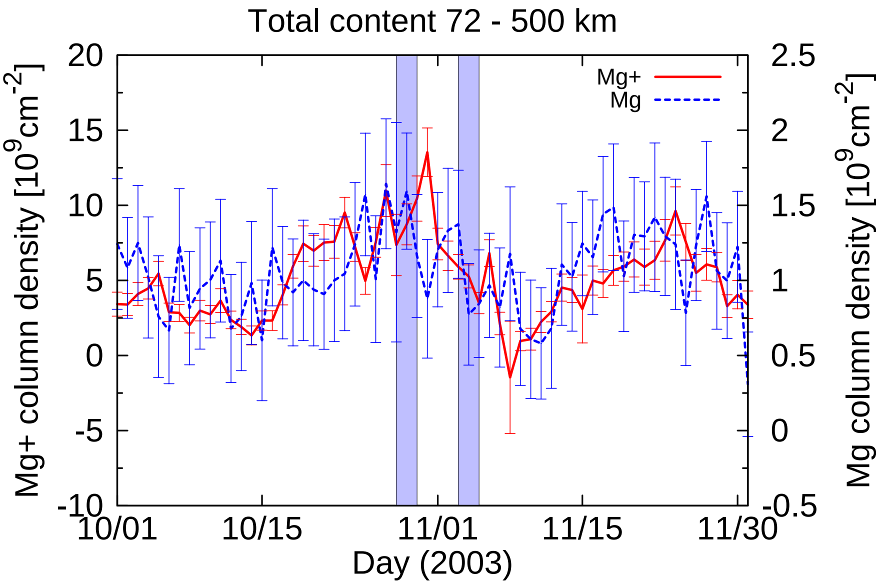

Figure 11.8: Total column densities of Mg$^+$ (solid) and Mg (dashed) during October and November 2003 **zonally averaged from 20°S – 20°N geographical latitude.** Blue strips refer to the first and second SPE under consideration, i.e. the time periods October 28 – 30 respectively November 3 – 5. Maximum proton fluxes occurred on October 29 and November 3, see Figure 11.1. Neither Mg$^+$ nor Mg is significantly affected on October 29 or November 3. However, on November 6, slightly increased column amounts of Mg$^+$ are observed.

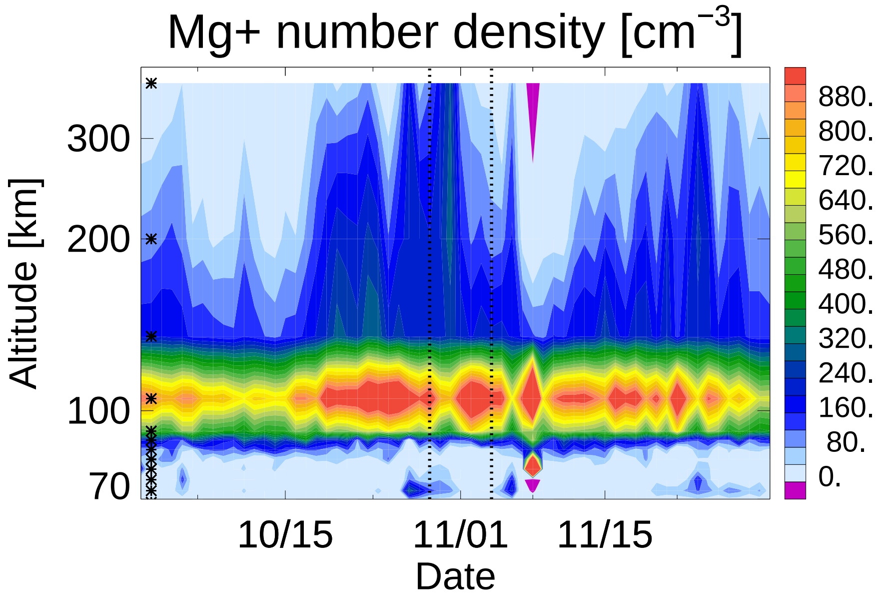

Figure 11.9: Average vertical distribution of Mg$^+$ during October and November 2003 **zonally averaged from 20°S – 20°N geographical latitude.** Asterisks on the left denote the center altitudes of the retrieval pixel grid, see Section 6.3.3. Slightly increased values of Mg$^+$ are observed on October 28/29 at low altitudes around 75 km.

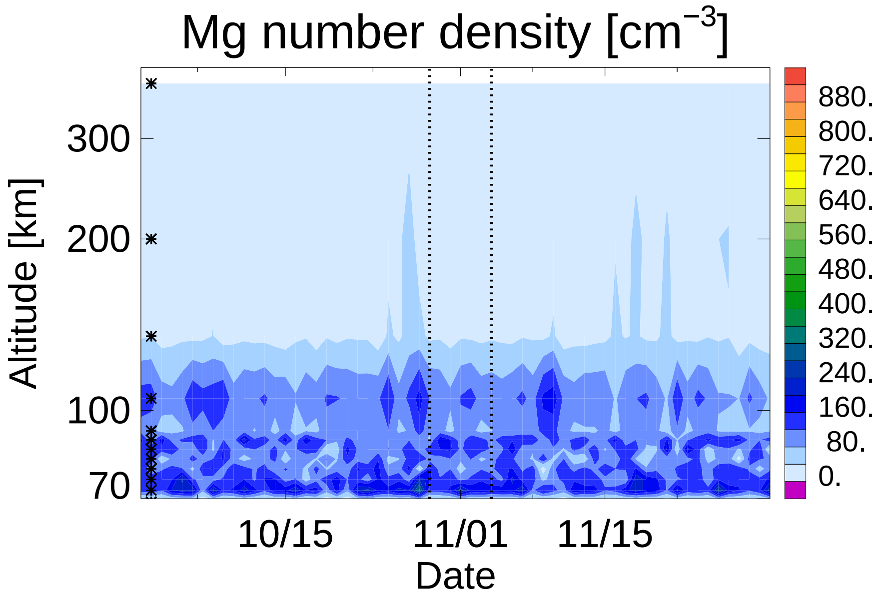

Figure 11.10: Average vertical distribution of Mg during October and November 2003 **zonally averaged from 20°S – 20°N geographical latitude.** Asterisks on the left denote the center altitudes of the retrieval pixel grid, see Section 6.3.3. Magnesium is only slightly affected at low altitudes around 75 km.

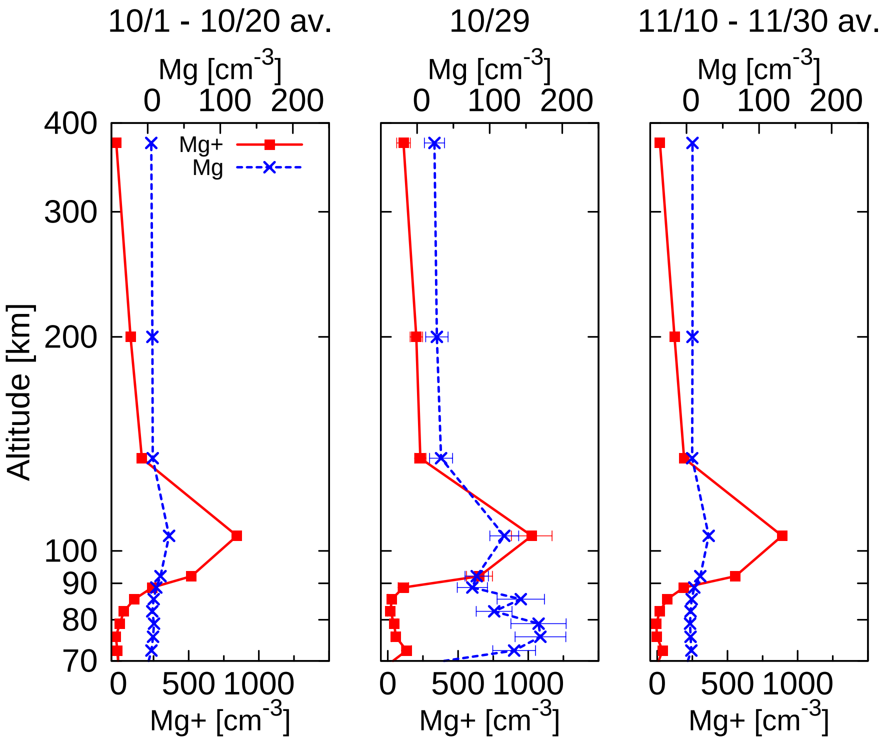

Figure 11.11: Average vertical profiles of Mg$^+$ (solid) and Mg (dashed) during October 10 – 20, October 29 and November 10 – 20, **zonally averaged from 20°S – 20°N geographical latitude.**Mg$^+$ is only slightly affected and shows increased number densities at approximately 75 km. Neutral Mg is increased significantly below 150 km.

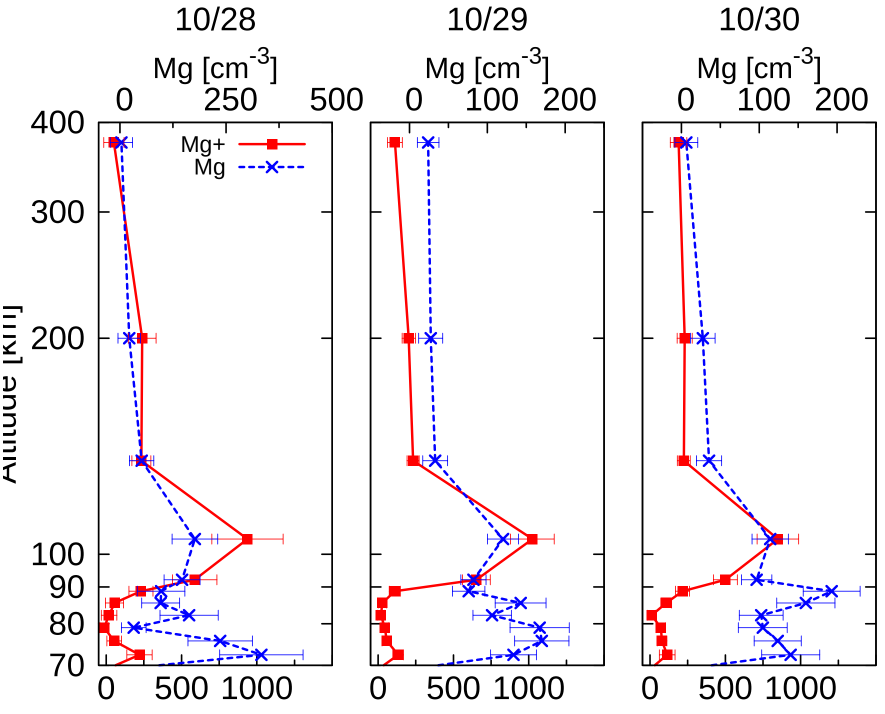

Figure 11.12: Daily average vertical profiles of Mg$^+$ (solid) and Mg (dashed) during October 28 – 30, **zonally averaged from 20°S – 20°N geographical latitude.** Mg$^+$ shows slightly increased concentrations compared to the October and November averages on all three days of the event. The Mg profiles is affected at all three days.

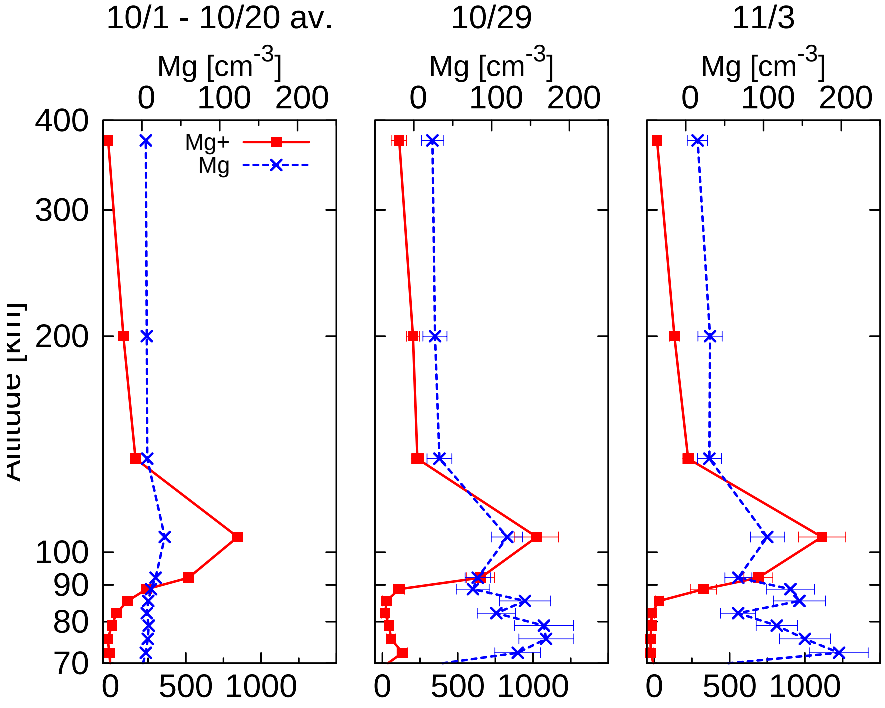

Figure 11.13: Average vertical profiles of Mg^+ (solid) and Mg (dashed) during October 29, and daily average profiles on October 29 and November 3/4, **zonally averaged from 20°S – 20°N geographical latitude.** The Mg^+ profiles of November 3 deviates from the October average profile at mid altitudes between 90 and 120 km. Neutral Mg is increased during both events, however.

11.1.3 Mid latitudes, $20^\circ < |\varphi| \leq 60^\circ$

Neutral magnesium is significantly increased on all three days of the October event at all altitudes below 150 km, see Figures 11.17 and 11.18. Maximum absolute values peak at 250 cm^{-3} . The Mg^+ does not show significantly increased values around 120 km during the October 29 event. Values are increased at approximately 400 km and below 100 km, though. Maximum gain is present at 89 km, Mg^+ values increase from approximately 250 cm^{-3} (October and November average) to ≈ 1200 cm^{-3} (Figure 11.17) .

Increased values of Mg^+ at high altitudes are observed two days after October 29. Maximum 400 km values of Mg^+ occur on October 31, see Figure 11.15. The same behaviour is observed in the total column (Figure 11.14). Maximum abundance of Mg^+ as well as Mg is present on October , 31. The Mg peak is not significant with respect to the total error, though.

The November 3/4 event exhibits slightly increased values of Mg^+ only at very low altitudes of 73 km and around 120 km, see Figure 11.19 and 11.15. No significant increase is observed between 120 and 75 km nor above 150 km. The neutral Mg is increased below 150 km, however (Figures 11.16 and 11.19). This does not contribute significantly to the total column, the corresponding values are increased on November 3. However, the increase is not significant, see Figure 11.14.

11.1.4 Polar regions

Geographic latitudes $60^\circ < |\varphi| \leq 90^\circ$

The strongest impact of the October 2003 SPE on the mesospheric and thermospheric magnesium species is present at polar latitudes (see Figure 11.20 and compare Figures 11.8 and 11.14).

The total content of Mg^+ and Mg exhibits a pronounced increase during October 28 and October 29. Values are still above the average on October 30. The November 3/4 event does not impact the total column significantly. A slight increase iun the ionic species is observed. See Figure 11.20.

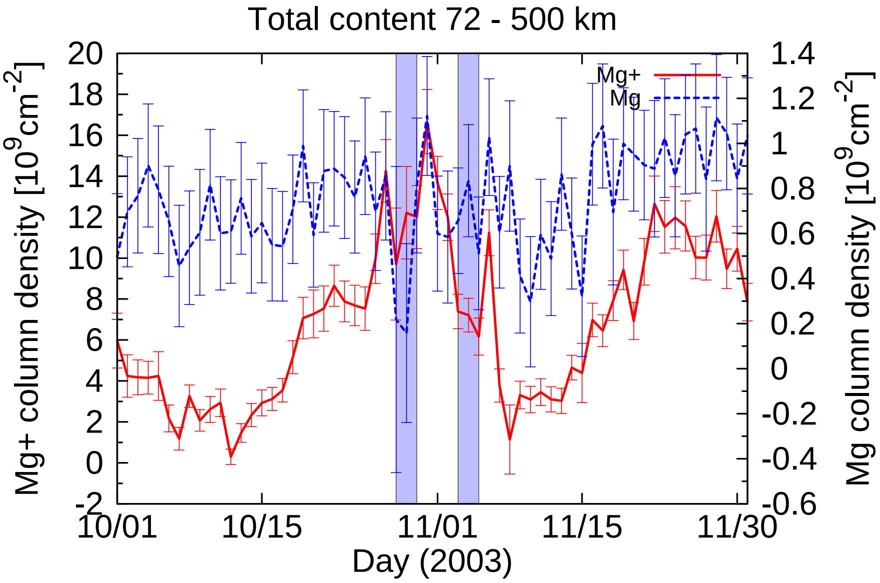

Figure 11.14: Total column densities of Mg$^+$ (solid) and Mg (dashed) during October and November 2003 **averaged from 60°S – 20°S and 20°N – 60°N geographical latitude and all longitudes.** Blue strips refer to the first and second SPE under consideration, i.e. the time periods October 28 – 30 respectively November 3 – 5. Maximum proton fluxes occurred on October 29 and November 3/4, see Figure 11.1. The Mg$^+$ time line exhibits maximum number densities on October 29. The November 3 concentrations are not significantly increased. However, on November 6, more Mg$^+$ is observed. The neutral Mg total content is not affected significantly during neither event.

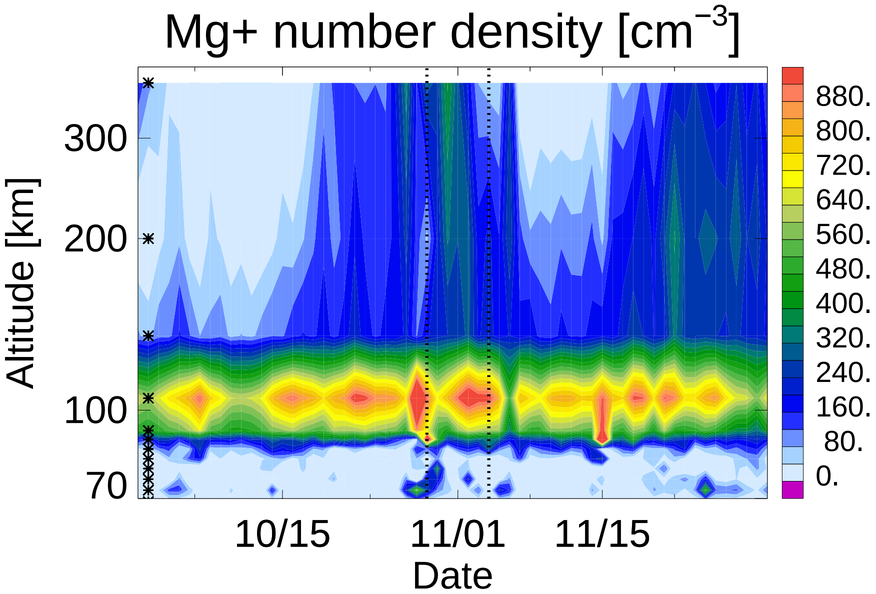

Figure 11.15: Average vertical distribution of Mg$^+$ during October and November 2003 **averaged from 60°S – 20°S and 20°N – 60°N geographical latitude and all longitudes.** Asterisks on the left denote the center altitudes of the retrieval pixel grid, see Section 6.3.3. Increased Mg$^+$ values are observed on October 29 at low altitudes below 120 km and on October 31 at high altitudes around 400 km. Additionally, increased values of Mg$^+$ at 400 km are observed on November 5/6, that is, one to two days after the November 3/4 event.

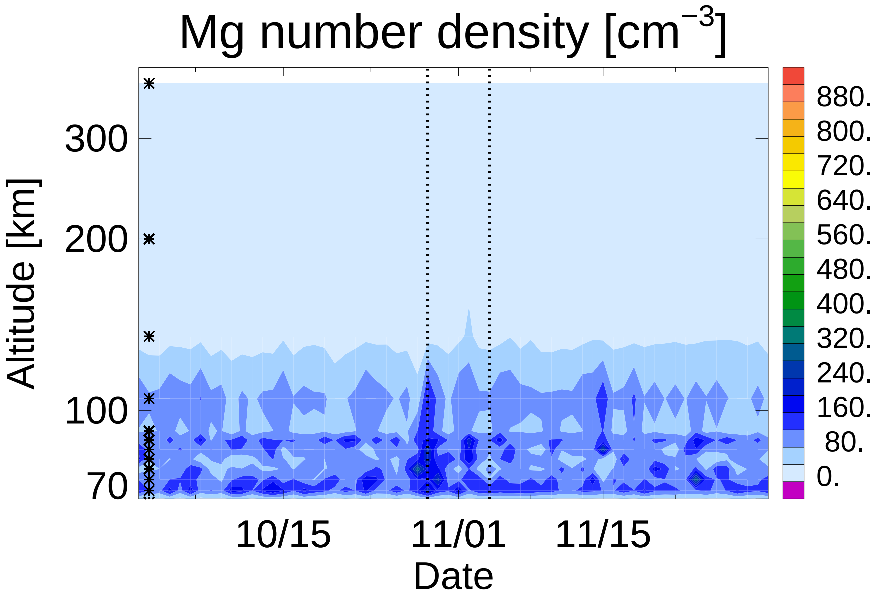

Figure 11.16: Average vertical distribution of Mg during October and November 2003 **averaged from 60°S – 20°S and 20°N – 60°N geographical latitude and all longitudes.** Asterisks on the left denote the center altitudes of the retrieval pixel grid, see Section 6.3.3. Increased neutral Mg concentrations are observed below 150 km on October 29.

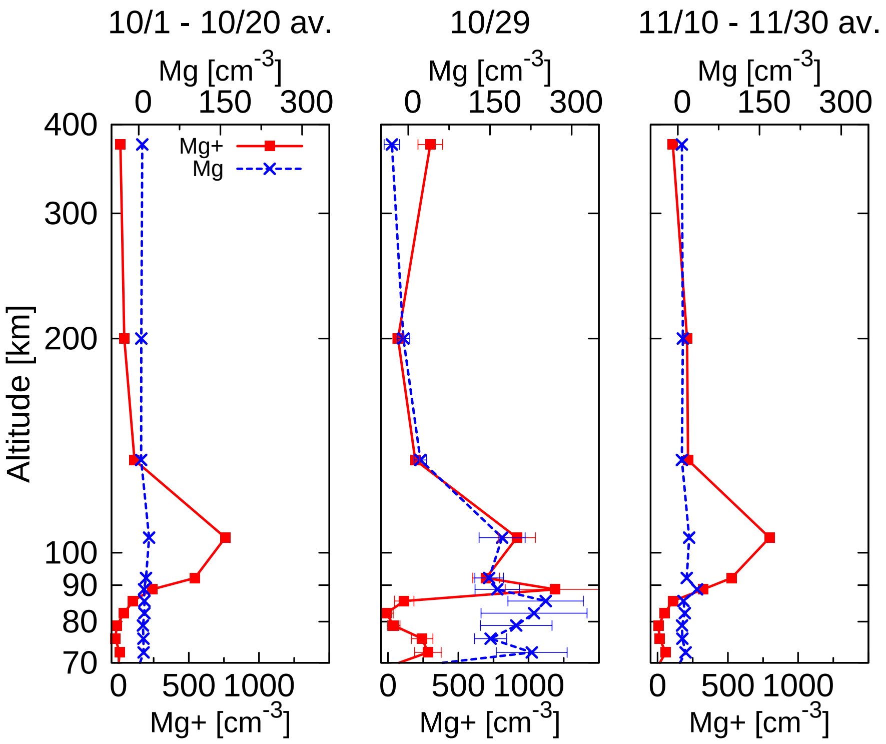

Figure 11.17: Average vertical profiles of Mg^+ (solid) and Mg (dashed) during October 10 – 20, October 29 and November 10 – 20, **averaged from 60°S – 20°S and 20°N – 60°N geographical latitude and all longitudes.** Mg^+ shows significantly increased values at all altitudes. Pronounced layers form around 89 km and between 70 and 80 km. The width of the 89 km layer is smaller than the vertical resolution of the retrieval, i.e. 5 km. The Mg profile is affected primarily below 150 km.

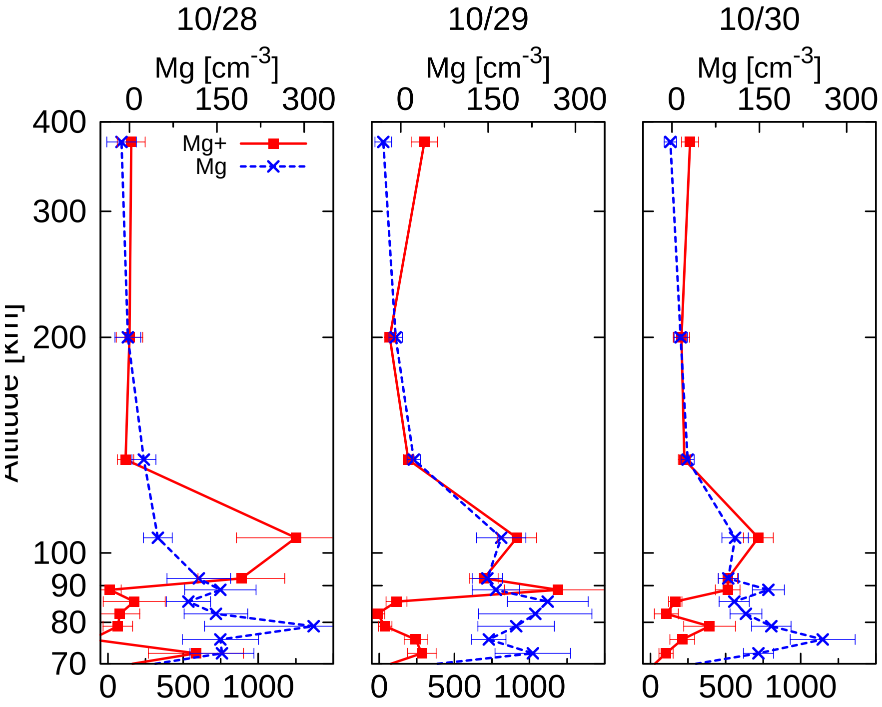

Figure 11.18: Daily average vertical profiles of Mg$^+$ (solid) and Mg (dashed) during October 28 – 30, **averaged from 60°S – 20°S and 20°N – 60°N geographical latitude and all longitudes.** High altitude concentrations (400 km) of Mg$^+$ are increased only on October 29. A 89 km layer of Mg$^+$ occurs solely on October 29. Number densities of neutral Mg are high during all three days of the event, but differ significantly from the October and November averages only at altitudes below 150 km.

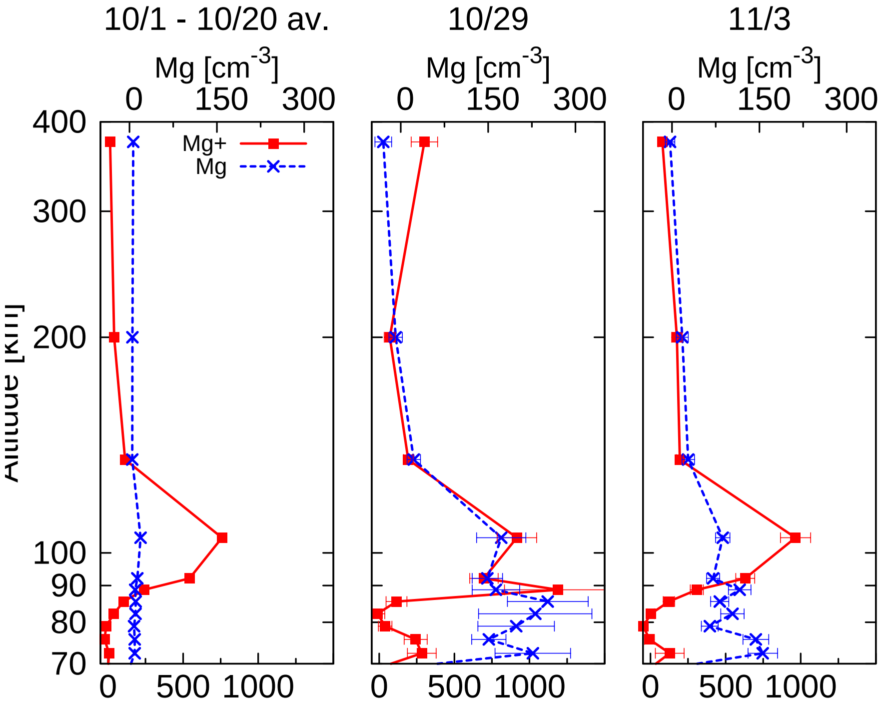

Figure 11.19: Average vertical profiles of Mg$^+$ (solid) and Mg (dashed) during October 29, and daily average profiles on October 29 and November 3, **averaged from 60°S – 20°S and 20°N – 60°N geographical latitude and all longitudes.** The impact of the November 3/4 event on both magnesium species is less compared to the October 29 event. Number densities of Mg$^+$ at high altitudes are not impacted, and the maximum Mg abundances are significantly less than those on October 29.

A strong increase of Mg^+ and neutral Mg is observed on October 29. Below 100 km, maximal Mg^+ values are approximately 750 cm^{-3} , whereas neutral Mg values reach 225 cm^{-3} at very low altitudes around 72 km (Figure 11.23).

A pronounced peak in the Mg^+ profile occurs at altitude 89 km, see Figure 11.23. The maximal number density is $\approx$ 800 cm^{-3} . One day before and after the October 29 event, this layer is not present (Figure 11.24).

Whereas the abundance of neither Mg^+ nor Mg is significantly increased at altitudes between 150 and 400 km, a pronounced increase of both Mg^+ and Mg is present at 400 km. Absolute values are 150 cm^{-3} for Mg and 500 cm^{-3} for Mg^+. This holds for all three days of the event, though neutral Mg at 400 km is already reduced on October 30.

The November 3/4 event shows up in the altitude profile of Mg^+ as well as Mg, see Figure 11.25. Values of both species are increased significantly at altitudes below 150 km, compared to the October and November average profiles. No pronounced Mg^+ layer as observed on October 29 is present, however. A significant increase at 400 km is not observed for neither species.

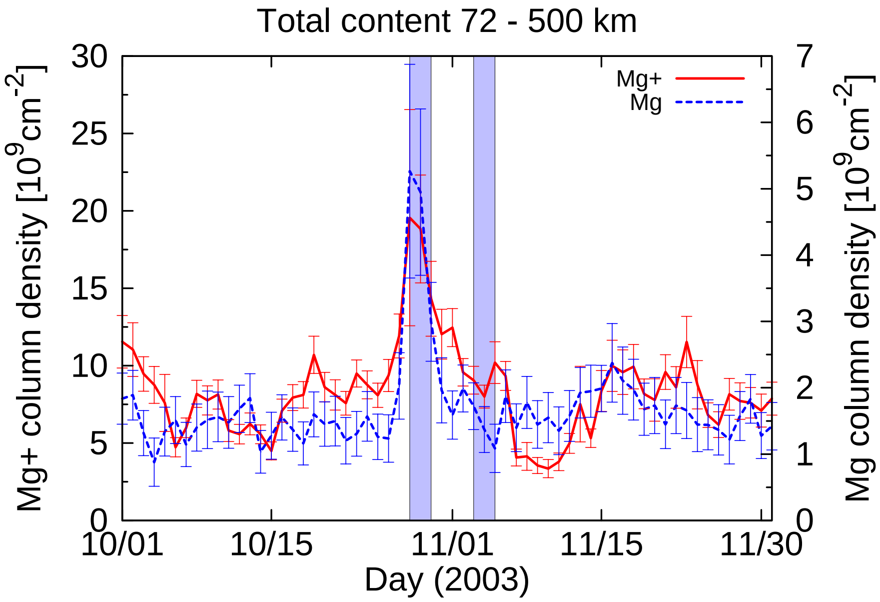

Figure 11.20: Total column densities of Mg^+ (solid) and Mg (dashed) during October and November 2003 **zonally averaged from 90°S – 60°S and 60°N – 90°N geographical latitude.** Blue strips refer to the first and second SPE under consideration, i.e. the time periods October 28 – 30 respectively November 3 – 5. Maximum proton fluxes occurred on October 29 and November 3/4, see Figure 11.1. Both magnesium species exhibit a pronounced isolated total content peak abundance during the October 29 event. The November 3/4 event is not visible in the total content, slightly increased values of both species are observed on November 6.

Geomagnetic latitudes $60° < |\varphi_{\mathbf{magnetic}}| \leq 90°$

The total content of both species is maximal on October 28 (Figure 11.26). The Mg^+ content at that day ($3.2 \cdot 10^{10}$ cm^{-2}) is a factor of three above the October/November average (10^{10} cm^{-2}). The same holds for the neutral Mg total content, this is increasing from a background level of $2 \cdot 10^9$ cm^{-2} to values of $6 \cdot 10^9$ cm^{-2}.

The November 3/4 SPE does not impact the total content of either species significantly (Figure 11.26). Weak effects are observed at low altitudes between 70 and 120 km, see Figure 11.31. The deviations to the October and November averages, however, are smaller than those during the October 29 event.

Mg^+ values are increased at all altitudes (Figures 11.27, 11.28). The 89 km layer of October 29 is broader compared to the other geographical regions (Figures 11.29 and 11.30). Maximal Mg^+ abundances do not occur at 120 km solely anymore. However, an equal abundance is observed at higher altitudes of 150 km.

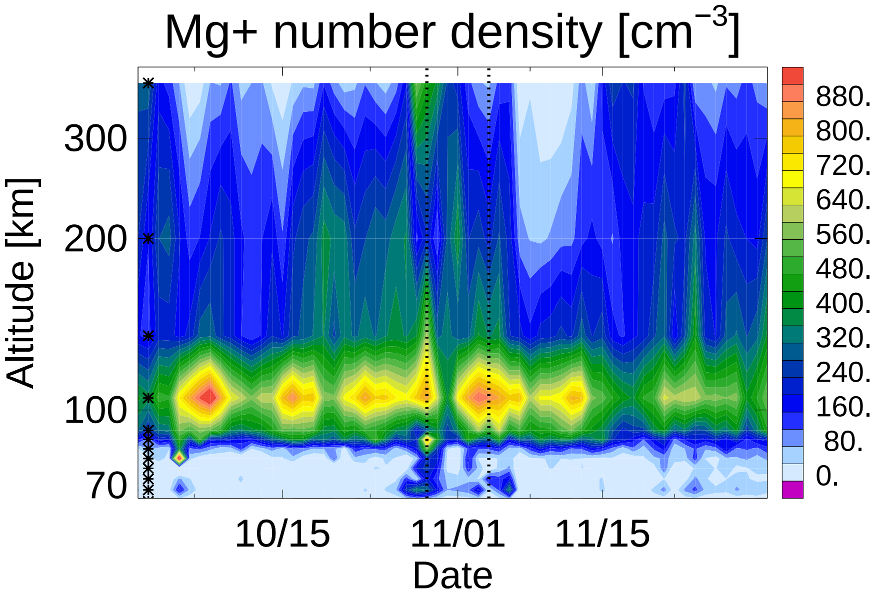

Figure 11.21: Average vertical distribution of Mg^+ during October and November 2003 **zonally averaged from 90°S – 60°S and 60°N – 90°N geographical latitude.** Asterisks on the left denote the center altitudes of the retrieval pixel grid, see Section 6.3.3. Increased values of Mg^+ above 150 km are observed during approximately 10 days before the first solar proton event on October 29. This event is clearly visible in the October 29 profile, Mg^+ exhibits increased values at high and low altitudes. The mid-altitude abundance around 200 km is not affected very much, however. During November 3, Mg^+ is increased only at low altitudes below 150 km.

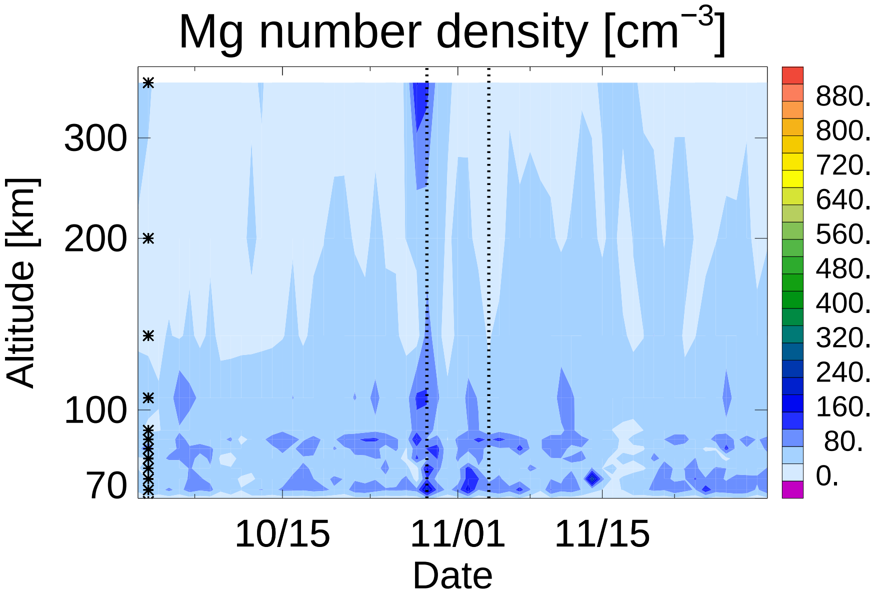

Figure 11.22: Average vertical distribution of Mg during October and November 2003 **zonally averaged from 90°S – 60°S and 60°N – 90°N geographical latitude.** Asterisks on the left denote the center altitudes of the retrieval pixel grid, see Section 6.3.3. Mg^+ is significantly increased at low and very high altitudes. The mid-altitude abundance (150 - 250 km) does not deviate significantly from the October and November average.

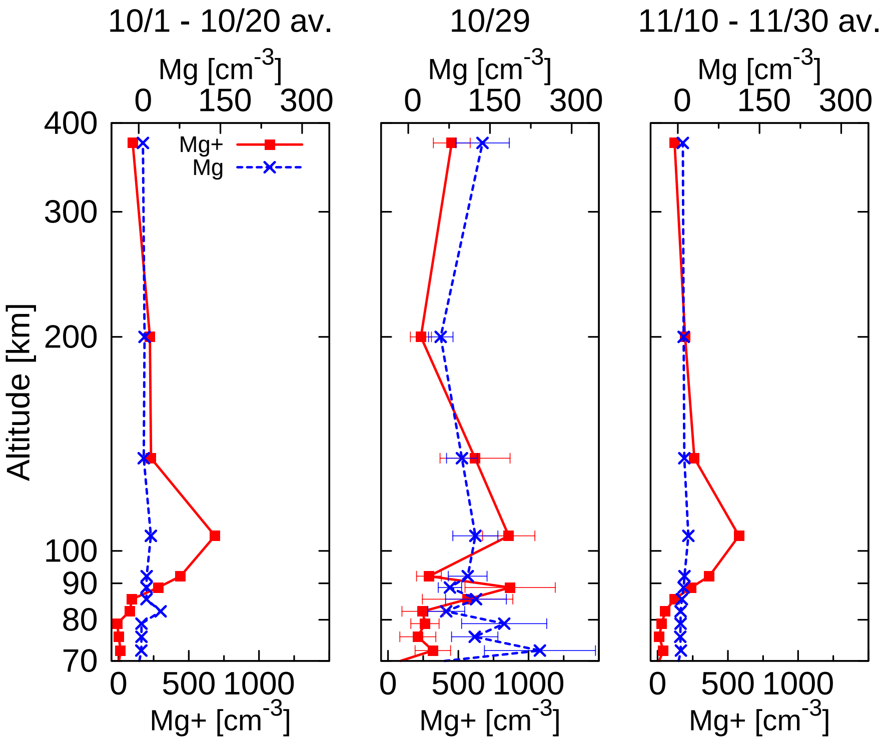

Figure 11.23: Average vertical profiles of Mg$^+$ (solid) and Mg (dashed) during October 10 – 20, October 29 and November 10 – 20, **zonally averaged from 90°S – 60°S and 60°N – 90°N geographical latitude.** Significant increases in Mg$^+$ occur on October 29 at all altitudes except around 200 km. A pronounced layer of Mg$^+$ is formed at 89 km.

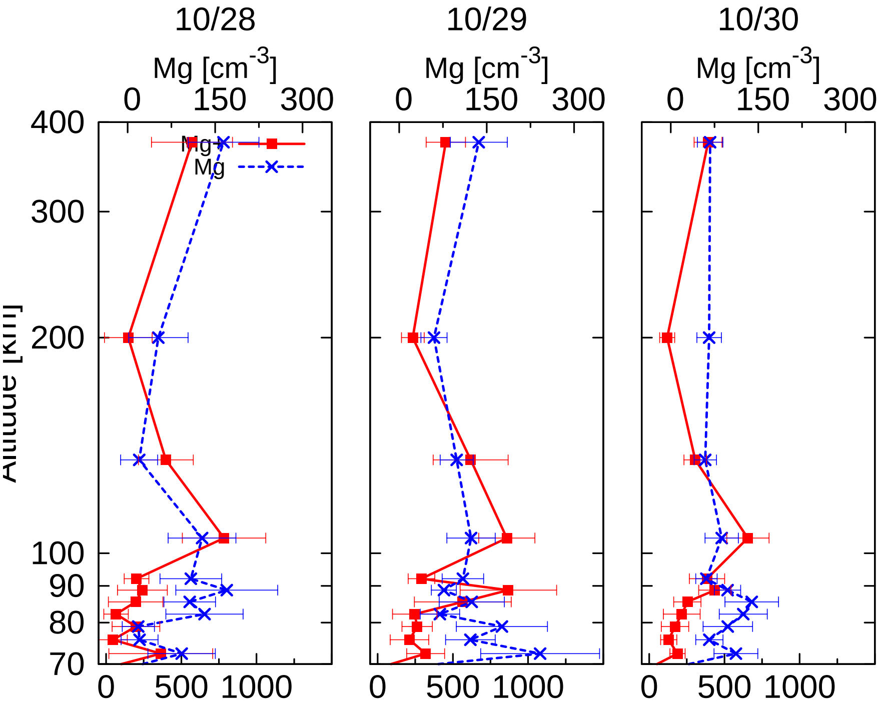

Figure 11.24: Daily average vertical profiles of Mg$^+$ (solid) and Mg (dashed) during October 28 – 30, **zonally averaged from 90°S – 60°S and 60°N – 90°N geographical latitude.** As already noted, the Mg$^+$ layer at 89 km is only observed on October 29. Mg$^+$ values at high altitudes around 400 km are increased during all three days of the event. Neutral Mg is increased at high altitudes around 400 km during the first two days of the event, is decreased on October 30, but remains above the average, though. Maximum values of Mg on October 28 are observed between 80 and 90 km and 400 km.

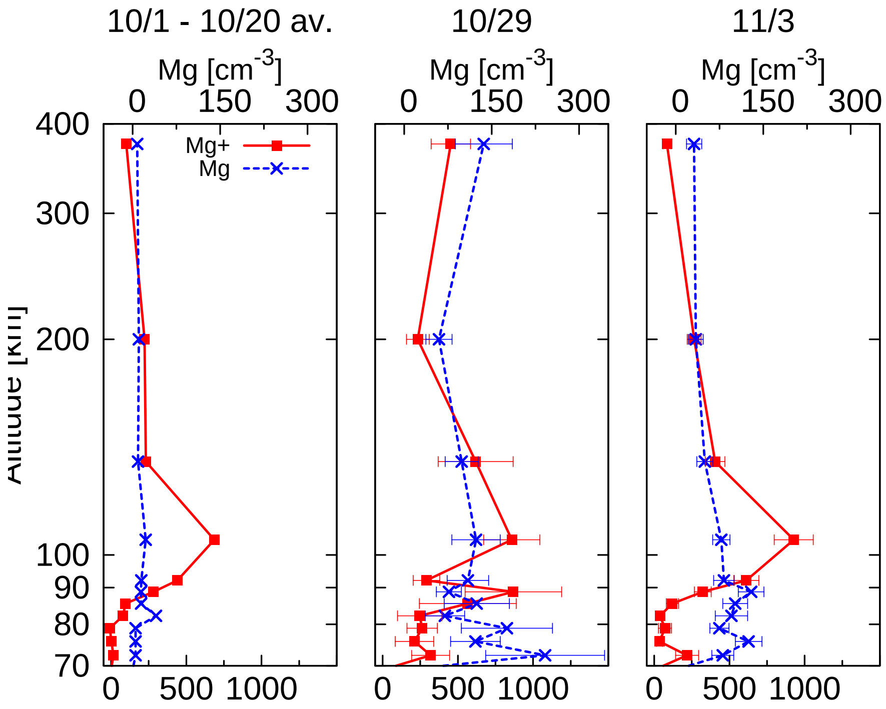

Figure 11.25: Average vertical profiles of Mg$^+$ (solid) and Mg (dashed) during October 29, and daily average profiles on October 29 and November 3, **zonally averaged from 90°S – 60°S and 60°N – 90°N geographical latitude.** The Mg$^+$ profile on November 3 deviates form the October average only at low altitudes between 70 and 80 km and around 120 km. Largest increases are observed at 72 km. Neutral Mg is increased on November 3 compared to the average, not as strong as during the October 29 event, though.

It should be noted that the impact of the SPE on high altitude Mg species is highest on October 28, see Figures 11.27 and 11.28. Values of neutral Mg at 400 km have already dropped to October average values on October 29. The Mg$^+$ concentration at 400 km is still high at that time, though smaller than the October 28 abundance. On October 30, values of Mg$^+$ are back to average as well.

11.1.5 Summary of observations during October/November 2003

Both species show significantly increased values during the October/November 2003 period of intense solar activity and strong particle fluxes. Abundances of neutral Mg are increased by more than a factor of 10 on October 29 at altitudes below 150 km. Increased values are observed at very high altitudes around 400 km as well for all three days of the first SPE. The strongest increase in Mg$^+$ is observed between 89 and 120 km. Values are high for all three days of the first event. On October 29, a pronounced layer of Mg$^+$ is formed around 89 km. The full-width-half maximum of this layer is smaller or equal than the vertical resolution of the retrieval, which is approximately 5 km. This can be seen from the fact that the values at the adjacent altitudes (92 and 86 km) do not differ significantly from the values on October 28 and October 30, where no peak at 89 km is observed.

The total content exhibits increases of both species on October 29. As could be expected, the largest variations compared to the average are observed in polar regions.

The impact of the November 4 SPE on the profiles as well as on the total content is less compared to the October 29 event. It is not clear whether the effects observed on November 4 are a result of the increased proton flux from the sun. It has to be noted that the spatial as well as temporal variability of both Mg species is quite large.

A possible source of systematic error for all observations presented here is a failed normalization of the radiances I (i.e. usage of a wrong solar spectrum). As described in Section 6, the retrieval measurement input is I/F, where I is the measured radiance and F is the solar

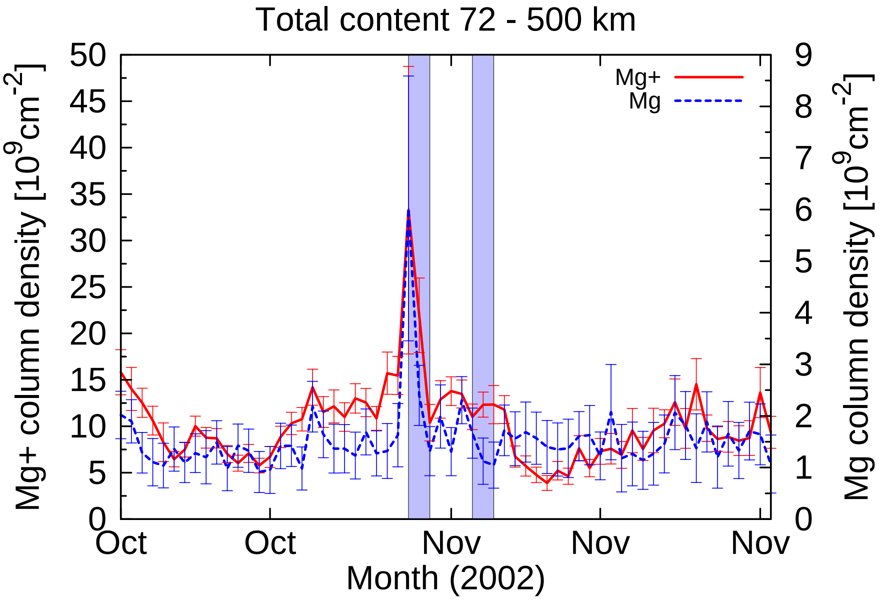

Figure 11.26: Total column densities of Mg^+ (solid) and Mg (dashed) during October and November 2003 **averaged from 60° to 90° geomagnetical latitude and all longitudes.** Blue strips refer to the first and second SPE under consideration, i.e. the time periods October 28 – 30 respectively November 3 – 5. Maximum proton fluxes occurred on October 29 and November 3–4, see Figure 11.1. Both magnesium species exhibit a pronounced isolated total content peak abundance on October 28, one day before the maximum of the particle fluxes on October 29. The November 4 event is not visible in the data, the total content does not change significantly during November 3 – 5.

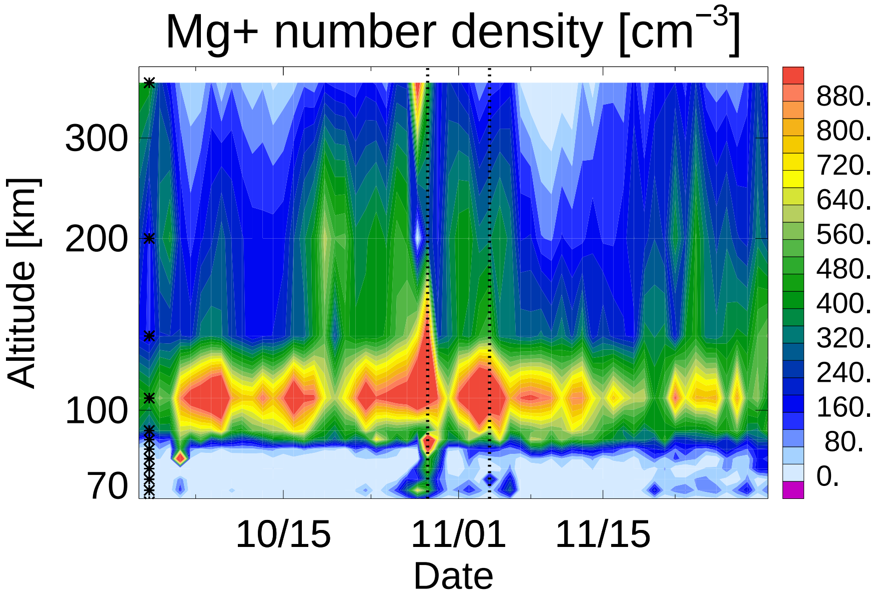

Figure 11.27: Average vertical distribution of Mg^+ during October and November 2003 **averaged from 90°S – 60°S and 60°N – 90°N geomagnetic latitude and all longitudes.** Asterisks on the left denote the center altitudes of the retrieval pixel grid, see Section 6.3.3. Increased values of Mg^+ above 150 km are observed during late October, early November and late November. The October 29 event is clearly visible in the data. However, Mg^+ exhibits maximal values around 400 km already on October 28, one day before the maximum of the particle flux (see Figure 11.1). The October 29 Mg^+ abundance at 400 km is lower than on October 28. Increased values below 120 km occur on October 28 (around 72 km) and October 29 (between 70 and 120 km). On November 3, Mg^+ is increased only at mid altitudes between 120 and 250 km.

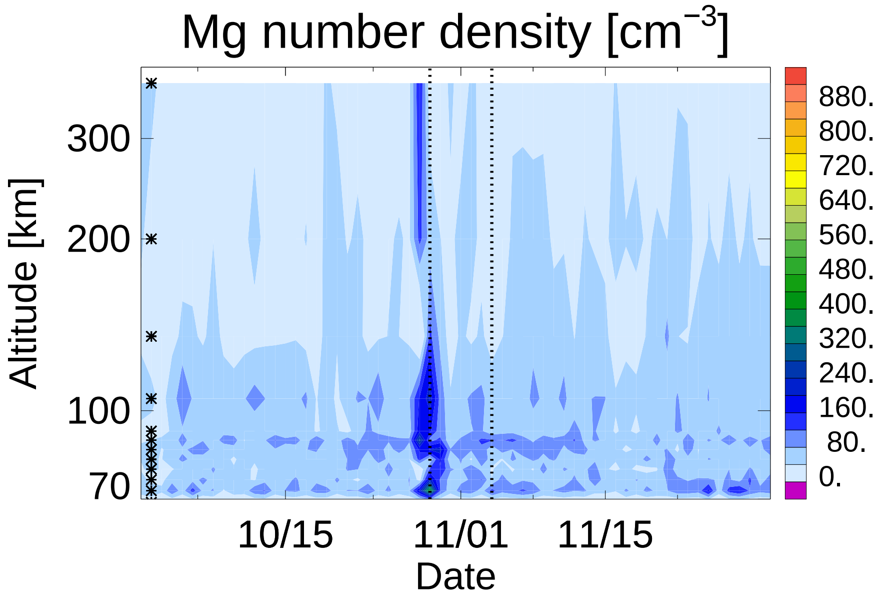

Figure 11.28: Average vertical distribution of Mg during October and November 2003 **averaged from 90°S – 60°S and 60°N – 90°N geomagnetic latitude and all longitudes.** Asterisks on the left denote the center altitudes of the retrieval pixel grid, see Section 6.3.3. Mg^+ is significantly increased at altitudes between 70 and 150 km on October 29. Note that highest abundances of Mg around 400 km are present on October 28, as is the case for Mg^+. One day later, the values are back to average again. The November 3/4 event is not visible in the data shown here.

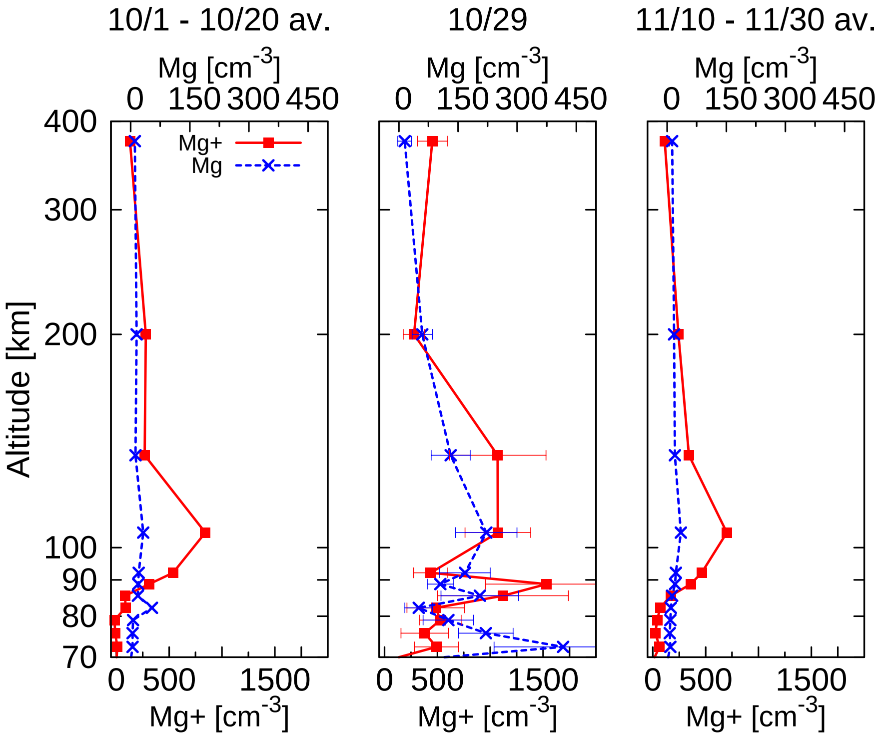

Figure 11.29: Average vertical profiles of Mg^+ (solid) and Mg (dashed) during October 10 – 20, October 29 and November 10 – 20, **averaged from 90°S – 60°S and 60°N – 90°N geomagnetic latitude and all longitudes.** Significant increases in Mg^+ occur on October 29 at all altitudes except around 200 km. A pronounced layer of Mg^+ is formed at 89 km. Note that this layer is broader compared to all other latitude regions, see Figures 11.11, 11.17, 11.23.

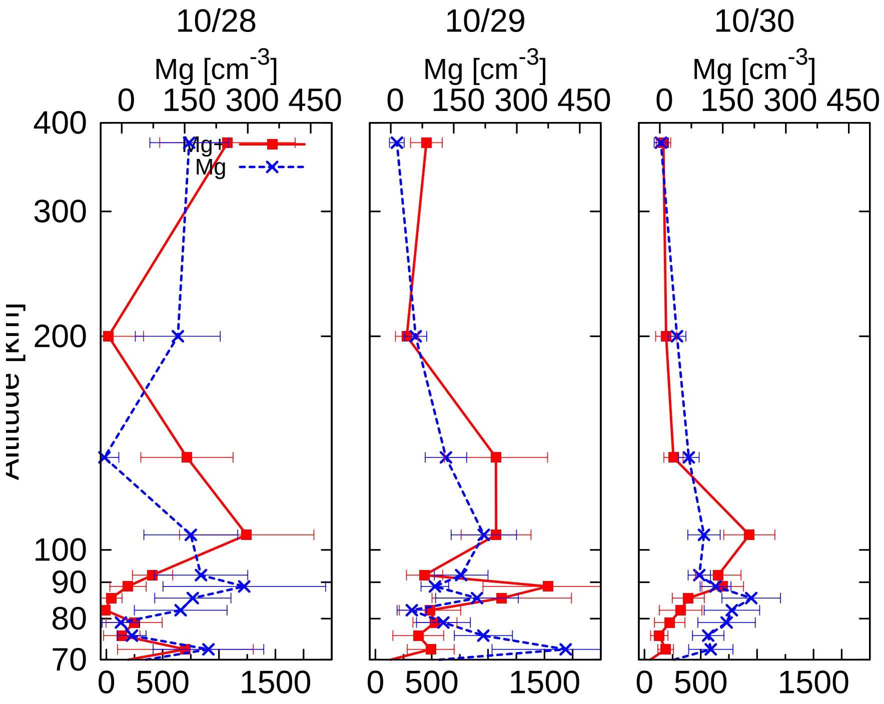

Figure 11.30: Daily average vertical profiles of Mg$^+$ (solid) and Mg (dashed) during October 28 – 30, **averaged from 90°S – 60°S and 60°N – 90°N geomagnetic latitude and all longitudes.** As already noted, the Mg$^+$ layer at 89 km is only observed on October 29. Mg$^+$ values at high altitudes around 400 km are increased during all three days of the event. Neutral Mg is increased at high altitudes around 400 km during the first two days of the event. On October 20, the Mg$^+$ abundance at 400 km is at average levels again. Neutral Mg is increased only during the first day of the event. Maximum values of Mg on October 28 are observed between around 89 km. Another layer of high abundance forms at low altitudes around 72 km. On October 29, Mg is maximal at 72 km. On October 30, this low-altitude maximum is not present any mor, maximal Mg abundances are now observed at 89 km.

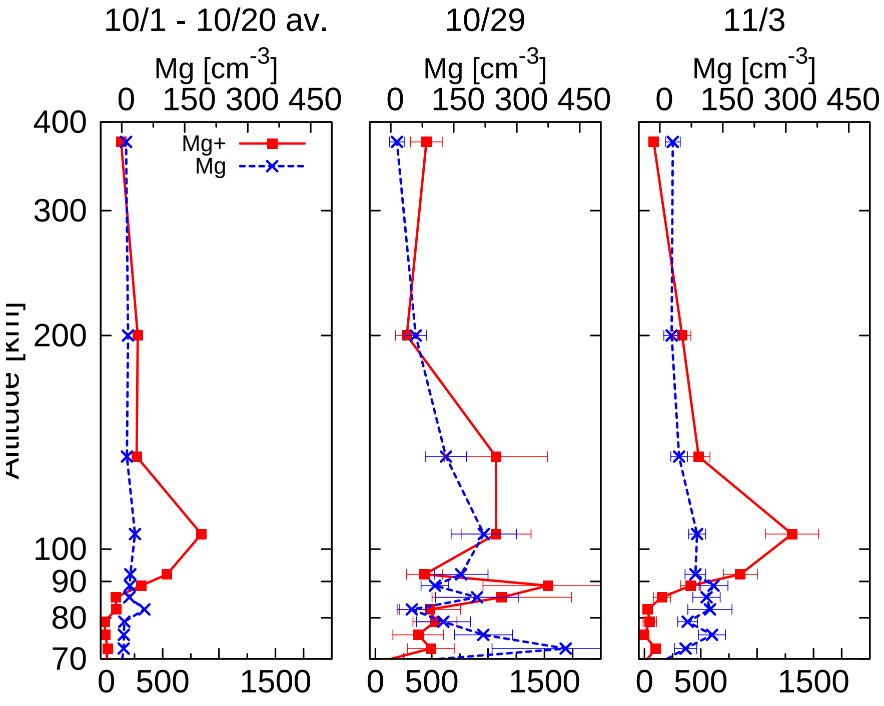

Figure 11.31: Average vertical profiles of Mg$^+$ (solid) and Mg (dashed) during October 29, and daily average profiles on October 29 and November 3, **averaged from 90°S – 60°S and 60°N – 90°N geomagnetic latitude and all longitudes.** The Mg$^+$ profile on November 3 exhibits significantly increased values around 120 km. However, low and high altitudes are not affected. The Mg profile is increased at low altitudes below 120 km. However, absolute values of October 29 exceed the November 3 values by a factor of more than three.

flux. If instead of the correct solar spectrum of the respective orbit, any arbitrary spectrum would be used, the retrieval results will be obviously wrong. If a solar spectrum with from a day with smaller MgII index would be used, the retrieval underestimates the true magnesium content. Accordingly, a falsely used spectrum with higher MgII index than in reality would lead to an overestimation of the true atmospheric state. However, this effect would then affect all latitude bands equally. The observations of the 2003 solar proton events in October and November, however, show distinct features in different latitude bands. The strongest variations are observed near the geomagnetic poles, the tropical atmosphere is rather less affected in comparison. It can thus be concluded that the normalization procedure was done correctly and the observed variations in the distribution of the magnesium species are in fact a result of atmospheric processes.

11.2 Discussion

It is reasonable to assume that the ionization rate to form Mg^+ from neutral Mg is increased during solar proton events. As a result of large perturbation in the Earth's magnetosphere and the increased particle impact in particular in polar regions, ionized species are more likely to exhibit high abundances. On the one hand, direct ionization due to particle impact to form Mg^+ from Mg is possible. On the other hand, charge transfer is increased.

As pointed out by Jackman et al. (2005), the October 2003 SPE led to largely increased production of odd nitrogen (NO_y). This production is a result of dissociation of nitrogen molecules and subsequent reaction with oxygen to form odd nitrogen species such as NO. At mesospheric altitudes, this NO is readily ionized either by photo-ionization or particle impact to form NO^+. This species is an important reaction partner for Mg to form Mg^+ by charge transfer (see reaction (4.1), Section 4).

A possible source for neutral Mg is presented by recombination of Mg^+ with e^-. The observation of higher Mg abundances is thus consistent with the higher concentration of both species during times of high solar proton fluxes. This is probably the source of neutral Mg at high altitudes around 400 km.

Jackman et al. (2005) reported significant losses of mesospheric ozone at altitudes of about 70 km, resulting from increased production of odd hydrogen (HO_x). A longer lasting ozone depletion was attributed to increased NO_y production during the event. A possible reason for the enhancements of neutral Mg at lower altitudes around 70 km is presented by lower ozone number densities, as reaction with ozone destroys neutral Mg (reaction (4.10), Section 4). It is, however, unlikely that the ozone depletion is the only source of Mg, as the ozone depletion lasts several days after the event (Jackman et al., 2005), whereas the Mg abundance is back to average values within one to two days after October 29.

Increased release from the reservoir species $Mg(OH)_2$ by reaction with atomic hydrogen is likely to be the main source of neutral Mg at lower altitudes (reactions (4.14), (4.15), see Section 4). This is consistent with model calculations that suggest increased OH levels at altitudes around 70 km (Jackman et al., 2005).

The formation of a pronounced Mg^+ layer at an altitude of 89 km exclusively on October 29 is restricted to mid and high latitudes and most pronounced in regions of high geomagnetic latitude (see vertical profiles as shown in Figures 11.17, 11.23, 11.29). It is noteworthy that a simultaneously occurring corresponding layer in the neutral Mg is not observed. Nor is Mg significantly depleted. Thus, a temporally and spatially restricted conversion of the neutral into the ionized species can be excluded. Model calculations carried out by Plane and Helmer (1995) and Fritzenwallner and Kopp (1998) suggested a layer of MgO^+ between 85 and 90 km (see Figure 11.32). A possible source of neutral Mg (which is rapidly ionized at within this altitude range) associated with the solar proton event is presented by the following reactions:

$$MgO^+ + e^- \rightarrow Mg + O \tag{11.1}$$
$$MgO^+ + O \rightarrow Mg^+ + O_2 \tag{11.2}$$

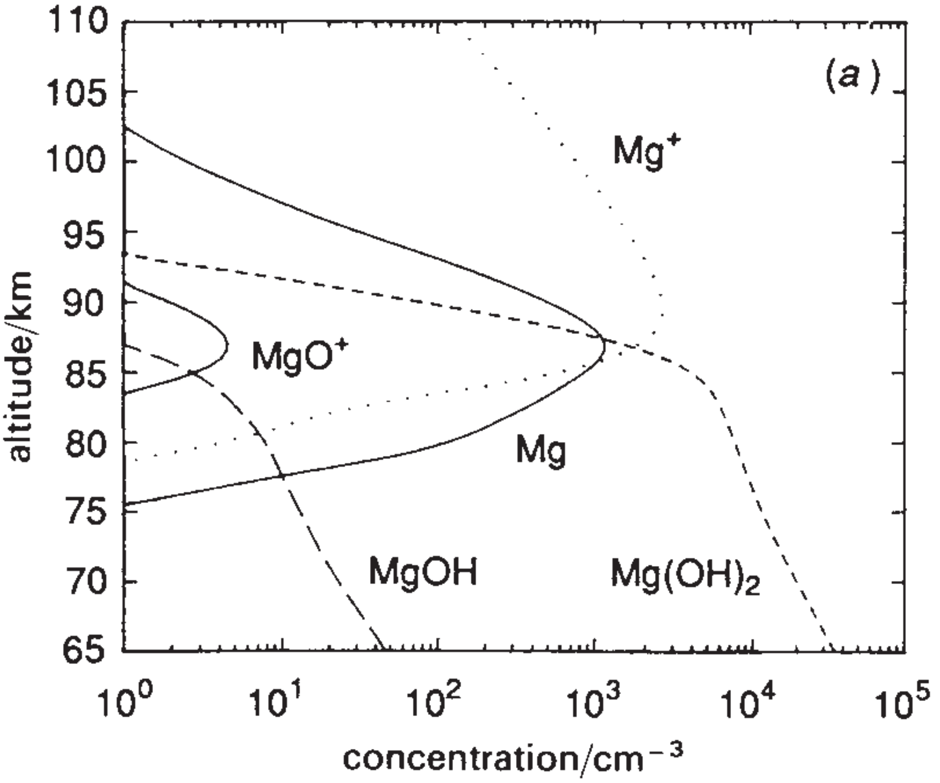

Figure 11.32: Vertical profiles of major magnesium species in the mesosphere for a mid-latitude winter daylight scenario (adapted from Plane and Helmer (1995)). A layer of MgO^+ is suggested by model calculations. This species may act as a vertically confined source of Mg^+ during periods of enhanced solar particle fluxes (reactions (11.1) and (11.2)). See text for details.

However, the peak abundance of MgO^+ within the layer was calculated to be just 10 cm^{-3} in times of average solar activity (neither Plane and Helmer (1995) nor Fritzenwallner and Kopp (1998) assume any particular solar conditions), i.e. even a complete conversion from MgO^+ to Mg^+ could not yield the observed peak concentration of 1000 – 1500 cm^{-3} . An increased production of MgO^+ to satisfy the increased Mg^+ abundance through reactions (11.1) and (11.2) may be resulting from reaction of Mg^+ with molecular oxygen and subsequent reaction with atomic O (which is increased during the solar proton event):

$$Mg^+ + O_2 + N_2 \rightarrow MgO_2^+ + N_2 \tag{11.3}$$
$$MgO_2^+ + O \rightarrow MgO^+ + O_2 \tag{11.4}$$

However, reaction (11.3) obviously depletes Mg^+. Thus, no conclusion can be given. It is desirable to carry out a more thorough model study including the mesospheric and thermospheric conditions during a solar proton event and the according particle fluxes into the Earth's atmosphere. A direct measurement of a number of molecular magnesium species (see Section 4) will certainly be the ideal way.

What remains unclear is the fact that tropical Mg^+ and Mg is increased at all. The direct particle impact can be assumed to be negligible, as solar particles are deflected by the Earth's magnetic field towards to poles. A similar argument holds for the mid-latitudes regions. The zonally averaged cross sections for tropical regions and mid-latitudes show increased number densities of Mg^+ at high altitudes shortly after the first event on October 29 (see Figures 11.9, 11.15).

Polar regions (Figures 11.21, 11.22), however, exhibit maximal number densities at high altitudes just on October 29, whereas the regions of high geomagnetic latitude (Figures 11.27, 11.28) exhibit increased high-altitude number densities already one on October 28. Note that the abundance of neutral Mg at high altitudes shows a behaviour similar to that of Mg^+ in polar regions (both geographical and geomagnetic), whereas the high-altitude abundance of neutral magnesium in the tropics and mid-latitudes is not affected during either event.

This observations give rise to the assumption that Mg^+ as well as neutral Mg is produced at high-latitude regions during the October 29 event. A significantly increased flux of energetic particles may have been arrived at the Earth even on October 28.If the energies of these particles are below 0.8 MeV, they are not observed by the GOES instrument (see Figure 11.1). The ionized species is then transported towards lower latitudes. This cannot be accomplished by neutral winds, as these would drive the neutral species as well. Additionally, the number density above 120 km is too low and thus the ion-neutral collision frequency is quite small. The motion of ionic species is thus dominated by interactions of the ionized particles with the E and the B fields. The transport of the ions is possible through gyro motion around the magnetic field lines similar to electrons and protons in the Van-Allen belts.

12 The 2005 magnesium anomaly

This section presents observations of a period od anomalous Mg and Mg^+ values in November and December 2005. A strong bloom of Mg is observed, coincident with a depletion in the ionic species.

12.1 Observations

In November and December 2005, a short anomalous period of increased values of neutral magnesium occurred. Figure 12.1 shows the daily averaged total column densities for November and December 2005 of both magnesium species. As can be seen, within two days, column densities of Mg increased by a factor of five compared to their average values of $1 \cdot 10^9$ cm^{-2} in November and December 2005. This high values are maintained for a period of approximately four weeks (November 22 – December 18). After this period, Mg column densities decreased within two days to average values.

A similar pronounced period of low values is found in the Mg^+ column densities. The increase in Mg coincides with the decrease in the Mg^+ columns, and accordingly for the decrease in Mg and the increase in Mg^+. The ionized species decreases from $6.5 \cdot 10^9$ cm^{-2} (average in November/December) to $2.5 \cdot 10^9$ cm^{-2} . Note that the absolute differences in column densities are $4 \cdot 10^9$ cm^{-2} for both species.

Figures 12.2 and 12.3 depict the zonally and daily averaged Mg^+ and Mg number densities at altitudes between 70 and 120 km. The depression in Mg^+ is clearly observed at virtually all altitudes below 120 km (Figure 12.2). Between 90 and 120 km, Mg^+ number densities diminish from average values of approximately 600 cm^{-3} to 100 – 200 cm^{-3} . Not shown are number densities above 120 km, the depression is present, but less pronounced in those altitude regions. Slightly increased values occur at the lowest retrieval altitude of 72 km. The neutral Mg, however, exhibits strongly increased values at all altitudes below 90 km. At the lowest retrieval altitudes, Mg number densities are increased by one order of magnitude. Between 120 and 150 km, the number densities are decreased, however (see Figure 12.3). Not shown are number densities above 120 km. During the period of anomalous high Mg values at low altitudes, a slight increase of Mg is observed between 150 and 500 km. Values increase from zero (within the measurement tolerances) to ≈ 150 cm^{-3} .

The depletion of Mg^+ as well as the bloom of Mg is observed at all latitudes. Compare Figures 7.3 and 7.4 in Section 7.1.2 for latitude-dependend time series of the total content values of both magnesium species. As can be seen from those figures, the increase in Mg is by a factor of two larger in the polar regions, compared to the increase in mid-latitude and tropical latitudes.

12.2 Discussion

The coincidence of the Mg increase and the decrease in Mg^+ and the fact that the column densities vary by the same amount of $4 \cdot 10^9$ cm^{-2} suggests a temporal conversion of Mg^+ into neutral Mg. In particular, no additional sources of neutral Mg are necessary to explain the column density behaviour. The question to answer now is whether chemical or dynamical effects dominate the processes during the four weeks between November 22 and December 18.

It is very unlikely that the solar activity plays a role in explaining the anomaly. As can be seen in Figure 12.4, neither the 10.7 cm solar flux as indicator for general solar activity nor

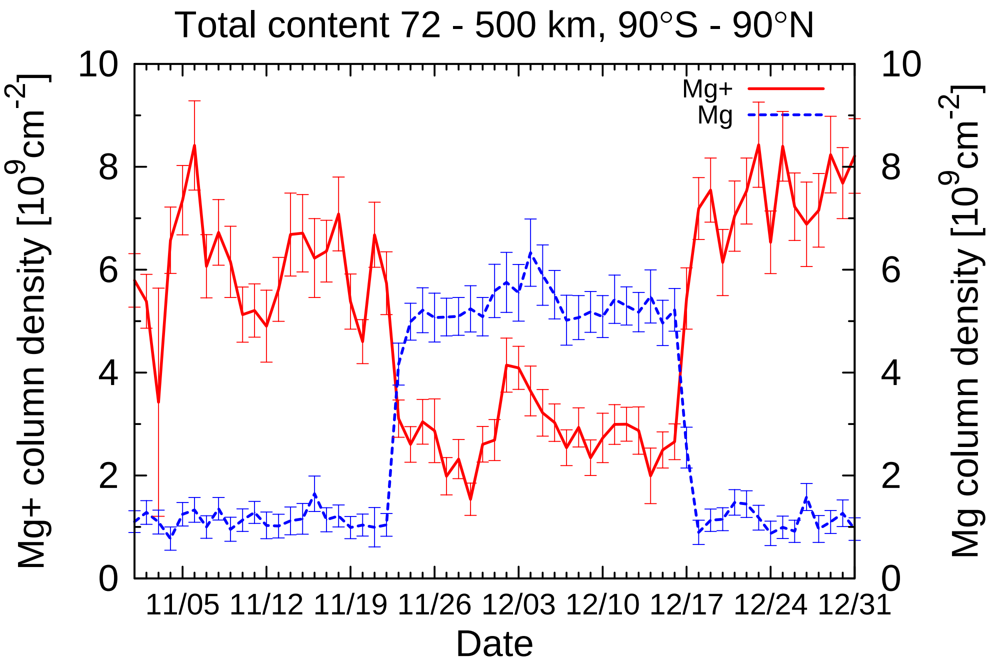

Figure 12.1: Total column densities for Mg^+ (solid) and Mg (dashed) during November and December 2005, daily averaged over all latitudes and longitudes. Between November 22 and November 24, neutral column densities increased by a factor of $5 \cdot 10^9$ from $1 \cdot 10^9$ cm^{-2} to $5 \cdot 10^9$ cm^{-2} . This level is maintained until December 16, as decrease to average values of $1 \cdot 10^9$ cm^{-2} began. On December 18, Mg is back to its average value. Increased values of Mg in November and December coincide with decreased column densities of ionized Mg^+. Average column density values in November and December are $6.5 \cdot 10^9$ cm^{-2} , during the anomalous Mg period, Mg^+ values are lowered by $4 \cdot 10^9$ cm^{-2} on average. Note that this is also the difference between average and increased Mg values. Average values of Mg and Mg^+ in November and December are calculated for November 1 – 21 and December 19 – 31.

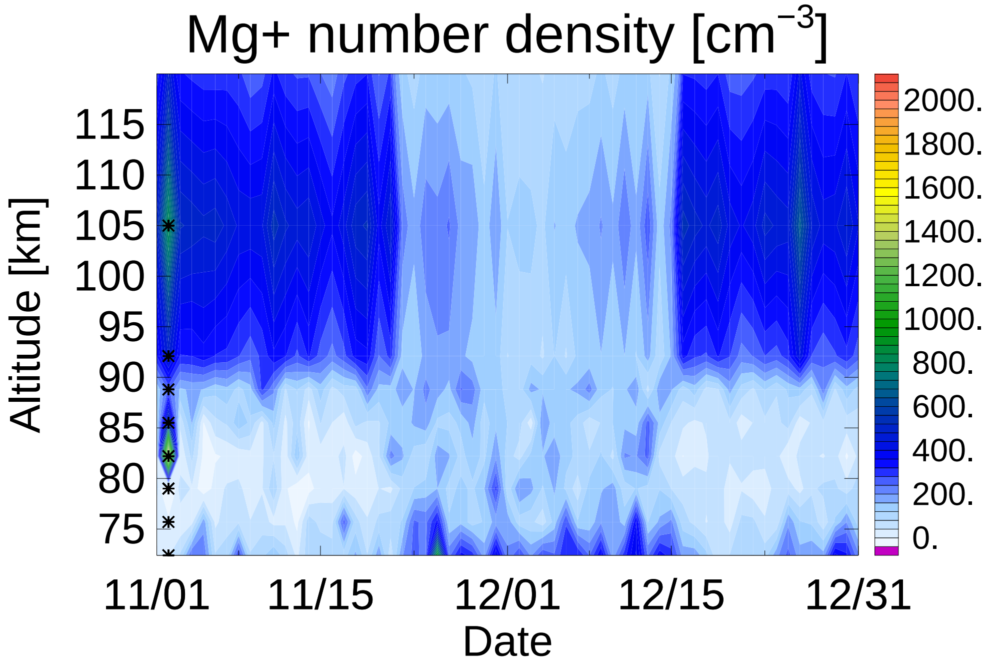

Figure 12.2: Daily and zonally averaged number densities of Mg^+ during November and December 2005. The depletion of the ion between November 24 and December 18 is clearly identified. Slightly increased values of Mg^+ are observed at the lowest retrieval altitude. Asterisks on the left denote the center altitudes of the retrieval pixel grid, see Section 6.3.3.

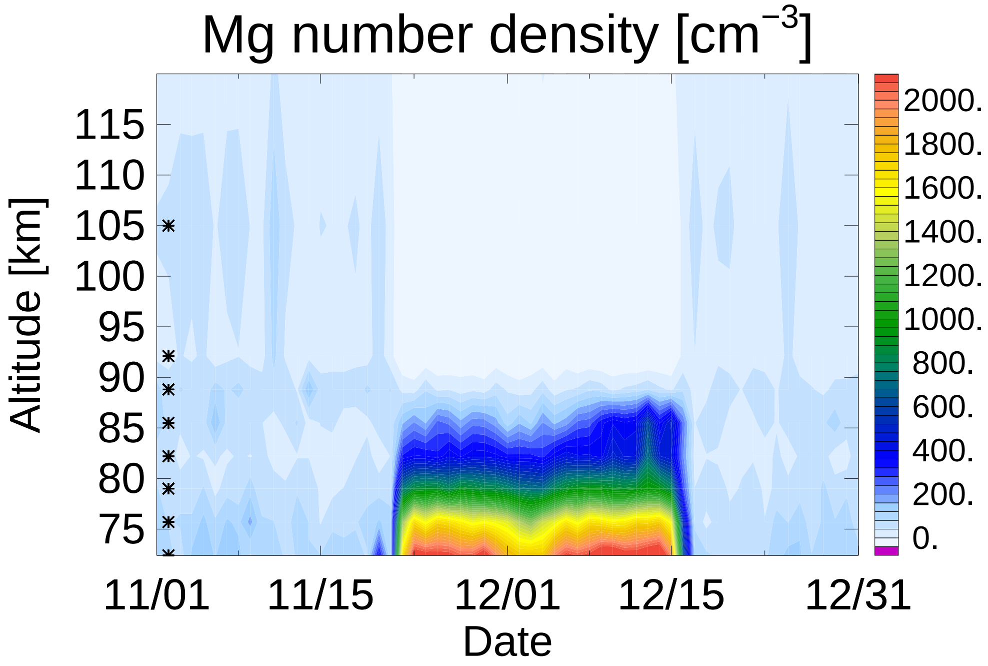

Figure 12.3: Daily and zonally averaged number densities of neutral Mg during November and December 2005. The period of increased number densities of the neutral species between November 24 and December 18 is clearly identified. The magnitude of the increase is larger at lower altitude. Near the bottom retrieval altitude, the number densities of Mg are increased by one order of magnitude.

the proton proton fluxes measured by GOES-12 exhibit singular features during November and December 2005.

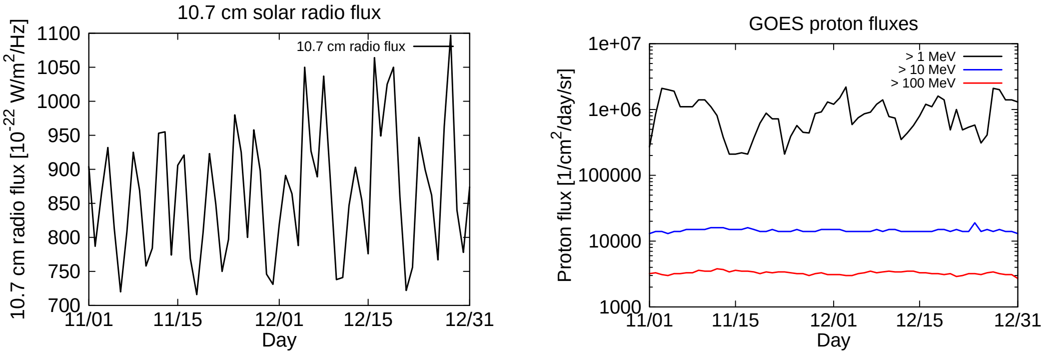

(a) Radio flux at 10.7 cm as proxy for the solar activity. The solar activity during the period of anomalous Mg/Mg$^+$ values (Nov 22 - Dec 18) does not differ from the solar activity during the rest of November and December. Variations are frequent anyway.

(b) GOES proton fluxes for different proton energies measured in November and December 2005. Neither energy channel shows particular enhancements or lowering during the period of anomalous Mg/Mg$^+$ values

Figure 12.4: Solar activity proxys during November and December 2005. No special features during November 22 – December 18 are observed. This suggests that the solar activity does not contribute significantly to the Mg$^+$ depletion respectively the Mg increase during November and December 2005.

Neutral Mg is produced from Mg$^+$ by two principal reactions, see Section 4, reactions (4.4), (4.7), (4.8). These are dissociative recombination of MgO$^+$ and MgO$_2^+$ and recombination of Mg$^+$ with e^- and subsequent photon emission. The recombination radiation at wavelength 162 nm is not within the wavelength range of SCIAMACHY. At least, increased electron densities would indicate increased reaction rates and thus increased Mg production at the expense of Mg$^+$. Figure 12.5 shows vertical electron density profiles during November and December 2005 for daylight conditions at 50°N , 0°E . Values are taken from NASA Goddard Space Flight Center (2007a). As can be seen, the profiles do not differ significantly throughout the two months. In particular, no significant depletion or enhancement of electrons is observed during the time period of anomalous magnesium values. It can be thus concluded that effects of varying electron density are unlikely to cause the anomaly.

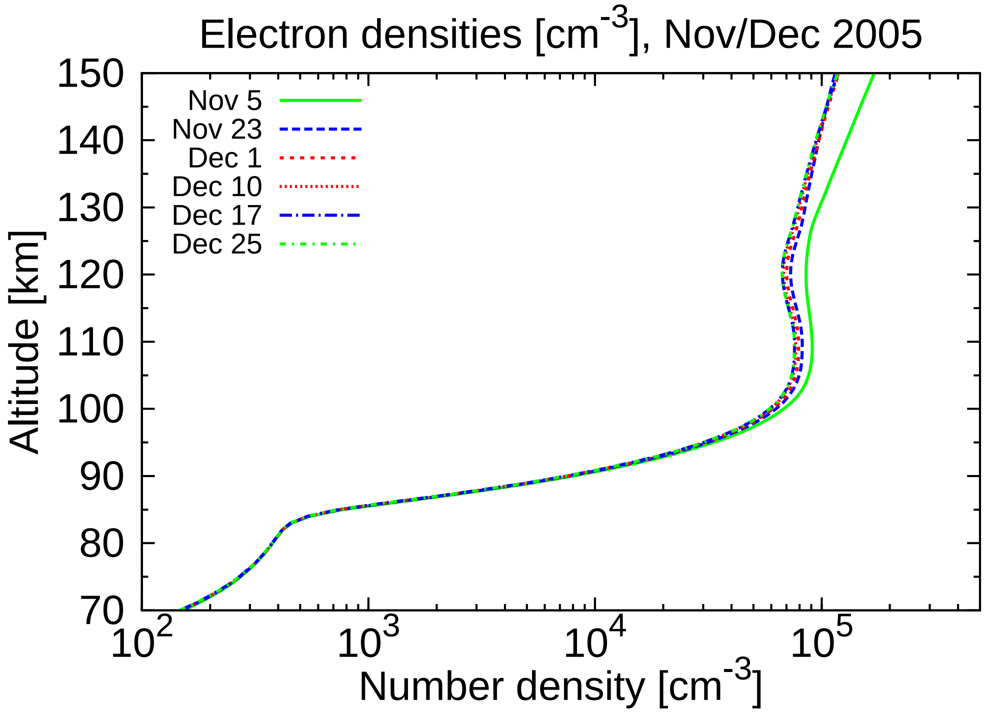

Figure 12.5: Electron densities between 70 and 150 km for a number of days in November/December 2005 for daylight conditions at 50°N , 0°E . Green lines correspond to times of undisturbed magnesium abundances, blue lines denote to Nov 22 and December 17, the days of largest total column gradients, see Figure 12.1. Red lines correspond to days during the anomaly. The five electron density profiles do not differ significantly. This suggests that ionization effects can be ruled out as explanation for the Mg/Mg$^+$ anomaly. Values are provided by NASA Goddard Space Flight Center (2007a), see also Bilitza (2001).

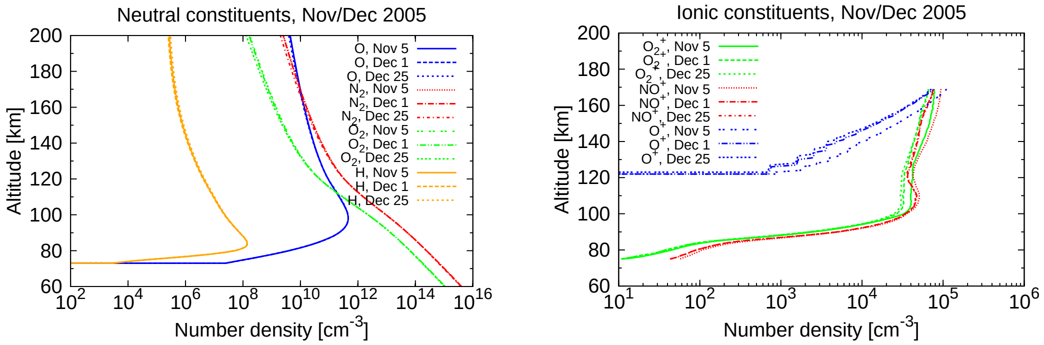

(a) Major neutral constituents in the mesosphere for November 5, December 1 and December 25, 2005. Blue: O, red: N, green: O$_2$, orange: H. The variation is rather small in both species.

(b) Major ionic constituents in the mesosphere for November 5, December 1 and December 25, 2005. Green: O$_2^+$, blue: O$^+$, red: NO$^+$.

Figure 12.6: Major mesospheric constituents in November and December 2005 for daylight conditions at 50° N, 0° E. Shown is one profile for November before the anomaly (Nov 5), one for December after the anomaly (Dec 25) and one during the anomaly (Dec 1). Ionic profiles are provided by the IRI model ((NASA Goddard Space Flight Center, 2007a), (Bilitza, 2001)), neutral species profiles are taken from NASA Goddard Space Flight Center (2007b), see also (Hedin, 1991).

In general, the composition of the mesosphere and lower thermosphere does not show any significant variations during November and December 2005. Figure 12.6 show vertical profiles of neutral (Figure 12.6(a)) as well as ionic (Figure 12.6(a)) species for three days in November and December 2005. The profiles for days before and after the anomaly (November 5 and December

25 do not differ significantly from the December 1 profile, the day just in the middle of the event.

As a conclusion, it is unlikely that the primary reason for the Mg^+ depletion and the concurrent Mg enhancement is neutral or ionic chemistry. Thus, an explanation of the 2005 magnesium anomaly has to incorporate dynamical effects. A possible mechanism comprises increased downwards transport into regions of higher ozone density. There, reaction of Mg^+ with ozone or oxygen and subsequent dissociative recombination provide a source of neutral Mg:

$$\begin{aligned} \mathrm{Mg^+ + O_3} &\rightarrow \mathrm{MgO^+ + O_2} && (12.1)\\ \mathrm{MgO^+ + O_2 + N_2} &\rightarrow \mathrm{MgO_2 + N_2} && (12.2)\\ \mathrm{MgO^+} + e^- &\rightarrow \mathrm{Mg + O} && (12.3)\\ \mathrm{MgO_2^+} + e^- &\rightarrow \mathrm{Mg + O_2} && (12.4) \end{aligned}$$

It can be assumed that a large-scale downward transport would affect other mesospheric species likewise. However, to the author's knowledge, no such downward transport was reported in the literature. It would thus be convenient to have a model for the mesospheric magnesium chemistry including a full dynamical treatment. Parameter studies with a number of different downward transport rates will be suitable to shed light on the 2005 Mg/Mg^+ anomaly.

13 Summary, conclusions and outlook

13.1 Summary and conclusions

The SCIAMACHY instrument onboard the ENVISAT satellite platform routinely observes emission features from mesospheric and thermospheric species. A retrieval scheme based on a simultaneous usage of limb and nadir data has been developed. SCIAMACHY measurement data of individual orbits are merged and evaluated at the same time using methods similar to Optimal Estimation. Thus, information from altitudes above the topmost respective tangent height at 92 km incorporates the retrieval results.

Using this scheme, number densities of neutral and singly ionized magnesium in the mesosphere and lower thermosphere region (MLT) between approximately 70 and 500 km altitude have been obtained. The vertical resolution of the retrieval was estimated to be approximately 5 km, which is a good value compared to the tangent height sampling rate of 3.3 km. At higher altitudes above the top tangent altitude, the vertical resolution increases to larger values of 30 km between 92 and 150 km, 100 km between 150 and 250 km and 250 km between 250 and 500 km. The horizontal resolution is approximately 10° along the orbit. This a comparatively good value with respect to the fact that two subsequent limb (or nadir) scans of SCIAMACHY are separated by approximately 7° . Note that the sampling rate presents a lower boundary for the resolution in vertical as well as horizontal direction. The average total error is 120 cm^{-3} .

A long-term study covering all six years of SCIAMACHY measurement has been carried out to investigate seasonal variations in the total content of Mg and Mg^+. Pronounced summer maxima in the total content of singly ionized magnesium are observed. This is attributed to a higher abundance of mesospheric hydrogen during the summer time, releasing neutral Mg from the reservoir species. As a result of fast ionization of Mg by charge transfer to form Mg^+, a corresponding seasonal variation in the neutral species Mg is not observed. As a result of this, the abundance of Mg^+ and Mg is highest near the sub-solar point.

Model results and sporadic satellite measurements of high-altitude ($\geq$ 100 km) abundances of ionized magnesium have been confirmed with respect to the global distribution. The SCIAMACHY results show uplift of primarily Mg^+ above near regions of the polar auroral belts and the sub-solar point. These uplifts can be attributed to Hall drifts near the equator and Joule heating and subsequent flow along electric and magnetic field lines near the auroral ovals. These observations are consistent with two major uplift mechanisms proposed in the 1970's and 1980's.

The total influx of cosmic material into the Earth's atmosphere has been estimated from the loss rates and the average total content of neutral magnesium. A value of approximately 55 t/d has been figured out. This is consistent with previous measurements and model results. However, a large range of uncertainty is contained in this figure, as the ablation process is still not fully understood. Based on estimations of the ablated fraction of the metallic content of meteoric particles, the average velocity of cosmic particles can be estimated to be approximately 11 km/s.

Though a number of regularly returning meteor showers can be observed throughout the year, no significant impact of the observable meteoric flux on the total content of either magnesium species can be detected. Within the error margins of the measurement, the total content of both Mg^+ and Mg remains unaffected by meteor showers such as the Leonids or the Perseids. Though meteor showers present a prominent phenomenon, the material influx can be assumed to be rather small and negligible compared to the background influx.

During times of quiet sun, no evidence was found that neither the total content nor the number density at any altitude is significantly related to the solar flux. This holds for the solar proton flux as measured by the GOES instrument as well as for the radiative flux. As proxy for the latter the 10.7 cm radio flux was used. Despite the fact that the X-ray or UV flux can be assumed to have a larger impact on the physics and chemistry of the upper atmosphere, the 10.7 cm flux is a good proxy for the total radiance.

Extreme solar activity, however, impacts the magnesium content to a large extend. Observation made during the 2003 "Halloween" solar proton event in October and November 2003 show increased abundances of both magnesium species in times near the event. This enhancements are focused on the polar regions, and this observation is consistent with the assumption that actually particle impact is the reason for enhanced Mg^+ and Mg values. It should be noted that only the most intense solar proton event among two events during October/November 2003 has a significant impact on the abundance of mesospheric and thermospheric magnesium. This fact can be interpreted to be a confirmation of the absence of any observation between the Mg and Mg^+ content and the usual solar activity. Extremely enhanced particle fluxes are thus needed to impact the magnesium chemistry significantly.

A period of anomalously enhanced Mg and an depleted Mg^+ values occurred in November and December 2005. Though the essential reason for this behaviour has not been figured out, it can be conjectured that the physics and chemistry of mesospheric and thermospheric magnesium is impacted by a number of quantities.

The mesosphere (and the thermosphere as well) is the transition region between atmosphere and space, and as a result of this, a number of influences from lower as well as from higher altitudes play a role in the chemistry and physics of this region. A synoptic view incorporating a number of instruments and data sets is thus essential for a thorough interpretation of the magnesium morphology in this atmospheric region.

13.2 Outlook

The results presented here are based on satellite measurements. Though this type offers a number of advantages, other means have to be included in the analysis of mesospheric and thermospheric metal species. A number of questions has to be left without answer or even discussion. The most prominent of these questions are the interactions of magnesium with polar mesospheric clouds (NLCs), the impact of meteoric smoke on the chemistry of the mesosphere and stratosphere – with a focus on ozone and water vapour formation and removal – and a more detailed view on the total influx of meteoric material.

The probably most challenging task in the analysis of mesospheric and thermospheric metal species is to incorporate neutral atmospheric chemistry and physics as well as ionospheric processes in the analysis. A number of topics has to be covered:

- Evaluate the morphology of other species of meteoric origin (Fe, Na, Si, ...) to compare the number densities with the results from the magnesium analysis.
- Identify emission or absorption features from molecular metal species such as $Mg(OH)_2$ or MgO^+. It may be necessary to carry out laboratory studies and/or quantum-mechanical calculations to investigate the emission or absorption features of molecular metallic species. The same task applies for other metal species likewise. Knowledge of molecular species provides a better estimate of e.g. the loss rate and thus the total influx of meteoric material.
- Carry out long-term model calculations to validate the seasonal variations observed in the Mg^+/Mg content. A model has to be developed and implemented that includes neutral atmospheric physics and chemistry as well as ionospheric processes.
- Extend the analysis of metal species to lower altitudes. It has been conjectured that metal compound play a role in the middle and upper stratosphere. Thus, it is desirable to carry out space-borne observations down to 30 – 40 km altitude.

Appendix

A Bibliography

Aikin, A. C., Chanin, M. L., Nash, J. and Kendig, D. J., 1991: Temperature trends in the lower mesosphere. *Geophysical Research Letters*, **18**, 416–419.

Aikin, A. C., Grebowsky, J. M. and Burrows, J. P., 2002: Satellite measurements of the atmospheric content of metallic ion and neutral species. In *COSPAR proceedings*.

Aikin, A. C., Grebowsky, J. M. and Burrows, J. P., 2004: Satellite measurements of the atmospheric content of metallic ion and neutral species. *Advances in Space Research*, **33**, 1481–1485.

Aikin, A. C. and McPeters, R. D., 1986: Meteoric material and the behavior of upper stratospheric polar zone. *Geophysical Research Letters*, **13**, 1300–1303.

Anderson, J. G. and Barth, C. A., 1971: Rocket Investigation of the MgI and MgII Dayglow. *Journal of Geophysical Research*, **76**, 16, 3723–3731.

Banwell, C. N., 1972: *Fundamentals of Molecular Spectroscopy.* second edn., London: McGraw-Hill.

Bilitza, D., 2001: International Reference Ionosphere 2000. *Radio Science*, **36**, 2, 261–275.

Bishop, R. L. and Earle, G. D., 2003: Metallic ion transport associated with midlatitude intermediate layer development. *Journal of Geophysical Research*, **108**, A1.

Bovensmann, H., Burrows, J. P., Buchwitz, M., Frerick, J., Noel, S. and Rozanov, V. V., 1999: SCIAMACHY: Mission Objectives and Measurement Modes. *Journal of Atmospheric Sciences*, **56**, 2, 127–150.

Brasseur, G. P. and Solomon, S., 1984: *Aeronomy of the Middle Atmosphere: Chemistry and Physics of the Stratosphere and Mesosphere.* third edn., Kluwer Academic Publishers.

Burrows, J. P., Dehn, A., Deters, B., S., H., Richter, A., Voigt, S. and Orphal, J., 1999: Atmospheric Remote–Sensing Reference Data from GOME: 2. Temperature–Dependent Absorption Cross Sections of O3 in the 231–794 nm range. *Journal of Quantitative Spectroscopy and Radiative Transfer*, **61**, 509–517.

Carbary, J., Morrison, G. J., D. Romick and Yee, J.-H., 2003: Leonid meteor spectrum from 110 to 860 nm. *Icarus*, **161**, 223–234.

Chandrasekhar, S., 1960: *Radiative Transfer.* New York: Dover Publications Inc.

Clemesha, B. R., 1995: Sporadic neutral metal layers in the mesosphere and lower thermosphere. *Journal of Atmospheric and Terrestrial Physics*, **57**, 7, 275–736.

Correira, J., Aikin, A. C., Grebowsky, J. M. and Burrows, J. P., 2005: Spatial and temporal enhancements of meteoritic metal ions in the upper atmosphere. *AGU Fall Meeting Abstracts*, A4+.

Covington, A. E., 1969: Solar Radio Emission at 10.7 cm, 1947-1968. *Journal of the Royal Astronomical Society of Canada*, **63**, 125–+.

Cziczo, D. J., Thomson, D. S. and Murphy, D. M., 2001: Ablation, Flux, and Atmospheric Implications of Meteors Inferred from Stratospheric Aerosol. *Science*, **291**, 1772–1775.

Daly, E. J., 1988: The Evaluation of Space Radiation Environments for ESA Projects. *ESA Journal*, **12**, 229.

Dominion Radio Observatory, Penticton, Canada, 2007: Solar Radio Monitoring Programme. http://www.drao-ofr.hia-iha.nrc-cnrc.gc.ca/icarus/www/sol_home.shtml.

Dymond, K. F., Wolfram, K. D., Budzien, S. A., Nicholas, A. C., McCoy, R. P. and Thomas, R. J., 2003: Middle ultraviolet emission from ionized iron. *Geophysical Research Letters*, **30**, 1, 1003.

Fesen, C. G. and Hays, P. B., 1982a: Mg^+ Morphology From Visual Airglow Experiment Observations. *Journal of Geophysical Research*, **87**, A11, 9217–9223.

Fesen, C. G. and Hays, P. B., 1982b: Two-dimensional inversion technique for satellite airglow data. *Applied Optics*, **21**, 20, 3784–3791.

Fesen, C. G., Hays, P. B. and Anderson, D. N., 1983: Theoretical Modeling of Low-Latitude Mg^+. *Journal of Geophysical Research*, **88**, A4, 3211–3223.

Fritzenwallner, J. and Kopp, E., 1998: Model Calculations of the Silicon and Magnesium Chemistry in the Mesosphere and Lower Thermosphere. *Advances in Space Research*, **21**, 6, 859–862.

Gardner, J. A., Broadfoot, A. L., McNeil, W. J., Lai, S. T. and Murad, E., 1999: Analysis and modeling of the GLO–1 observations of meteoric metals in the thermosphere. *Journal of Atmospheric and Solar–Terrestrial Physics*, **61**, 545–562.

Gérard, J. C. and Monfils, A., 1978: The MgII Equatorial Airglow Altitude Distribution. *Journal of Geophysical Research*, **83**, A9, 4389–4391.

Goldberg, R. A. and Aikin, A. C., 1973: Comet Encke: Meteor Metallic Ion Identification by Mass Spectrometer. *Science*, **180**, 294–296.

Golub, G. H. and v. Loan, C. F., 1996: *Matrix Computations.* third edn., Baltimore and London: The John Hopkins University Press.

Grainger, J. and Ring, J., 1962: Anomalous Fraunhofer lines profiles. *Nature*, **162**, 762.

Granier, C., Jegou, J. P. and Megie, G., 1989: Iron atoms and metallic species in the Earth's upper atmosphere. *Geophysical Research Letters*, **16**, 3, 243–246.

Gumbel, J., Fan, Z. Y., Waldemarsson, T., Stegman, J., Witt, G., Llewellyn, E. J., She, C.-Y. and Plane, J. M. C., 2007: Retrieval of global mesospheric sodium densities from the Odin satellite. *Geophysical Research Letters*, **34**, L04813.

Hamilton, D. R., 1947: The Resonance Radiation Induced by Elliptically Polarized Light. *Astrophysical Journal*, **106**, 457–465.

Hanson, W. B. and Sterling, D. L., 1972: Source and Idetification of Heavy Ions in the Equatorial F Layer. *Journal of Geophysical Research*, **77**, 28, 5530–5541.

Hedin, A., 1991: Extension of the MSIS Thermosphere Model into the Middle and Lower Atmosphere. *Journal of Geophysical Research*, **96**, 1159.

Horwitz, J. R. and Lockwood, M., 1985: The Cleft Ion Fountain: A Two-Dimensional Kinetic Model. *Journal of Geophysical Research*, **90**, A10, 9749–9762.

Hughes, J. P., 1978: *Cosmic Dust.* first edn., J.A.M. McDonell, Ed. J. Wiley.

Hunten, D. M., 2004: An Iron Deficiency in Polar Mesospheric Clouds. *Sience*, **304**, 395–396.

Jackman, C. H., DeLand, M. T., Labow, G. J., Fleming, E. L., Weisenstein, D. K., Ko, M. K. W., Sinnhuber, M. and Russell, J. M., 2005: Neutral atmospheric influences of solar proton events in October–November 2003. *Journal of Geophysical Research*, **110**.

Joiner, J. and Aikin, A. C., 1996: Temporal and spatial variations of upper atmosphere Mg^+. *Journal of Geophysical Research*, **101**, 5239–5250.

Kaiser, J., 2001: *Atmospheric Parameter Retrieval from UV–Visible–NIR Limb Scattering Measurements.* Ph.D. thesis, University of Bremen, Institute of Environmental Physics.

Kalashnikova, O., Horányi, M., Thomas, G. E. and Toon, O. B., 2000: Meteoric smoke production in the atmosphere. *Geophysical Research Letters*, **27**, 3293–3296.

Kazeminejad, S., Sinnhuber, M., Notholt, J., von Savigny, C., Winkler, H. and Burrows, J. P., 2006: Response of the Middle Atmosphere's Chemical Composition due to Solar Proton Events. *AGU Fall Meeting 2006, Poster presentation*, **P23A-0052**.

Lockwood, M., Horwitz, J. R., Chandler, M. O., Waite, J. H., Moore, T. E. and Chappell, C. R., 1985: The Cleft Ion Fountain. *Journal of Geophysical Research*, **90**, A10, 9736–9748.

Lübken, F. and Höfner, J., 2004: Experimental evidence for ice particle interaction with metal atoms at the high latitude summer mesopause region. *Geophysical Research Letters*, **31**, L08103.

McBride, N. and McDonnell, J. a. m., 1999: Meteoroid impacts on spacecraft:sporadics, streams, and the 1999 Leonids. *Planetary and Space Science*, **47**, 1005–1013.

McDonnell, J. A. M., 1980: *Mircoparticle studies by space instrumentation (in* Cosmic Dust*).* first edn., New York: John Wiley.

McNeil, W. J., Shu, T. L. and Murad, E., 1998: Differential ablation of cosmic dust and implications for the relative abundances of atmospheric metals. *Journal of Geophysical Research*, **103**, D9, 10,899–10,911.

Minschwaner, K., Shukla, N., Fortna, C., Budzien, S., Dymond, K. and McCoy, R., 2004: Observations of Ultraviolet Emission from Mg^+ in the Lower and Middle Thermosphere. *AGU Fall Meeting 2004, Poster presentation*, **SA21A-0337**.

Moore, T. E., Lockwood, M., Chandler, M. O., Waite, J. H., Chappell, C. R., Persoon, A. and Sugiura, M., 1986: Upwelling O^+ Ion Source Characteristics. *Journal of Geophysical Research*, **91**, A6, 7019–7031.

Murad, E., Swider, W. and Benson, S. W., 1981: Possible role for metals in stratospheric chlorine chemistry. *Nature*, **289**, 273–+.

Murphy, D. M., Thomson, D. S. and Mahoney, M. J., 1998: In Situ Measurements of Organics, Meteoritic Material, Mercury, and Other Elements in Aerosols at 5 to 19 Kilometers. *Science*, **282**, 1664–+.

NASA Goddard Space Flight Center, N., 2007a: NASA Goddard Modelweb Online resource. http://modelweb.gsfc.nasa.gov/models/iri.html.

NASA Goddard Space Flight Center, N., 2007b: NASA Goddard Modelweb Online resource. http://modelweb.gsfc.nasa.gov/models/msis.html.

NIST, 2005: National Institute of Standards and Technology: Atomic Spectra Database. http://physics.nist.gov/PhysRefData/ASD/lines_form.html.

NOAA, 1976: *U.S. Standard Atmosphere*. Tech. Rep. NOAA-S/T 76-1562, U.S. Government Printing Office.

NOAA/National Weather Service, 2007: Solar and Geomagnetic Indices. http://www.sec.noaa.gov/Data/index.html#indices.

Noel, S., Bovensmann, H., Burrows, J. P., Frerick, J., Chance, K. V. and Goede, A. H. P., 1999: Global Atmospheric Monitoring with SCIAMACHY. *Physics and Chemistry of the Earth(C)*, **24**, 5, 427–434.

Plane, J. M. C., 2003: Atmospheric Chemistry of Meteoric Metals. *Chemical Reviews*, **103**, 2003, 4963–4984.

Plane, J. M. C. and Helmer, M., 1995: Laboratory Study of the Reactions Mg + O_3 and MgO + O_3, Implications for the Chemistry of Magnesium in the Upper Atmosphere. *Faraday Discussions*, **100**, 411–430.

Plane, J. M. C., Murray, B. J., Chu, X. and Gardner, C. S., 2004: Removal of Meteoric Iron on Polar Mesospheric Clouds. *Science*, **304**, 426–428.

Roddy, P. A., Earle, G. D., Swenson, C. M., Carlson, C. G. and Bullett, T. W., 2004: Relative concentrations of molecular and metallic ions in midlatitude intermediate and sporadic E–layers. *Geophysical Reseach Letters*, **31**.

Rozanov, A., 2001: *Modeling of radiative transfer through a spherical planetary atmosphere*. Ph.D. thesis, University of Bremen, Institute of Environmental Physics.

v. Savigny, C., Bramstedt, B., Noel, S., Sinnhuber, M. and Taha, G., 2006: *Comparison of SCIAMACHY pointing retrievals in limb and Occultation geometry*. Tech. Rep. TN–IUP/IFE–2006–cvs–03, University of Bremen, Intitute of Environmental Physics.

v. Savigny, C., Kaiser, J. W., Bovensmann, H., Burrows, J. P., McDermid, I. S. and Leblanc, T., 2005: Spatial and temporal characterization of SCIAMACHY limb pointing errors during the first three years of the mission. *Atmospheric Chemistry and Physics*, **5**, 2593–2602.

von Savigny, C., Rozanov, A., Bovensmann, H., Noel, S., Gottwald, M. and Slijkhuis, J., S.and Burrows, 2007: Studying Envisat Attitude with SCIAMACHY Limb-scatter Measurements. In *Proceedings of the Envisat Symposium, ESA Special Publication SP-636*.

Scharringhausen, M., Aikin, A., Burrows, J. P. and Sinnhuber, M., 2006: First Space-Borne Measurements of the Altitude Distribution of Mesospheric Magnesium Species. *Atmospheric Chemistry and Physics*. Submitted.

Schmahl, E. J. and Kundu, M. R., 1994: Solar cycle variation of the microwave spectrum and total irradiance. *Solar Physics*, **152**, 167–173.

Sierk, B., Richter, A., Rozanov, A., v. Savigny, C., Schmoltner, A. M., Buchwitz, M., Bovensmann, H. and Burrows, J. P., 2006: Retrieval and Monitoring of Atmospheric Trace Gas

Concentrations in nadir and Limb Geometry Using the Space–Born SCIAMACHY Instrument. *Environmental Monitoring and Assessment.*

Stevens, M. H., 1995: Nitric oxide γ band fluorescent scattering and self–absorption in the mesosphere and lower thermosphere. *Journal of Geophysical Research*, **100**, A8, 14,735–14,742.

Summers, M. E. and Siskind, D. E., 1999: Surface recombination of O and H_2 on meteoric dust as a source of mesospheric water vapor. *Geophysical Research Letters*, **26**, 1837–1840.

Tapping, K. and Murdin, P., 2000: Solar Activity Indices. *Encyclopedia of Astronomy and Astrophysics.*

Viereck, R. A. and Puga, L. C., 1999: The NOAA MgII core-to-wing solar index: Construction of a 20-year time series of chromospheric variability from multiple satellites. *Journal of Geophysical Research*, **104**, 9995–10 005.

Vountas, M., 1999: *Die Modellierung und Parametrisierung des Ring Effektes.* Ph.D. thesis, University of Bremen, Institute of Environmental Physics.

de Vries, J. and Hoogeveen, R., 1999: *Optec 2 Cold Tests Instrument Performance Evaluation Report.* Tech. Rep. RP-SCIA-0000FO/207, SCIAMACHY Joint Team FS-TPD-SRON.

Wasson, J. T. and Kyte, F. T., 1987: Comment on the letter 'On the influx of small comets into the earth's atmosphere. II - Interpretation'. *Geophysical Research Letters*, **14**, 779–+.

Wayne, R. P., 2000: *Chemistry of Atmospheres.* third edn., Oxford: Oxford University Press.

Weber, M., 1999: Solar activity during solar cycle 23 monitored by GOME. In *Preprint, Proc. European Symposium on Atmospheric Measurements from Space (ESAMS 1999), Noordwijk.*

B Danke!

Eine Doktorarbeit ist niemals das Werk eines Einzelnen, sondern immer eine Mannschaftsleistung. Viele Menschen tragen direkt oder indirekt dazu bei, dass die Arbeit gelingt. Hier sollen einige Menschen gewürdigt werden, die zu meiner Promotion beigetragen haben.

An erster Stelle muss natürlich mein Betreuer Prof. Dr. John P. Burrows erwähnt werden. Von seiner Leidenschaft und Begeisterung für die Wissenschaft und die Betreuung seine Mitarbeiter kann sich so mancher Professor eine Scheibe abschneiden.

Dieses Projekt wäre schon allein finanziell nicht möglich gewesen ohne die Initiative und die Vermittlung von Dr. Art Aikin. Darüber hinaus hatte ich das Vergnügen und die Freude, in mehreren persönlichen Treffen einen außergewöhnlich sympathischen Kollegen kennenzulernen und viele interessante Gespräche zu führen. Mittlerweile genießt er seinen wohlverdienten Ruhestand. Dennoch hoffe ich, dass noch viele Studenten und Doktoranden wie ich von seiner Erfahrung und Begeisterung profitieren.

Das „Tagesgeschäft“ wurde mit mindestens ebenso großer Hingabe von Dr. Miriam Sinnhuber übernommen. In ihr hatte ich stets eine geduldige und kompetente Ansprechpartnerin sowohl für die langfristige Planung meiner Promotion als auch für die vielen tausend kleinen Fragen und Probleme, die ich während meiner Promotion zu lösen hatte. Wie viele Stunden haben wir damit verbracht, Programmierfehler im Quellcode unserer Routinen zu suchen...

Dank gebührt Prof. Dr. Justus Notholt dafür, mir die Chance zu geben, ein wenig in den universitären Lehrbetrieb hineinzuschnuppern. Seinen wundervoll bissigen Humor habe ich stets genossen. Ich hoffe, selbst nie allzu respektlos ihm gegenüber gewesen zu sein (schade, dass ich die Wette um sein Büro nicht angenommen hatte – gewonnen hätte ich...).

Eine neue Anstellung bringt immer die Befürchtung mit sich, sich im Kreis der neuen Kollegen unwohl oder nicht willkommen zu fühlen. Das war nicht anders, als ich ich 2004 meine Stelle als Doktorand hier Institut für Umweltphysik angetreten habe. Aber gleich vom ersten Tag an habe ich mich hier wohl gefühlt und die Arbeitsatmosphäre genossen. Das gilt insbesondere für die Arbeit mit den Mitgliedern der Arbeitsgruppe um Miriam Sinnhuber, denen ich mich besonders verbunden fühle (in alphabetischer Reihenfolge): Shahin Kazeminejad („ba-ba-beluba“), Nadine Wieters und Holger Winkler (für Euch alles Gute und viel Glück für Eure persönlichen Projekte!).

Darüber hinaus sind im Laufe der Jahre viele nette Kollegen gekommen und gegangen, und mit vielen habe ich die vollen drei Jahre verbracht. Doch trotz ausgiebiger Suche habe ich niemanden gefunden, der nicht ein paar Minuten Zeit für einen unerfahrenen Doktoranden erübrigt hätte. Leider kann ich nicht alle hier nennen, hervorheben möchte ich dennoch einige: Dr. Christian v. Savigny (eine unglaubliche Allgemeinbildung – viel Glück mit der Habilitation!), Dr. Stefan Noël und Dr. Klaus Bramstedt (für die stets geduldige Beantwortung aller meiner Fragen zu SCIAMACHY und dem dazugehörigen Datensatz).

Würde man bei uns im Institut für Umweltphysik auf einen Schlag die Hälfte aller Wissenschaftler entfernen, würde das die Arbeit der übrigen wahrscheinlich nur marginal beeinträchtigen. Ich behaupte aber, dass ein Ausfall von nur vier Personen ausreicht, die Arbeit des Institutes empfindlich zu beeinträchtigen. Namentlich sind dies Petra Horn (neu zu uns gekommen für Sabine Packeiser-Pohl), Heidemarie Krug, Birgit Teuchert und Susanne Themm, die Verwaltungskräfte der Gruppen Burrows und Notholt, mit denen ich des öfteren in finanziellen Angelegenheiten zu tun hatte. Danke für Eure Geduld und Unterstützung!

Es brauchte jedoch nicht nur Menschen aus der Wissenschaft, um mich durch meine Promotion zu bringen. Von Zeit zu Zeit hatte ich es bitter nötig, mal wieder in die „reale“ Welt zurückgeholt zu werden und meine Zeit mit gänzlich unphysikalischen Dingen zu verbringen.

Dabei haben mich tatkräftig unterstützt (eine äußerst unvollständige Liste!): René Bendschneider, Boris Behnke, Stefan Trotzky, Holger Bremer, Katinka Petersen, Jörg Warneke, Michael v. Thaden, Philipp Körner, die gesamte Familie Bendschneider, die gesamte Familie Böse, Janina Timmermann u.v.m.

Weder das Abitur, noch das Studium und schon gar nicht die Promotion wären möglich gewesen ohne die Liebe und Unterstützung meiner Familie und insbesondere meiner Eltern. Danke für alles!

Eine besonders stressige Zeit meines Lebens wurde mir erleichtert durch die wichtigste Person in meinem Leben: meine Sylvia! Danke für Deine Geduld und Deine Liebe!